ISSN :0011-748X

Volume 75, Issue 1, January 2025

Defence Science Journal

https://publications.drdo.gov.in/ojs/index.php/dsj

DRDO

Published by Defence Research & Development Organisation

DEFENCE SCIENCE JOURNAL

A Publication of DRDO

Defence Science Journal is a peer reviewed, bi-monthly, multi-disciplinary defence research journal of the Defence Research & Development Organisation (DRDO), Ministry of Defence, Govt of India, published by the Defence Scientific Information & Documentation Centre, Delhi. It is brought out in the months of January, March, May, July, September, and November. The Journal publishes research papers, review papers, short communications, and research notes in various disciplines of science and technology.

Papers published in the Journal are covered/indexed by-Cambridge Scientific Abstracts, Chemical Abstracts, Embase, Compendex, Geobase, Embiology, Elsevier Biobase, Fluidex, World Textiles, Scopus, Indian Science Abstracts, International Aerospace Abstracts, Science Citation Index, Omnifile Full-text Mega, Omnifile Full-text Select, ProQuest, World News Connection, Google Scholar, Indian Citation Index. Online published papers are assigned with Digital Object Identifier (DOI).

Editorial Desk
Ph: 011-2390 2469/65/64
E-mail: dsj.desidoc@gov.in

Printing
Mr. Rajesh Kumar Singh

For New Subscription, Renewals, Inquires, and Cheque Address
Ms. Dipti Arora
DESIDOC, Metcalfe House, Delhi-110 054
Ph: 011-2390 2612 ; Fax: 011-2381 9151
E-mail: marketing.desidoc@gov.in

Annual Subscription

₹ 3000.00 (INR)

(*Discount: 15 % to Publishers, Vendors and Individuals*)

Subscription to be paid in advance by bank draft in the favour of **Director, DESIDOC**. Local subscribers may pay by cheque, payable at Delhi.

Current and back issues are available at: **https://publications.drdo.gov.in/ojs/index.php/dsj**

CODEN: DSJOAA

ISSN: 0011-748X (Print)
ISSN: 0976-464X (Online)

DEFENCE SCIENCE JOURNAL

VOLUME 75 **NUMBER 1** **JANUARY 2025**

IN THIS ISSUE

Missile Systems

Naval Systems

Defence Science Journal, Vol. 75, No. 1, January 2025, pp. 3-9, DOI : 10.14429/dsj.19883

Aerodynamic Impacts of Convergent Slot Implementation on Hinged and Morphed NACA 0012 Airfoil Operating at a High Reynolds Number

Ravi Kumar and Santanu Ghosh*

Department of Aerospace Engineering, IIT Madras, Chennai – 600 036, India
**E-mail: sghosh1@smail.iitm.ac.in*

ABSTRACT

Trailing-edge modifications on the NACA 0012 airfoil for lift enhancement are numerically investigated at a Reynolds number 4.58×10^6. Specifically, three variations in the trailing-edge geometry are tested: a hinged flap with hinge location at 70 % of chord, and two variations of continuous camber-morphed trailing edge: from 70 % chord to 100 % chord and from 70 % chord to 90 % chord. Reynolds-Averaged Navier-Stokes (RANS) simulations are performed using ANSYS Fluent with Menter's SST k-ω two-equation turbulence model. Predictions of aerodynamic characteristics reveal that the continuous morphing of trailing edge enhances lift generation and improves aerodynamic efficiency compared to the hinged flap. Further, for an angle of attack of 10^{o}, it is shown that boundary-layer separation is less for both camber-morphed trailing-edge configurations compared to hinged flap configuration. The introduction of a convergent slot just upstream of the hinge/start-of-morphing location results in the elimination of flow separation in all cases, and improved aerodynamic efficiency, especially for the hinged-flap configuration.

Keywords: Aerodynamic efficiency; RANS, Camber-morphed flap; Convergent slot; Flow separation

NOMENCLATURE

c	: Chord length
LE	: Leading edge
TE	: Trailing edge
M	: Mach number
Re	: Reynolds number
β	: Flap angle
k	: Turbulence kinetic energy
ω	: Specific rate of diffusion
b	: Trailing edge flap length
c_l	: Sectional coefficient of lift
c_d	: Sectional coefficient of drag
c_p	: Coefficient of pressure
$\varphi(x)$	: Polynomial expression for morphing surfaces
x/c	: Running distance in stream-wise direction
y/c	: Running distance in transverse direction

1. INTRODUCTION

Lift augmentation in wings can be achieved by using trailing-edge flaps, which effectively change the camber of the wing section discretely when the flap is deflected. An alternative to using flaps or discrete camber morphing is the application of continuous camber morphing near the trailing edge Daynes[1], *et al.* The concept of morphing in aircraft has been developed by observing the ability of insects and birds to change their wing shape during flight in a wide range of situations. Various morphing techniques include changing the camber of the wing section (airfoil) (Daynes[1], *et al.*), increasing the planform area (Skillen[2], *et al.*), bending (Lingling[3], *et al.*) and twisting (Aso[4], *et al.*) the wing in a lateral direction, etc. Parker[5], dealt with the problem of the narrow speed range of an airplane using camber morphing. Specifically, he increased the maximum speed by varying the camber of a wing surface using loads and thus presented the Parker variable wing configuration in a biplane or triplane aircraft. Spillman[6], *et al*. showed that using variable camber flaps on NACA 64012 at cruise conditions reduces drag by 23 %. Dhileep[7], *et al.* investigated the aerodynamic characteristics of NACA 0012 airfoil morphed using a Single Corrugated Variable-Camber (SCVC) morphing technique and found that in terms of aerodynamic efficiency and endurance factor morphing is beneficial for moderate to high lift requirements. Woods[8], *et al.* proposed the Fishbone Active Camber Concept (FishBAC) based on the Euler-Bernoulli beam theory for deformation, and it was found that the FishBAC airfoil has much lower drag and higher lift than a hinged flap airfoil. In the recent past, Kumar[9], *et al.* studied the combined effect of morphing and corrugation on the airfoil surface. It is found that corrugated camber-morphed airfoils are more efficient than the conventional hinged flap but less efficient than the smooth skin morphed airfoil for all sets of low to medium values of angles of attack when operated at high Reynolds number. Jawahar[10], *et al.* studied aerodynamic performance, pressure distribution, etc., for various trailing edge camber profiles applied to the NACA 0012 airfoil at different angles of attack at a moderate Reynolds number of 0.35 million. The authors reported improved aerodynamic performance with flow separation, which shifted downstream at higher angles of attack for the cambered flap.

Received : 06 February 2024, Revised : 06 August 2024
Accepted : 24 September 2024, Online published : 10 January 2025

For controlling flow separation and managing the boundary layer over the airfoils, numerous methods have been studied in the past. One of the passive methods considered is the use of slotted airfoils, which was first introduced to enhance the lifting characteristics of airplane wings by Parker[5] and Weick[11], *et al.* This method involves a slot that extends from the pressure side of the airfoil to the suction side. Due to the pressure difference between these sides, air flows through the slot, injecting momentum into the boundary layer on the suction side, thus improving aerodynamic performance. In the recent past, researchers Fawzi[12], *et al.* worked to enhance airfoil efficiency for applications in wind turbines, aircraft, propellers, and helicopters by using a slotted airfoil to overcome flow separation at high angles of attack. Numerical simulations with ANSYS Fluent showed that the optimised slotted design significantly increases the lift-to-drag ratio and delays stall, with the most effective slot configuration found at 60 % chord, 65° slope, and 1 % chord width. Whitman[13], *et al.* examined the impact of various configurations of the slot on the stall angle for an airfoil similar to the NACA 65(3)-618. Results show that slotted airfoils generate higher lift coefficients above 15° and lower drag coefficients at low angles of attack compared to a solid airfoil, with the small slotted airfoil performing best at high angles of attack. Beyhaghi[14], *et al.* introduced a narrow span-wise slot near the leading edge of a cambered airfoil to study its aerodynamic performance impact. Using NACA 4412 as the baseline and varying slot parameters at a Reynolds number of 1.6 million, CFD simulations and wind tunnel experiments show that optimal slot configurations can improve lift by up to 30 % with minimal drag penalty across various angles of attack.

This paper compares the aerodynamic performance of three different trailing-edge modifications: a discrete linear hinged flap with a hinge location at 0.7c and two variations of continuous trailing-edge camber-morphing that extend from 0.7c - 1.0c and from 0.7c - 0.9c on the NACA 0012 airfoil, for a Reynolds number of 4.58×10^6 and a fixed trailing-edge deflection of 10° using numerical simulations. The reason for using a continuous camber-morphing configuration that has the last 10 % of the chord unmorphed is due to the following: In general camber-morphing wing designs, the morphing is generally introduced in such a way that some portion of the airfoil trailing-edge is kept unmorphed Woods[8], *et al.* to ensure the structural integrity of the wing during the wide range of flight conditions.

Further, the effect of a slot (that connects the pressure side to the suction side of the airfoil) introduced just upstream of the hinged/morphed trailing edge is investigated. Specific attention is provided to the flow simulation with an angle of attack of 10°, which is typical for the take-off flight stage, wherein the deployment of the flaps is required for augmenting lift and lowering stall speeds.

2. METHODOLOGY

2.1 Model Setup & Computational Details

The baseline NACA 0012 airfoil coordinates are taken from the website www.airfoiltools.com. The airfoil with hinged flap has a hinge location at 0.7c and is constructed using the method as described in Jawahar[9], *et al.* The coordinates of the camber-morphed trailing edge, in which the morphing starts at 0.7c, are generated using a cubic polynomial, Eqn. (1-3), defined in Daynes[1], *et al.*

$$w(x) = \varphi(x) \sin(\beta) \quad (1)$$

$$\varphi(x) = 0 ; \qquad 0 \le x < c\text{-}b \quad (2)$$

$$= \frac{(c-x-b)^3}{b^2} ; \qquad c\text{-}b \le x < c \quad (3)$$

where,

$w(x)$: Change in the baseline airfoil's y-coordinate
$\varphi(x)$: Cubic polynomial for morphing
β: Flap deflection angle in radians
x: Chord wise position
b: Trailing-edge flap length
c: Chord length

Figure 1(a) shows the trailing-edge geometry for the baseline NACA 0012 airfoil along with the trailing-edge modifications investigated in this work. For all the simulations presented in this work that involve trailing edge modification, either with a hinged-flap or camber morphing, a positive trailing edge deflection of 10° was considered. Reynolds-Averaged Navier-Stokes (RANS) simulations for flow at Re: 4.58×10^6 and M: 0.1969 are performed using ANSYS Fluent using the steady pressure-based solver with Menter's Shear Stress Transport (SST) k-ω turbulence model. Least squares cell-based gradient, and a second-order upwind scheme are used to discretize the viscous and inviscid terms in the momentum equations, whereas a first-order upwind scheme is employed to discretize turbulent kinetic energy and dissipation rate terms. A C-type domain has been used for the simulations (shown in Fig. 1(b) with boundary conditions indicated), and a 2-D structured mesh is generated for all the cases, as shown in Fig. 1(c), using commercially available grid generation software, Pointwise V17.3 R3. In the wall-normal direction (Fig. 1(d), the grid is stretched, with the y^+ value of the first node from the airfoil surface being less than unity for most of the airfoil length to resolve the laminar sub-layer.

2.2 Domain and Grid Convergence

Three sizes of the computational domain (10c, 30c, and 100c) are tested to check for domain size convergence, and it is found that the lift coefficient hardly changes when the domain size varied from 30c to 100c, as observed in Fig. 2(a). As such, a domain of 30c is considered for the study presented herein. A grid-convergence study (Fig. 2(b)) is performed for the baseline, hinged-flap, and the two variations of camber-morphed configurations with the number of grid nodes ranging from 8,660 to 562,080 and a mesh with 34,920 grid nodes was chosen. Also, a grid convergence test is performed (Fig. 2(c)) for the slotted configurations (slotted hinged, and slotted camber-morphed) trailing edge with the number of grid nodes ranging from 16,324 to 754,062 and a mesh with 55,567 grid nodes was determined to be sufficient. The grid resolution studies are shown for an angle of attack (α) of 10°. A grid was determined to have sufficient resolution for a particular case (baseline or with camber morphed trailing edge etc.) if further refinement of the grid did not produce any appreciable change

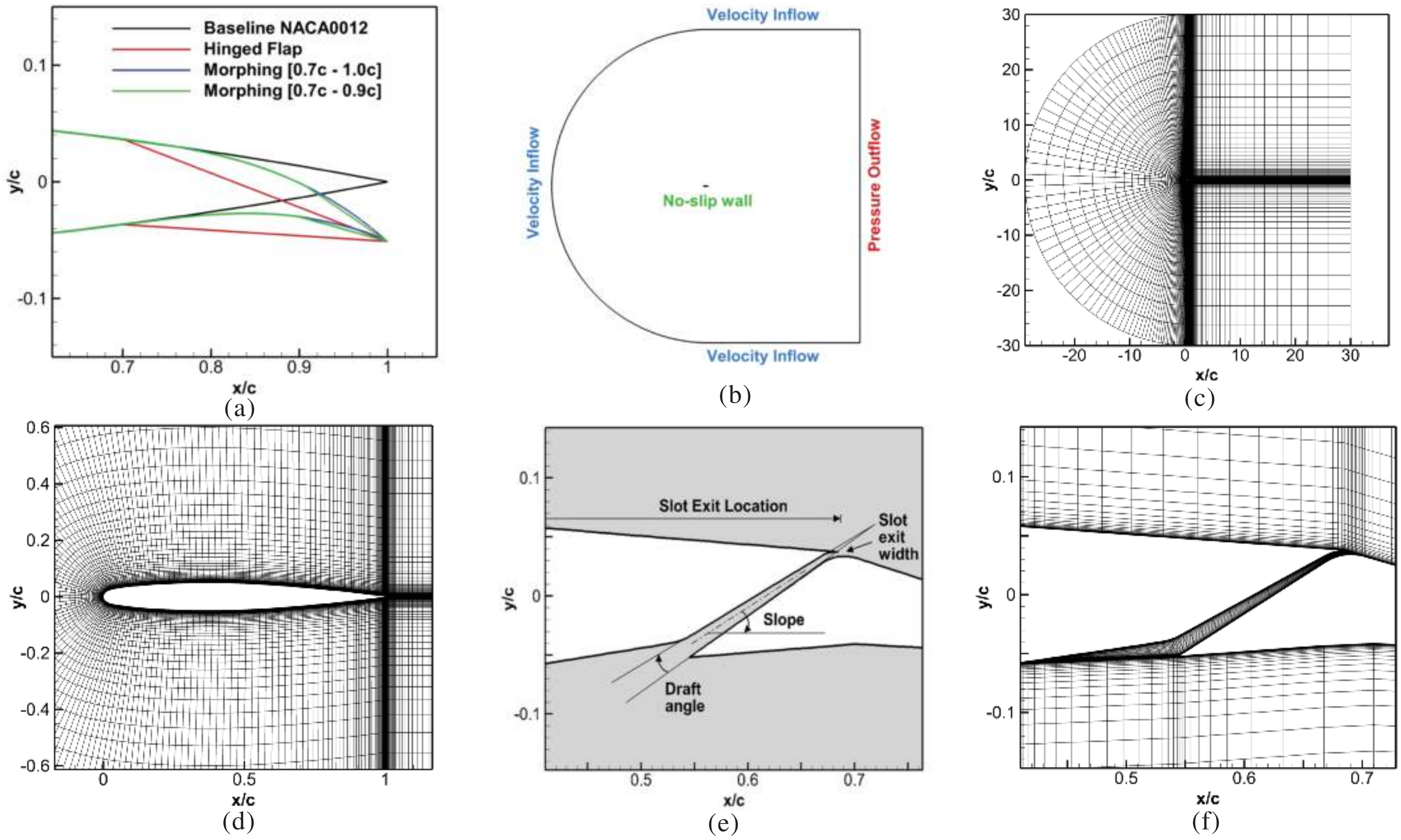

Figure 1. (a) Trailing-edge geometry of baseline and other configurations of NACA 0012 airfoil (10° TE deflection for hinged and camber-morphed airfoils); (b) C-type domain used for the computations; Structured mesh for (c) Full domain, (d) Near the airfoil; (e) Geometry of the slot; and (f) Structured mesh in and around the slot. For clarity, alternate grid nodes are omitted.

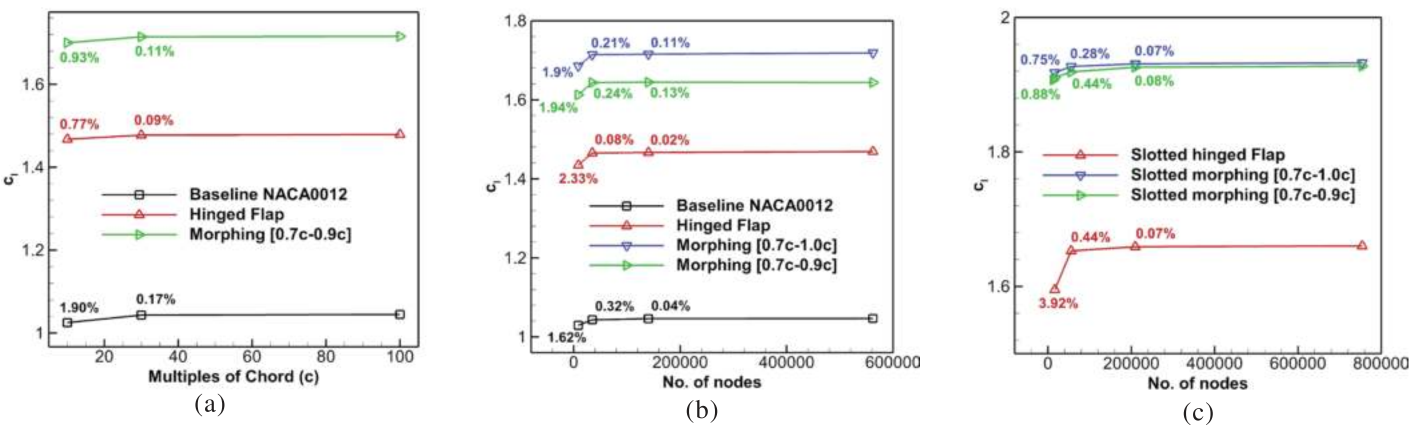

Figure 2. (a) Domain-size convergence test; Grid convergence tests for (b) Non-slotted airfoils and (c) Slotted airfoils.

(more than 5 %) in the lift coefficient. The percentage change in the c_l value compared to c_l of the most refined mesh is also illustrated in Fig. 2.

2.3 Slot Design

For finalising the contour of the converging type (non-linear) trailing edge slot for all three cases (hinged and two morphed configurations), a total of three parameters are considered: slope, draft angle, and slot exit width, as shown in Fig. 1(e). The different values of the parameters for which the slot effectiveness is checked for getting the maximum value of c_l are summarized in Table 1. On simulating the slot geometry for various combinations of the discrete values of the three parameters provided in the table below (a total of 80 cases), the best combination for the optimised geometry is determined to be 30°-4°-0.004c (written in the sequence: slope–draft angle–

Table 1. Parameters considered for the slot geometry optimisation

Parameters	Values
Slope	15°, 20°, 25°, 30° and 35°
Draft angle	2°, 4°, 6° and 8°
Slot exit width	(0.003*c*, 0.004*c*, 0.005*c*, 0.006*c*)
Slot exit location	0.7*c* (Fixed)

slot exit width). The "best" values of the parameters are found by varying only one parameter at a time.

For all these cases, the slot exit location is set at 0.7*c*, which corresponds to the root location of the hinged flap/camber-morphed trailing edge. The entry and the exit geometry of the slot were kept smooth to avoid flow separation at those locations. Fig. 1(e) shows the optimised slot geometry and Fig. 1(f) shows the structured mesh in and around the slot.

A convergent slot is chosen so that the flow accelerates through the slot while exiting (like a nozzle working at subsonic flow regime) tangentially to the suction surface and energizes the near-surface flow on the upper airfoil surface downstream

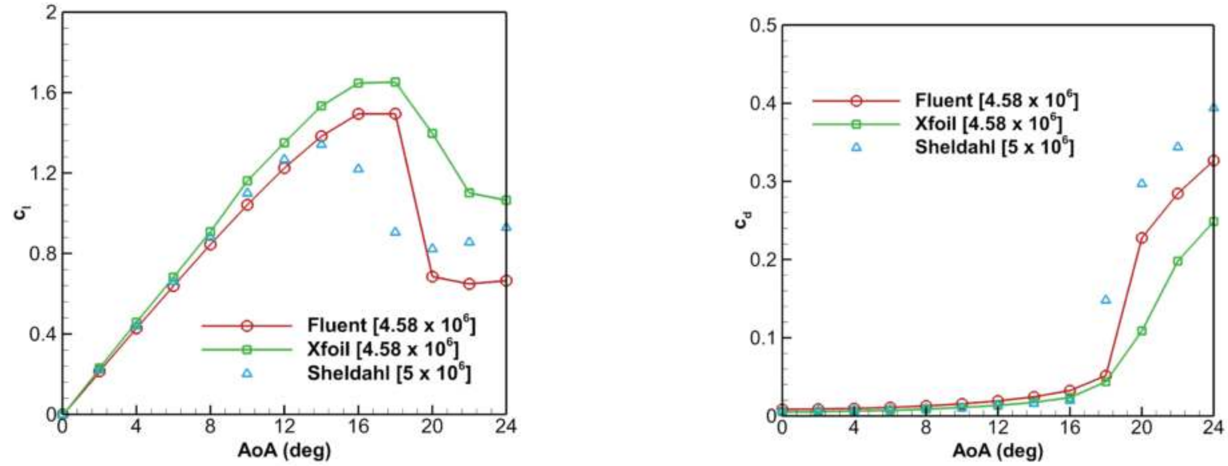

(a) (b)

Figure 3. c_l **and** c_d **comparisons of Fluent with Xfoil predictions at Re: 4.58 × 10**^{6} **and experimental data at Re: 5×10**^{6} **(Sheldahl[15], *et al.*).**

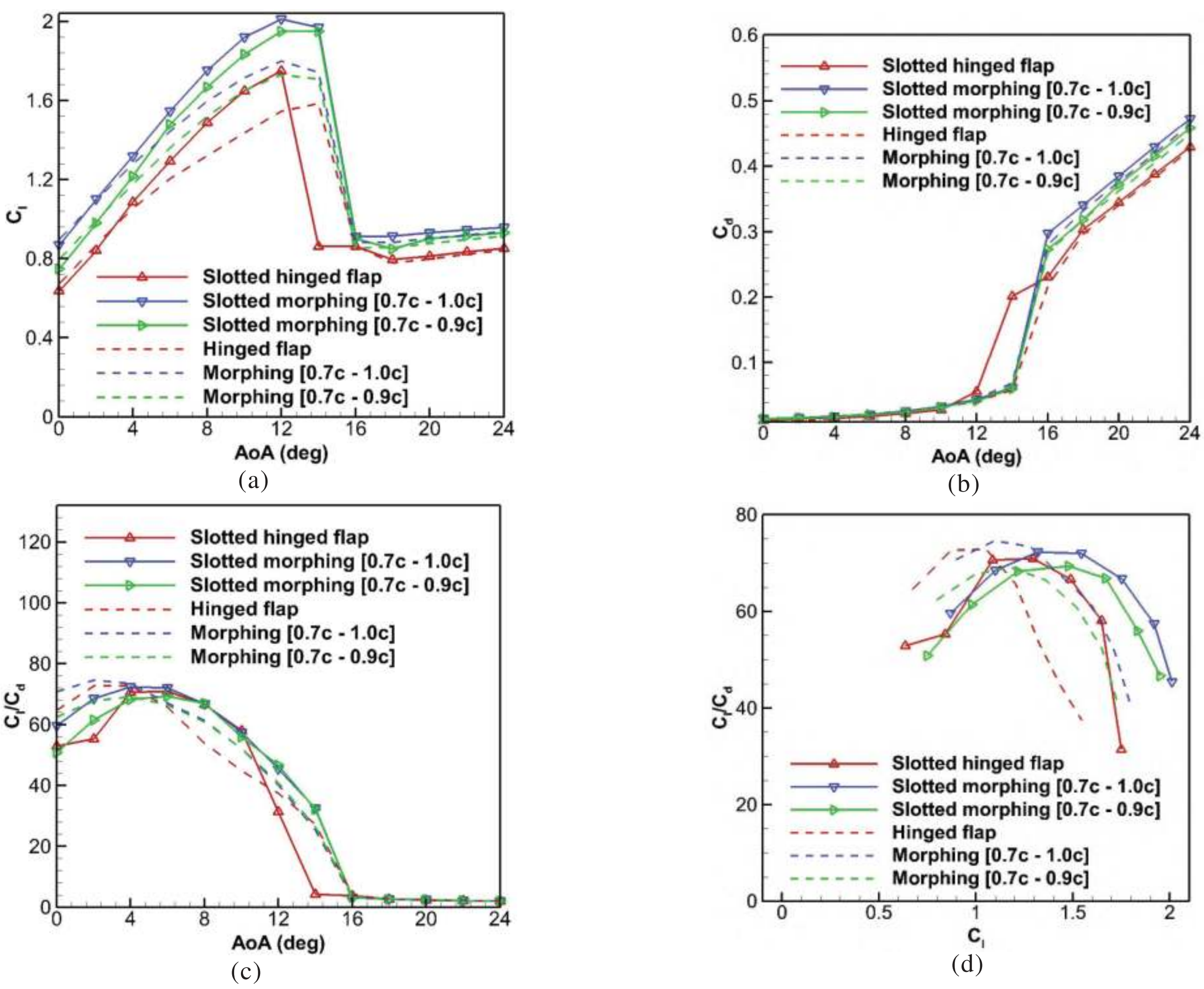

Figure 4. (a) c_l **vs** α**; (b)** c_d **vs** α**; (c)** c_l/c_d **vs** α **and (d)** c_l/c_d **vs** c_l **comparisons among the slotted hinged and slotted camber-morphed airfoils.**

Table 2. Comparison of lift (c_l), drag (c_d), and their ratios (c_l/c_d) for airfoils with different trailing-edge shapes with a slot (α: 10°); the change in values from the no-slotted cases are also included in parenthesis for reference

	Baseline NACA 0012	Hinged flap	Camber-morphed [0.7*c*-1.0*c*]	Camber-morphed [0.7*c*-0.9*c*]	Slotted hinged flap	Slotted camber-morphed [0.7*c*-1.0*c*]	Slotted camber-morphed [0.7*c*-0.9*c*]
c_l	1.04	1.43	1.71	1.65	1.65 (+0.22)	1.92 (+0.21)	1.83 (0.18)
c_d	0.0144	0.0321	0.0330	0.0316	0.0285 (-0.0036)	0.0334 (+0.0004)	0.0328 (+0.0012)
c_l/c_d	72.5	44.72	51.95	52.24	57.95 (+8.23)	57.38 (+5.53)	55.96 (+3.72)

of the slot that can help to delay/eliminate the flow separation near the airfoil trailing edge.

3. RESULTS AND DISCUSSION

3.1 Validation

For validating the computational setup, numerical predictions of lift (c_l) and drag coefficients (c_d) of the baseline NACA 0012 airfoil are compared with results from Xfoil and experimental data reported in the work by Sheldahl[15], *et al.* It can be observed from Fig. 3(a) and 3(b) that the present computations are in fair agreement with the result from Xfoil and literature until the stall is reached. Further, for angles of attack post-stall, the CFD predictions are observed to be closer to the experimental data. However, at low to moderate angles of attack, higher drag is predicted by the CFD computations compared to both Xfoil predictions and the experimental data[15]. This can be due to the fact that flow transition is not accounted for in the present computations.

3.2 Aerodynamic Performance

For the case of non-slotted airfoils, as observed in Fig. 4(a) and Table 2, the coefficient of lift (c_l) is enhanced by the introduction of a hinged flap (having a flap deflection of 10°) in the baseline airfoil. This is expected as the flap increases the effective camber of the airfoil. Compared to the hinged flap configuration, however, the camber-morphed airfoils (having a flap deflection of 10°) generate higher lift values for all the angles of attack (α). The camber-morphed [0.7*c*-1.0*c*] configuration is seen to generate slightly higher lift values than the camber-morphed [0.7*c* -0.9*c*] configuration. The coefficient of drag (c_d) values (Fig. 4(b)) with the trailing-edge modifications is also higher than that for baseline airfoil, which is expected as the trailing edge modifications introduce an effective camber. Minor differences, if any, are only observed in the predicted drag coefficients among the airfoils with trailing edge modifications at least still, the airfoil stalls.

From Fig. 4(c), observation can be made that the aerodynamic efficiency (c_l/c_d) of the hinged-flap airfoil lies between the smooth morphed [0.7*c* - 1.0*c*] and the smooth morphed [0.7*c* - 0.9*c*] configurations at low angles of attack (α < 6°). However, at higher angles of attack, the airfoils with smooth morphed trailing edges perform better than the hinged-flap configuration.

It can also be observed that the maximum value of (c_l/c_d) does not change appreciably with trailing edge deflection. Fig. 4(d) shows the comparison of aerodynamic performance (c_l/c_d) with respect to lift coefficient (c_l) among all the airfoils. It can be seen that for high values of the lift coefficient (c_l >1.2), the airfoils with smoothly morphed trailing edge perform much better than the airfoil with hinged trailing edge flap. The lift augmentation achieved with the trailing edge deflections (hinged flap or camber morphing) compared to the baseline airfoil is also clear from this plot. When comparing with the slotted airfoils, it can be observed from Figs. 4(a), 4(c), and Table 2, that the introduction of the slot resulted in improvements in c_l and c_l/c_d when compared to the non-slotted cases.

For the angle of attack (α) less than 10°, no perceptible change in c_d is observed in Fig. 4(b) when compared to the corresponding non-slotted configurations. However, from Table 2, it is evident that while the drag increases slightly with the introduction of the slot for the smooth morphed trailing edges, it drops for the hinged-flap trailing edge configuration. The stall angle remains unchanged for both the morphed trailing edge configurations: [0.7*c*-1.0*c*] and [0.7*c*-0.9*c*].

3.3 Pressure Distribution

To further investigate the reason for the difference in the lift generated by the different non-slotted trailing-edge configurations, the c_p plot at an angle of attack (α) of 10° is plotted in Fig. 5(a). It can be observed from the plot that for the airfoil portion aft of the hinge location, i.e., $x/c \geq 0.7$, c_p values for the camber-morphed flaps are higher than for the hinged flap airfoil on the pressure surface, and lower on the suction surface, which results in generation of higher normal force and consequently higher lift. This clearly suggests that camber-morphing enhances lift compared to a hinged flap.

Also, from the plot, it can be observed that the pressure recovery on the suction surface of camber-morphed airfoils happens further downstream compared to the hinged flap case, which is expected to delay flow separation on the suction side. The c_p plot for the slotted configurations shown in Fig. 5(b) indicates that c_p values between the upper (suction) and the lower (pressure) airfoil surfaces for the slotted airfoil cases have increased for all the three modifications aft of the slot as compared with non-slot cases (Fig. 5(a)). This explains the generation of the higher lift values for this case compared to the non-slot configurations.

3.4 Flow near the trailing-edge

As observed in Fig. 6, lift-augmentation with a hinged-flap (Fig. 6(a)) or continuous camber morphing (Fig. 6(b)

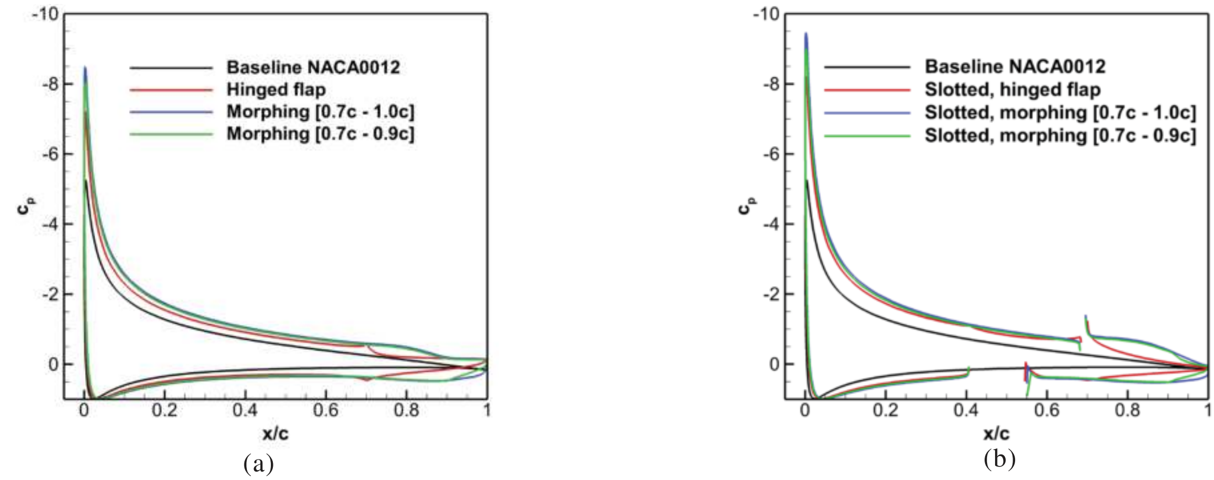

Figure 5: c_p comparison for (a) non-slotted and (b) slotted airfoil configurations (α: 10°).

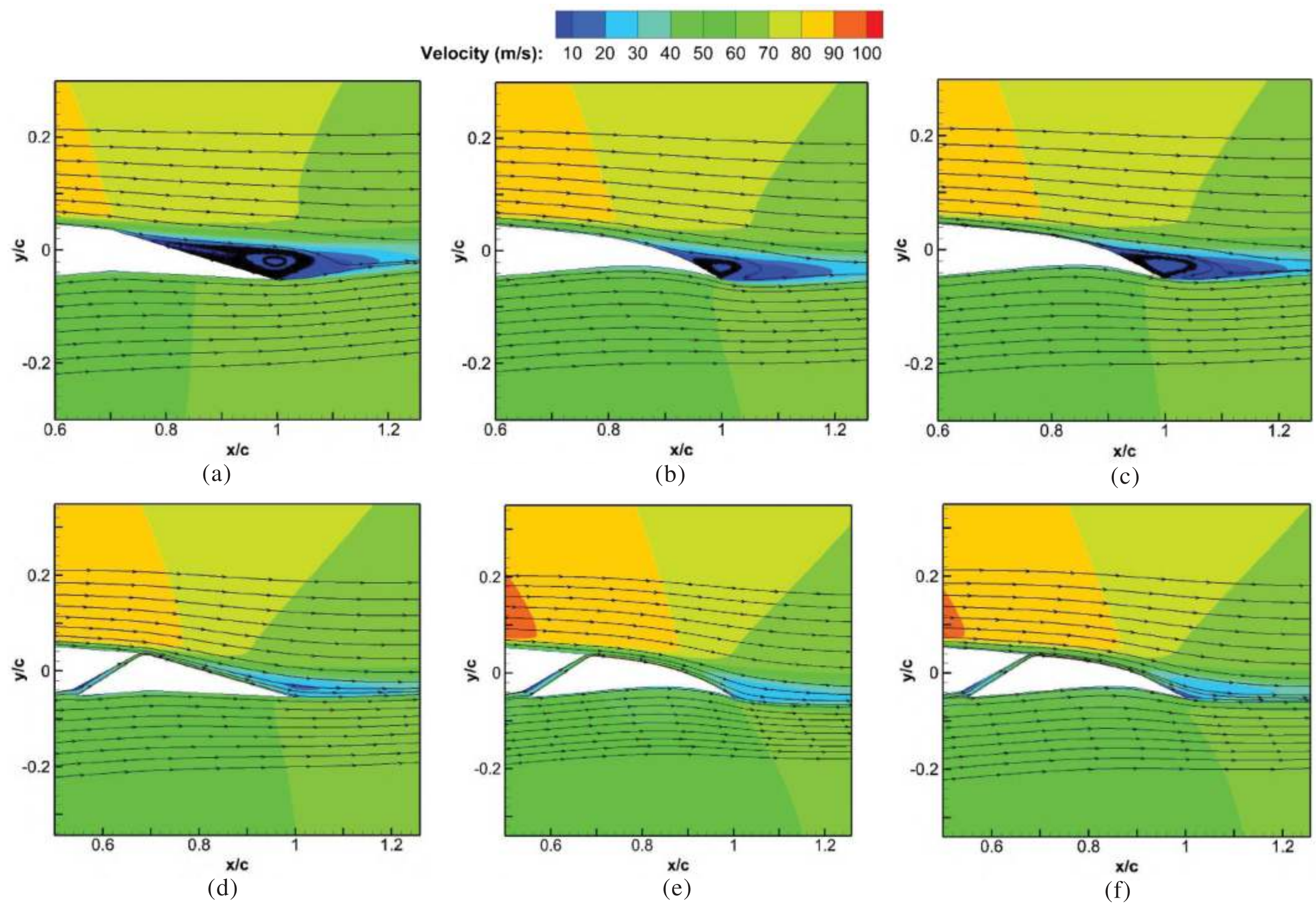

Figure 6. Velocity contours with streamlines for non-slotted airfoils (a) to (c) and for slotted airfoils (d) to (f) with different trailing edge modifications (α: 10°). (a) Hinged flap; (b) Camber-morphing [0.7c-1.0c]; (c) Camber-morphing [0.7c-0.9c]; (d) Slotted hinged flap TE; (e) Slotted camber-morphing [0.7c-1.0c]; (f) Slotted camber-morphing [0.7c-0.9c].

and Fig. 6(c)) of the trailing edge results in flow separation near the trailing edge at α: 10°. In order to investigate whether boundary-layer blowing can nullify the separation and improve the aerodynamic performance of the airfoil with trailing edge deflection, a convergent slot (as discussed in Section 2.3) is introduced just upstream of the start of the hinge/morphing location. With the introduction of a slot, which acts as a flow-separation passive control method for all the three modifications of the airfoil trailing edge, the flow separation is seen to be fully eliminated at the trailing edge as observed in Fig. 6(d), Fig. 6(e) and Fig. 6(f). The contours shown are presented for an angle of attack (α) of 10°.

4. CONCLUSION

Numerical investigations of flow past NACA 0012 airfoil are presented in this work that compare the efficacy of continuous camber-morphing (of the trailing edge) to a hinged flap at a high Reynolds number of 4.58 million. Results show that smooth camber-morphing of the trailing edge results in higher lift and (in most cases) better lift-to-drag ratios compared to the use of a hinged flap. Further, investigation of flow streamlines near the trailing edge at an angle-of-attack of 10^o, which is a typical value for aircraft take-off, reveal that flow separation is less with the use of continuous camber morphing than with the use of a hinged flap. Both effects are more pronounced when the morphing is carried out from 70 % of the chord all the way to the trailing edge. With the introduction of a convergent non-linear slot whose exit is fixed near the hinge/start-of-morphing location for both hinged and morphed trailing-edge configurations of the NACA 0012 airfoil, flow separation is eliminated, and lift generation is enhanced. The study shows that continuous camber morphing has the potential to improve aerodynamic performance during take-off/landing at high Reynolds number, which can be of interest for the passenger aircraft industry and large UAVs.

REFERENCES

1. Daynes, S. & Weaver, P.M. A morphing trailing edge device for a wind turbine. *J. Intelligent Material Syst.*, 2012, **23**(6).
doi:10.1177/1045389X12438622
2. Skillen, M.D. & Crossley, W.A. Morphing wing weight predictors and their application in a template-based morphing aircraft sizing environment II. NACA Report No. 20080009778. February 2009.
3. Chu, L.; Li Q.; Gu F.; Du X.; He Y. & Deng Y. Design, modeling, and control of morphing aircraft. *Chinese J. Aeronautics*, 2022, **35**(6), 220-246.
doi:10.1016/j.cja.2021.09.013
4. Aso, A.; Perrey, M. & Tanaka, H. Experimental study on wing twist-morphing structure using a double-tube cylinder. *Japan Soc. Aeronautical and Space Sci.*, 2017, **15**(a1-a6).
doi:10.2322/tastj.15.a1
5. Parker, H.F. The variable camber wing. NACA Report No. 77, 1920.
6. Spillman, J.J. The use of variable camber to reduce drag, weight and costs of transport aircraft. *The Aeronautical J.*, 2016, **96**(951), 1-9.
doi:10.1017/S0001924000024404
7. Dhileep, K.; Kumar, D.; Gautham Vigneswar, P.N.; Soni, P.; Ghosh, G.; Ali, S.F. & Arockiarajan, A. Aerodynamic study of single corrugated variable-camber morphing aerofoil concept. *The Aeronautical J.*, 2021, **126**(1296), 316-344.
doi:10.1017/aer.2021.71
8. Woods, B.K.S. & Friswell, M.I. Preliminary investigation of a fishbone active camber concept, ASME 2012 Conference on Smart Materials, Adaptive Structures and Intelligent Systems, *SMASIS,* 2013, pp. 555-563.
doi:10.1115/SMASIS2012-8058
9. Kumar, R. & Ghosh, S. Numerical investigation of the trailing edge morphing using corrugated skin at a high reynolds number for NACA 0012 & NACA 64(1)-612 airfoils, AIAA Aviation 2023 forum- Applied Computational Fluid Dynamics III.
doi:10.2514/6.2023-4088
10. Jawahar, H.K.; Ai, Q. & Azarpeyvand, M. Experimental and numerical investigation of aerodynamic performance for airfoils with morphed trailing edges. *Renewable Energy*, 2018, **127**(1), 355-367.
doi:10.1016/j.renene.2018.04.066
11. Weick, J.A. The effect of multiple fixed slots and a trailing-edge flap on the lift and drag of a Clark Y airfoil. NACA Report No.427, 6, 1933
12. Fawzi, S. & Ali, A. H. Slot design procedure for a NACA 4412 at high angle of attack. *J. Mech. Engine. Res. and Developments*, 2021, **44**(8), 188-203.
doi:10.13140/RG.2.2.18732.54402
13. Whitman, N.; Sparks, R.; Ali, S. & Ashworth, J. Experimental investigation of slotted airfoil performance with modified slot configurations. *In* Applied Aerodynamics Conference, 2012.
doi:10.2514/6.2006-3481
14. Beyhaghi, S. & Amano, R.S. Parametric study on LE slots used on wind turbine airfoils at various angles of attack. *J. Wind Engine. Industrial Aerodynamics*, 2018, **175**, 43-52.
doi:10.1016/j.jweia.2018.01.007
15. Sheldahl, R.E. & Klimas, P.C. Aerodynamic characteristics of seven symmetrical airfoil sections through 180° angle of attack for use in aerodynamic analysis of vertical axis wind turbines. Sandia National Laboratories Energy Report No. SAND-80-2114, 1981.
doi:10.2172/6548367

CONTRIBUTORS

Mr Ravi Kumar is currently pursuing a PhD in the Department of Aerospace Engineering at the IIT, Madras, India. His research focuses on the investigation of camber-morphing at both the wing and system levels for applications in low and high-speed flows, utilising Computational Fluid Dynamics (CFD).
For the current study, he has worked on the conceptualisation of the problem, performed numerical simulations, presented the results through plots and tables, drafted the initial version of the manuscript and worked on corrections suggested by the reviewers.

Dr Santanu Ghosh obtained his PhD from North Carolina State University (NCSU), United States of America and working as an Associate professor in the Department of Aerospace Engineering at the IIT, Madras, India.
In the current study, he has provided resources for the study, co-drafted the initial version of the manuscript and edited the final versions pre- and post- review.

Defence Science Journal, Vol. 75, No. 1, January 2025, pp. 10-18, DOI : 10.14429/dsj.20038

Acoustic Modality in Passive Detection Technology

Meshram Devendra M.[#,*] and Pushpa Mala S.[$]

[#]DRDO-Aeronautical Development Establishment, Bengaluru - 560 075, India

[$]Dayananda Sagar University, Harohalli, Bangalore 562112, India

[*]E-mail: m.devendra.ade@gov.in

ABSTRACT

Utilising the acoustic modality for passive detection and localisation of low-flying aircraft and gunshots is vital for border security and situational awareness. This paper presents a comprehensive experimental approach for detecting and estimating the direction of arrival of a single acoustic source using a single vector sensor and two different algorithms: acoustic intensity and velocity covariance. The study includes a thorough comparison of both algorithms for the direction of arrival estimation of a stationary continuous sound source, a hovering drone, and a propeller-driven two-seater manned aircraft flying at low altitudes in various environments. The research findings, which show that both algorithms provide similar estimates for the direction of arrival of the acoustic target in the frequency and time domains, provide a solid foundation for further exploration. Additionally, the results of an array of scalar sensors towards the direction of arrival estimation, using the cross-correlation method at the lab level, are also presented to complement the acoustic vector sensor. A system built around acoustic vectors and scalar sensors can serve as a passive surveillance and target detection system, providing a comprehensive solution for defence and acoustics.

Keywords: Direction of arrival; Acoustic vector sensor; Detection; Localization; cross-correlation

1. INTRODUCTION

During World War I, humans utilised mechanical waves to enhance situational awareness in aerial battlefield settings[1]. However, radar technology advancements displaced mechanical waves in surveillance applications. The emergence of radar-evading low-flying threat platforms such as small fixed-wing manned aircraft, helicopters, and the increasingly prevalent drones of various configurations has contributed to the resurgence of the acoustic. The acoustic signal propagation characteristics of helicopters, propeller aircraft, and Unmanned Aerial Vehicles (UAVs) are significant for two reasons. Firstly, these aircraft can be used for hostile actions on land and sea-based infrastructure because they can fly at low altitudes, making them difficult to detect by air defence radar[2-3]. Secondly, their sound can be used to passively detect and locate them over land[3-7] and sea. Additionally, modern Digital Signal Processing (DSP) hardware and advanced algorithms allow for real-time computations of acoustic measurements[5-6].

Acoustic waves in the air can be captured to extract signal characteristics and gain insights into the source. This passive approach uses acoustic receivers at strategic points to capture sound emissions. It offers a cost-effective solution for applications that include target detection, bearing estimation, localization, classification, and optical sensor cueing. The critical components in acoustics are pressure, particle velocity, and density. Notably, while particle velocity is familiar in acoustics, implementing true particle velocity sensors is a recent development. The Microflown sensor, a key technological advancement, has made it possible to measure the true particle velocity. Particle velocity is a vector quantity and is a crucial aspect of a sound wave, combined with pressure, which is a scalar quantity. Due to the additional information it provides, the Microflown sensor has become popular in noise source detection and localisation in the automotive industry[8]. In recent years, research has significantly increased, focusing on using acoustic methods to detect and locate low-flying aircraft in defence and civil sectors[9-11].

H-E de Bree[4], *et al.* experimentally showed that the spaced pressure probe concept could find a single source's bearing, elevation, and range with advanced processing. The spaced Acoustic Vector Sensor (AVS) concept can find the bearing, elevation, and range of a single source with simple processing and the bearing, elevation, and range of two sources with advanced processing. H-E de Bree[4], *et al.* presented that a single Acoustic Vector Sensor (AVS) can easily give a bearing estimate of a gunshot using the intensity method and that the upper limit to find the location of uncorrelated sources is (4n-2) where n is the number of AVS's. Sutin[12], *et al.* used a cluster of microphones and geophones known as an Acousto Seismic Air Detection (ASAD) system for the detection, bearing estimation, and classification of low-flying targets. Mezei, *et al.* employed two approaches - the audio fingerprints technique and correlation analysis methods - for sound detection of drones[13]. Harvey[14], *et al.* experimentally demonstrated a non-cooperative aircraft collision avoidance system using an

Received : 17 May 2024, Revised : 18 July 2024
Accepted : 23 September 2024, Online published : 10 January 2025

acoustic sensing system comprising a pair of microphones fixed onboard drones. Blanchard*, et al.* exploited the intrinsic harmonic structure of the sound emitted by the UAV using a pitch detection algorithm and selective bandpass filtering for localization and tracking of multi-rotor UAVs using an array of microphones[15]. Fang*, et al.* proposed and demonstrated the detection of slow-moving UAVs by implementing a biologically inspired vision approach to acoustic detection methods[16]. Grumiaux*, et al.* used neural network-based sound source localization of single and multiple targets in indoor environments[17]. Zhang[18]*, et al.* explored the benefits of combining acoustic characteristics of different aircraft with Automatic Dependent Surveillance-Broadcast (ADS-B) for detecting single and multi-engine aircraft within a range of 5 km to 7.5 km.

The study of the positioning of Acoustic Vector Sensors (AVS) and microphone arrays about Earth's magnetic field is critical in accurately estimating the Direction Of Arrival (DOA) and tracking air targets. Comparing time domain and frequency domain intensity-based algorithms, as well as intensity-based and velocity covariance-based algorithms in the frequency domain using AVS for various air targets in different environments, has yet to be thoroughly explored. A simple and effective method is developed to ensure the precise alignment of AVS with the Earth's magnetic field, leading to consistent and reliable DOA estimation, particularly in identifying the azimuth angle of UAVs/drones.

Through a series of experiments, this research successfully demonstrates the precision and versatility of the measurement techniques in capturing detailed acoustic data from flying sources. A single AVS can detect and estimate the azimuth of a radar-evading low-flying threat platform, sniper, and tank in a battlefield scenario. The sensor can function as an array of wirelessly networked systems for border security and situation awareness. Such a network of acoustic systems can be deployed on naval ships, airships, UAVs, and on the ground, as well as on floating buoys, for early detection of low-flying threat platforms over land and sea in unattended multi-sensor network scenarios. These practical applications highlight the significance of the research in enhancing defence and security operations.

The paper is structured as follows: - Section 2.0 introduces the working principle of the AVS sensor, and subsection 2.1 outlines the existing algorithms from the literature for Direction of Arrival (DOA) estimation. Subsection 2.2: Describes the experiment conducted in the hemi-anechoic room to assess the AVS performance using existing DOA estimation algorithms from the literature in both the frequency and time domains. Section 3.0: Presents acoustic propagation measurements for DOA estimation in the context of a drone and low-flying propeller-driven manned aircraft. - Subsection 3.1: Explores the threshold setting of a flying target. - Subsection 3.2: Briefly discusses the results of an array of acoustic scalar sensors. - Section 4: Concludes the findings of the study.

2. WORKING PRINCIPLE OF AVS AND DOA ESTIMATION

The Microflown sensor is a Micro-Electromechanical System (MEMS) that utilizes two extremely thin heated platinum wires[4,6,8] to generate its output. This innovative sensor is a successful result of research conducted at the University of Twente in the Netherlands and operates based on the principle of a hot wire anemometer. As air flows over the heated wires, sound waves create a temperature difference in the wires[4,8], generating a voltage difference proportional to the airflow (particle velocity) and directional. This sensor is designed to withstand extreme ambient conditions, including high temperatures, dirt, and moisture. It has no moving parts, does not exhibit resonances, and therefore can be reliable.

An in-air Acoustic Vector Sensor (AVS) comprises three particle velocity sensors denoted as '*u*', '*v*' and '*w*' which are mutually placed orthogonal to each other around a microphone. The commercially available AVS includes an outer protective metallic shell similar in size to a half-inch microphone and a separate signal conditioner and power supply module. Compared to the standard version, as presented in the paper, an ultra-small AVS with a small signal conditioner that is compact and lightweight signal conditioner was utilized for DOA estimation. This article provides valuable insights into the application of passive acoustic sensor technology for estimating an acoustic source's Direction Of Arrival (DOA), explicitly focusing on the azimuth angle. It delves into the limitations of small amplitude acoustic waves, known as linear acoustics, in the audible range of 20-20 kHz.

2.1 Algorithm for DOA Estimation

This study implemented two algorithms developed by Nehorai and Paldi[19] to estimate the DOA of a single acoustic source using measurements from a single vector sensor. The first algorithm, acoustic intensity-based measurement, utilizes 4-D acoustic pressure and particle-velocity output. In contrast, the second algorithm, velocity covariance-based measurement, uses only the 3-D acoustic particle-velocity output. The performance of both algorithms was rigorously compared for DOA estimation of a static sound source, drone, and a propeller-driven two-seater manned aircraft in different environments. An alternative to using a vector sensor was discovered by exploring an array of scalar acoustic sensors for DOA estimation at the laboratory level.

The assumptions made for the free-space measurements are as follows[19-20]: (1) Acoustic waves travel in a homogeneous, quiescent, and isotropic fluid; (2) Acoustic waves are considered as plane waves at the sensor, (3) Acoustic perturbations are small fractions of their static values, (4) The spectrum signal is considered to be band-limited. This paper describes two different algorithms, one in subsection 2.1.1 and another in subsection 2.1.2, for estimating the DOA of a single acoustic source using a single vector sensor in free space.

2.1.1 4-D Acoustic Intensity-Based Algorithm

Pressure fluctuation, p and particle velocity, u, the two main parameters of a sound wave, are functions of distance, r, and time, t

$$p = p(r,t) = A \times \cos\omega(t - r/c) \qquad (1)$$

$$u = p/(\rho c) \qquad (2)$$

where, ρ is the density of air and c is the speed of sound in air.

Instantaneous acoustic intensity, $I(t)$[21] at a distance, r, from the sound source is a function of the instantaneous sound pressure, the area normal to the flow, the distance, and time.

$$I(t) = p(t)dAdr / dtdA \tag{3}$$

The equation of instantaneous intensity in the direction of r can be expressed as follows:

$$I(t) = p(t)u(t) \tag{4}$$

Out of the two components of the instantaneous particle velocity, $u(t)$, the active component, which is in phase with the sound pressure, gives a time-averaged product with the pressure, $p(t)$ called the acoustic intensity, I in the same direction as the particle velocity.

$$I = \frac{1}{T}\int_0^T p(t)u(t)dt \tag{5}$$

Based on the definition of intensity and using AVS output signals, the sound intensity in the x, y and z directions can be determined as I_x, I_y and I_z and. The azimuth angle, ϕ of an acoustic source is determined as:

$$\phi = \tan^{-1}(I_y / I_x) \tag{6}$$

And the elevation angle, θ is determined as

$$\theta = \sin^{-1}(I_z / I_n) \tag{7}$$

where, $(I_n = I_x^2 + I_y^2 + I_z^2)$

When analysing an impulse signal, time domain analysis can be used to evaluate intensity. However, intensity is assessed in the frequency domain for a continuous signal. It involves using the real part of cross-spectral density between pressure and particle velocity to obtain DOA estimation[19] as given in Eqn. (8); $y_p(t)$ and $y_v(t)$ are, respectively, the measured phasor pressure and phasor velocity vector at the sensor.

$$\hat{S} = \frac{1}{N}\sum_{t=1}^{N} \mathrm{Re}\{y_p(t)y_v(t)\} \tag{8}$$

2.1.2 3-D Acoustic Particle Velocity-Based Algorithm

This algorithm estimates the DOA using the measured acoustic particle velocity in three directions and its covariance matrix structure. It computes the covariance matrix[19], $\hat{R}$, as given in Eqn. (9).

$$\hat{R} = \frac{1}{N}\sum_{t=1}^{N} \mathrm{Re}\{y_v(t)y_v^*(t)\} \tag{9}$$

($y_v^*(t)$ is the conjugate transpose of $y_v(t)$)

The azimuth angle is determined from the leading eigenvector of the matrix above, corresponding to the largest eigenvalue. In the frequency domain, it is necessary to evaluate the real part of the cross-spectral density between particle velocities for DOA estimation.

2.2 DOA Estimation in Hemi-Anechoic Room

A meticulously planned experiment was carried out in a hemi-anechoic room to analyze the capabilities of AVS in accurately determining the direction of arrival (DOA) of a stationary sound source within a 360° area of interest in space. The primary goal was to devise a method for positioning the AVS, particularly aligning vector sensors u, v and w with the Earth's magnetic field to consistently and reliably estimate the DOA of an acoustic source. The secondary objective involved comparing the efficacy of intensity and velocity covariance methods in assessing the DOA of a stationary sound source. The schematic view (Fig. 1) illustrates the strategic positioning of AVS, with the particle velocity sensors (u, v, w) aligned along the Earth's magnetic direction. During the experiment, the quadrant system, delineated by the vertical axis North-South (N-S) and horizontal axis East-West (E-W) of AVS, as depicted in Fig. 1, guided the speaker's placement. Starting from the West (W) and moving in a clockwise direction, the first quadrant is the North- West (N-W) quadrant, and lastly, the fourth quadrant is the South-West (S-W) quadrant. The B&K Pulse software and LanXI system created a 1 kHz sine wave signal, played through a speaker to produce a continuous 1 kHz sound. The distance between the speaker and AVS was maintained during the experiment at 1 m. The AVS was fixed on a tripod 0.9 m above the floor. In this experiment, the sensor remained stationary. At the same time, the sound source (the speaker) was placed in four specifically defined locations in a hemi-anechoic room using a magnetic compass to match the quadrant for the given AVS configuration. These locations were in the first quadrant (N-W: 65°) second quadrant (N-E: 110°), third quadrant (S-E: 270°), and fourth quadrant (S-W: 290°). The sine tone signal generated by the speaker in each quadrant was recorded through the AVS. The four voltage signals of AVS, pressure (p), and three particle velocities (u, v, w) were acquired using the PC-based Prosig Data Acquisition (DAQ) system at a 5 kHz sampling rate for 30 s. The offline analysis of signals in MATLAB effectively estimated the DOA of the speaker in the frequency domain using algorithms from subsections 2.1.1 and 2.1.2, Eqn. (8-9). A detailed comparison of the estimated DOA using both algorithms is visually represented in Fig. 2(a), 2(b), 2(c), and 2(d), showcasing a comprehensive time versus azimuth angle plot for each quadrant measurement and a compass plot that reveals the speaker's DOA using the intensity method Eqn. (6) with a time-domain approach. It is worth noting that the azimuth angles align closely and fall within the same quadrant,

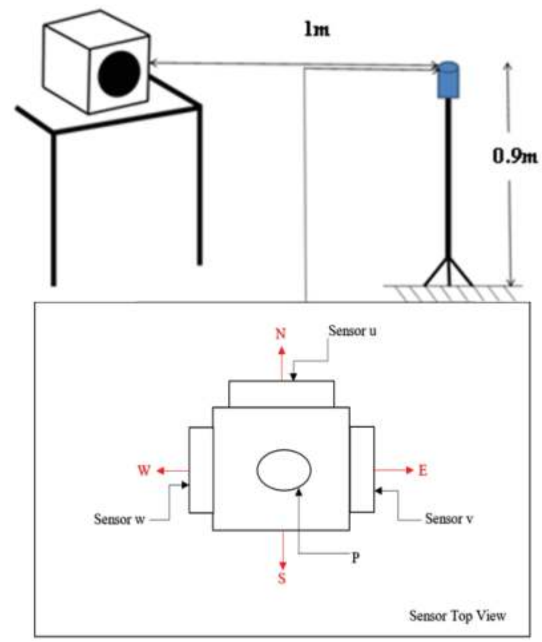

Figure 1. Experimental setup for DOA estimation.

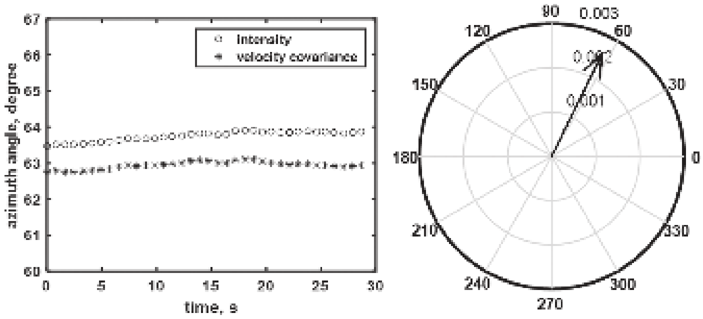

(a)

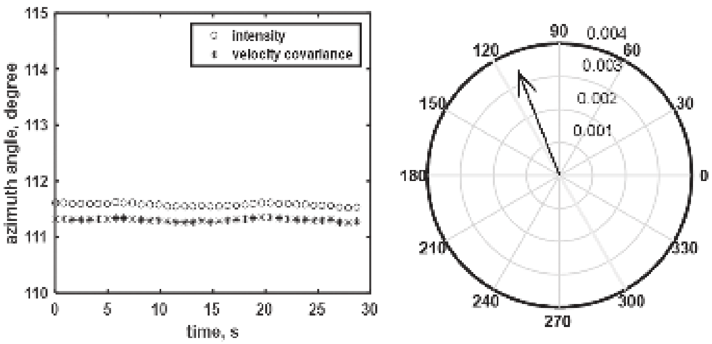

(b)

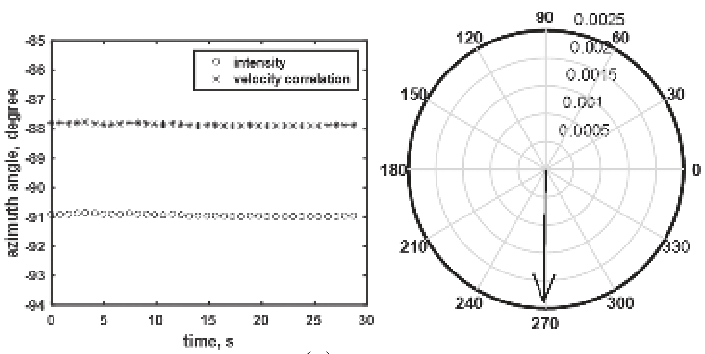

(c)

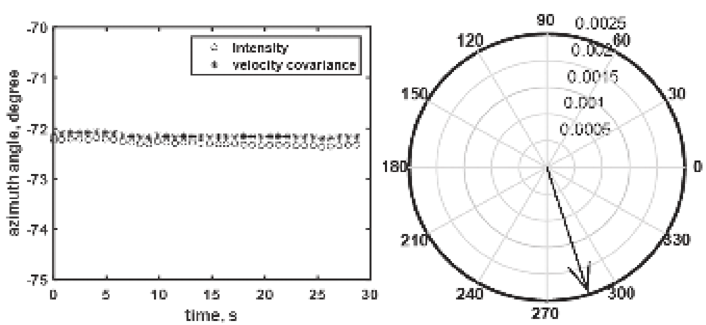

(d)

Figure 2. (a) DOA estimation in the first quadrant (N-W); (b) DOA estimation in the second quadrant (N-E); (c) DOA estimation in the third quadrant (S-E); and (d) DOA estimation in the fourth quadrant (S-W)

and validation was verified using a magnetic compass.

This approach efficiently identifies the azimuth angle of the acoustic source within the sensor coordinate quadrant, with the error in the azimuth angle estimation being less than 5 %. Negative values depicted in Fig. 2(c) and Fig. 2(d) must be regarded as 360° + (angle with sign). The time-domain approach offers a faster method for estimating DOA than the frequency-domain approach, with no processing required. It is ideal for analysing impulse signals like a gunshot, especially when dealing with a single frequency and time-invariant signal, as in the lab experiment.

3. DOA ESTIMATION OF FLYING TARGET

The experiments in the previous section confirmed the AVS's ability to estimate the DOA for ground-based acoustic

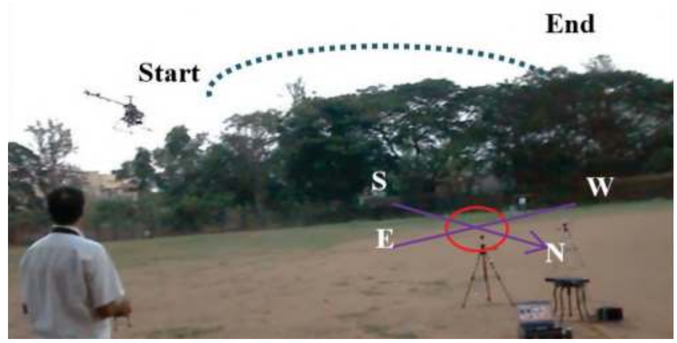

(a)

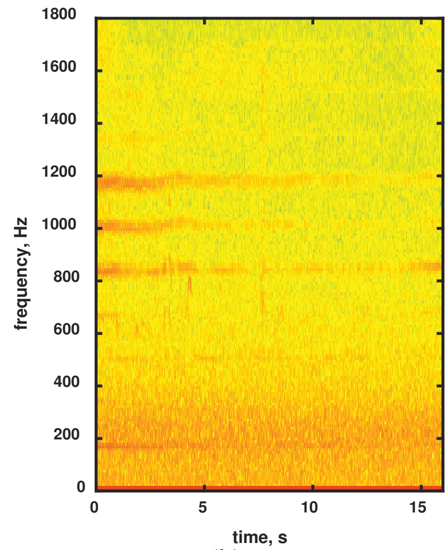

(b)

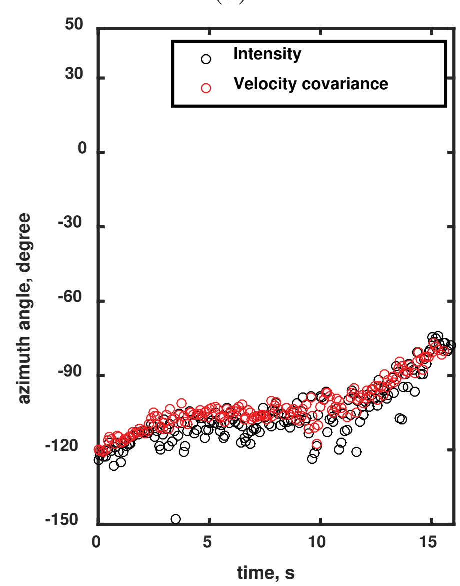

(c)

Figure 3. (a) An AVS with a hovering helicopter; (b) Spectrogram of particle velocity component; and (c) Comparison of DOA estimation method.

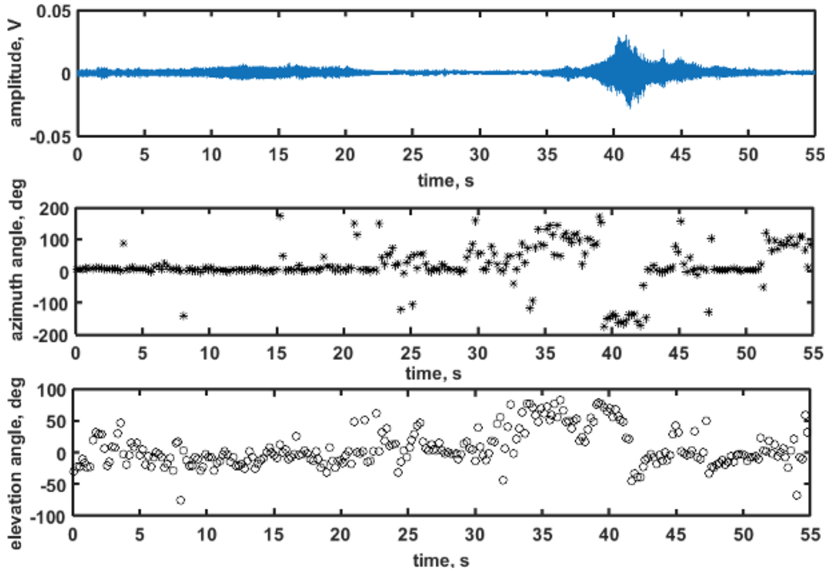

(a)

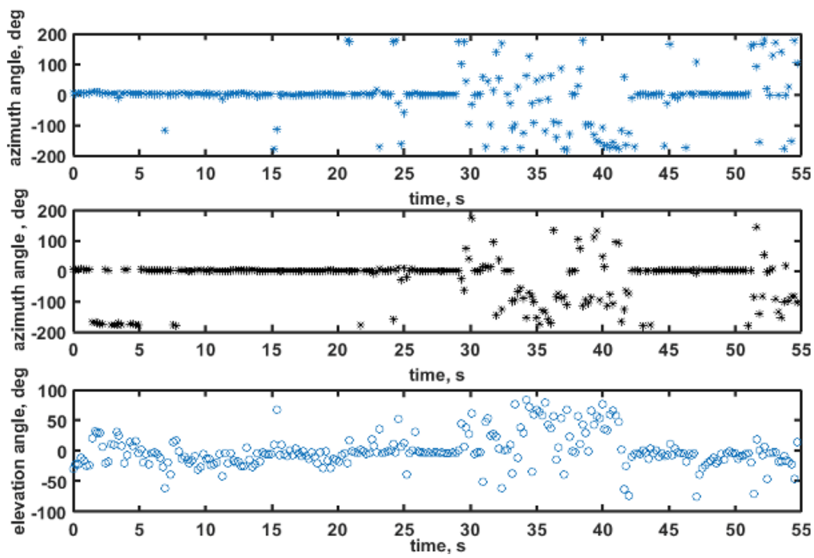

(b)

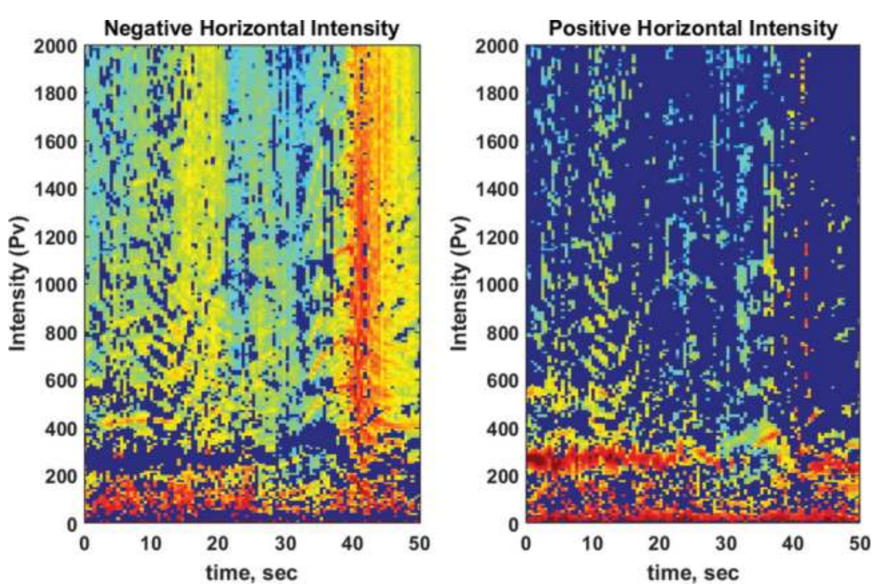

(c)

Figure 4. (a) Time domain intensity based azimuth angle and elevation angle; (b) Frequency domain intensity and covariance-based azimuth and elevation angles; and (c) Intensity-based spectrogram.

sources. Acoustic propagation measurements of a 10 kg class drone and flight trials of a two-seater propeller aircraft were conducted to advance airborne target DOA estimation further. Acoustic signals from the drone were captured using a Prosig DAQ at a 48 kHz sampling rate with an in-air AVS positioned along Earth's magnetic directions. The drone flew from South-East to South-West, captured in Fig. 3(a). The horizontal particle velocity '*v*' spectrogram in Fig. 3(b) helped identify the drone's propeller blade frequency. Spectral lines within the 1100-1250 Hz frequency range over 0-16 sec were selected for DOA estimation.

Both methods, acoustic intensity and velocity covariance in the frequency domain, show a consistent azimuth angle, as seen in Fig. 3(c). Notably, the drone's movement from the South East (S-E) to the South West (S-W) direction has been verified through the magnetic compass angle and experimental results from the hemi-anechoic room.

It is essential to carefully consider the placement of the AVS and quadrant for accurate DOA estimation, as they differ from the standard coordinate system. In another acoustic measurement, a flight trial was conducted with a two-seater propeller aircraft flying in a circular path over an AVS. The aircraft flew from West to East and back to West at 1000 feet above the ground. The plot of the acoustic pressure, results of the intensity-based azimuth angle, and elevation angle using the time domain approach are depicted in Fig. 4(a). Furthermore, Fig. 4(b) shows the results for intensity-based azimuth angle, velocity covariance-based azimuth angle, and elevation angle using the frequency domain approach. The azimuth angle plot in Fig. 4(a) and Fig. 4(b) shows that the aircraft is approaching the sensor from the West (refer to section 2.2, W: 0° and E: 180°). After taking a turn over the sensor, the aircraft returns to a westward direction. At 40 s, the elevation angle is 90° as the aircraft flies directly above the sensor. The horizontal intensity spectrogram ($I_y=pv$) for the given flight is depicted in Fig. 4(c) with a spectral pattern of negative (left figure) and positive (right figure) intensity of the aircraft signal. The intensity spectrogram directly estimates the time to the closest point of approach, precisely 40 s, with no left-right direction ambiguity[20].

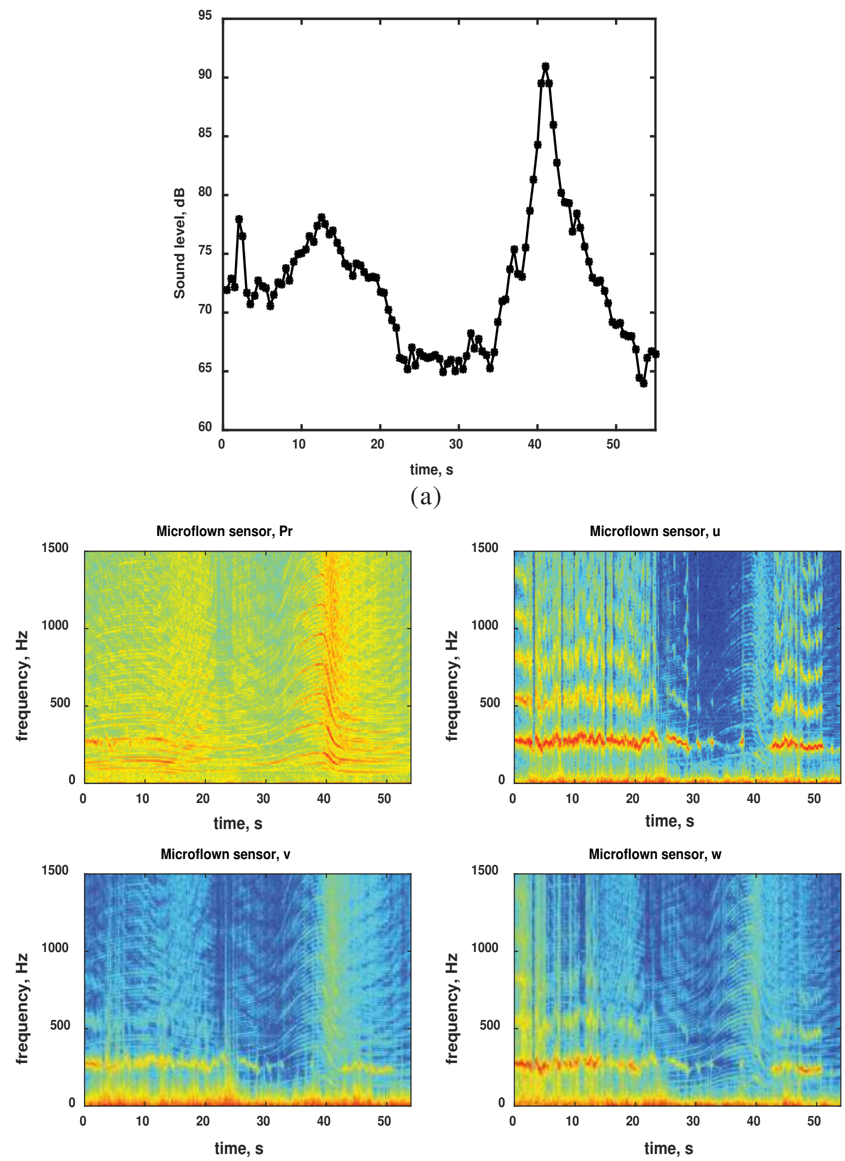

Figure 5. (a) Sound pressure level plot.; and (b) Spectrogram plot of microflown pressure, particle velocity signals - u, v, and w.

The occurrence of spectral patterns in the negative horizontal intensity spectrogram indicates approaching aircraft to the sensor from the left side, which in the present experiment is in the West direction. The occurrence of spectral patterns in the positive horizontal intensity spectrogram indicates the aircraft flying away from the sensor to the right side, which in the present experiment is in the East direction. In the negative horizontal intensity spectrogram Fig. 4(c) (left side figure), the spectral patterns are observed before 40 s, indicating that the aircraft approached the sensor from the West. The spectral patterns after 40 s means the aircraft circled back westward. However, in the positive horizontal intensity spectrogram Fig. 4(c) (right side figure), no spectral patterns are observed after 40 s, confirming that the aircraft did not cross over to the East side of the sensor and instead flew back towards the West. The sensor was strategically placed approximately 2.75 m above the ground during the flight trial. The free space model was adopted, eliminating any ground reflections.

3.1 Threshold Setting for Detection of Flying Target

To aid in aircraft detection and avoid false alarms, the plot of Sound Pressure Level (SPL) and time-frequency (spectrogram)[5,22] reveals blade pass frequency and its harmonic patterns[3] typical of any propeller aircraft, indicating the presence of a flying acoustic source. Fig. 5(a) shows a plot of the variation in sound pressure level over time as a propeller aircraft flies over the sensor, with the maximum sound pressure level exceeding 90 dB at 40 s when the aircraft is directly above the sensor, decreasing to 66 dB as the aircraft flies away. In addition, Fig. 5(b) shows the spectrograms of all four acoustic signals. The spectrogram clearly illustrates the spectral pattern of the aircraft up to 55 s. The aircraft can be detected easily up to a distance of 2.75 km from the sensor, considering the speed of the aircraft to be 50 m/s.

Setting the threshold value in Sound Pressure Level (SPL) and analysing the spectral pattern can be an initial step to prevent false alarms and reduce the computational cost of estimating the DOA, leading to reduced power consumption.

An AVS, constructed using DSP hardware and an advanced algorithm equipped with a standalone power supply, can function as an array of wirelessly networked systems for border security and situation awareness. The detection capabilities of an aircraft can be improved through network-based AVS sensors[20]. The communication from this network can be sent to the central server or a patrolling ship to take counteractive action. An acoustic system built around an array of acoustic scalar sensors complements an AVS system toward detection and DOA estimation. Though its footprint is more significant than AVS, it can be economically viable.

3.2 Acoustic Scalar Sensor for DOA Estimation

The microphone is an acoustic sensor that measures only the magnitude of a sound or noise. It has been widely used for research and development in aerospace, automotive, and acoustic engineering[23]. When a pair of microphones is placed at a fixed distance in the same plane, they can determine the direction of a sound source in terms of azimuth angle using a cross-spectrum method[24]. The condenser microphones are precise sensors, and a pair of two microphones can be a more cost-effective solution for single source detection and DOA estimation but may not eliminate an AVS. The experiment involved using a set of four microphones positioned in an equilateral triangle to determine the azimuth angle of an acoustic source[7]. The microphones are spaced approximately 0.18 m apart, with one microphone (mic1) at the center, at a height of 0.33 m, as shown in Fig. 6; mic2 faces East, mic 3 faces North-West, and mic 4 faces South-West. In the counter-clockwise direction from East, the first quadrant is North-East (N-E), and the fourth is South East (S-E).

In the experiment, the speaker was positioned 2 m away from the array in front of two microphones for three separate measurements: between mic2-mic3 in the N-E quadrant, mic3-mic4 in the West, and mic4-mic2 in the S-E quadrant. A standard speaker that produced 1 kHz sine tone was utilized to evaluate the perfor-mance of the acoustic scalar array in estimating the azimuth angle.

Signals from all four microphones were simultaneously acquired for 15 s at a 5 kHz sampling rate using a PC-based Prosig DAQ. Based on the cross-correlation method[7], the analysis is presented in Table 1, showing that the measured azimuth angles are in a similar range with actual values verified by the magnetic compass. The array can estimate the DOA for both continuous and transient signals.

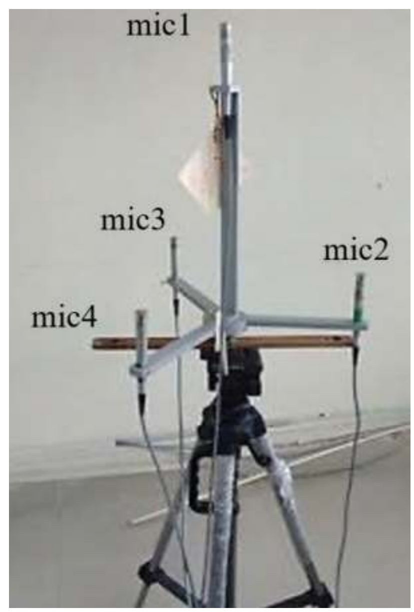

Figure 6. An array of acoustic scalar sensors.

Table 1. Estimated azimuth angle using acoustic scalar sensor array

Position of Source	Measured angle, degrees	Actual angle, degrees
North-East (N-E)	34.21	35
West	149.45	150
South-East (S-E)	-77.63 (282.37)	280

4. CONCLUSION

Experimental studies were conducted using two different algorithms to estimate a single acoustic source's Direction

Of Arrival (DOA). The tests were conducted at the lab level and during aircraft flight trials. It was observed that a single Acoustic Vector Sensor (AVS) can accurately estimate the azimuth angle of both fixed and moving acoustic targets. A system built around it can be a target detection and passive surveillance system. Threshold settings for detecting and analysing the acoustic source's spectral patterns could reduce a standalone system's computational cost and power consumption and prevent false alarms. Additionally, studies on an array of acoustic scalar sensors showed economically viable solutions for passive detection technology to aid in situational awareness. It is recommended that a network of acoustic systems utilizing sensors in the air and underwater can be deployed on naval ships, UAVs, and on the ground, as well as on floating buoys, for early detection of low-flying threat platforms over land and sea in unattended multi-sensor network scenarios.

REFERENCES

1. Johnson, D.H. & Dudgeon, D.E. Array signal processing: concepts and techniques. Introduction, Prentice Hall, Englewood Cliffs, NJ, 1993. pp.1-7.
2. Saraswat, V.K. Missile technologies and future trends. *J. of Aero. Sci. and Technol*., 2009, **61**(1), 12-21. doi:10.61653/joast.v61i1.2009.603
3. Schiller, J. Detection and bearing angle estimation of low flying aircraft by acoustical means. *In* IEEE International conference on Acoustic, Speech and Signal processing, 1982, pp. 1124-1127. doi: 10.1109/ ICASSP.1982.1171571
4. De Bree, H.E. A perspective on acoustic vector sensors in passive surveillance: Real world measurements, algorithm and applications. *J. of Aero. Sci. and Technol*., 2009, **61**(1), 271-282. doi: 10.61653/joast.v61i1.2009.651
5. Sadasivan, S.; Gurubasavaraj, M. & Ravi Sekar, S. Acoustic signature of an unmanned air vehicle: Exploitation for aircraft localisation and parameter estimation. *Def. Sci. J.*, 2001, **51**(3), 279-284. doi: 10.14429/DSJ.51.2238
6. Technical closure report of project environmental acoustics remote sensing station (EARSS) – Development and evaluation, TD PX-04/ADE-191, 2007.
7. Antonov, V.P.; Kuzmenko, A.K.; Svet, V.D. & Spitsyn, E.I. Experimental study of the acoustic navigation of a helicopter by its noise radiation. *Acoust. Phy.*, 2000, **46**(6), 648–654. doi:10.1134/1.1326718.
8. Wolff, O.; Tijs, E. & de Bree, H.E. A PU probe array based panel noise contribution analysis whilst driving. *In* Noise and Vibration conference and exhibition, SAE, 2009. doi.:10.4271/2009-01-2123.
9. De Bree, H.E.; Leussink, P.; Korthorst, T.; Jansen, H.; Lammerink, T. & Elwenspoek, M. The microflown: A novel device measuring acoustical flows. *Sen. and Act.: A Phys.*, 1996, **54**(3), 552-557. doi.:10.1109/SENSOR.1995.717278
10. 3D acoustic situational awareness. www.microflown-avisa.com
11. Basten, T.; de Bree, H.E. & Sadasivan, S. Acoustic eyes, a novel sound source localization and monitoring technique with 3d sound. *In* Proceedings of the biennial ISMA conference on Noise and Vibration Engineering, Leuven, 2008.
12. Sutin, A.; Salloum, H.; Sedunov, A. & Sedunov, N. Acoustic detection, tracking and classification of low flying aircraft. *In* IEEE International Conference on Technologies for Homeland Security, 2013. doi:10.1109/THS.2013.6698990
13. Mezei, J.; Fiaska, V. & Molnár, A. Drone sound detection. *In* Proceedings of the 16th IEEE International Symposium Computational Intelligence and Informatics. Budapest, Hungary, 19–21November, 2015, pp. 333 – 338. doi: 10.1109/CINTI.2015.7382945
14. Harvey, B. & O'Young, S. Acoustic detection of a fixed-wing UAV. *Drones*, **2**(1), 2018. doi:10.3390/drones2010004
15. Blanchard, T.; Thomas, J.H. & Raoof, K. Acoustic localization and tracking of a multi-rotor unmanned aerial vehicle using an array with few microphones. *J. Acoust. Soc. Am.*, 2020, **148**, 1456–1467. doi:10.1121/10.0001930
16. Fang, J.; Finn, A.; Wyber, R. & Brinkworth, R. Acoustic detection of unmanned aerial vehicles using biologically inspired vision processing. *J. Acoust. Soc Am*., 2022, **151**(2), 968. doi: 10.1121/10.0009350
17. Grumiaux, P.A.; Kitić, S.; Girin, L. & Guérin, A. A survey of sound source localization with deep learning methods, *J. Acoust. Soc. Am.,* 2022, **152**, 107–151. doi.:10.1121/10.0011809
18. Zhang, X.; Hayward, C.; McComas, S. & Arrowsmith, S. Exploring acoustic characteristics of different aircraft types by fusing with aircraft tracking data. *J. Acoust. Soc. Am.*, 2023, **153** (5), 3138-3150. doi:10.1121/10.0019594
19. Nehorai, A. & Paldi, E. Acoustic vector-sensor array processing. *IEEE Transaction on signal processing,*1994, **42**(9), 2481-2491. doi: 10.1109/78.317869.
20. Sadasivan, S.; Basten T. & de Bree, H.E. Acoustic vector sensor based intensity measurements for passive localisation of small aircraft, *J. of Acoust. Soc. Ind.*, 2009, **36**(1), 8-13.
21. Ruijgrok, J.G.J.J. Elements of aviation acoustics, Yes Dee Publishing, Indian Reprint, 2009. pp.13-14.
22. Gade, S. & Herlufsen, H. Windows to FFT Analysis - Part I. Bruel and Kjaer, Technical Review No.3, 1987.
23. Taniguchi, H.H. & Rasmussen, G. Microphone selection and use for engine and aircraft noise. Bruel and Kjaer, Technical Review No.4, 1980.
24. Bendat, J.S. & Piersol, A.G. Engineering applications of correlation and spectral analysis, Ed. 2, Wiley, New York, 1993.

CONTRIBUTORS

Mr Meshram Devendra M. obtained his M.S by research in Aerospace Engineering from IITM, Chennai. He is working at DRDO-ADE, Bengaluru. His areas of research include: Passive detection and localisation of low flying aircraft using acoustic modality involving intra-sensor and inter-sensor collaboration. Also worked in the areas: Aero-acoustics, Integrated Vehicle Health Monitoring (IVHM), aircraft structural dynamics, signal processing and thermo-acoustic instability.

In the current study, he made a literature review, carried out acoustic experiments that involved instrumentation, measurement, signal processing, data analysis, results interpretation and comparison and prepared the manuscript.

Dr Pushpa Mala S. obtained her PhD in Electronics Engineering from Jain University, Bengaluru. She is an Associate Professor in the department of Electronics and Communications, Dayananda Sagar University, Bengaluru. Her areas of interests are VLSI sub-system designs, image processing and signal processing.
In the current study, she gave valuable feedback, direction to research methodology and helped in reviewing the manuscript.

Defence Science Journal, Vol. 75, No. 1, January 2025, pp. 19-26, DOI : 10.14429/dsj.20276

Tactical UAV Flight Performance Estimation and Validation

Miodrag Milenković-Babić*, Biljana Dovatov, Branislav Ostojić, Vuk Antonić,
Milenko Trifković and Dušan Ivković

Military Technical Institute, Belgrade – 11000, Serbia
**E-mail: miodragmbm@yahoo.co.uk*

ABSTRACT

The information presented in this paper describes the procedure for flight performance estimation of a single pusher-propelled Tactical unmanned aerial vehicle and the flight test verification of its results. The aerodynamic data has been obtained from several sources and integrated into the flight mechanics equations of motion for a typical unmanned aerial vehicle configuration to provide a sufficient basis for estimating flight performance. Subsequently, the development of the UAV's flight performance equation is described. The implemented numerical method is a proven standard in the aircraft industry and should produce reliable results with deviations up to 10 %. Finally, flight tests have been conducted to validate the performance estimation results.

Keywords: UAV; Flight testing; Aerodynamics; Flight performance

NOMENCLATURE

UAV	: Unmanned Aerial Vehicles
HALE	: High Altitude and Long Endurance
VTI	: Military Technical Institute, Belgrade
CFD	: Computational fluid dynamics
RPM	: Revolutions per minute
J	: Advance ratio
V	: Airspeed
N	: Propeller rotational speed
D	: Propeller diameter
t	: Time
c_t	: Thrust specific fuel consumption
T	: Thrust
W	: UAV's weight
C_L	: Lift force coefficient
C_D	: Drag force coefficient
m	: UAV mass
g	: Acceleration due to gravity
ρ	: Air density
S	: Wing surface area
P_R	: Required power
P_A	: Available power
P_{engine}	: Engine power
η_{engine}	: Engine efficiency
η	: Propeller efficiency
γ	: Flight path angel
T_R	: Necessarily thrust
D	: Drag force
R_{cScA}	: Range at constant airspeed/constant attitude cruise
R_{cAcA}	: Range at constant altitude/constant attitude cruise
BHP_{ALT}	: Engine break horsepower at some altitude
BHP_{SL}	: Engine break horsepower at sea level altitude
σ	: Ratio of density at sea level/density at some altitude
V_{TAS}	: True airspeed
V_i	: Indicated airspeed
V_{min}	: Minimum airspeed
$V_{\max}$	: Maximum airspeed
V_W	: Airspeed for best rate of climb
$_{SL}$	: Sea level
$_{ALT}$	: Some altitude
cScA	: Constant airspeed/constant attitude
cAcA	: Constant altitude/constant attitude
w	: Climb speed

Received : 04 June 2024, Revised : 27 September 2024
Accepted : 21 October 2024, Online published : 10 January 2025

1. INTRODUCTION

The history of Unmanned Aerial Vehicles (UAV) has undergone a significant change in the past few decades. In the twenty-first century, there has been a constant increase in interest in the design and application of UAVs. The most fascinating concepts include MALE (Medium Altitude and Long Endurance) UAVs such as Tactical UAV presented in this paper, and UAVs with VTOL (Vertical Take-off and Landing) capabilities. The dramatic improvement in aeronautical and aerospace technology promises to deliver solutions to many problems present in the civil and especially military sectors.

Fixed-wing UAVs have become popular due to their relatively simple and well-known design, as well as their potential for excellent aerodynamic characteristics. They typically exhibit excellent endurance and range, with adequate stability and control characteristics. Since one of the first successful remotely piloted UAV solutions[1], many UAVs have been constructed, built, and evaluated through flight tests, achieving varying levels of success. All of them aim to capitalize on improved performance characteristics. The presented design incorporates the effect of twin fins on an isolated horizontal tail[2]. This design is widely used as it exhibits good stability and control characteristics, and a rearward position of the centre of gravity compared to the conventional tail configuration[3-4]. These UAV solutions are popular in military applications and can be used for rescue operations, public safety assessments, data acquisition, mapping buildings in hard-to-reach areas, surveillance, and more. Every day, new users employ UAVs in different applications. The flight performance estimation and validation of these UAVs have been well documented in the recent works[5-7].

Aerodynamic, geometric, and inertial data for Tactical UAVs analysed in this paper have been provided from research programs at the Military Technical Institute (VTI Belgrade). These data have been integrated with propeller efficiency and engine data sheets into the flight mechanics equations of motion for a typical unmanned aerial vehicle configuration to provide a sufficient basis for estimating flight performance. The Tactical UAV has been analysed[8-9] aerodynamic optimisation were formed. Researchers from VTI have generated a large number of relevant reports[10]. The research program was carried out by the Military Technical Institute in partnership with China[11], achieving the first international project of UAV design in the Republic of Serbia. The UAV is controlled by a military-grade flight control system with an advanced fibreoptic gyro-based inertial navigation system that provides adequate levels of stability and control characteristics, as well as reliable attitude and position measurement.

Estimating the UAV flight performance requires a representative mathematical model of the object of interest. In the first steps the aerodynamic data of the Tactical UAV has been estimated in commercial ANSYS Fluent software by the finite volume methods. Next, the performance has been estimated by standard flight mechanics equations. After successfully meeting all the initial requirements, the UAV configuration is frozen, and prototype fabrication is taken up for flight testing. Initial flight tests were carried out to demonstrate take-off and landing performance[12] which was then followed by subsequent flight tests to validate the aircraft performance. The results of the above flight tests and their comparison with the theoretical predictions will be presented in this paper.

2. FLIGHT PERFORMANCE

Any flight can be divided into several segments, each clearly distinguished by its nature[13]. These segments include take-off, cruise, descent, landing, and climb. This paper will evaluate the cruise speed, maximum speed, maximum climb speed, and endurance of the Tactical UAV (Fig. 1) in an unarmed configuration.

It is well known that UAVs can be sold based on their performance, additional value to the customer, and payload. The method for estimating aircraft performance presented[13], is a proven standard in the aircraft industry. However, the accuracy of calculations depends heavily on the quality of the aerodynamic and inertial properties data used. The lift and drag force coefficients were provided in the Military Technical Institute[14] and are given in Fig. 2. This report included Computational Fluid Dynamics (CFD) analysis of the Tactical UAV model. As a part of the analysis[14], Fig. 3 shows the contours of static pressure around the UAV.

CFD analysis is a useful tool for predicting aerodynamic characteristics[15] at low Reynolds numbers, which is especially important for nonconventional shapes such as electro-optic

Figure 1. Tactical UAV.

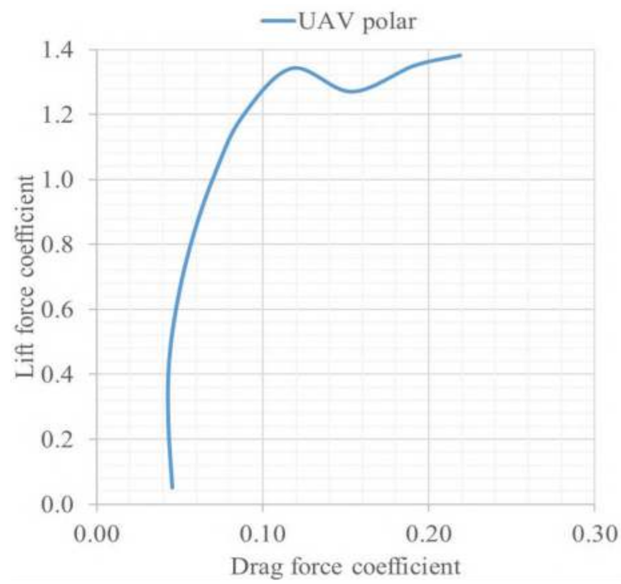

Figure 2. Tactical UAV polar.

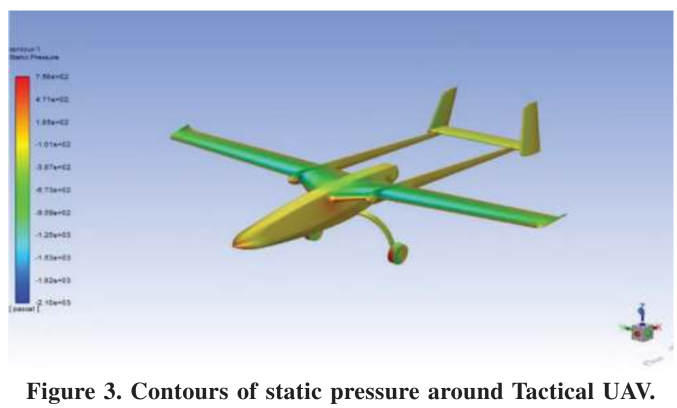

Figure 3. Contours of static pressure around Tactical UAV.

payloads. Wind tunnel tests can be prohibitively expensive for this type of UAV, so commercially available software like ANSYS Fluent has been used. The Reynolds average Navier Stokes system of equations was solved for compressible flow using a pressure-based solver. Different turbulent models and mesh sizes have been used for different UAV configurations. As one example, for the UAV in clean configuration with the payload in the fuselage, a half model has been used in order to speed up the calculation process. The mesh used for this case has 4.7 million cells. K-ω SST turbulent model has been chosen. The working fluid has been defined as an ideal gas (air). Velocity inlet boundary conditions have been used for defining the velocity and direction of the free stream. Computations have been done until the convergence criteria has been achieved.

The main reason why the CFD result has been used during detailed UAV design is that it has good agreement with the result from the wind tunnel test for the full-scale UAVs in previous project[16]. In this test, the lift and drag force have been investigated in detail, and excellent agreement between the CFD and wind tunnel test result has been reached for the UAV Sparrow (up to 10 % for angle of attack up to 12 degrees). Additional benefit from CFD was the possibility to test UAV at a high angle of attack that was impossible in a wind tunnel (usually 20-25 degrees). The obtained CFD data are also useful for estimating the UAV loading and stability characteristics, but they will not be discussed in this paper.

The report[14] contains CFD analysis results for the Tactical UAV model in various configurations, ranges of sideslip and angle of attack, and control surface deflections. These results are especially useful in predicting stall and separation characteristics as they are presented in Fig. 4.

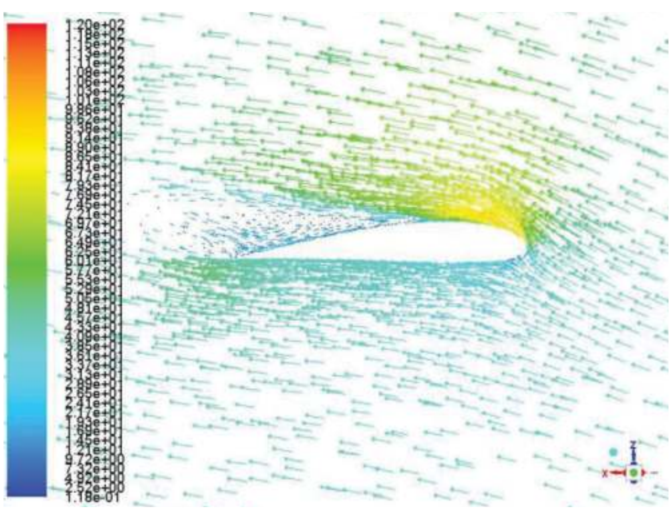

Figure 4. Prediction of local airflow separation on the wing.

However, it is important to note that the CFD results are best used in the final stages of the design and construction phases, while standard aerodynamic equations[17-18], should be used for conceptual design. The main challenge with using standard aerodynamic equations[17-18] is that the semiempirical constants are typically confirmed for higher Reynolds numbers.

As it can be seen from initial UAV[10], and data presented in Table 1, the maximum UAV mass increased as a consequence

Table 1. The UAV geometry

Wing span (with winglet)	7.025 m
Wing aspect ratio	9.08
Length	5.556 m
Mean aerodynamic chord	0,736 m
Wing area	4.33 m^2
Engine power	38.8 KW
Propeller diameter	0.86 m
Maximal mass of UAV	265 kg
Maximal mass of usable fuel	70 kg

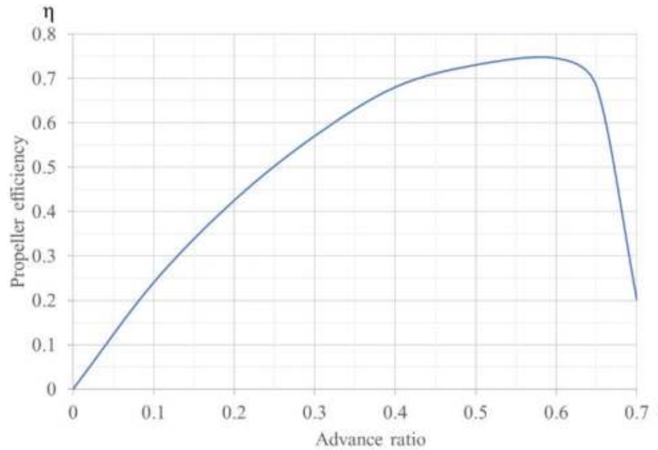

Figure 5. Propeller efficiency.

of arming the UAV, which led to a change in wing geometry and installed engine power. In the presented case, we have a pusher propeller engine. Figure 5 presents the propeller efficiency.

The propeller efficiency depends on the propeller RPM, true airspeed, and propeller diameter. All of these parameters can be represented by a single non-dimensional parameter called the advance ratio, which is given by Eqn. (1):

$$J = \frac{V}{ND}. \tag{1}$$

In Eqn. (1), N represents the propeller rotational speed, D is the propeller diameter, and V is the true airspeed. As shown in the diagram (Fig. 5), increasing the UAV airspeed improves the propeller performance until the maximum designed speed is reached. Given a known true airspeed, chosen propeller size, and propeller rotational speed, the advance ratio and propeller efficiency can be completely defined. To estimate the UAV's performance, an engine data sheet was obtained[19]. By analysing the nature of the forces that act on UAVs in steady-state conditions of level flight, climb, or turn, the performance characteristics of any UAV in various attitudes of flight can be easily determined[20].

The available power from the engine at the same speed determines climb or level flight characteristics. Available and required power determine maximum and minimum speed if minimum speed is not determined by the maximum lift force coefficient.

The best rate of climb can easily be determined numerically by finding the speed at which the difference between the available and required power is greatest. Range and endurance, or the time that a UAV can spend in the air while consuming available fuel[13], is one of the most important UAV characteristics. From Eqn.:

$$dt = \frac{-1}{c_t T} dW \quad (2)$$

The endurance estimation can be solved through numerical integration. In the previous equation, the limits represent the final and initial weight during the analysed segment. This is commonly known as the "Breguet" endurance Eqn. In Eqn. (2), t represents time, c_t represents thrust-specific fuel consumption (in 1/sec), T represents thrust (in N), and W represents the UAV's weight (in N). It is important to mention that when using the International System of Units (SI), some constants given in[13], must be converted into an SI system. The estimation of flight performance can be summarized in a few steps: For the chosen flight speed V and altitude, the lift force coefficient is calculated using the equation:

$$C_L = \frac{2mg}{\rho V^2 S}. \quad (3)$$

From known aircraft polar drag force coefficient can be determined:

$$C_D = f(C_L). \quad (4)$$

Required power is estimated by the equation:

$$P_R = mg\frac{C_L}{C_D}V. \quad (5)$$

Available power is determined by the Eqn.:

$$P_A = P_{engine}\eta_{engine}\eta. \quad (6)$$

As it can be seen from Fig. 6 the maximum UAV speed at a standard atmosphere altitude of 0 m is defined by P_A=P_R and the minimum speed is defined by lift capabilities. It is important to mention that propeller efficiency is a function of the advance ratio and that the calculated performance has been done with the goal to have propeller efficiency as close to the maximum value (0.73). Engine RPM has been optimized at different airspeeds in order to have maximum propeller efficiency. This is the reason for the available power curve changing its slope in Fig. 6.

In order to estimate the climb performance, the lift force coefficient is defined by the Eqn.:

$$C_L = \frac{2mg\cos\gamma}{\rho V^2 S}. \quad (7)$$

where, γ represents flight path angle. In this case the required thrust force is increased by the gravity component:

$$T_R = \mathrm{D} + \mathrm{mg}\sin\gamma. \quad (8)$$

Required power is estimated by Eqn.:

$$P_R = T_R V. \quad (9)$$

The climb speed is estimate by Eqn.:

$$w = V\sin\gamma. \quad (10)$$

This system of Eqn. with the defined limits has been solved numerically for selected altitudes, airspeed range (90-160 km/h) and flight path angle range (0°-20°). It was assumed that thrust line inclination to UAV X axis is equal zero. It is usually a small angle, and its contribution can be neglected for standard UAV configuration and aircraft or UAV without thrust vectoring. In order to get representative results, taking in mind that maximum power or thrust cannot be used continuously for a long time and that aircraft or UAVs cannot stay on the corner of the flight envelope for a long time, the numerical results must be reduced. Usually the maximum continuous power is 80 % of the maximum power for piston engines so a reduction of 15 % - 20 % should give representative results. Figure 7 provides an estimate of the tactical UAV's performance. In Fig. 7, the minimum speed has been defined by the maximum lift force coefficient, the maximum speed has been defined by PA=PR, and the climb speed and UAV speed for the best rate of climb have been determined by numerical methods in the defined airspeed range (90-160 km/h).

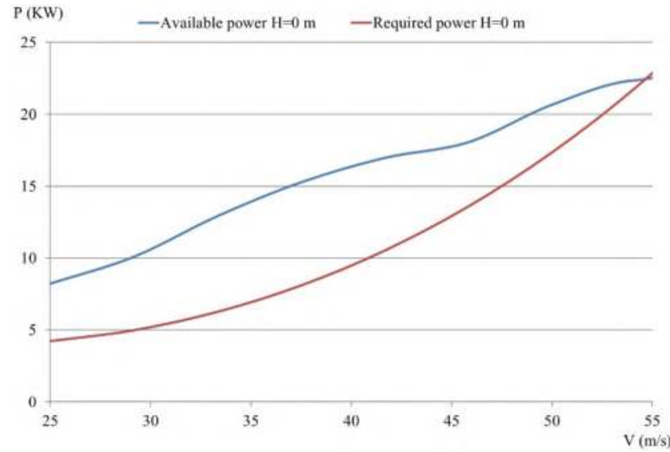

Figure 6. Maximum UAV speed from calculated data.

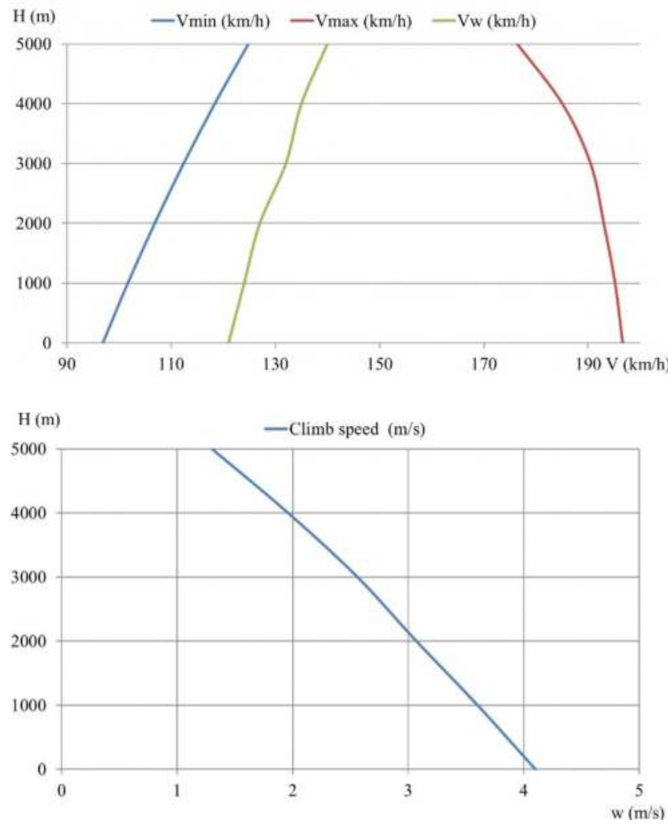

Figure 7. Estimated Tactical UAVs performance chart.

In order to estimate range/endurance it is necessary to find the specific fuel consumption[19].:

- Constant airspeed/constant attitude cruise (cScA),
- Constant altitude/constant attitude cruise (cAcA),
- Constant airspeed/constant altitude cruise.

In this paper, we have applied the first two methods to the Eqn.:

$$R_{cScA} = \frac{V}{c_t}\frac{C_L}{C_D}\ln\left(\frac{W_{initial}}{W_{final}}\right),$$

$$R_{cAcA} = \frac{1}{c_t C_D}\sqrt{\frac{8C_L}{\rho S}}\left(\sqrt{W_{initial}} - \sqrt{W_{final}}\right). \quad (11)$$

The changes in engine power with altitude are estimated using the Eqn.12[21]:

$$BHP_{ALT} = BHP_{SL}\left(\sigma \cdot \frac{1-\sigma}{7.55}\right) \text{ where } \sigma = \frac{\rho_{ALT}}{\rho_{SL}}, \quad (12)$$

The results of the just mentioned analysis are given in the Table 2, and the results of the analytically calculated UAV capabilities are given in the standard performance diagram[22] (Fig. 7).

Table 2. Estimated tactical UAVs endurance

V (km/h)	T_{cScA} (h)	t_{cAcA} (h)
120	12.67	12
135	11.28	10.45
150	10.5	9.73

3. FLIGHT TESTING

The well-known procedure for testing aircraft or UAVs has a similar description in all regulations[23-24]. The primary objective of the mentioned test is to verify the tactical and technical requirements, which are partially presented in this paper as UAVs performance. Initial requirements are a maximum speed of not less than 180 km/h, a service ceiling of not less than 5000 m, and an endurance of not less than 10 hours. When testing the maximum speed, the UAVs are in the initial flight-testing conditions that are defined by altitude >2000 m and true airspeed >180 km/h, where true airspeed is defined by the equation:

$$V_{TAS} = V_i\sqrt{\frac{\rho_{SL}}{\rho_{ALT}}}. \quad (13)$$

The procedure is done in two directions to eliminate the wind effect. The same applies to the cruise speed, which has varying speed limits between 130 km/h and 150 km/h. On the other hand, when testing for service ceiling, it is just necessary that UAVs reach an altitude that is greater than 5000 m. During this test, it is possible to evaluate the rate of climb. Finally, to evaluate endurance, the UAV climbs to the cruise altitude, adjusts the engine throttle to an appropriate level, and then the UAV will fly at the cruise speed at a defined altitude >2000 m. UAV must spend more than 10 hours in the air and the remaining fuel amount in UAV after landing must be greater than some safe reserve.

4. FLIGHT TEST RESULTS

All flight tests were conducted in an environment where the air temperature at the ground ranged from 17° to 35° Celsius and the wind speed was up to 3 m/s. RTK (Real-time kinematics) GNSS (Global Navigation Satellite System) was used with no less than nine satellites for precise measurement of UAV position, attitude, and speed. The Fiber-optic gyroscope, RTK GNSS, and MEMS (microelectromechanical systems) integrated into the UAV allowed the accurate measurement. Airspeed and barometric altitude were measured using the Air Data Unit, which contains a high-accuracy, temperature-calibrated pitot sensor, and static air data sensor. The unit is connected to an Inertial Navigation System (INS) to provide navigation accuracy when GNSS is not available. The flight test data presented in Fig. 8 - Fig. 11[25], is used to verify the performance of the Tactical UAV.

During all the analysed flight segments presented in this paper, the UAV was in autonomous flight mode. Taking in mind that the UAV has been driven by a fixed-pitch propeller, the engine throttle settings and RPM have been controlled by the flight control computer in order to satisfy the predefined limits.

5. ANALYSES OF THE RESULTS

Key parameter indices of all UAVs are minimum power consumption[13], maximum possible angle of attack, platform geometry, optimal throttle settings, and minimum time to reach targets. Therefore, a well-optimised conceptual design and estimated flying qualities of UAVs[26], are essential for their optimisation.

Flight test data given in Fig. 8 - Fig. 11 provides data for the verification of the tactical and technical requirements of Tactical UAV. The presented flight test data given in Fig. 8

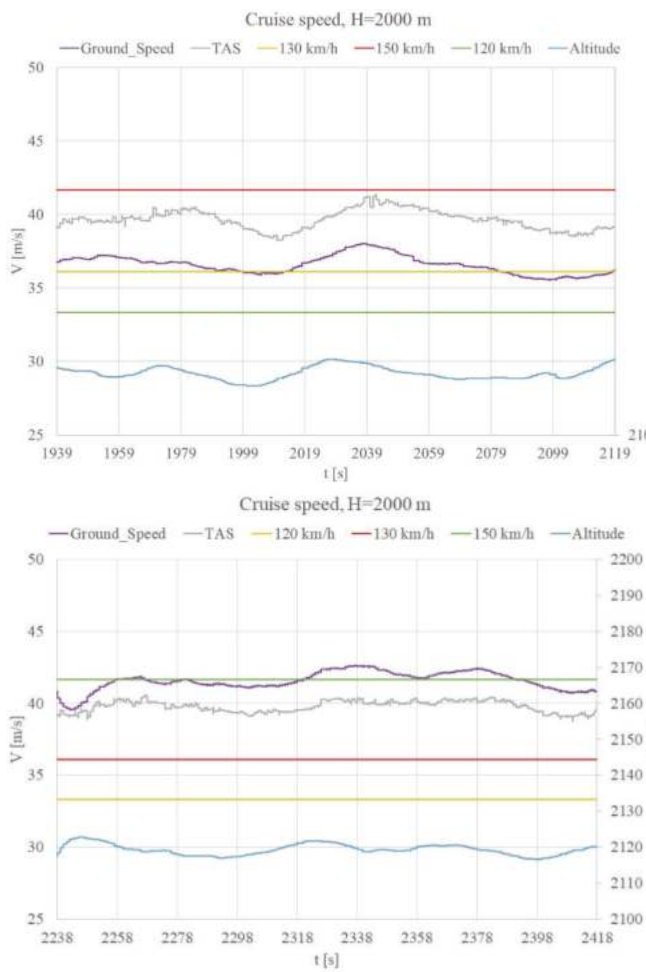

Figure 8. Altitude and velocity holding during flight test at cruise speed.

and Fig. 9 show that a Tactical UAV can easily control flight speed and altitude within pre-defined limits. Data given in Fig. 7 suggested that the theoretical service ceiling is somewhere between 5500 m and 6000 m. Since the calculated rate of climb at an altitude of 5000 m is 1.3 m/s (Fig. 7), and the rate of climb decreases by 0.6 (m/s)/km higher altitudes than 5000 m are possible according to the calculated results. As the service ceiling of not less than 5000 m has been an initial goal and there was limited time for all flight testing the maximum UAV climb altitude has not been determined.

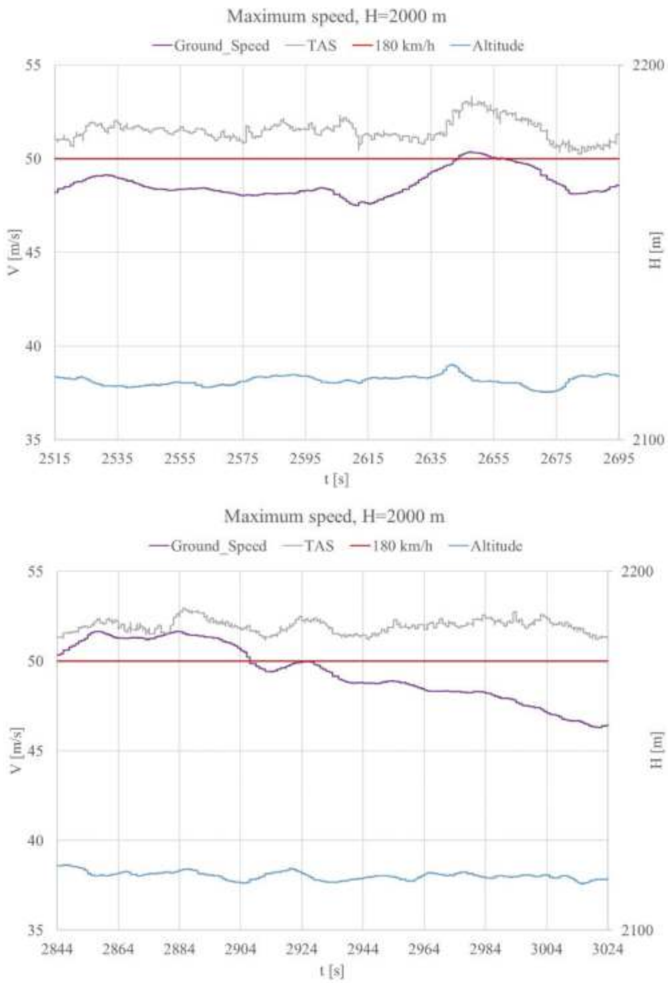

Figure 9. Altitude and velocity holding during flight test at maximum speed.

Calculated data suggested an even higher service ceiling, but it must be the consequence of using the Eqn. 12 for estimated engine power with the altitude. Eqn. 12 should give accurate results for reciprocating engines[21], but caution is necessary if extrapolating engine power with altitude for more than 3000 m.

Data given in Fig. 10 shows that in flight, the rate of climb became less than 1 m/s at an altitude of 5000 m. It will close to 0.5 m/s (service ceiling) at altitudes between 5300 m and 5600 m. The highest reached altitude was 5188 m, according to the measured flight test data.

When analysing the data given in Fig. 11, it is important to mention that the maximum endurance must be evaluated with precise measurement of the remaining fuel after the landing.

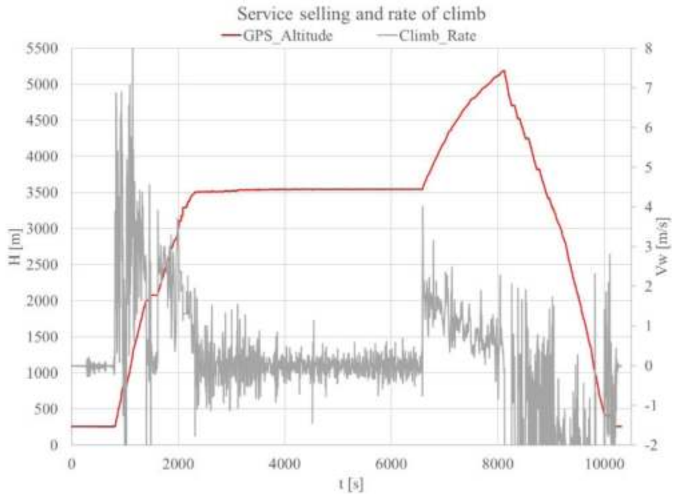

Figure 10. Service ceiling and rate of climb from flight tests.

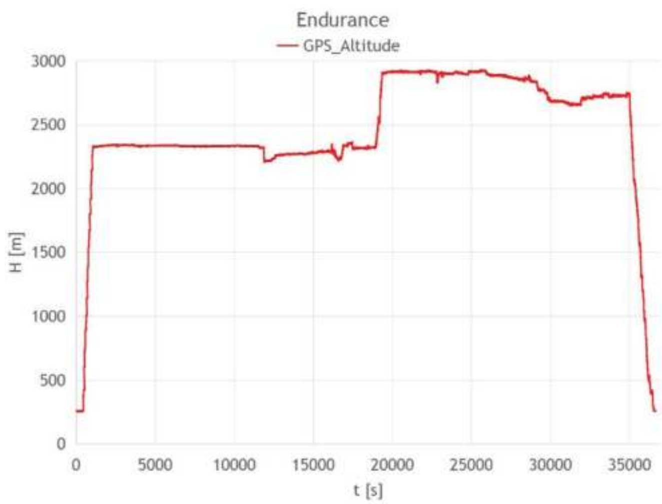

Figure 11. Endurance from flight tests.

The flight was performed with maximum UAV mass and full fuel capacity at take-off.

By taking this information into account, the actual flight endurance can be greater than 12 hrs. The maximum required UAV speed of not less than 180 km/h has been confirmed by the data given in Fig. 9. By comparing the results of flight tests and numerical simulations (Table 3), it is evident that Tactical UAV exceeds the initial tactical and technical requirements and should be evaluated in the next testing phase.

Table 3. Required, estimated, and flight test data

	V_{max} [km/h]	H_{max} [m]	t [h]	w_{max} [m/s]
Required value	180	5000	10	-
Estimated value	196	6000	11.3	4.1
Flight test data	191	5188	12	5.3

The maximum flight speed and endurance have excellent agreement (less than 6 % deviations). The service ceiling error is 15.7 % but it will be less than 10 % if the UAV has reached the practical service ceiling. The rate of climb estimation has the highest error of 22.6 %. The reason for this big deviation is the conservative approach when calculating climb speed by numerical method and sensitivity of measure result to the weather condition.

The objective of this paper was to do a comparison of flight performance from theoretical methods with the flight testing results. It was possible to predict stall and separation characteristics of the UAV and estimate lift and drag force accurately in order to estimate flight performance. Additionally, it was possible to estimate UAV lift and drag force coefficients at high angles of attack. The implemented design method has provided adequate results that completely eliminated the need for wind tunnel testing.

6. CONCLUSION

The mathematical models used for performance evaluation of the twin-boom horizontal tail UAV configuration appear to be satisfactory for low-speed flight dynamics.

To predict the UAV performance, the propeller efficiency and engine data must be provided from other sources. A sufficiently precise CFD UAV model should be created, an adequate turbulent model must be selected, defined calculated domain and boundary conditions, and this process requires a significant amount of time.

Based on the flight test data, it can be concluded that the Tactical UAV meets the initially defined requirements in its unarmed configuration and validates the performance estimation results. Compared to the state-of-the-art result in CFD analysis[15,27], the implemented CFD approach (by using the commercial software ANSYS Fluent) has been able to discover complex aerodynamic phenomena such as local airflow separation on the wing and UAV stall characteristics. The dynamic flight manoeuvres had not been analysed but it would certainly require a dynamic mesh technique and additional time to obtain accurate results. The flight test results also indicate that the UAV has capabilities beyond the initial requirements and may need further testing and evaluation in the future. The importance of good aerodynamic design and optimization for UAVs is highlighted by the success of Tactical UAV in meeting its performance goals.

Flight testing indicates that the lowest UAV airspeed is defined by maximum lift capabilities. The combination of flight testing and computational fluid dynamics has proven to be a reliable approach for evaluating UAV performance and improving their design. This approach allows for a more comprehensive evaluation of the UAV's aerodynamic characteristics and flight performance, including its stability and controllability. This is especially important when there is a need to predict aerodynamic characteristics at low Reynolds numbers, and when the experimental results for the nonconventional shape of electro-optics payload solutions for providing optimal observation, surveillance, tracking, and targeting capabilities are not known. As such, it is likely that this approach will be used more in future UAV development to ensure that new designs meet the required tactical and technical requirements and possess desirable flight characteristics.

The presented work with the cooperator[11], indicates that future development of UAVs can be successfully carried out in collaboration with international partners[28-29], to gain benefits that domestic industries may not possess. In the next phase of development, it will be necessary to define the ultimate UAV performance at the edge of the flight envelope.

REFERENCES

1. Newcom, Laurence R. Unmanned aviation: A brief history of Unmanned Aerial Vehicles. American Institute of Aeronautics and Astronautics, Inc., 2004, 176 p.
2. ESDU 91009, Effect of twin fins on isolated tailplane lift-curve slope, 1993.
3. Milenković-Babić, M. Propeller thrust force contribution to airplane longitudinal stability. *Aircr. Eng. Aerosp. Tech.,* 2018, **90**(9), 1474-1478. doi:10.1108/AEAT-04-2017-0104
4. Kurukularachchi, P.L.; Munasinghe, S.R. & De Silva, H. R.P. Stability analysis for a twin boom H-tail Medium Scale UAV through simulated dynamic model. *In* 2016 Moratuwa Engineering Research Conference, 2016. doi:10.1109/MERCon.2016.7480177
5. Wang, K. & Zhou, Z. An investigation on the aerodynamic performance of a hand-launched solar-powered UAV in flying wing configuration. *Aerosp. Sci. Technol.,* 2022, **129**, 107804. doi:10.1016/j.ast.2022.107804
6. Yıldırım, Ş.; Çabuk, N. & Bakırcıoğlu, V. Experimentally flight performances comparison of octocopter, decacopter and dodecacopter using universal UAV. *Measurement*, 2023, **213**, 112689. doi:10.1016/j.measurement.2023.112689
7. Zhang, Y.; Zhang, X.; Li, Y.; Chang, M. & Xu, J. Aerodynamic performance of a low-Reynolds UAV with leading-edge protuberances inspired by humpback whale flippers. *Chinese J. Aeronaut.,* 2021. doi:10.1016/j.cja.2020.11.004
8. Ilić, I. Numerical modelling of aircraft structural parts made of laminated composite materials in the area of geometrical nonlinear behaviour. University of Belgrade, Belgrade, Serbia, 2016. (PhD Thesis in Serbian).
9. Ivković, D. Aerodynamic optimization of winglets for unmanned aerial vehicles., University of Belgrade, Belgrade, Serbia, 2021. (Master's thesis in Serbian).
10. Velimirović, Kosta. Tactical unmanned aerial vehicles equipped with piston engine, determination flight performances, Military Technical Institute, Belgrade, Serbia, 2013. 80 p. (Monograph in Serbian).
11. Novosti. Pegazov let u vojsku Srbije: Vojnotehnički institut spreman za isporuku prvih domaćih bespilotnih letelica. 1.1.2023. (Serbian). https://www.novosti.rs/c/drustvo/vesti/1187452/pegazov-let-vojsku-srbije-vojnotehnicki-institut-spreman-isporuku-prvih-domacih-bespilotnih-letelica (Accessed on 18 February 2023).
12. Milenković-Babić, M.; Ivković, D.; Ostojić, B.; Trifković, M. & Antonić, V. Take-off and landing performance of Tactical UAV. *Sci. Technol. Rev.,* 2023, **73**(2), 7-12. doi:10.5937/str2302004M
13. Snorri, Gudmundsson. General aviation aircraft design: Applied methods and procedures. *Elsevier Inc*, 2014. 1034 p.
14. Calculation of the aerodynamic characteristics of the medium-range tactical unmanned aerial vehicle - PEGAZ, by using CFD. VTI report No. B3–600-П-06,

2020 (Serbian).
15. Vijayakumar, M.; Parammasivam, K.M.; Rajagopal, S. & Balaji, C. Effect of localised pressure depression and rain on aerodynamic characteristics of Male UAV. *Def. Sci. J.,* 2023, **73**(4), 385-393. doi:10.14429/dsj.73.17481
16. Investigating the possibility of improving the quality of measurements in the T-35 wind tunnel. VTI report No. B3–581-И-06, 2016 (Serbian).
17. USAF stability and control DATCOM. McDonnell Douglas Corporation, Douglas Aircraft Division, 1978.
18. Raymer, Daniel P. Aircraft design: A conceptual approach. AIAA education series, 2012.
19. Zanzottera engines. 630HS Engine. https://www.zanzotteraengines.com/engines/630hs-engine/ (Accessed on 18 February 2023)
20. Perkins, Courtland D. & Hage, Robert E. Airplane performance stability and control. John Wiley & Sons, 1949, 504 p.
21. Kimberlin, Ralph D. Flight testing of fixed-wing aircraft. American Institute of Aeronautics and Astronautics, 2003, 441 p.
22. Remote piloted UAV PEGAZ – performance. VTI report No. B3–602-П-06, 2020 (Serbian).
23. EASA CS-23. Certification specifications for normal, utility, aerobatic, and commuter category aeroplanes. 2014.
24. STANAG 4671. UAV Systems Airworthiness Requirements (USAR) for North Atlantic Treaty Organization (NATO) Military UAV Systems. 2007.
25. Remote piloted UAV PEGAZ - ground and flight test report. VTI report No. B3–602-И-06, 2022 (Serbian).
26. Cook, M.V. & De Castro, H.V. The longitudinal flying qualities of a blended-wing-body civil transport aircraft. *The Aeronautical J.*, 2004, 75-84. doi: 10.1017/S0001924000005029
27. Dean, J.; Clifton, J.; Bodkin, D.; Morton, S. & McDaniel, D. Determining the applicability and effectiveness of current CFD methods in store certification activities, 48th AIAA Aerospace Sciences Meeting Including the New Horizons Forum and Aerospace Exposition, 2010, 4-7 January, Orlando, Florida. doi:10.2514/6.2010-1231
28. AIRBUS SIRTAP Awaits financing. 2023, **6**. https://www.edrmagazine.eu/airbus-sirtap-awaits-financing (Accessed on 18 February 2023)
29. Airbus sirtap, Tactical unmanned aircraft system. 2023, **6**. https://www.militaryfactory.com/aircraft/detail.php?aircraft_id=2502 (Accessed on 18 February 2023)

ACKNOWLEDGEMENT

The authors are grateful to the colleagues from Military Technical Institute and the Chinese co-operator, for their assistance and support. Their work is greatly appreciated.

CONTRIBUTORS

Dr Miodrag Milenković-Babić obtained PhD from Faculty of Mechanical and Civil Engineering in Kraljevo, University of Kragujevac. He is working at the Military Technical Institute in Belgrade, sector for Aeronautics in Aerodynamics Department. His current areas of interests include: Applied computational aerodynamics, flight mechanics and flight testing.
In the current study he has provided computational aerodynamics results, flight testing and analysis of flight-testing results.

Ms Biljana Dovatov graduated in Mechanical Engineer from the Faculty of Mechanical Engineering, University of Belgrade. She is working at the Military Technical Institute in Belgrade, sector for Aeronautics in Aerodynamics Department. Her current areas of interests include: Flight loads and CFD analysis.
In the current study she has contributed in the CFD simulation and model design results.

Mr Branislav Ostojić obtained his MSc (Aerospace Engineering) from the Faculty of Mechanical Engineering, University of Belgrade. He is working at the Military Technical Institute in Belgrade, sector for Aeronautics in Aerodynamics Department. His current areas of interests include: Applied computational aerodynamics (derivatives and stability analysis) and flight testing.
In the current study, he has provided flight testing and analysis of flight-testing results.

Mr Vuk Antonić obtained his MSc (Aerospace Engineering) from the Faculty of Mechanical Engineering, University of Belgrade. He is working at the Military Technical Institute in Belgrade, sector for Aeronautics as an Aircraft Design Engineer, mostly concerning Aircraft Control Systems, Flight Testing Equipment and Cabin Layout Design.
In the current study he has provided preparation of the UAV for flight-testing and analysis of flight-testing results.

Mr Milenko Trifković is an Aeronautical Engineer that obtained his MSc (Aerospace Engineering) from Faculty of Mechanical Engineering, University of Belgrade. He is working at the Military Technical Institute in Belgrade, sector for Aeronautics in Aerodynamics Department. His current areas of interests include: Flight testing.
In the current study he has provided preparation of the UAV for flight-testing and analysis of flight-testing results.

Mr Dušan Ivković obtained his MSc (Aerospace Engineering) from the Faculty of Mechanical Engineering, University of Belgrade. His areas of interests include: Conceptual aircraft design and flight testing.
In the current study, he has provided flight testing and analysis of flight-testing results.

Defence Science Journal, Vol. 75, No. 1, January 2025, pp. 27-34, DOI : 10.14429/dsj.20149

Designing Simulation Logic of Cyber Operations on Physical Space Using C2 Effectiveness Measurement

Sangjun Lee and Dongsu Kang*

Department of Computer Science and Engineering, Korea National Defence Univ., Nonsan - 330 21, Republic of Korea
**E-mail: dasekang@korea.kr*

ABSTRACT

The existing cyber operations training is based on working units, which makes it difficult to expect timely orders from commanders conducting physical warfare-focused operations. This study applies the effectiveness measurement and damage assessment quantification methods of the targeting assessment process to design a simulation logic for cyber operations training in conjunction with physical warfare. Random information variables are substituted into the command and control (C2) effectiveness measurement methodology to assume the impact of modulation attacks on C2 capabilities. The value of enemy assets determined in physical space and information errors in cyberspace are used as variables to measure operational effectiveness, converted into parameters, and entered into the simulator to assess damage. By applying the proposed simulation logic to the air operations case, it can be demonstrated that the increase in information error and the value of enemy assets reduces the operational effectiveness and increases the damage. By visualising this in a training model of a constructive environment, cyber operations command and response procedures can be mastered simultaneously.

Keywords: Simulation logic; Cyber operation training; Cyberspace quantification; Cyber measure of effectiveness; Cyber battle damage assessment

NOMENCLATURE

σ_a^2 : Information errors after a cyberattack (Initial value is σ^2, no errors)
p : Probability value (Initial value is p_c)
C_1 : Arbitrary constant
α : Probability multiplier
K : Effectiveness multiplier

1. INTRODUCTION

In the face of escalating military tensions with North Korea, the United States and the Republic of Korea have recently developed joint guidelines specifying detailed standards for cybersecurity, and continue to expand their capabilities to conduct joint operations in all areas, including cyberspace, by mastering and sharing information and response procedures through cyber alliance training[1].

However, the current level of cyber operation training is a red-teaming type[2], which may be suitable for specific cyber defence organisations or individual professionals to enhance their tactical abilities. Because of the lack of coordination with physical warfare units, these cases can act as factors that do not significantly recognise the importance of cybersecurity. Therefore, it is necessary to shift to a complex and expanded training method that connects cyber operations and physical space by merging existing types and table top types[3]. To this end, this study aims to contribute to multidomain integrated operations by visualising the quantified impact of adversary cyberattacks on physical warfare in the Modelling and Simulation (M&S) in a constructive environment.

The rest of the paper is organised as follows. Section 2 presents limitations and alternatives to existing studies for quantifying cyberspace, and Section 3 designs a procedure for simulating cyber operations in the M&S model. Section 4 validates the designed simulation logic with an air operations effectiveness measurement and damage assessment case study, and Section 5 concludes with a summary of the research.

2. LITERATURE REVIEW

2.1 Quantification of Cyber Operations

In physical warfare, all targets must be evaluated organically to derive missions (or end states) at the war level[4]. The targeting assessment process is divided into two parts: assessment metrics to measure the task, effectiveness, and evaluation objectives (e.g., Measure of Effectiveness (MOE)), and the Combat Assessment (CA), such as the Battle Damage Assessment (BDA), which measures the results of the engagement conducted by the task force. The outputs of the CA feed back into the combat task at the tactical level, which is the first step in the targeting assessment process[5]. In contrast to physical space, operational activities in cyberspace, which is defined as a virtual environment, are classified as noncombatant forces comprising intangible elements. As these elements are diverse and complex, which limits instrumentation and measurement, research is being conducted to quantify them by relating to the aforementioned procedures[6].

Received : 30 April 2024, Revised : 05 September 2024
Accepted : 06 September 2024, Online published : 10 January 2025

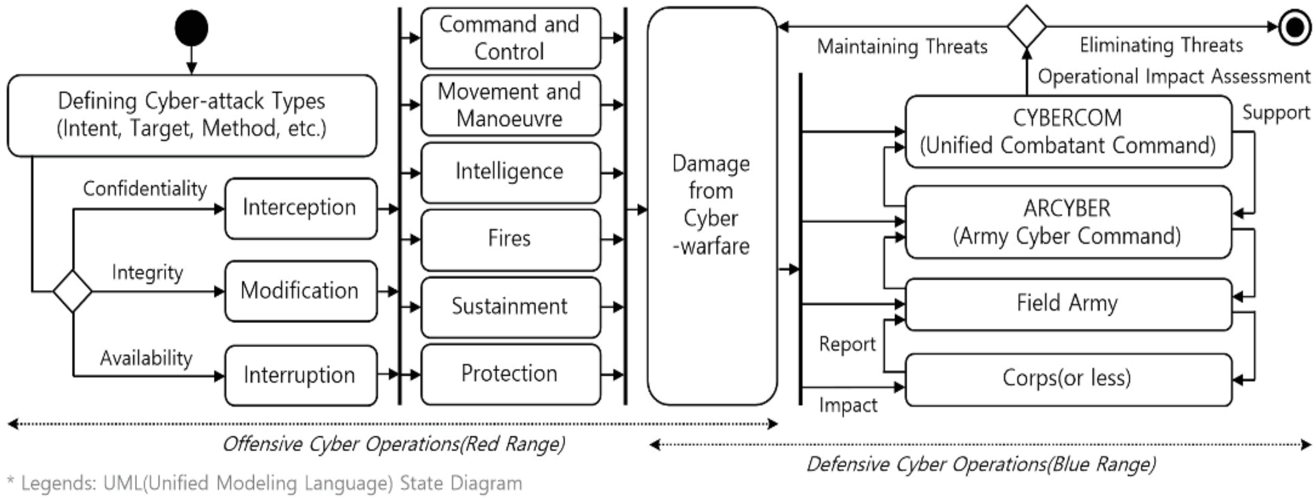

Figure 1. Cyber operations procedure.

However, the methods presented may lead to different assessment results depending on the subjective view of the expert or the environment in which the actual operation is conducted[7-14]. In particular, a CA calculated without considering assessment metrics cannot create a cycle of the targeting assessment process and may fail to provide the information required between operations. Therefore, the M&S requires the design of a formalised analysis tool to simulate the effects of cyber operations in conjunction with physical warfare, as well as a procedure to simultaneously measure and assess MOE and BDA throughout a single operation in a unified process.

2.2 Cyber Operation Algorithms

Cyberattacks are carried out to destroy the three goals of information security: Confidentiality, Integrity, and Availability, and MITRE Corp. has standardised the effects of cyberattacks into six categories: Degradation, Interruption, Modification, Fabrication, Unauthorised Use, and Interception[15]. The types of cyberattacks can be broadly categorised as interception, modification, and interruption based on the three objectives of the attacks on each information security target, and other similar categories can be further classified into different types of sub-attacks.

The U.S. Army's Field Manual for Operations (FM 3-0) identifies six warfighting functions as the core capabilities for achieving operational objectives: C2, Movement and Manoeuvre, Intelligence, Fires, Sustainment, and Protection[16]. In cyber operations, the warfighting functions are targeted by the adversary, and the cyber operations performance based on the type and objective of the proposed attack is shown in Fig. 1[17].

When a cyberattack of the defined type is executed against interception, modification, and interruption arise as damage caused by cyber warfare to the six major warfighting functions of friendly forces. In the military domain, the ultimate goal of an adversary cyberattack is to interrupt the C2. Therefore, the scope of this study is limited to the direct impact of modification attacks that compromise the integrity of the C2 and the indirect impact on fires function.

2.3 C2 Effectiveness Measurement Method

US DARPA (Defence Advanced Research Projects Agency) recognised the problem that C2 provides significant influence in winning or losing wars. To apply advanced C2 concepts to combat management, the Office of Naval Intelligence, which participated in the study, presented a methodology for quantifying the value of C2's information acquisition, processing, and exchange performance parameters in engagements between weapon systems.

By substituting the pre- and post-engagement relative combat power ratios, as measured by improvements such as information sharing and enhancement and force coordination, into a generalised form of Lanchester's Law, the method was able to derive the impact of enhanced or degraded C2 system performance on combat outcomes under certain conditions, confirming that C2 can be a significant force factor in combat outcomes.

Improvements are a key factor in determining the value of enemy and friendly assets, which are divided into two main categories: probability multipliers, consisting of non-combat factors (time, information, etc.), and ratio multipliers, consisting of combat factors (maximum range of a weapon, etc.), and are affected by the number and type of weapons, including troops[18].

To measure the impact of errors in information caused by a tampering attack, a type of cyberattack intended to threaten the integrity of data, on the C2 capabilities of the friendly forces targeted by the attack, a parametric function is needed to quantify it. To this end, we apply C2 effects measurement, which can efficiently measure the increase or decrease in C2, to measure and evaluate the impact of cyber operations on physical space. For this purpose, the degree of information error is set as a variable and data is calculated from the information engineering perspective, and the following four points are assumed.

- The change in the error variable of the information would have been caused by an adversary cyberattack
- To analyse only the operational impact of the information variable between effectiveness calculations, combat

power factors (ratio multipliers) such as the detailed specifications of the weapon system are not considered
- If there are no errors in the information, the combat effectiveness of the weapon system is not reduced and the operation has a 100 % chance of success
- At the command post, there is no change in the time required for C2 of the target detection to attack the decision phase of the emergency targeting process.

3. CYBER OPERATION PROCEDURE

3.1 Designing Simulation Procedure

In the military domain, to link cyber operations to physical warfare, an integrated simulation process can be designed to quantify impacts through a targeting assessment process and plot the results into an M&S in a constructive environment, as shown in Fig. 2.

First, the Red Operator conducts both physical and cyberattacks on friendly power assets operating under random battlefield conditions. The Blue Operator, who has the value of a specific asset, will be affected by the enemy's physical attack reflecting the battlefield change factors, and the time and combat power of the operation will be affected, as the value of the enemy's asset increases, the decline in combat power will also increase. In addition, cyberattacks can cause errors in the information provided by weapon systems that rely on the control system, causing indirect damage to the operator.

Indicative information errors are considered along with the increasing value of enemy assets to feed into the C2 effectiveness method and are used to analyse the MOE degraded by cyber operations. The operational impact of the BDA assessment from the previously measured MOE is then simulated and visualised in the M&S through the simulator.

The evaluated BDA supports the commander's command decision by feeding back into the tasking process, and after simulating the impact of the M&S, the cyber crisis judgement and information judgement are provided to the operators, enabling commanders and staff to master the command process of cyber operations and practitioners in cyber protection units to master the response process.

3.2 Occurring Weapon Control System Error

A modification of the integrity of the data will result in errors in the information the system presents to the user. Because the degree of information error may vary depending on the intent, method, and target of the attack and cannot be explicitly measured, the M&S requires a variable determination process through a simulated random sampling method for decision-making under general uncertainty conditions to determine the degree of information error. The representative simulated random sampling methods are Monte Carlo (MCS) and Latin Hypercube Sampling (LHS). MCS relies on randomness to draw two random samples from the entire uniformly distributed area, which has the disadvantage that the samples drawn may tend to be biased toward a particular space. The LHS relies on uniformity, or planned randomness, to divide the entire area into small similar intervals and sample each interval in

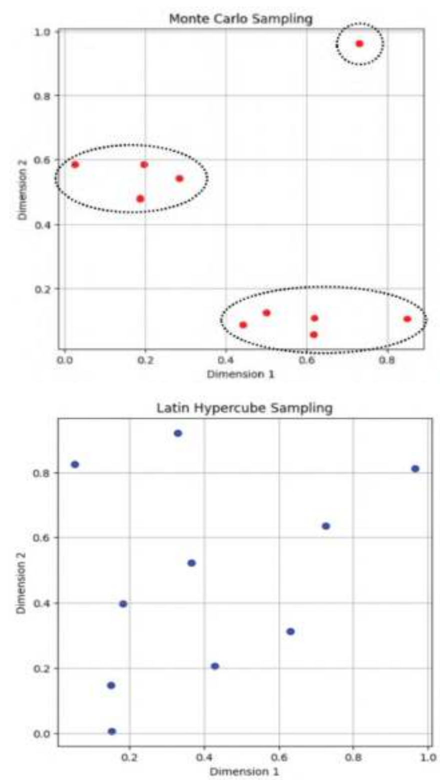

Figure 3. Sampling results using MCS, LHS.

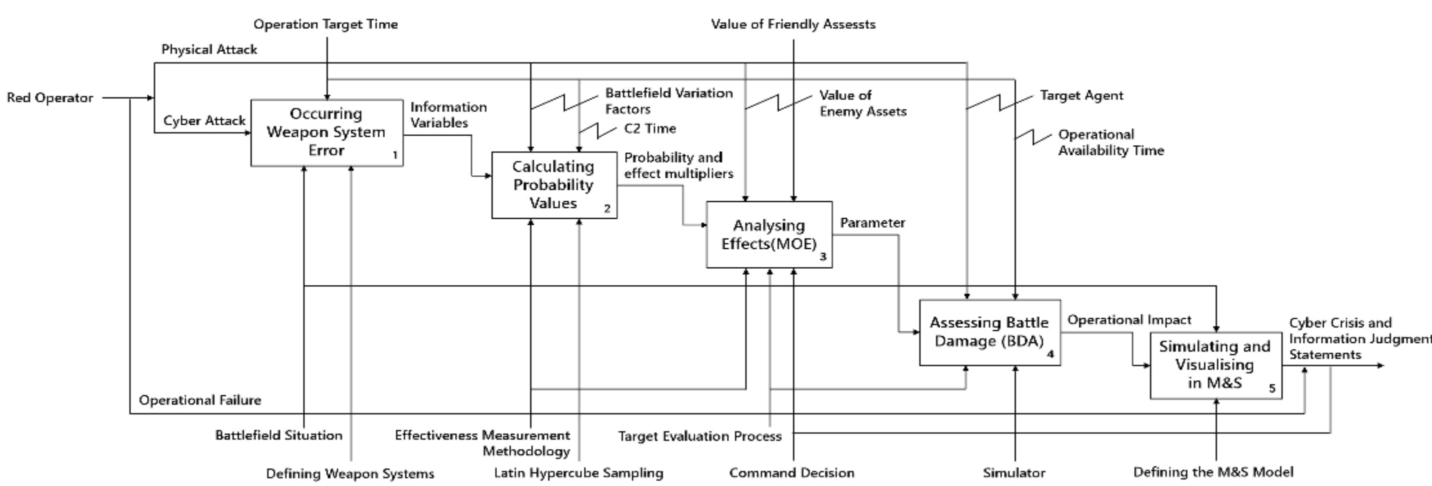

Figure 2. Procedure of cyber operation in conjunction with physical warfare.

rotation to avoid overlap as much as possible. Therefore, the samples are distributed over the area. Fig. 3 is an example of ten random numbers generated by the Python code to compare each sampling method. In this study, we use LHS, a relatively uniform sampling method in the M&S, to determine the degree of information error.

3.3 Calculating Probability Values

In the C2 effectiveness measurement, under the condition that hostile objects are randomly distributed in the area of interest A (ρ), the uncertainty of area (ΔA) is a function of the velocity of the platform (v_p), the accuracy of the initial information, and the C2 turnaround time (t_{cs}, control system). The probability value of detection and correct association within t_{cs} is defined as given in Eqn. (1).

$$p_c = \frac{1}{1+\rho\Delta A} = \frac{1}{1+C_1\rho v_p t_{cs}^2 \sigma^2} \tag{1}$$

In the probability value, the response preempted time of the operational force is the sum of the control system time and the available response time ($T_p = t_{cs} + t_a$). It must also satisfy $p = \alpha p_c$ ($\alpha > 1$) by α, which is a potential that represents the increment between p_c and p due to the improvement of C2 system performance. Therefore, α is derived from the difference in available time, which depends on the C2 system performance, and the preset degree of information error, as shown in Eqn. (2).

$$\alpha = \frac{1-\sigma_a^2}{p(1-\sigma_a^2)+(1-p)(1-\sigma^2)} \tag{2}$$

3.4 Analysing Operations Effects

To calculate the MOE, both the probability multiplier and the rate multiplier must be considered simultaneously. In the M&S, the ratio multiplier is a factor that can be automatically determined by the physical battlefield configured in the constructive environment, the MOE calculation only considers α constructed around the information variables. Substituting the value of enemy and and friendly assets (N', M') in a linear state into Lanchester's Square Law, the MOE calculation that reflects the changed value of enemy and friendly assets ($<N'^2>_j$, $<M'^2>_j$) after a single engagement j is shown in Eqn. (3). Accordingly, the MOE changed by the adversary's cyberattack can be presented as Eqn. (4), taking into account the α.

$$\text{when} \quad <MOE>_j = \frac{<N'^2>_j - <M'^2>_j}{N^2} \tag{3}$$

N', M': the value of friendly and enemy asset

$$\text{where} \quad <\hat{MOE}>_j = \frac{\alpha <N'^2>_j - <M'^2>_j}{N^2} \tag{4}$$

N', M': the value of cyber friendly and enemy assets

The rate of increase in MOE without accounting for the combat power factor, K, can be expressed as Eqn. (5), and based on the calculated probability value, multiplier data, and the C2 effectiveness measurement, because the change in C2 system performance can be measured ($\hat{MOE} = K \times MOE$).

$$K = \frac{<\hat{MOE}>_j}{<MOE>_j} = \frac{\alpha <N'^2>_j - <M'^2>_j}{<N'^2>_j - <M'^2>_j} \tag{5}$$

N', M': the value of cyber friendly and enemy assets

3.5 Assessing Battle Damage and Simulation

To apply the C2 theory to cyber operations, it is critical to quantify noncombat power, and the method defines noncombat power as a function of information error and time available. If operational effectiveness was measured based on information errors caused by adversary cyberattacks, the BDA can be evaluated with time available as a variable based on the calculated MOE to assess the full range of non-combat power factors defined by the method.

In the military M&S, a weapon score approach is applied to evaluate BDA, which takes into account the performance of multifunctional weapon systems[19]. However, since these approaches contain sensitive information and it is difficult to obtain public data, the study utilised the AnyLogic simulator, an object-oriented software that supports multi-modeling. The evaluation was performed using an agent-based technique, and the simulation identified two factors: the number of units that can be destroyed within the initial assigned operational time and the time required to destroy all assigned units, as shown in Fig. 4.

4. CASE STUDY: CLOSE COMBAT ATTACK

We analyse and assess the operational impact of an adversary cyberattack on a close combat attack (CCA). CCA is an operation in which attack helicopters are deployed in groups of two to four to conduct real-time attacks on temporary targets

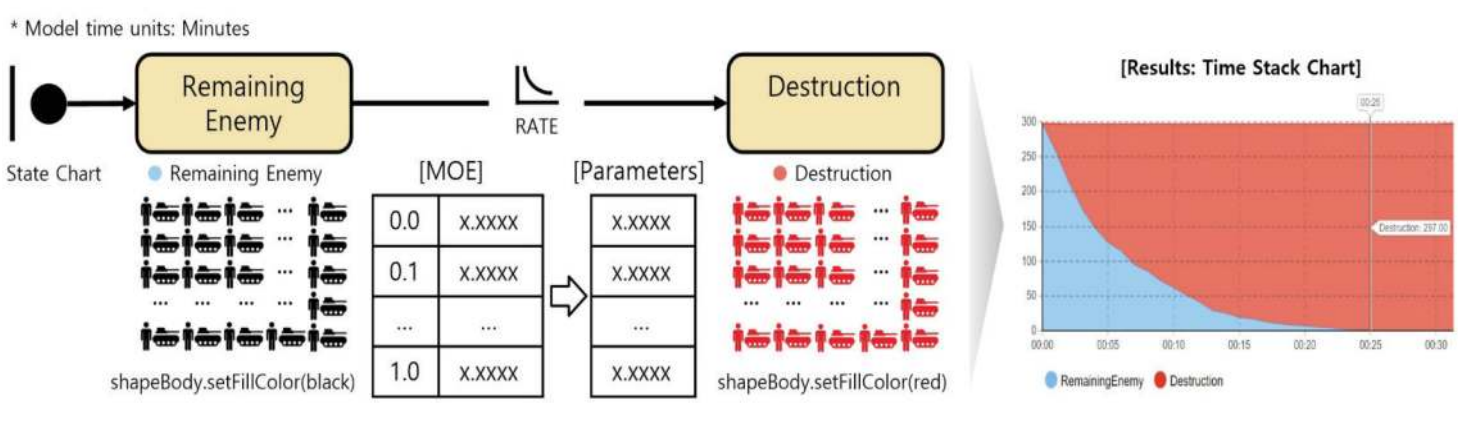

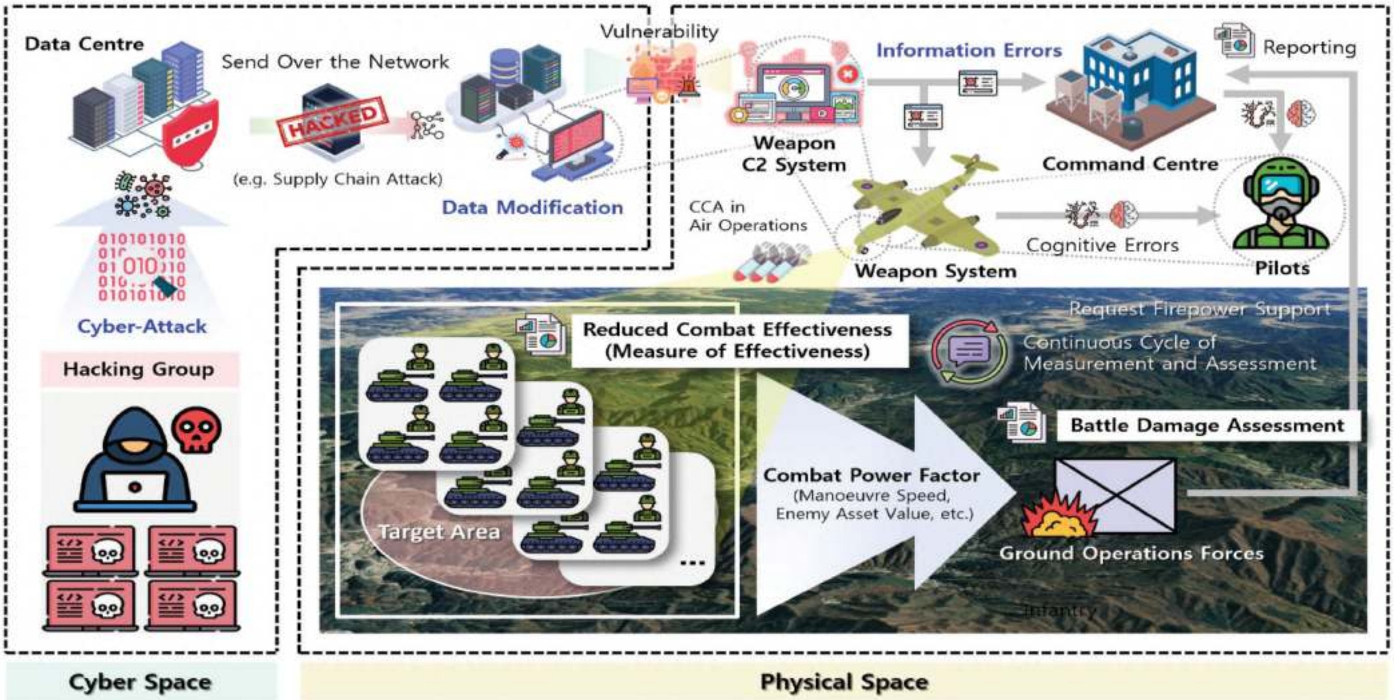

Figure 5. Engagement scenario for CCA operations.

within 1–2 km of ground forces[20]. The goal is a preemptive strike within 30 min using the kill chain concept dynamic targeting assessment process[21]. The target information is primarily directed at enemy mechanised infantry, which is highly mobile. In particular, the North Korean mechanised infantry is a brigade-centric enemy mobile force[22] whose mobility is typically estimated at 5 to 15 km/h.

The following are engagement scenarios. A manoeuvre battalion of a North Korean mechanized infantry brigade is approaching the front of a friendly ground operation force at 15 km/h, the maximum manoeuvring speed (v_p) for mechanised units, and the ground operation force has requested a CCA from its superior unit for target "1" ($\rho = 0.6666\ldots$) in a 1.5 km^2 (1.5 km wide × 1 km long) area of interest. It was determined that 5 min (0.0833 hr) would be required for C2 (t_{cs}) out of the operational target time (T_p) of 30 min, resulting in a total of 25 min of tactical availability (t_a). At this time, since cyberattacks, such as supply chain attacks, are carried out by malicious actors in cyberspace, much (or all) of the information provided by the attack helicopter's C2 system becomes erroneous (σ_a^2) due to the manipulation of data stored by the weapon system. Errors in the information directly affect command posts and weapon systems located in physical space and indirectly lead to cognitive errors in the pilots receiving the information from these systems.

The resulting effects are manifested as reduced effectiveness of weapon systems and increased damage to friendly forces in parallel with other elements of combat power, such as the value of enemy assets, in the physical space of the battlefield.

The calculated MOE and BDA are reported to the command post to iterate on C2 procedures and procedures for responding to an attack. The battlefield situation constructed based on these settings is shown in Fig. 5.

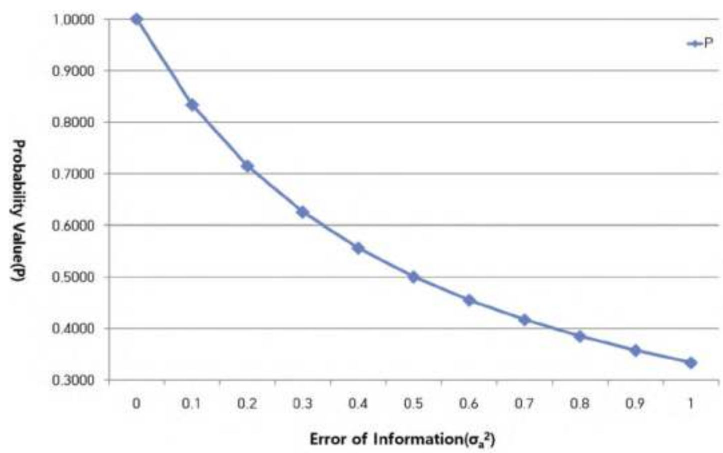

Figure 6. Changing probability values.

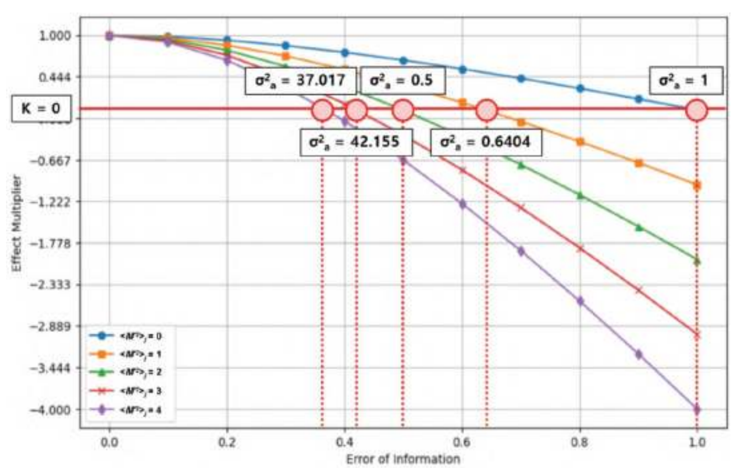

Figure 7. Changes in effectiveness multiplier.

Table 1. Calculation of multiplier based on '*p*'

Information error (σ_a^2)	Probability values (p)	Probability multiplier (α)	Effectiveness multiplier (K)				
			$\langle M'^2 \rangle_j = 0$	$\langle M'^2 \rangle_j = 1$	$\langle M'^2 \rangle_j = 2$	$\langle M'^2 \rangle_j = 3$	$\langle M'^2 \rangle_j = 4$
0.0	1.0000	1.0000	1.0000	1.0000	1.0000	1.0000	1.0000
0.1	0.8333	0.9818	0.9818	0.9636	0.9455	0.9273	0.9091
0.2	0.7143	0.9333	0.9333	0.8667	0.8000	0.7334	0.6667
0.3	0.6250	0.8615	0.8615	0.7231	0.5846	0.4462	0.3077
0.4	0.5556	0.7714	0.7714	0.5429	0.3143	0.0858	- 0.1428
0.5	0.5000	0.6667	0.6667	0.3334	0.0000	- 0.3333	- 0.6666
0.6	0.4546	0.5500	0.5500	0.1000	- 0.3500	- 0.8000	- 1.2499
0.7	0.4167	0.4235	0.4235	- 0.1529	- 0.7294	- 1.3058	- 1.8823
0.8	0.3846	0.2889	0.2889	- 0.4222	- 1.1333	- 1.8444	- 2.5555
0.9	0.3572	0.1474	0.1474	- 0.7053	- 1.5579	- 2.4105	- 3.2631
1.0	0.3333	0.0000	0.0000	- 1.0000	- 2.0000	- 3.0000	- 4.0000

Table 2. Information errors and the impact of asset value on MOEs

MOE	σ_a^2	$\langle M'^2 \rangle_j = 0$			$\langle M'^2 \rangle_j = 1$			$\langle M'^2 \rangle_j = 2$		
		MÔE	Difference	Decline (%)	*MÔE*	Difference	Decline (%)	*MÔE*	Difference	Decline (%)
	0.0	1.0000	0.0000	0.00	1.0000	0.0000	0.00	1.0000	0.0000	0.00
	0.1	0.9818	0.0182	1.82	0.9636	0.0364	3.64	0.9455	0.0545	5.45
	0.2	0.9333	0.0667	6.67	0.8667	0.1333	13.33	0.8000	0.2000	20.00
	0.3	0.8615	0.1385	13.85	0.7231	0.2769	27.69	0.5846	0.4154	41.54
	0.4	0.7714	0.2286	22.86	0.5429	0.4571	45.71	0.3143	0.6857	68.57
1.0000	0.5	0.6667	0.3333	33.33	0.3334	0.6666	66.66	0.0000	1.0000	100.00
	0.6	0.5500	0.4500	45.00	0.1000	0.9000	90.00	- 0.3500	1.3500	135.00
	0.7	0.4235	0.5765	57.65	- 0.1529	1.1529	115.29	- 0.7294	1.7294	172.94
	0.8	0.2889	0.7111	71.11	- 0.4222	1.4222	142.22	- 1.1333	2.1333	213.33
	0.9	0.1474	0.8526	85.26	- 0.7053	1.7053	170.53	- 1.5579	2.5579	255.79
	1.0	0.0000	1.0000	100.00	- 1.0000	2.0000	200.00	- 2.0000	3.0000	300.00

Set a randomly sampled σ_a^2 as the information variable to calculate the p. The constant (C_1) applied to it was assigned a value of 28.8259 so that with an information error of 0.5, the probability value also becomes 0.5. The probability value is calculated by Eqn. (1). The probability value decreases proportionally to the information error, and the graph in Fig. 6 shows an exponential function.

According to the third assumption, in Eqn. (5), K must also be 1 when α is 1. Therefore, the value of the friendly asset required to calculate K is automatically determined by the number that the difference from the value of the enemy asset can be 1 ($\langle N'^2 \rangle_j$ - $\langle M'^2 \rangle_j = 1$). As a result, this can represent a state in which the value of the friendly asset remains intact in the absence of the enemy's physical threat, and does not take into account situations in which the number of friendly forces or combat power in the existing possession increases or decreases beyond a certain level compared to the value of the enemy asset.

Then, the α based on p, and K based on the change in friendly and the enemy asset value can be calculated, as shown in Table 1. Since p decreases as σ_a^2 increases, α also decreases proportionally to the p. It can be seen that K, which is affected by α, has the same value as α when there is no impact from the value of the enemy asset ($\langle M'^2 \rangle_j = 0$). However as the value of $\langle M'^2 \rangle_j$ increases, K decreases to a greater extent. The point

Table 3. Simulation results for physical space impact of cyber operations

MÔE	Parameter	Destroy units within available time (25min)	Time to complete the operation
1.0000	0.1650	297	25 min
0.9818	0.1620	297 (± 0)	25 min (± 0)
0.9333	0.1540	295 (- 2)	27 min (+ 2min)
0.8615	0.1421	293 (- 4)	29 min (+ 4min)
0.7714	0.1273	290 (- 7)	32 min (+ 7min)
0.6667	0.1100	284 (- 10)	37 min (+ 12min)
0.5500	0.0908	272 (- 25)	45 min (+ 20min)
0.4235	0.0699	242 (- 55)	58 min (+ 33min)
0.2889	0.0477	206 (- 91)	85 min (+ 60min)
0.1474	0.0243	147 (- 150)	166 min (+ 141min)
0.0000	0.0000	0	-

at which K becomes zero due to increasing information error as shown in Fig. 7.

The MOE changes proportionally to the number of friendly troops (N) according to Eqns. (3-4), so we used $N = 1$. The changes in the MOE as a function of the information error and the value of enemy assets are shown in Table 2. From the point at which K becomes zero, which is the data calculated earlier, the desired operational effectiveness by friendly forces can no longer be achieved through combat (red square area). As a result, when the battlefield in physical space is significantly affected by the enemy, it becomes difficult to achieve the desired operational effectiveness even with information errors caused by relatively small data modulations as shown in Fig. 8.

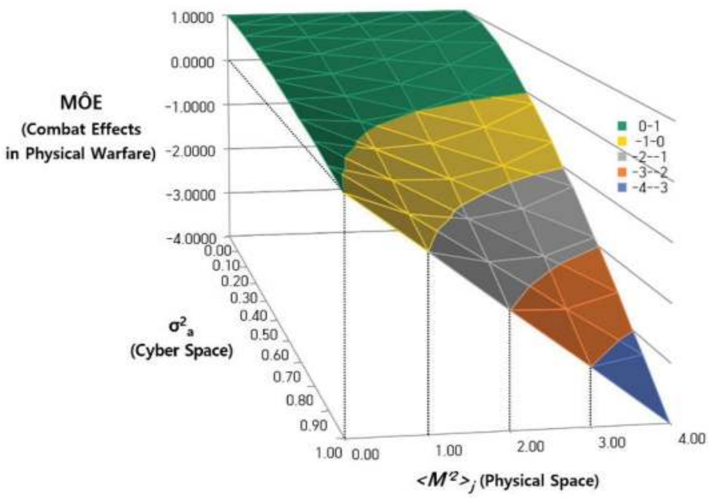

Figure 8. MOE effect reduction.

The values assigned to the simulator are shown in Table 3. The first unit is based on a common, unspecified size of a mechanised infantry battalion, giving a total of 297 units with 270 men (1 squad of 10 men × 3 squads × 3 platoons × 3 companies) and 27 armoured vehicles (1 squad of 1 vehicle × 27 squads). Differences in combat power between agents, determined by weapon scores in the M&S, were not accounted for between experiments. The initial parameter of 0.1650 was applied, a value that could destroy all 297 units initially assigned at 25 min (t_a), the launch attack, which is the final phase of dynamic targeting. The parameters for the BDA assessment were adjusted in proportion to the rate at which the MOE decreases with increasing information error.

The simulation results show that as MOE, decreases, the number of units that can be destroyed within the operational time available (t_a) decreases, and the time required to complete the operation to destroy all target units increases, as shown in Fig. 9.

This situation causes a shift from a traditional mission to defeat the enemy at a complete level to an incomplete mission of deterrence, repulsion, and delay where the enemy is still present. In other words, if the commander focuses on defeating the target unit, the time to complete the mission will increase and the survivability of the weapon system cannot be guaranteed. Conversely, if the focus is on maintaining operational availability, the threshold for the target unit is lowered, causing a loss of power due to fighting more enemy forces at a defence point where friendly forces are concentrated. This means that it can create favourable conditions for the enemy, upsetting the balance between mission completion and the commander's requirements.

5. CONCLUSION

Since military operations are centred on physical warfare, it is essential to introduce a tabletop cyber operations training method that complements the current red teaming type. This study proposes a simulation procedure for cyber operations in

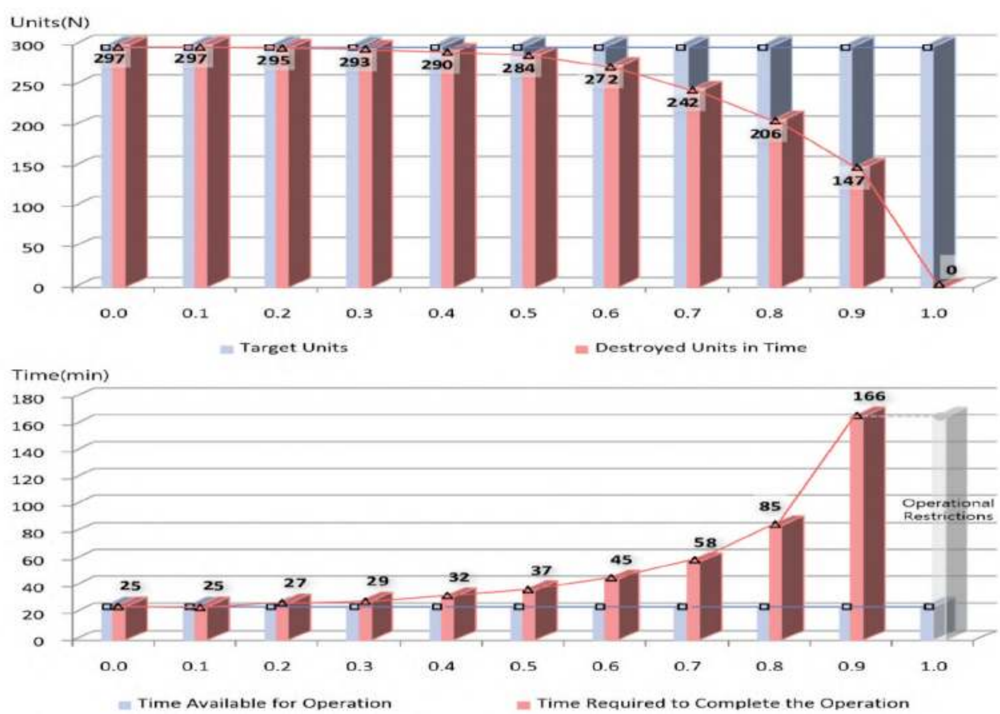

Figure 9. BDA evaluation results by simulator.

conjunction with physical warfare in the M&S, and a method for measuring effectiveness and assessing damage through it. In addition, to specify the logic of cyber operations simulation, detailed elements were determined and simulation feasibility was verified using a CCA engagement scenario. It is expected to raise awareness of the importance of cyber operations through the portrayal of situations between large-scale exercises that can simultaneously master the command procedures and the response procedures of units conducting cyber operations.

REFERENCES

1. Lee, S. & Kang, D. Designing simulation logic of UAV cyber operation using cyber security framework. *IEEE Access*, 2024, **12**, 3488-3498. doi:10.1109/access.2023.3349131.
2. Kang, D. & Lee, M. A study of cyber warfare war games in modern warfare. Research Institute for National Security Affairs, Research Report. 2020. (Korean).
3. U.S. Joint chiefs of staff. Joint publication 5-0 joint planning. pp. IV 27-28, December 2020.
4. U.S. Joint chiefs of staff. Joint publication 3-60 joint targeting. pp. Appendix D 1-10, January 2013.
5. U.S. Joint chiefs of staff. CJCSI 3162.02 Methodology for combat assessment. Instruction, pp. Enclosure B 1-10, March 2019.
6. Choi, S.; Kwon, O.; Oh, H. & Shin, D. Method for effectiveness assessment of electronic warfare systems in cyberspace. *MDPI Symmetry*, 2020, **12**(12). doi:10.3390/sym12122107.
7. Bodeau, D.J.; Graubart, R.D.; McQuaid, R.M. & Woodill, J. Cyber resiliency metrics, measures of effectiveness, and scoring: Enabling systems engineers and program managers to select the most useful assessment methods. MITRE Corp., Tech. Rep. No. 18-2579. September 2018. https://www.mitre.org/news-insights/publication/cyber-resiliency-metrics-measures-effectiveness-and-scoring
8. Kim, Duhoe; Kim, Doyeon; Shin, Dongil; Shin Dongkyoo & Kim, Y. Cyber battle damage assessment framework and detection of unauthorized wireless access point using machine learning. *In* Proceedings of the 6th Int. Conf. on Frontier Computing, Kuala Lumpur, Malaysia, July 3-6, 2018. doi:10.1007/978-981-13-3648-5_59.
9. Nesbit, R. & Thaer, L.V. Study on cyber defence management. Defence Science Board, September 2016.
10. Thiem, L.S. A study to determine damage assessment methods or models on air force networks. Air Force Institute of Technology, Wright Patterson AFB., OH, USA, 2005. (M.S. Thesis)
11. Fortson, L.W. Jr. Towards the development of a defensive cyber damage and mission impact methodology. Air Force Institute of Technology, Wright Patterson AFB.,OH, USA, 2005.(M.S. Thesis)
12. Ostler, R.T. Defensive cyber battle damage assessment through attack methodology modeling. Biblioscholar Publisher, 2012.
13. Kim, S.; Jang, J.; Kwon, O.; Kim, J. & Shin, D. Study on cyberattack damage assessment framework. *IEEE Access*, 2022, **10**, 59270-59276. doi:10.1109/access.2022.3179977
14. Neace, D.L. Measuring cyber operations effectiveness. Air Univ. Research Rep., November 2014.
15. Musman, S.; Temin, A.; Tanner, M.; Fox, D. & Pridemore, B. Evaluating the impact of cyberattacks on missions. MITRE Corp., Tech. Rep., 2010.
16. U.S. Army. Field manual 3-0 operations. pp. Ch. 2 1-3, October 2022.
17. Kang, D. Lee, S. & Yoon, J. A study of GPS jamming and cyber operation simulation logic for the army synthetic battlefield training system. Korea Nat. Defence Univ., Technical Report 2023MNS03-3. October 2023. (Korean).
18. Schutzer, D.M. Selected analytical concepts in command and control; C2 theory and measure of effectiveness, vol. 2. Gordon and Breach Science Publishers, NY, USA, 1982, pp. 119-144.
19. Alle, P. Situational force scoring: Accounting for combined arms effects in aggregate combat models. RAND Inst., Tech. Rep. No. N-3423-NA. 1992.
20. Park, N.A Study on an option to replace air force CAS by army attack helicopters. Kook-min Univ., Seoul, ROK, 2023. (M.S. Thesis). (Korean).
21. Kim, K. A study on integrating multidimensional information for effective preemptive surgical strike. Korea Univ., Seoul, ROK, 2019. (PhD Thesis). (Korean).
22. Noh, Y.; Shin, J. & Lee, J. A study on the organization of basic tactical forces in the future ground forces. Korea Institution of National Defence Development, Research Rep. No. KIND-2012-12. September 2012. (Korean).

CONTRIBUTORS

Mr Sangjun Lee is currently pursuing an MS degree in computer engineering with Korea National Defence Univ., Nonsan, Republic of Korea. He is a Cyber Specialised Officer in the Ministry of Defence. His current research interests include: Defence M&S, cyber warfare, and cyber security.
In the current study, he conceived the idea for applying the method to cyber operations and wrote the original draft manuscript.

Prof Dongsu Kang is currently Professor of Computer Science and Engineering and the Director of the Department of Defence Science, Korea National Defence University. His main area of expertise is software security testing, penetration testing and AI-based systems testing.
In the current study, he was responsible for validating the results of the analysis, editing and improving the manuscript.

Defence Science Journal, Vol. 75, No. 1, January 2025, pp. 35-43, DOI : 10.14429/dsj.20014

Predictive Factor Analysis of Air-to-Air Engagement Outcomes Using Air Combat Manoeuvring Instrumentation Data

Gyuejeong Lee[#], Yong-hwan Kim [$], and Daeyoung Choi[!,*]

[#]SAKAK Co., Ltd., Seoul - 04147, Republic of Korea
[$]Defense Acquisition Program Administration, Gwacheon - 13809, Republic of Korea
[!]Division of Artificial Intelligence and Data Science, The Cyber University of Korea, Seoul - 02708, Republic of Korea
[*]E-mail: choidy@cuk.edu

ABSTRACT

This study presents a novel predictive factor analysis of air-to-air engagement outcomes using a decade of air combat manoeuvring data (2009-2019) from the Air Combat Manoeuvring Instrumentation (ACMI) system of the Republic of Korea Air Force (ROKAF). The objective was to construct and evaluate an air-to-air combat hit prediction model using the ACMI system data to identify the critical factors influencing engagement outcomes. This methodology encompasses data preprocessing, feature engineering, binary classification model development, and model interpretation. This study utilises 17 features, including the attitude and speed of both aircraft, along with five additional features derived from the domain knowledge of the relative positions of the two aircraft. Four machine-learning algorithms were employed: logistic regression, random forest, XGBoost, and CatBoost. The best-performing model achieved an accuracy of 83.0 %, noticeably outperforming the baseline at 76.2 %. The analysis revealed that positional information is more crucial than attitude information in predicting engagement outcomes, with the spatial separation between aircraft emerging as the most influential factor. This study showcasings a standard procedure for utilising ACMI system data and demonstrating the effectiveness of machine learning in analysing air combat data.

Keywords: Air combat manoeuvring instrument (ACMI); Air-to-air engagement; Machine learning; Air-to-air combat hit-prediction model

1. INTRODUCTION

Air superiority is essential in modern warfare[1-3]. Air superiority refers to controlling the battlefield sky against an enemy. Once air superiority is achieved, friendly forces, including ground forces, can manoeuvre without prohibitive interference from enemy forces[4,5]. Air combat is a tactical method used to achieve air superiority, and various studies have been conducted to improve its efficiency[6-9]. In this study, we focus on the critical factors of air combat against an enemy's aerial vehicle regarding Air Combat Manoeuvres (ACM).

Regarding ACM, it is essential to develop effective combat tactics and train fighter pilots to improve the win rate in air-to-air combat. However, due to costs, the use of fighters and weapons for developing or evaluating tactics and training or testing pilot skills is limited[10]. Thus, air-to-air combat training is mostly conducted in virtual environments, and the development of precise ACM performance measurements is becoming increasingly important to ensure the reliability of air combat tactics and pilot skills in real-world scenarios.

Existing research approaches to ACM performance measurements mainly focus on combining analytical and empirical methodologies to develop appropriate measurement structures and algorithms[11]. Candidate measurements such as positional advantage and weapon events have been developed based on the state information of both aircraft and weapons, and various studies have utilised these candidates[12-17]. Waag[18], *et al.* proposed a composite measure to predict engagement outcomes during ACM. Krusmark[12], *et al.* assessed the effectiveness of the traditional Grade sheet used to measure air-combat performance. ARAR[19], *et al.* proposed a flexible rule-based framework for a pilot performance analysis.

However, while the utility and effectiveness of both simulation systems and ACM performance measurements have been demonstrated regarding training fighter pilots and developing air combat tactics, more debate still needs to be had on their reliability and validity in real-world environments[20-21]. Balcerzak[22], *et al.* insisted that there was a shortage of research demonstrating the validity of simulation systems, citing the case of civilian aircraft, and that it was more apparent whether the skills learned in simulations were appropriately applied to actual flights. This debate has significant implications for the military domain. Therefore, providing feedback based on actual manoeuvring track data analysis is essential for calibrating measurements developed in a virtual environment. However, a statistical approach to ACM based on actual data has rarely been studied in this domain because acquiring the actual manoeuvring data of an aircraft is limited because of cost and safety concerns.

Received : 26 March 2024, Revised : 15 September 2024
Accepted : 04 November 2024, Online published : 10 January 2025

Air Combat Manoeuvring Instrumentation (ACMI) systems may be an alternative to resolve these limitations. An ACMI system records in-flight data, such as positional information, aircraft state, and weapon events, using pod devices attached to the aircraft, and the recorded data are used for debriefing. The system consists of aircraft pods and a ground system. ACM data are transmitted from the pod to the ground system for recording, displaying, and debriefing[23]. In addition, these data have been consistently accumulated and managed for over a decade. Thus, given the various attributes and quantities of ACMI data, they can be used in data-driven research[24-25].

Motivated by the need for more realistic and data-driven analyses of air combat engagements, this study presents a comprehensive study based on extensive real-world ACMI data from training engagements. Our objectives are threefold: First, to demonstrate a standard procedure for utilising ACMI system data, encompassing feature extraction, selection, and effective modelling of a hit-prediction problem. Second, an air-to-air engagement hit prediction model was constructed using machine learning algorithms, which allowed us to determine the most dominant components of the ACM in deciding engagement outcomes. Third, interpretable machine-learning techniques were applied to rank the key factors for successful engagement. We analyze feature importance using correlation coefficients, feature importance scores, and SHAP (SHapley Additive exPlanations) values[26]. This approach also allowed us to validate conventional methods, differentiating our work from previous studies that relied primarily on simulated or limited flight test data.

The ACMI data are provided by the Republic of Korea Air Force (ROKAF) for research purposes only and are not publicly accessible.

The remainder of this paper is organized as follows. Section 2 describes the problem definition and data. Sections 3 and 4 demonstrate the results of feature engineering and the analysis details, respectively, followed by a discussion and conclusion in Section 5.

2. PROBLEM DEFINITION AND DATA

According to the ROKAF training protocol, air-to-air combat training can be divided into the five categories listed in Table 1. This study only focused on the BFM training procedure. Let BLUE be a fighter of friendly forces and RED

Table 1. Categories of air-to-air combat training

Category	Description
BFM	Basic Fighter Manoeuvring (Most basic form) - Two fighters train together (attacker, defender)
ACM	Air Combat Manoeuvring (Advanced BFM) - Two fighters attack or defend against a RED
ACT/ DACT	Air combat tactics/dissimilar air combat training air-to-air combat without prior agreements between BLUE and RED. (2:2, 2:4, 4:4, 4:2, etc.)
TI/TIN	Tactical intercept/tactical intercept night capture enemy aircraft using fighter radar with the assistance of air traffic control
WA	Weapon to air fighter practices gun firing.

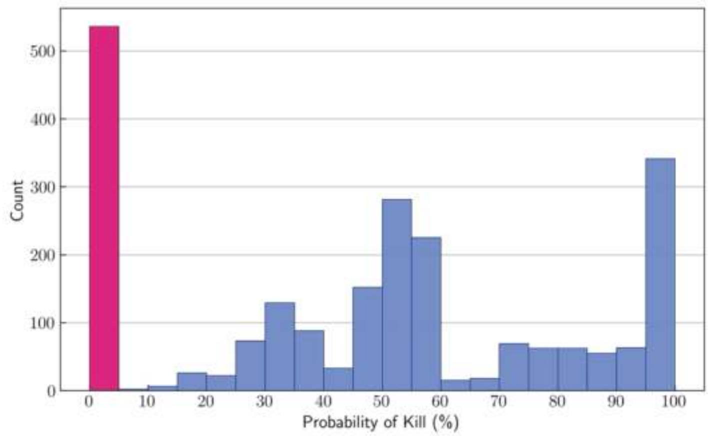

(a)

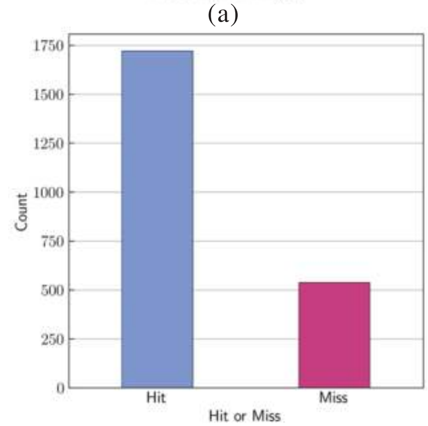

(b)

Figure 1. Distributions of Attributes. (a) Probability of kill (PK) ranges between 0 and 1; and (b) 'Hit' and 'Miss' are defined by whether the probability of kill is greater than 0.

Table 2. Attributes of the data

Attribute		Type	Description	Unit
BLUE	RED			
B_xpos	R_xpos	Position	X position coordinate	degree
B_ypos	R_ypos	Position	Y position coordinate	degree
B_zpos	R_zpos	Position	Z position coordinate	m
B_roll	R_roll	Attitude	Rotation around the front-to-back axis	radian
B_pitch	R_pitch	Attitude	Rotation around the side-to-side axis	radian
B_yaw	R_yaw	Attitude	Rotation around the vertical axis	radian
B_aoa	R_aoa	Attitude	Angle between the oncoming air and a reference line on the aircraft	radian
B_speed	R_speed	Kinetic energy	Speed of an aircraft	Mach
B_g,	R_g,	Kinetic energy	Gravity of an aircraft	G

be an adversarial fighter in an air combat training scenario. BLUE and RED are the same type of fighter, F-16, who engage in Within-Visual Range (WVR) combat. BLUE fires AIM-9 IR (infrared) tracking-guided air-to-air missiles to shoot down RED[27]. During training, the ACMI pods collected the maneuvering data of both aircraft, except for the RED probability of kill (PK) value. The PK value, which represents the extent to which BLUE's missile damages RED and ranges from 0 to 1, was calculated internally using the ACMI system. This calculation method has not yet been publicly disclosed. Thus, this study assumed that the PK value calculated by the system adequately reflects the damage to the actual air-to-air engagement.

Based on maneuvering data and PK values, we formulate the hit-prediction model to predict a 'Hit' or 'Miss' from the maneuvering and weapon event data of BLUE and RED. The '0' PK value indicates 'Miss,' which means no damage to RED, and the others are converted to 'Hit,' which means sufficient damage to RED. The distribution of PK values and the distribution of 'Hit' and 'Miss' are shown in Fig. 1.

The data for training the hit prediction model were obtained from the ACMI system operated by the ROKAF, where the collection period was from 2009 to 2019. To prepare the data, we applied several pre-processing steps. First, we addressed data quality issues by removing outliers and missing data points, which often result from the high-speed data acquisition inherent to the ACMI system. Next, data consistency was ensured by standardizing the units of speed and angle across all attributes. However, we did not perform data normalization because the machine-learning algorithms employed were designed to appropriately handle varying scales of input features. After pre-processing, the dataset contains 2,258 instances corresponding to 2,258 missile launches (hits or misses). Of the total, 1,721 instances were labeled as 'Hit' and 537 as 'Miss,' yielding a hit ratio of 76.2 % and establishing the baseline performance. Table 2 lists the 18 attributes used in this study.

3. FEATURE ENGINEERING

In this section, we leverage the domain knowledge extracted from the data to facilitate air-to-air missile hit predictions. We performed feature extraction by focusing on identifying pertinent features. Although the original attributes in the dataset alone may be sufficient for missile hit prediction, extracting additional features can enhance the predictive performance of machine-learning algorithms. To conclude this section, we examined the correlations to ascertain the relationship between the features and missile hits.

3.1 Feature Extraction

In this study, domain knowledge was employed to extract five features. Here, domain knowledge refers to the specific methodology of BFM used in air-to-air combat, which provides insight into attacking adversaries. In BFM air combat scenarios, BLUE manoeuvres to achieve an optimal position and energy state relative to RED before launching a missile. Based on the methodology concerning relative position, we first considered the differences in three-dimensional spatial distances (BR_dist) and altitudes (BR_alt) between BLUE and RED. These differences were computed from attributes representing the position types, namely, B_xpos, B_ypos, B_zpos, R_xpos, R_ypos, and R_zpos. These features are significant because air-to-air missiles can only be hit within a specific range. Second, energy is divided into potential and kinetic energies, with the

Table 3. Extracted features

Feature	Description	Unit
BR_dist	Distance between blue and red	m
BR_alt	Difference of the altitude of blue and that of red	m
BR_speed	Difference of the speed of blue and that of red	Mach
BR_hca	Angular difference between the heading of blue and that of red	degree
BR_aa	Angle measured from the tail of red to blue	degree

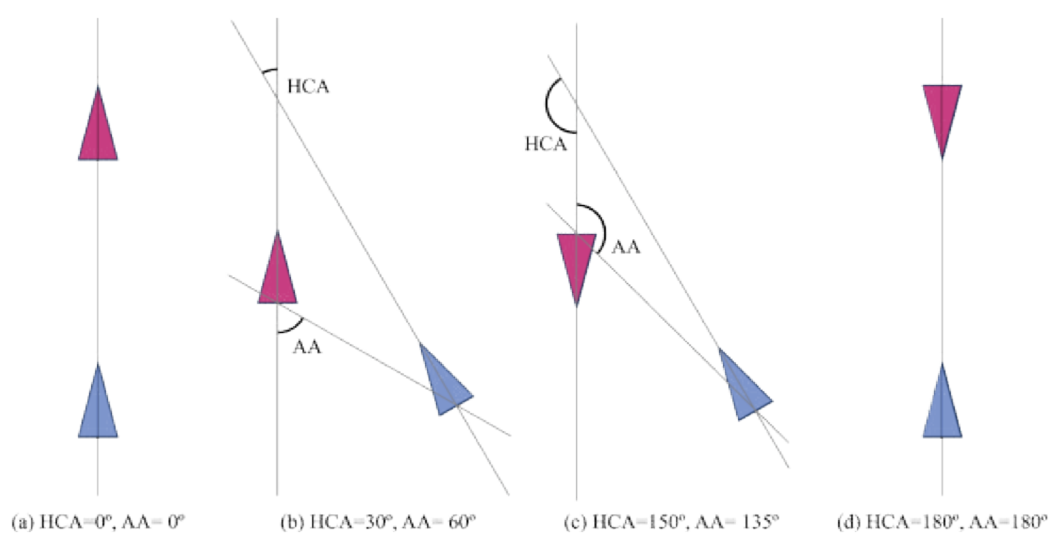

Figure 2. Illustration of HCA and AA. The triangles represent blue and red aircraft. It is shown that (a) and (d) have the same relative position but have different HCA and AA according to the aircraft's heading, which also can be applied to (b) and (c).

altitude difference (BR_alt) and speed difference (BR_speed) playing a pivotal role. Higher altitudes and speeds increase the potential and kinetic energies, allowing aircraft to strategically exchange altitude and speed in three positions based on the BFM principles during air-to-air combat.

In addition to the features based on the relative values above, we further incorporated crucial features considering the BFM. These features encompass the Heading Cross Angle (HCA) and Aspect Angle (AA), as shown in Fig. 2. HCA represents the angular difference in the headings between the two aircrafts, and AA indicates the angle from the tail of RED to the direction of BLUE. Because missiles exhibit higher hit probabilities within specific angular ranges, HCA and AA are recognised as significant features. A summary of the five features mentioned above and their respective units is presented in Table 3. Similarly, in addition to considering the relative positions of the two aircraft, one may also regard the relative values of attributes, such as attitude and gravity, as features.

However, based on domain knowledge, the relative values of the aircraft attitude and gravity have limited significance. By contrast, the absolute values of an aircraft's attitude and gravity are more important than their relative values. Consequently, we refrained from using the relative values of attitude and gravity as additional features.

3.2 Feature Selection

Finally, we obtained 23 features comprising 18 original attributes and five additional features derived through feature extraction. To refine the feature-selection process, we utilized domain knowledge to exclude unnecessary features. Specifically, we omitted six attributes related to the aircraft position. Although three-dimensional terrain information is crucial in air-to-air combat, the data under analysis lacks such terrain data. In addition, utilizing terrain information in model construction may hinder generalization. Ultimately, we obtained a final set of 17 features: B_roll, B_pitch, B_yaw, B_aoa, B_speed, B_g, R_roll, R_pitch, R_yaw, R_aoa, R_speed, R_g, BB_dist, BR_alt, BR_speed, BR_hca, and BR_aa, as shown on the vertical axis in Fig. 3.

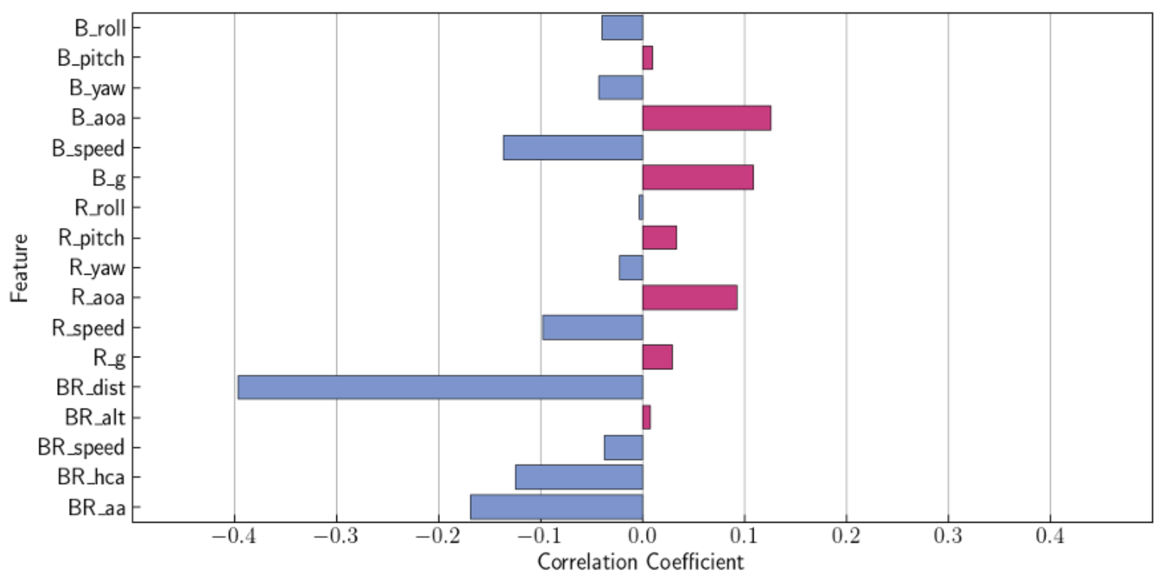

Figure 3. Correlation coefficient between 'Hit' and 17 features. Only one feature (BR_dist) has a significant correlation coefficient, and the features using relative position between BLUE and RED tend to be relatively more significant than the others.

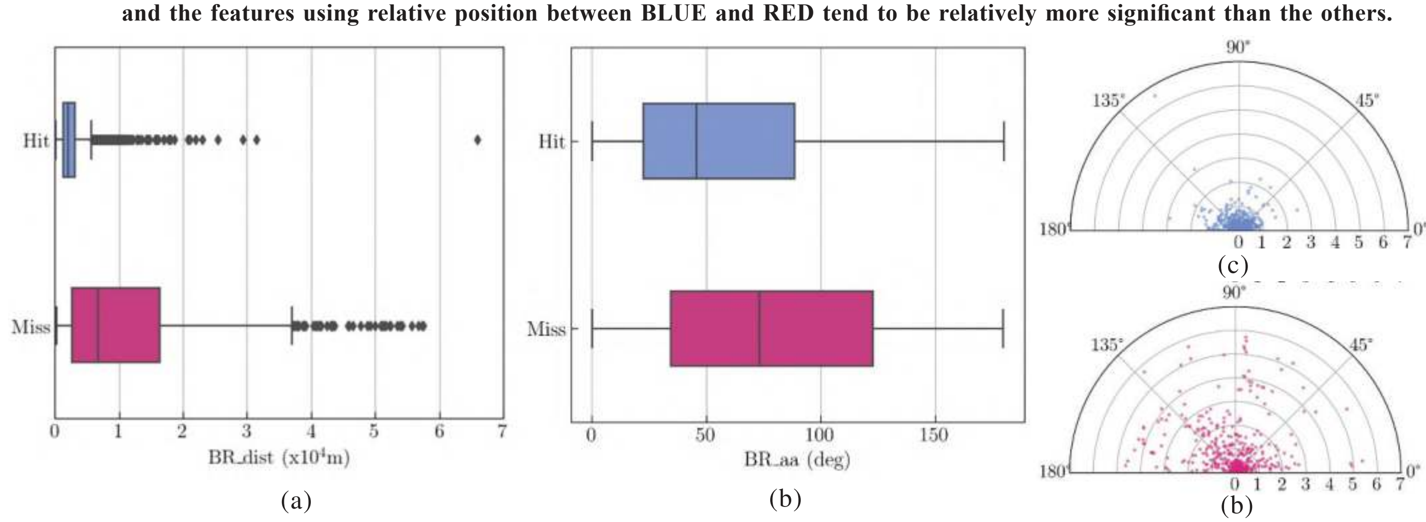

Figure 4. The distribution of missile hit and miss. Blue and red represent 'Hit' and 'Miss.'; (a) boxplots for BR_dist (b) BR_aa.; (c) half-polar plots for BR_dist; and (d) BR_aa.

3.3 Relation Between Missile Hit and Features

We investigated the impact of the features on missile hit prediction using correlation coefficients. The correlations between each feature and the missile hits are shown in Fig. 3. Most of the correlation coefficients were relatively low. Only BR_dist showed a strong linear correlation with the number of missile hits. In addition, features using the relative positions between BLUE and RED, such as BR_hca and BR_aa, tended to be relatively significant.

We also constructed hit prediction models using a single feature. However, the results demonstrated overfitting, indicating poor generalisation. Although the training accuracy ranged from 60 % to 80 % depending on the feature, the test accuracy for most features remained at approximately 50 %. Only BR_dist achieved a test accuracy of approximately 60 %, which is below the baseline performance. This implies that single features alone cannot adequately distinguish between hits and misses and that multiple features must be combined for successful classification.

When combining the features for modeling, it outperforms the baseline, as discussed in Section 4. For instance, Fig. 4 shows two boxplots for BR_dist (left) and BR_aa (middle), and two half-polar plots of BR_dist (upper) and BR_aa (lower) for missile hits and misses. The combination of these two features improves the prediction performance.

4. EXPERIMENT

4.1 Experimental Setting

In this study, we investigate the performance of four machine learning algorithms: logistic regression (LR), random forests (RF), XG Boost (XGB), and Cat Boost (CATB) for classification. Logistic regression served as the baseline model, providing a simple yet effective means of examining the relationships among variables. Random forests, XG Boost, and Cat Boost, while all tree-based ensemble algorithms, differ in their approach: random forests use bagging techniques to create independent trees, XG Boost employs gradient boosting to sequentially improve weak learners, and Cat Boost introduces ordered boosting and processing of categorical features. These algorithms excel in handling tabular data classification problems, each leveraging its unique strengths[28,35-37]. Furthermore, we also explored the performance of Gradient Boosting and Light GBM within the boosting family[38-39]. However, a comparative evaluation revealed that their performances were closely aligned with those of XG Boost and Cat Boost. We also evaluated Multilayer Per Ceptrons (MLPs) that are generally known to underperform on tabular data such as those used in our experiments; indeed, the results were not promising[28]. The training and test data were divided at an 8:2 ratio. The hyperparameter selection for each algorithm was accomplished through Bayesian optimization, and the determination of optimal hyperparameters was achieved through 5-fold cross-validation.

4.2 Performance Result

Table 4 presents the experimental outcomes of the four algorithms using the two feature sets. The first set, labelled ‘All,’ encompasses all 17 features, while the second, ‘Observable,’ is composed of only 12 features, excluding four features that cannot be acquired in (near) real-time from RED. The ACMI data included information from both the BLUE and RED gathered from POD sensors in the training scenarios. However, in actual air-to-air combat cases, BLUE can only access a partial, near real-time stream of RED’s information, with ‘observation’ referring to data obtained through sensors or surveillance systems and transmitted to BLUE almost instantly. Capturing real-time observations of RED’s attitude features (R_roll*, et al.*) and gravity (R_g) from BLUE is difficult. In contrast, positional features (R xpos*, et al.*) and speed (R_speed) are more easily observable and collectible. Thus, the features BR dist, BR_alt, BR_speed, BR_hca, and BR_aa were derived from the observable positional features and speed to construct the model.

Performance assessment was based on accuracy, precision, recall, F1 score, and area under the receiver operating characteristic curve (AUC). Given the class imbalance of the data, it is crucial to interpret the accuracy carefully. Table 4 shows that the performances of the four algorithms are similar, with random forests and XG Boost slightly outperforming the others for the five performance metrics. This indicates a potential link between algorithmic behavior and data characteristics, which can affect performance measures differently.

The performance of the model with the’ Observable’ feature set is nearly on par with using all features, as demonstrated in Table 4. This is consistent with the fact that the RED features have less influence, as reflected by their reduced importance in the evaluation process, as illustrated in Figs. 3, Fig. 5, and Table 5. In summary, given a baseline accuracy of 76.2 %, the performance enhancement with the ‘All’ feature set ranges from approximately 5.9 % to 6.5 %. In contrast, with the ‘Observable’ feature set, it falls within the range of approximately 5.0 % to 6.8 %.

Table 4. Performance comparison of ‘All’ and ‘Observable’ feature sets using four algorithms

Feature set	Algorithm	Accuracy	Precision	Recall	F1 score	AUC
All	LR	0.821	0.815	**0.985**	0.892	0.653
	RF	**0.827**	0.826	0.976	**0.895**	0.676
	XGB	0.821	**0.828**	0.962	0.890	**0.677**
	CATB	0.823	0.823	0.974	0.892	0.670
Observable	LR	0.812	0.807	**0.985**	0.887	0.636
	RF	0.825	0.827	0.971	0.893	0.677
	XGB	**0.830**	**0.833**	0.968	**0.895**	**0.689**
	CATB	0.827	0.828	0.974	**0.895**	0.679

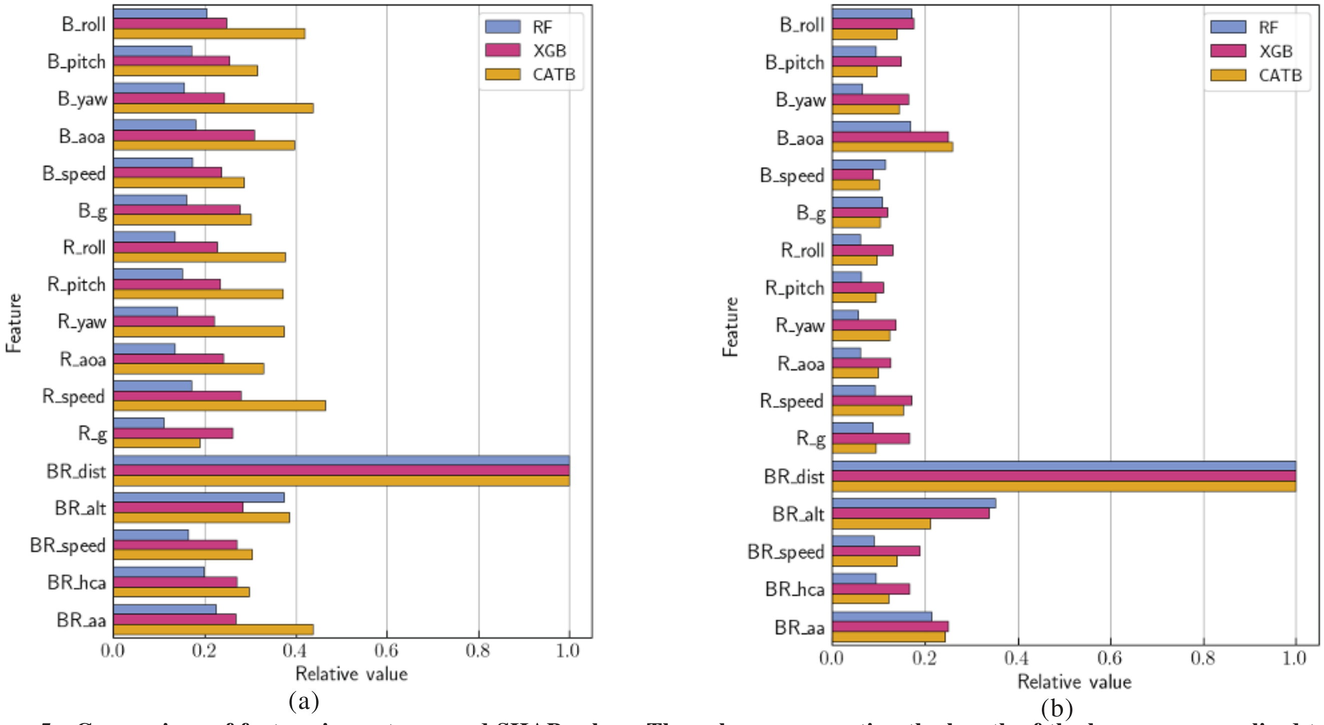

Figure 5. Comparison of feature importance and SHAP values. The values representing the length of the bars are normalised to the largest value per algorithm and measure, thus presented as relative values; (a) Feature importance; and (b) SHAP value.

Table 5. Feature rankings based on both feature importance and SHAP values. Orange, blue, and red represent features belonging to BR, BLUE, and RED, respectively. Each column lists the rankings of the 17 features in descending order, with higher rankings indicating more significant influence.

Rank	Overall	Correlation coefficient	Feature importance			SHAP value		
			RF	XGB	CATB	RF	XGB	CATB
1	BR_dist	BR_dist	BR_dist	BR_dist	BR_dist	BR_dist	BR_dist	BR_dist
2	BR_alt	BR_aa	BR_alt	B_aoa	R_speed	BR_alt	BR_alt	B_aoa
3	BR_aa	B_speed	BR_aa	BR_alt	B_yaw	BR_aa	BR_aa	BR_aa
4	B_aoa	B_aoa	B_roll	R_speed	BR_aa	B_roll	B_aoa	BR_alt
5	R_speed	BR_hca	BR_hca	B_g	B_roll	B_aoa	BR_speed	R_speed
6	B_roll	B_g	B_aoa	BR_hca	B_aoa	B_speed	B_roll	B_yaw
7	BR_hca	R_speed	B_speed	BR_speed	BR_alt	B_g	R_speed	BR_speed
8	B_g	R_aoa	B_pitch	BR_aa	R_roll	B_pitch	BR_hca	B_roll
9	B_yaw	B_yaw	R_speed	R_g	R_yaw	BR_hca	R_g	R_yaw
10	B_speed	B_roll	BR_speed	B_pitch	R_pitch	R_speed	B_yaw	BR_hca
11	R_pitch	BR_speed	B_g	B_roll	R_aoa	BR_speed	B_pitch	B_g
12	BR_speed	R_pitch	B_yaw	B_yaw	B_pitch	R_g	R_yaw	B_speed
13	R_yaw	R_g	R_pitch	R_aoa	BR_speed	B_yaw	R_roll	R_aoa
14	R_aoa	R_yaw	R_yaw	B_speed	B_g	R_pitch	R_aoa	R_roll
15	R_roll	B_pitch	R_roll	R_pitch	BR_hca	R_roll	B_g	B_pitch
16	B_pitch	BR_alt	R_aoa	R_roll	B_speed	R_aoa	R_pitch	R_pitch
17	R_g	R_roll	R_g	R_yaw	R_g	R_yaw	B_speed	R_g

4.3 Feature Importance

For missile hit prediction, we analysed the feature importance and SHAP values of random forests, XG Boost, and Cat Boost to assess the individual significance of the features. The decrease in the average impurity within each tree determines the feature importance values in random forests. In XG Boost and Cat Boost, the feature importance is evaluated by the number of times a feature is used to split the data across all trees. The SHAP values represent the average of all the marginal contributions across all possible coalitions. In Fig. 5, these values are normalised to the largest value per algorithm and measure and are therefore presented as relative values. Despite potential variations owing to algorithmic differences, both the feature importance and the SHAP value consistently emphasize that BR_dist is significantly more influential than the other features, echoing the results in Fig 3.

To identify primary features, we conducted a single-feature ranking analysis using the method outlined by Guyon[34]. We ranked features based on seven normalized measures: feature importance, SHAP values from three tree-based ensemble methods, and correlation coefficients. The overall rank for each feature was determined by averaging the rankings across the seven measures.

The features in Table 5 are ranked and color-coded according to each measure. BLUE, RED, and BR are represented by orange, blue, and red, respectively. The rankings of the 17 features were listed in descending order, with higher rankings indicating a more significant influence. While slight color variations exist across measures, orange features generally dominate the top positions, followed by blue in the middle, and red at the bottom. In the overall ranking, three of the top five positions belonged to BR, whereas five of six features of RED ranked outside the top ten.

5. DISCUSSION AND CONCLUSION

5.1 Comparison with the Conventional Performance Measurement

Our hit prediction model, built on ACMI data, shows promising effectiveness in predicting engagement outcomes. With accuracies ranging from 82.1 % to 83.0 % across the different algorithms and feature sets (Table 4), the model outperformed the baseline accuracy by 76.2 % and by 5.9 % to 6.8 %. This improvement suggests that the model effectively captures the complex dynamics of hit predictions from ACMI data. The results in Fig. 5 and Table 5 show that the positional features of the two fighters were significant for the outcome of the air-to-air engagement. This result is analogous to those of conventional ACM performance-measurement studies. As demonstrated in reference[18,35], positional advantage measurements, such as the all Aspect Manoeuvring Index (AAMI)[15], were the most related to air-to-air engagement outcomes. The AAMI includes a range of fighters.

Experimental results can also be rationally translated using the air combat manoeuvring manual. According to reference[36], BLUE requires the ability of the BFM to enter the RED weapons envelope, and this BFM aims to reduce the range, aspect angle, and angle off to ensure that it can fire weapons at the RED. Based on this analogy and rationality, a data-driven analysis can be used as a verification or refinement methodology for conventional performance measurements in simulation systems.

5.2 Limitation

One of the two limitations of this study is that only the data from the time and from 0.1 s before the missile launch of BLUE was utilised for analysis out of the entire manoeuvring data. Although the information at the missile launch moment is crucial for predicting the hit probability of air-to-air missiles, it is probably necessary to consider the manoeuvres of both BLUE and RED before the launch, as they influence the positioning at the launch moment. Therefore, we must incorporate data from the period preceding a missile launch to extend the applicability of the findings beyond hit prediction and utilize them as feedback information in actual training scenarios. Utilizing such time-series data and employing deep learning algorithms of the RNN family, such as Long Short-Term Memory (LSTM) or Gated Recurrent Unit (GRU), could potentially enhance both predictive performance and interpretability[37-42].

The second is the inherent limitation caused by the use of the ACMI system. While manoeuvring information is acquired from the pods, weapon events, including engagement outcomes, are simulated by the ACMI system. Therefore, the data utilized can be regarded as partially simulated data and analyzed with respect to hit probability.

5.3 Contribution and Future Work

This study demonstrates a standard procedure for utilising ACMI system data, encompassing feature extraction, selection, and effective modelling of a hit-prediction problem. By employing interpretable machine learning techniques, we developed an accurate predictive model and uncovered the most influential factors affecting air-to-air engagement outcomes. This approach bridges the gap between data-driven analysis and traditional air combat performance metrics, thereby offering valuable insights for tactical development and training.

In future work, a refinement model design for fine-tuning the parameters of conventional performance measurements using a data-driven analysis can be suggested. In addition, building an enhanced hit prediction model can be recommended using the RNN family algorithm to exploit the time-series features of the ACMI data. Finally, a multimodal hit prediction model can be proposed for development. Various aspects of air-to-air engagement can be analyzed to train the hit-prediction model using different types of information, such as the aircraft state or pilot information.

REFERENCES

1. Saunders, R. & Souva, M. Air superiority and battlefield victory. *Res. & Politics*, 2020, **7**(4). doi: 10.1177/2053168020972816
2. Jones, R.D. Israeli Air Superiority in the 1967 Arab-Israeli War: An Analysis of Operational Art. Naval War Coll Newport Ri Joint Military Operation Dept, Technical Report No. ADA311683. June 1996.
3. Keaney, T.A. & Cohen, E.A. Gulf war air power survey: Summary Report Vol. 2. Office of the Secretary of the Air Force, USA, 1993. 276 p.
4. AAP-06: NATO glossary of terms and definitions. North Atlantic Treaty Organization (NATO), 2021.
5. Meilinger, P.S. 10 Propositions regarding air power. Air Force History and Museums Program, USA, 1995. 86 p.
6. Dwivedi, P.P. & Sharma, D.K. Selection of combat aircraft by using shannon entropy and VIKOR method. *Def. Sci. J.*, 2023, **73**(4). 411-419

doi: 10.14429/dsj.73.17996

7. Jain, S.K.; Jain, T.K.; Shanker, S. & Srivastava, S. Rapid and accurate INS transfer alignment for air launched tactical missile using kalman filter. *Def. Sci. J.*, 2023, **73**(4) 496-502.
doi: 10.14429/dsj.73.18435
8. Lee, G.; Kwon, J.; Kwak, N. & Yang, E. Robust measurement validation for radar target tracking using prior information. *IET Radar, Sonar & Navigation*, 2019, **13**(10) 1842-1849.
doi: 10.1049/iet-rsn.2019.0019
9. Lee, G.; Lee, S.; Kim, K. & Kwak, N. Probabilistic track initiation algorithm using radar velocity information in heavy clutter environments. *In* 15th European Radar Conference(EuRAD) IEEE 2018, Madrid, Spain, 2018.
doi: 10.23919/EuRAD.2018 .8546666
10. Thurman, R.A. & Mattoon, J.S. Virtual reality: Toward fundamental improvements in simulation-based training. *Edu. Technol.*, 1994 , **34**(8), 56-64.
11. Kelly, M.J.; Lee Wooldridge, A.; Hennessy, R.T. & Reed, J.C. Air combat manoeuvring performance measurement. Proceedings of the Human Factors Society Annual Meeting. 1979, **23**(1), pp. 324-328.
doi: 10.1177/107118137902300183
12. Krusmark, M.; Schreiber, B.T. & Bennett, W. The effectiveness of a traditional gradesheet for measuring air combat team performance in simulated Distributed Mission Operations. United States Air Force Research Laboratory, Scientific and Technical Information No. AFRL-HE-AZ-TR-2004-0090. May 2004.
13. Van Horn, H.J. Can simple models predict air combat results? *J.Aircraft*, 2011,**48**(2), 652-659.
doi: 10.2514/1.C031202
14. Mansikka, H.; Virtanen, K.; Harris, D. & Salomäki, J. Live–virtual–constructive simulation for testing and evaluation of air combat tactics, techniques, and procedures, Part 1: Assessment framework. *J. Def. Model. Simul.*, 2021, **18**(4), 285-293.
doi: 10.1177/ 1548512919886375
15. McGuinness, J.; Forbes J.M. & Rhoads J.E. Air combat manoeuvring performance measurement system design. Williams Air Force, Technical Report No. AFHRL-TP-83-56. Oct 1984.
16. Breidenbach, S.T.; Clavarelli, A.P. & Sievers, R. Measurement methods and metrics for aircrew assessment during close-in air-to-air combat. Naval Training Systems Center, Naval Air Systems Command, Technical Report No.ADA1168066. September 1985.
17. Rajabally, E.; Valiusaityte, I. & Kalawsky, R. Aircrew performance measurement during simulated military aircrew training: A review. *In* AIAA Modeling and Simulation Technologies Conference, Chicago, USA, 2009.
doi:10.2514/6.2009-5829
18. Waag, W.L.; William B.R. & Jeffrey L.L. Development of a composite measure for predicting engagement outcome during air combat manoeuvring. Armstrong Laboratory, Air Force Systems Command, Technical Report No.AL-TR-1992-0002, May 1992.
19. ARAR, Ö.F. & Ayan, K.A flexible rule-based framework for pilot performance analysis in air combat simulation systems. *Turkish J. Electric. Engin. Comput. Sci.*, 2013, **21**(8), 2397-2415.
doi: 10.3906/elk-1201-50
20. Saastamoinen, K. & Maunula, K. Usefulness of flight simulator as a part of military pilots training–case study: Grob G 115E. *Procedia Comput. Sci.*, 2021, **192**, 1670-1676.
doi: 10.1016/j.procs. 2021.08.171
21. Cross, J.; Boag-Hodgson, C.; Ryley, T.; Mavin, T.J. & Potter, L.E. Using extended reality in flight simulators: a literature review. *IEEE Transact. Visual. Comput. Graphics*, 2022, **29**(9), 3961-3975.
doi: 10.1109/TVCG.2022.3173 921
22. Balcerzak, T. & Katarzyna, K. Flight simulation in civil aviation: Advantages and disadvantages. Revista europea de derecho de la navegación marítima y aeronáutica, 2018, **35**, 35-68.
23. Panarisi, M.T. A comparative analysis of internal and external solutions to provide air combat manoeuvring instrumentation functionality. Air University Press, USA, 2001. 88 p.
24. Dantas, J.P.; Costa, A.N.; Medeiros, F.L.; Geraldo, D.; Maximo, M.R. & Yoneyama, T. Supervised machine learning for effective missile launch based on beyond visual range air combat simulations. *In* 2022 Winter Simulation Conference (WSC) IEEE, Singapore, 2022.
doi: 10.1109/WSC 57314.2022.10015384
25. Kim, D.; Arjit, S. & Rhea P.L. Data-enhanced dynamic flight simulations for flight performance analysis. *Aerospace Sci. and Technol.*, 2022, **121**, 1-28.
doi: 10.1016/j.ast.2022.107357
26. Lundberg, S.M. & Lee, S. A unified approach to interpreting model predictions. Advances in neural information processing systems(NIPS 2017), CA, USA, 2017.
27. https://www.af.mil/About-Us/Fact-Sheets/Display/Article/104557/aim-9-sidewinder/,
(Accessed on 25 March 2024).
28. Borisov, V.; Leemann, T.; Seßler, K.; Haug, J.; Pawelczyk, M. & Kasneci, G. Deep Neural Networks and Tabular Data: A Survey. IEEE Transact. *Neural Networks and Learning Syst.*, 2022, Early Access, 1-21.
doi: 10.1109/ TNNLS.2022.3229161
29. Breiman, Leo. Random forests. Machine learning, 2001, 45. 5-32.
doi: 10.1023/A:1010933404324
30. Chen, T. & Carlos, G. Xgboost: A scalable tree boosting system. Proceedings of the 22nd acm sigkdd international conference on knowledge discovery and data mining, NY, USA, 2016.
doi: 10.1145/2939672.2939785
31. Prokhorenkova, L.; Gusev, G.; Vorobev, A.; Dorogush, A.V.; & Gulin, A. CatBoost: Unbiased boosting with categorical features. Advances in neural information processing systems(NIPS 2018). Montreal, Canada, 2018.

32. Friedman, J.H. Stochastic gradient boosting. *Comput. Stat. Data Analysis*, 2002, **38**(4), 367-378. doi:10.1016/S0167-9473(01)00065-2
33. Ke, G.; Meng, Q.; Finley, T.; Wang, T.; Chen, W.; Ma, W. & Liu, T.Y. Lightgbm: A highly efficient gradient boosting decision tree. Advances in neural information processing systems(NIPS 2017) , CA, USA, 2017.
34. Guyon, I. & Elisseeff, A. An introduction to variable and feature selection. *J. Machine Learn. Res.*, 2003, **3**, 1157-1182. doi: 10.55 55/944919.944968
35. Kelly, M.J. Performance measurement during simulated air-to-air combat. *Human Factors*, 1988 , **30**(4), 495-506 doi: 10.1177/001872088803000 410
36. Shaw, R.L. Fighter Combat: Tactics and Manoeuvring. Naval Institute Press Annapolis, USA, 1985. 428 p.
37. Zhang, J.D.; Yu, Y.F.; Zheng, L.H.; Yang, Q.M.; Shi, G.Q. & Wu, Y. Situational continuity-based air combat autonomous manoeuvring decision-making. *Def. Technol.*, 2022, **29**, 66-79. doi: 10.1016/j.dt.2022.08.010
38. Shi, Z.; Xu, M.; Pan, Q.; Yan, B. & Zhang, H. LSTM-based flight trajectory prediction. *In* 2018 International Joint Conference on Neural Networks (IJCNN) IEEE, Rio de Janeiro, Brazil, 2018. doi: 10.1109/IJCNN.2018.8489734
39. Bae, J.H.; Jung, H.; Kim, S.; Kim, S. & Kim, Y.D. Deep reinforcement learning-based air-to-air combat manoeuvre generation in a realistic environment. *IEEE Access*, 2023, **11**, 26427-26440. doi: 10.1109/ACCESS.2023.3257849
40. Wang, X.; Wang, Y.; Su, X.; Wang, L.; Lu, C.; Peng, H. & Liu, J. Deep reinforcement learning-based air combat manoeuvre decision-making: literature review, implementation tutorial and future direction. *Artificial Intell. Rev.* , 2024, **57**(1), 1. doi: 10.1007/ s10462-023-10620-2
41. Xi, Z.; Kou, Y.; Li, Z.; Lv, Y. & Li, Y. An air combat manoeuvre pattern extraction based on time series segmentation and clustering analysis. *Def. Technol.*, 2024, **36**, 149-162. doi: 10.1016/j.dt.2023.11.010
42. Wang, H.; Zhou, Z.; Jiang, J.; Deng, W. & Chen, X. Autonomous air combat manoeuvre decision-making based on PPO-BWDA, *IEEE Access*, 2024, **12**, 119116 – 119132. doi: 10.1109/ ACCESS.2024.3419889

CONTRIBUTORS

Dr Gyuejeong Lee obtained his PhD in Computer Science from Seoul National University. He currently serves as the leader of the AI/Data Laboratory at SAKAK Co., Ltd. His research interests include: Data science, machine learning, deep learning, and trustworthy artificial intelligence.
In this study, he conceptualised the research framework, conducted a comprehensive literature review, and developed the methodology.

Dr Yong-hwan Kim obtained his PhD in Defense Fusion Engineering from Yonsei University. He currently serves as the Air Force Program Manager at the Republic of Korea Embassy in the United States, bringing his experience as a fighter pilot to the role. His research focuses on: Artificial intelligence and data science applications in the defense sector.
In this study, he contributed to methodology development and was responsible for data collection and curation.

Prof Daeyoung Choi obtained his PhD in Computer Science from Seoul National University (2019). He is currently working as an Assistant Professor in the Division of Artificial Intelligence and Data Science at The Cyber University of Korea. His research interests include: Edge AI, federated learning, and data science.
In this study, he developed the methodology and performed machine learning modeling and data analysis.

Defence Science Journal, Vol. 75, No. 1, January 2025, pp. 44-51, DOI : 10.14429/dsj.20551

An Application of Machine Learning in Empirical and Variational Mode Decomposition with SVM Classifier to Enhance Diagnostic Accuracy for Disease Detection in Soldier`s Eyes

Pooja Manghnani* and Asmita A. Moghe

University Institute of Technology, Rajiv Gandhi Proudyogiki Vishwavidyalaya, Bhopal - 462 033, India

**E-mail: poojam2673@gmail.com*

ABSTRACT

Soldiers rely heavily on their vision, which is crucial not only for daily activities but also for the effective operation of defense systems, weaponry, and other military applications. However, various eye disorders, such as those related to increased intra-ocular pressure, can lead to irreversible vision loss, severely impacting a soldier's operational capabilities. While extensive research has been conducted on detecting such ocular conditions, there remains a critical need for more accurate diagnostic methods to ensure early detection and treatment. In this study, we propose a novel approach combining Empirical Mode Decomposition (EMD) and Variational Mode Decomposition (VMD) for enhanced detection of eye disorders from retinal fundus images. The proposed method includes a comprehensive preprocessing phase, followed by decomposition using EMD and VMD techniques. The decomposed images undergo feature extraction through feature combination, with subsequent normalization and selection using z-score and the Relief method, respectively. Classification is performed using Support Vector Machines (SVM) with various kernels, including cubic, Gaussian, linear, and quadratic. The results demonstrate that the proposed method achieves high accuracy, with SVM kernel functions yielding accuracies of 98.30 %, 96.59 %, 96.59 %, and 97.87 % for 10-fold cross-validation, respectively. Additionally, the evaluation metrics, including sensitivity and specificity, indicate superior performance compared to state-of-the-art methods for similar datasets. This advanced diagnostic approach offers significant improvements in detecting eye disorders, which could be crucial in defense applications. Early and accurate diagnosis by military ophthalmologists can lead to better decision-making and timely interventions, ultimately preserving the vision and effectiveness of soldiers in the war.

Keywords: Eye disorders; Defense applications; Empirical Mode Decomposition (EMD); Support Vector Machines (SVM); Retinal fundus images; Early diagnosis

NOMENCLATURE

EMD : Empirical mode decomposition
VMD : Variational mode decomposition
SVM : Support vector machines
PCA : Principal component analysis
OHAWT: Optimal hyper analytic wavelets transform
CVMD : Compact variational mode decomposition
IMFs : Intrinsic mode functions
BDIMFs: Bidimensional intrinsic mode functions

1. INTRODUCTION

The human eye is an essential part of the body, especially in defense, where a soldier's readiness and effectiveness on the battlefield depend heavily on sharp vision. In the chaos of war, with guns firing, smoke filling the air, and explosions lighting up the sky, the ability to see clearly can mean the difference between life and death. However, certain ocular ailments, like those caused by increased intra-ocular pressure, can lead to devastating consequences such as permanent vision loss or blindness. These conditions, which develop insidiously, gradually damage the optic nerves within the eye, reducing a soldier's capability to operate in environments filled with flames, explosions, and other hazards. The World Health Organization has identified this condition as the second leading cause of vision loss worldwide, with the number of affected individuals expected to rise to 111.8 million by the year 20401[1-5].

1.1 Literature Review

Various works have been reported for the glaucoma detection in the last decade. Bock*, et. al.*[1] implemented Principal Component Analysis (PCA) on a transformed images followed by classification using a Support Vector Machine (SVM). Raja[6], *et. al.* proposed automated glaucoma detection approach using Optimal Hyper Analytic Wavelets Transform (OHAWT). Maheshwari[7], *et. al.* proposed variational mode decomposition (VMD) method-based glaucoma detection. Kirar[8]*, et. al.* proposed Discrete Wavelet Transform (DWT) and empirical wavelet transform (EWT) methods-based glaucoma detection. Kirar[9]*, et. al.* designed an automated glaucoma detection method using Compact Variational Mode Decomposition (CVMD). Agrawal[10], *et. al.* proposed Quasi-Bivariate Variational Mode Decomposition (QB-VMD) method-based glaucoma detection using. Further, Kirar[12]*, et. al.* proposed

Received : 13 September 2024, Revised : 22 October 2024
Accepted : 06 November 2024, Online published : 10 January 2025

new approach using DWT image channels. Diaz-Pinto[13], *et. al.* proposed and developed new ACRIMA image dataset with 705 images for glaucoma detection using Convolutional Neural Network (CNNs). Further, various works[10-20] have been reported on this recent popular ACRIMA dataset[13]. Serte*, et. al.*[14] implemented his work on ACRIMA dataset for glaucoma detection using Deep Learning (DL). Claro[15]*, et. al.* developed new approach using Transfer Learning (TL), hybrid feature and Random Forest (RF) classifier. Liu[17]*, et. al.* added deep NN for feature extraction and classification. Elangovan[18]*, et. al.* modeled a standard CNN using softmax classifier. Kirar[19]*, et. al.* in new research work, implemented QB-VMD in two stages with SVM. Galarraga[20]*, et. al.* successfully implemented image processing techniques for glaucoma detection. Devi[21]*, et. al.* also implemented successfully various texture-based method for feature extraction and classification. Manghnani[22]*, et. al.* proposed an improved method using bidimensional EMD (BD-EMD) for glaucoma detection. Devecioglu[23]*, et. al.* developed a compact Self-Organized Operational Neural Networks method for glaucoma detection.

Some most recently published articles include, Singh[24]*, et. al.* proposed a multimodality-based approach for efficient glaucoma prediction. Early fusion and late fusion both were implemented in this work. Machine Learning and Deep learning were implemented using feature level fusion and image level fusion respectively. Approach was tested on three benchmark datasets and four combinations of these datasets. Classification accuracy up to 92.14 % was achieved through this approach using ACRIMA dataset. Sonti[25]*, et. al.* implemented QB-VMD with shape and texture-based features for better performances. Other works also proposed enhanced glaucoma detection from fundus images[26-28]

1.2 Limitations in Existing Research Work

Research work published for glaucoma detection[1-7,25-35] reported less accuracy. It may be due to having some demerit or due to limitation of methods used or have not utilized the contribution of all components. Methods used based on DWT[7-9] have interference with little resolution. Methods used based on EWT[5] suffer from redundancy. Methods used based on EMD[17] and VMD[7-24] the EMD have problem of boundary distortion which is overcome by use of VMD based methods. VMD based methods are better. Further, VMD is also limited to large and varied data set. There is lack of contribution of all color components in the methods used based on ML DL[36-45] and DL[13-18, 46-58] However, there is a scope to develop a model for improved glaucoma detection by combining EMD and VMD based methods.

1.3 Contributions in the Proposed Work

During image capturing, if precautions are not taken then the image quality may degrade by the addition of some nearby noise and artefacts. Continuing with the research work[22], we further propose a combination of EMD and VMD based methods for improved glaucoma detection from retinal fundus images. This paper includes the following contributions:

- It involves the study of latest research work for glaucoma detection
- Images are subjected to preprocessing using rescaling and decomposition into its gray scale, green, red and blue components
- All components are subjected to EMD and VMD methods for decomposition into their corresponding small, moderate and high frequency components
- Further, extracted and selected features are classified with SVM–based kernels, like Linear, Quadratic, Cubic, and Gaussian. SVM with Cubic kernel gives the best performance.

2. Proposed Research Work

This section describes the proposed research work in detail as shown in Fig.1 First of all, ACRIMA images are rescaled and subjected to decomposition to gray scale, green, red and blue components. Then each component is subjected to EMD and VMD based methods separately. Then all the decomposed frequency components, intrinsic mode functions (IMFs) are subjected to features extraction methods. Finally, obtained features are combined and subjected to z-score normalization and relief features selection followed by classification using support vector machines (SVM) with its different kernels like linear, quadratic, cubic, and gaussian. Performance metrics are evaluated and compared with state of art work.

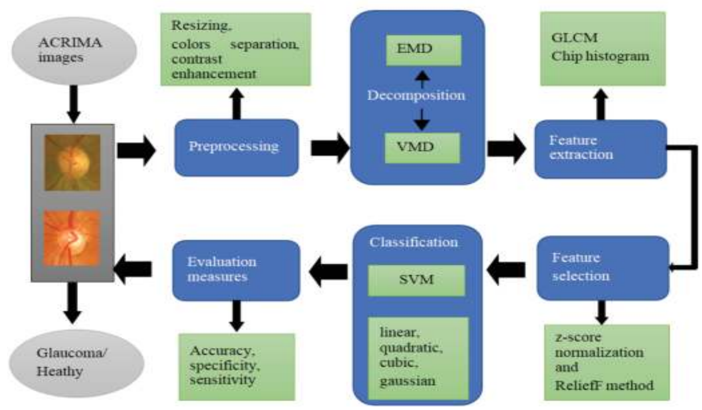

Figure 1. Block diagram of the proposed work.

2.1 ACRIMA Images Data Set

This dataset includes a total 705 images (396 Glaucoma+ 309 Healthy) and available in .jpg image format publically[13]. ACRIMA images are captured with a field of view of 35° and pixel values vary from 178×178 to 1420×1420.

2.2 Pre-Processing

Image capturing process may add some unwanted noised and artefacts, which is responsible for the lower image quality and hence somewhat reduced performance. To enhance the performance rescaling and contrast enhancement are applied to the images[1]. This work includes rescaling and decomposition into its gray scale, green, red and blue components followed by equalisation and filtering[29]. Outputs of all steps involved in preprocessing of glaucoma and healthy images are shown in Fig. 2 & 3.

2.3 Empirical Mode Decomposition

This section explains the empirical mode decomposition

(EMD). It is adaptive in nature. Its bi-dimensional form (BDEMD) decomposes input image into three frequency components, Intrinsic Mode Functions (IMFs) and one residue. It has the advantage to decompose the image into small, moderate & high frequency components, bidimensional IMFs (BDIMFs)[31] The decomposition of image I(x,y) using BDEMD is carried out as follows:

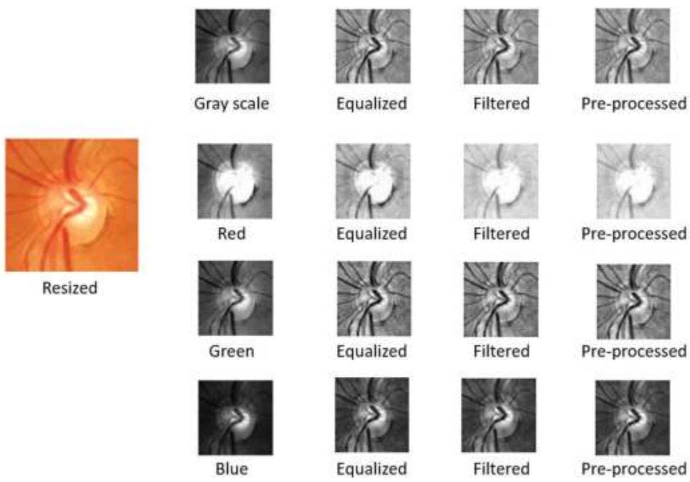

Figure 2. Outputs of all steps involved in preprocessing of glaucoma image.

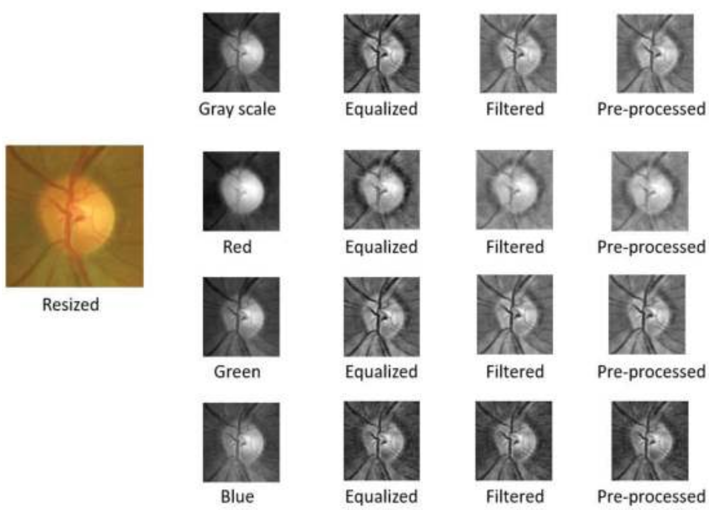

Figure 3. Outputs of all steps involved in preprocessing of healthy image.

- Calculation of maxima and minima of I(x,y).
- Calculation of upper and lower envelope of I(x,y).
- Calculation average envelope by adding upper and lower envelope of I(x,y) and dividing by 2.
- Subtraction of the average envelope from input image. Then we check the result for stopping criterion. If a match occurs implies it is a BDIMF and we move ahead to the next step (v) Else are go back and start from step(i)-(iii). Taking the result as input, we find new BDIMF.
- Calculate remaining BDIMFs, taking result of step (iv) as input and repeat steps (i-iv).

Finally, BDEMD decomposes image as a sum of BDIMFs (s=1 to 3) and one residue as given in Eqn. (1). Where s is from 1 to 3.

$$I(x,y) = \sum_{s=1}^{S} BDIMF_s(x,y) + Res(x,y) \quad (1)$$

2.4 Variational Mode Decomposition

This section explains the variational mode decomposition (VMD). It is non-stationary and fully adaptive in nature. Its two-dimensional form (2DVMD) decomposes input image into five frequency components, intrinsic mode functions (IMFs). It is more advantageous than conventional methods to decompose the image into small, moderate & high frequency components (VMDIMFs) because it has no mode mixing problems. VMDIMFs are band limited and centered around a specific frequency, which are calculated using Eqn. (2-6) as follows[32]:

Variational problem for VMD

$$\min_{z_n \omega_n} \left\{ \sum_n \left\| dt \left[\left(\delta(t) + \frac{i}{\pi t} \right) * z_n(t) \right] e^{-i\omega_t} \right\|^2 \right\} \quad (2)$$

Such that

$$\sum_n z_n = S \quad (3)$$

The above Eqn. is rewritten as:

$$\mathcal{L}(Z_{n,} W_n, \beta) = \alpha \sum_n \left\| dt \left[\left(\delta(t) + \frac{i}{\pi t} \right) * Z_n(t) \right] e^{-iw_n t} \right\|_2^2 + \left\| s(t) - \sum_n Z_n(t) \right\|_2^2 + \left\langle \beta(t), s(t) - \sum_n u_n(t) \right\rangle \quad (4)$$

The estimated n^{th} VMDIMFs are given as:

$$\hat{z}_n^{m+1}(\omega) = \frac{\hat{S}(\omega) - \sum_{j \neq n} \hat{y}_j(\omega) + \frac{\hat{\beta}(\omega)}{2}}{1 + 2\alpha(\omega - \omega_n)^2} \quad (5)$$

The center frequency can be expressed as:

$$\omega_n^{m+1} = \frac{\int_0^\infty \omega \left| \hat{z}_n(\omega) \right|^2 d\omega}{\int_0^\infty \left| \hat{z}_n(\omega) \right|^2 d\omega} \quad (6)$$

where, S = signal, α =balancing parameter, z_n=VMDIMFs, and ω_n=center frequency of n^{th} VMD component.

2.5 Feature Extraction and Selection

Total 4-GLCM (Gray-Level Co-Occurrence Matrix) and 6-chip histogram features[34] as listed in Table1 are extracted from all decomposed components. We have extracted 40 features from EMDIMFs and 40 features from VMDIMFs i.e. a total of 80 features have been extracted.

Table 1. Features extracted from various components

Features	No of features	Name of features
GLCM	4	Contrast Correlation Energy Homogeneity
Chip histogram features	6	Energy Mean Entropy Variance Kurtosis Skewness

These 80 features are subjected to z-score normalisation[22] and ReliefF features selection method[35] for obtaining important features only. This step is used to increase the performance of SVM classifier. A z-score normalization ($\hat{F}$) is calculated using Eqn. (7).

$$\hat{F} = \frac{F - m(F)}{sd(F)} \tag{7}$$

where, *sd*=standard deviation, *m*=mean, *F*= extracted features data.

2.6 Classification

Widely used classifier in the medical image field is support vector machine[36,59-62]. This research work is implemented using SVM with its kernels like Cubic, Gaussian, Linear, Quadratic and hence named as C-SVM, G-SVM, L-SVM, and Q-SVM. The SVM and performance evaluation measures[30-71] include accuracy (Acc), sensitivity (Sen), and specificity (Spe), which are calculated using Eqn. (8-10).

$$Acc = \frac{TP + TN}{TP + TN + FP + FN} \times 100 \tag{8}$$

$$Sen = \frac{TP}{TP + FN} \times 10 \tag{9}$$

$$Spe = \frac{TN}{TN + FP} \times 100 \tag{10}$$

where,
TP=True+Positive. TN=True+Negative, FP=False+Positive and FN=False+Negative.

3. EXPERIMENTAL RESULTS

In this paper a combination of EMD and VMD based methods for improved glaucoma detection is implemented on ACRIMA[13] image dataset. Two input images of glaucoma (Im638_g_ACRIMA.jpeg) and healthy (Im056_ACRIMA.jpeg) are given in Fig. 4. After applying preprocessing and decomposition methods, separately. We obtained various frequency components (EMD-imfs and VMD-imfs) from low to moderate, and moderate to high using EMD[69-76] and VMD[52-68] as shown in Fig. 4. The evaluated matrices like accuracy, sensitivity, and specificity of proposed work using 10-fold cross validation are presented in Table 2. The achieved accuracy using SVM with its kernel functions like cubic, gaussian, linear, quadratic is 98.30 %, 96.59 %, 96.59 %, and 97.87 %, respectively Fig. 4.

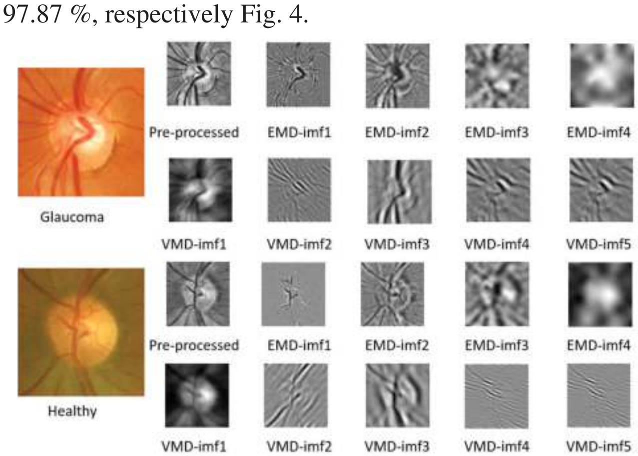

Figure 4. Input sample images along with sample images along with preprocessed and EMD-imfs and VMD-imfs.

Table 2. Performance for the proposed work after 3, 5, & 10 fold cross validation with different kernel

k-FCV	SVM Kernels	Acc (%)	Sen (%)	Spe (%)
3	Linear	95.74	97.47	93.51
	Quadratic	97.3	98.48	95.78
	Cubic	97.59	98.48	96.43
	Gaussian	95.86	99.74	90.91
5	Linear	96.16	97.73	94.16
	Quadratic	97.3	98.23	96.1
	Cubic	97.87	98.74	96.75
	Gaussian	96.31	99.24	92.53
10	Linear	96.59	98.23	94.48
	Quadratic	97.87	98.74	96.75
	Cubic	98.3	98.48	98.05
	Gaussian	96.59	99.75	92.53

In Fig. 5, we have plotted a curve for performance (in percentage) of proposed research work using 4 types of SVM-kernel for 2-to-13-fold cross validation. In Fig. 5, we obtained better accuracy using cubic and quadratic kernels with SVM for 10-fold cross validation. However, C-SVM achieved highest accuracy with better sensitivity and specificity. This showed that 10-fold is better for C-SVM.

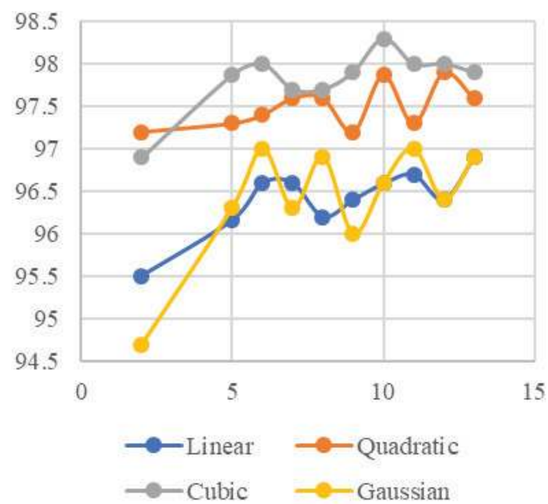

Figure 5. Plot for accuracy (in %) versus SVM-Kernels for 2-to-13-fold cross validation.

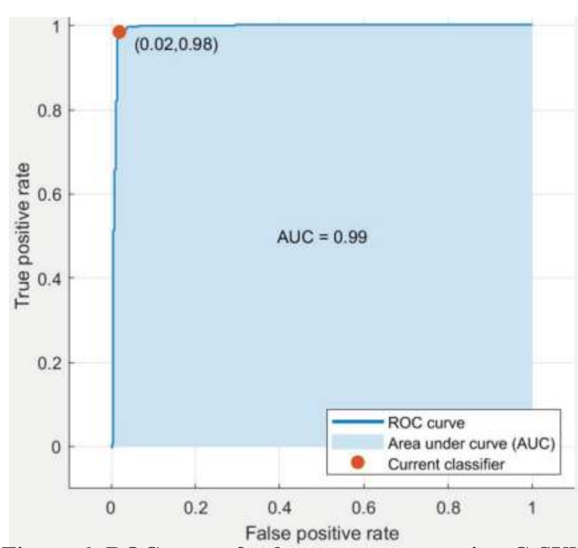

Figure 6. ROC curve foe better accuracy using C-SVM.

Further, we have also plotted a ROC curve for better accuracy using C-SVM in Fig. 6 for 10-fold cross validation.

4. COMPARATIVE ANALYSIS OF PROPOSED AND EXISTING RESEARCH WORK

This section presents an experimental comparison of proposed research work and recent state-of-the-art method for glaucoma detection.

Table 3. Comparison of methods (ACRIMA dataset)

Research work	Performances (%)		
Author/ref./year	Acc.	Sen.	Spe.
Pinto, *et. al.*[13]/2019	70.21	68.93	70.2
Serte, *et. al.*[14]/2019	65	NR	87
Claro et. al al.[15]/2019	95.31	NR	NR
Liu, *et. al.*[17]/2020	85.1	85.4	84.3
Elangovan, *et. al.*[18]/2020	96.64	96.07	97.39
Kirar, *et. al.*[19]/2021	92.06	91.42	92.89
Galarraga, *et. al.*[20]/2021	94.61	94.57	92.5
Devi, *et. al.*[21]/2021	95	94.11	95.91
Manghnani, *et. al.*[22]/2021	97.02	98.23	95.46
Devecioglu, *et. al.*[23]/2022	91.8	93.6	88.8
Singh, *et. al.*[24]/2022	92.14	92	90
Sonti, *et. al.*[25]/2022	96.7	98.32	94.62
Bouris, *et. al.*[71]/2024	92	98	80
Wiharto, *et. al.*[72]/2024	97.99	97.99	97.71
Manghnani, *et. al.*[73]/2024	91.6	96.3	96.7
Proposed work	98.29	98.48	98.05

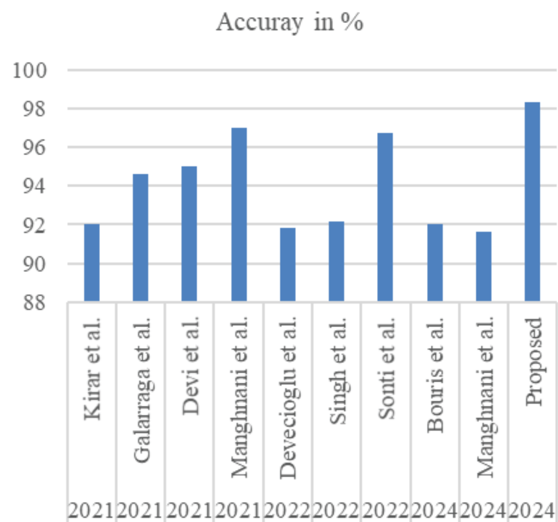

Figure 7. Accuracy comparison for recent methods only (in %).

Various work has been studied in the literature survey part; here we compared some research work implemented on ACRIMA dataset[13]. Pinto[13], *et. al.*, Serte[14], *et. al.*, Claro[15], *et. al.*, Liu[17], *et. al.*, Elangovan[18], *et. al.* , Kirar[19], *et. al.*, Galarraga[20], *et. al.*, Devi[21], *et. al.*, Manghnani[22], *et. al.*, Devecioglu[23], *et. al.*, and Singh[24], *et. al.*, Sonti[25], *et. al.* Compared research work[13-25] reported comparatively less accuracy. It may be due to limitation of methods used or have not utilised the contribution of all components.

Proposed research work achieved better results. We have obtained highest accuracy, which is 98.30 %, using C-SVM. The achieved accuracy using SVM with its kernel functions like cubic, gaussian, linear, quadratic is 98.30 %, 96.59 %, 96.59 %, and 97.87 %, respectively. The performances comparison of this work and recent published work has been given in Table 3 and plotted in Fig. 7.

5. CONCLUSIONS AND FUTURE WORK

This research presents a combined Empirical Mode Decomposition (EMD) and Variational Mode Decomposition (VMD) approach for enhanced detection of ocular diseases from retinal fundus images. In defense scenarios, where soldiers, fighter pilots, tank operators, and infantry must maintain peak visual performance amidst the chaos of war-guns firing, rockets launching, cannons booming, and explosions lighting up the battlefield-accurate and early diagnosis of eye conditions is crucial. By preprocessing and decomposing all color components using EMD and VMD into EMD-imfs and VMD-imfs, the accuracy of detecting these conditions has been significantly improved. The C-SVM classifier achieved the highest accuracy of 98.30 %, demonstrating superior performance on the ACRIMA image dataset with 10-fold cross-validation. The achieved accuracies using SVM with cubic, Gaussian, linear, and quadratic kernels were 98.30 %, 96.59 %, 96.59 %, and 97.87 %, respectively. When compared to other methods, our proposed approach outperforms state-of-the-art techniques, leading to better results for detecting ocular diseases.

This method, with its improved accuracy, can assist military ophthalmologists in making better decisions for the diagnosis of eye conditions in defense applications. The ability to diagnose eye diseases early can help maintain the readiness and effectiveness of soldiers, pilots, and other defense personnel in high-stress environments filled with flames, explosions, and smoke. As future work, this approach could be extended to include deep learning features for detecting not only ocular diseases but also other conditions such as diabetes and retinopathy, further advancing its application in defense contexts.

REFERENCES

1. Sharma, A.; Patra, G.K. & Naidu, V.P.S. Machine learning based bearing fault classification using higher order spectral analysis. *Def. Sci. J.*, 2024, **74**, 505-516. doi:10.14429/dsj.74.19307.
2. Priyadarshini, S.; Gourab, M.K.; Mandal, U. & Roy, A. A comparative study on various flight termination system technologies. *Def. Sci. J.*, 2023, **73**, 351-361. doi:10.14429/dsj.73.18334.
3. S, G.; T, D. & Haldorai, A. A supervised machine learning model for tool condition monitoring in smart manufacturing. *Def. Sci. J.*, 2022, **72**, 712-720. doi:10.14429/dsj.72.17533.
4. Bock, R.; Meier, J.; Nyúl, L.G.; Hornegger, J. & Michelson, G. Glaucoma risk index: automated glaucoma detection from color fundus images. *Med. Image Anal.*, 2010, **14**(3), 471-481. doi:10.1016/j.media.2009.12.006.

5. Tham, Y.C.; Li, X.; Wong, T.Y.; Quigley, H.A.; Aung, T. & Cheng, C.Y. Global prevalence of glaucoma and projections of glaucoma burden through 2040: A systematic review and meta-analysis. *Ophthalmol.,* 2014, **121**(11), 2081-2090. doi:10.1016/j.ophtha.2014.05.013.
6. Raja, C. & Gangatharan, N. Optimal hyper analytic wavelet transform for glaucoma detection in fundal retinal images. *J. Electr. Eng. Technol*., 2015, **10**(4), 1899-1909. doi:10.5370/jeet.2015.10.4.1899.
7. Maheshwari, S.; Pachori, R.B.; Kanhangad, V.; Bhandary, S.V. & Acharya, U.R. Iterative variational mode decomposition based automated detection of glaucoma using fundus images. *Comput. Biol. Med*., 2017, **88**, 142-149. doi:10.1016/j.compbiomed.2017.06.017.
8. Kirar, B.S. & Agrawal, D.K. Computer aided diagnosis of glaucoma using discrete and empirical wavelet transform from fundus images. *IET Image Process*., 2019, **13**(1), 73–82. doi:10.1049/iet-ipr.2018.5297.
9. Kirar, B. & Agrawal, D. Current research on glaucoma detection using compact variational mode decomposition from fundus images. *Int. J. Intell. Eng. Syst*., 2019, **12**(3), 1–10. doi:10.22266/ijies2019.0630.01.
10. Agrawal, D.K.; Kirar, B.S. & Pachori, R.B. Automated glaucoma detection using quasi-bivariate variational mode decomposition from fundus images. *IET Image Process*., 2019, **13**(13), 2401–2408. doi:10.1049/iet-ipr.2019.0036.
11. Rathore, N. & Chana, I. Job migration with fault tolerance based QoS scheduling using hash table functionality in social grid computing. *J. Intell. Fuzzy Syst*., 2014, **27**(6), 2821–2833. doi:10.3233/ifs-141243.
12. Kirar, B.S.; Agrawal, D.K. & Kirar, S. Glaucoma detection using image channels and discrete wavelet transform. *IETE J.* Res., 2022, **68**(6), 4421–4428. doi:10.1080/03772063.2020.1795934.
13. Diaz-Pinto, A.; Morales, S.; Naranjo, V.; Köhler, T.; Mossi, J.M. & Navea, A. CNNs for automatic glaucoma assessment using fundus images: an extensive validation. *Biomed. Eng. Online*., 2019, **18,** 1-19. doi:10.1186/s12938-019-0649-y.
14. Serte, S. & Serener, A. A generalized deep learning model for glaucoma detection. *In* 3rd International Symposium on Multidisciplinary Studies and Innovative Technologies (ISMSIT), 2019, 1-15. doi:10.1109/ismsit.2019.8932753.
15. Claro, M.; Veras, R.; Santana, A.; Araújo, F.; Silva, R.; Almeida, J. & Leite, D. An hybrid feature space from texture information and transfer learning for glaucoma classification. *J. Visual. Commun. Image Represent*., 2019, **64**, 102597. doi:10.1016/j.jvcir.2019.102597.
16. Chana, I. A sender initiate based hierarchical load balancing technique for grid using variable threshold value. 2013, 1-6. doi:10.1109/ispcc.2013.6663440.
17. Liu, H.; Zhang, N.; Jin, S.; Xu, D. & Gao, W. Small sample color fundus image quality assessment based on gcforest. *Multimed., Tools Appl*. 2021, **80**, 17441–17459. doi:10.1007/s11042-020-09362-y.
18. Elangovan, P. & Nath, M.K. Glaucoma assessment from color fundus images using convolutional neural network. *Int. J. Imaging Syst. Technol*., 2020, **31**, 955–971. doi:10.1002/ima.22494.
19. Kirar, B.S.; Reddy, G. R. S. & Agrawal, D.K. Glaucoma detection using ss-qb-vmd-based fine sub-band images from fundus images. *IETE J. Research*., 2021, **69**, 4909–4920. doi:10.1080/03772063.2021.1959424.
20. Almeida-Galarraga, D.; Benavides-Montenegro, K.; Insuasti-Cruz, E.; Lovato-Villacis, N.; Suarez-Jaramillo, V.; Tene-Hurtado, D.; Tirado-Espin, A. & Villalba-Meneses, G.F. Glaucoma detection through digital processing from fundus images using MATLAB. *In* 2nd *Int. Conf. Inf. Syst. Software Technol. (ICI2ST)*, 2021. doi:10.1109/ici2st51859.2021.00014.
21. Devi, K.„ *et. al.* Texture Based Feature Extraction and Classification of Retinal Fundus Image for Glaucoma Detection. Proceedings of the 2nd International Conference on Smart Electronics and Communication (ICOSEC), 2021, pp. 1302–1307.
22. Manghnani, P. & Moghe, A. Glaucoma detection using bi-dimensional empirical mode decomposition from retinal fundus images. *Int. J. Intell. Eng. Syst*., 2021, **14**, 249–257. doi:10.22266/ijies2021.1231.23.
23. Devecioglu, O.C.; Malik, J.; Ince, T.; Kiranyaz, S.; Atalay, E. & Gabbouj, M. Real-time glaucoma detection from digital fundus images using self-onns. *IEEE Access*., 2021, **9**, 140031–140041. doi:10.1109/access.2021.3118102.
24. Singh, L.K.; Pooja, N.; Garg, H.; Khanna, M. & Bhadoria, R.S. An enhanced deep image model for glaucoma diagnosis using feature-based detection in retinal fundus. *Med. Biol. Eng. Comput*., 2021, **59**, 333–353. doi:10.1007/s11517-020-02307-5.
25. Sonti, K. & Dhuli, R. Shape and texture based identification of glaucoma from retinal fundus images. *Biomed. Signal Process. Control*., 2022, **73**, 103473. doi:10.1016/j.bspc.2021.103473.
26. David, D.S.; Selvi, S. a. M.; Sivaprakash, S.; Raja, P.V.; Sharma, D.K.; Dadheech, P. & Sengan, S. Enhanced detection of glaucoma on ensemble convolutional neural network for clinical informatics. *Comput. Mater. Contiua*., 2022, **70**(2), 2563–2579. doi:10.32604/cmc.2022.020059.
27. Chana, I. A cogitative analysis of load balancing technique with job migration in grid environment. World congr. Inf. Commun. Technol. (WICT), Mumbai, IEEE proc. Paper, 2011, 77-82. doi:10.1109/WICT.2011.6141221.
28. Pin, K.; Chang, J.H. & Nam, Y. Comparative study of transfer learning models for retinal disease diagnosis from fundus images. *Comput. Mater. Contiua.,* 2022, **70**(3), 5821–5834.

doi:10.32604/cmc.2022.021943.
29. Zuiderveld, K. Contrast limited adaptive histograph equalization. *In* Proc. of Graphic Gems IV, San Diego, Academic Press Professional., 1994, pp. 474–485.
30. Chana, I. Variable threshold-based hierarchical load balancing technique in Grid. *Eng. comput*., 2015, **31**, 597-615. doi:10.1007/s00366-014-0364-z.
31. Nunes, J.C.; Guyot, S. & DeleChelle, E. Texture analysis based on local analysis of the bidimensional empirical mode decomposition. *Mach. Vis. Appl*., 2005, **16**, 177–188. doi:10.1007/s00138-004-0170-5.
32. Dragomiretskiy, K. & Zosso, D. Two-Dimensional variational mode decomposition. *In Lect. Notes Comput. Sci.,* 2015, 197–208. doi:10.1007/978-3-319-14612-6_15.
33. Agrawal, D.K.; Kirar, B.S. & Pachori, R.B. Automated glaucoma detection using quasi-bivariate variational mode decomposition from fundus images. *IET Image Process*., 2020, ***13***, 2401–2408. doi:10.1049/iet-ipr.2019.0036.
34. Gonzalez, R.C. & Woods, R.E. *Digital Image Process*. 3rd ed. 2014.
35. Kononenko, I. Estimating attributes: analysis and extensions of relief. Lect. Notes Comput. Sci., 1994, 171–182. doi:10.1007/3-540-57868-4_57.
36. Suykens, J.; Lukas, L.; Van Dooren, P. & Vandewalle, J. Least squares support vector machine classifiers. *Neural Process*., 1999, **9**, 293–300. doi:10.1023/A:1018628609742.
37. Srinivas, B. & Rao, G.S. Segmentation of Multi-Modal MRI brain tumor sub-regions using deep learning. *J. Electr. Eng. Technol*., 2020, **15**, 1899–1909. doi:10.1007/s42835-020-00448-z.
38. Yadav, A.K.; Pateriya, R.K.; Gupta, N.K.; Gupta, P.; Saini, D.K. & Alahmadi, M. Hybrid machine learning model for face recognition using SVM. *Comput. Mater. Contiua*, 2022, **72**, 2697–2712. doi:10.32604/cmc.2022.023052.
39. Almalki, Y.E.; Shaf, A.; Ali, T.; Aamir, M.; Alduraibi, S.K.; Almutiri, S.M.; Irfan, M.; Basha, M.A.A.; Alduraibi, A.K.; Alamri, A.M.; Azam, M.Z.; Alshamrani, K. & Alshamrani, H.A. Breast cancer detection in Saudi Arabian women using hybrid machine learning on mammographic images. *Comput. Mater. Continua,* 2022, **72**, 4833–4851. doi:10.32604/cmc.2022.027111.
40. Bhujade, R.K. & Asthana, S. An extensive comparative analysis on various efficient techniques for image Super-Resolution. *Int. J. Emerging Technol. Adv. Eng*., 2022, **12**, 153–158. doi:10.46338/ijetae1122_16.
41. Guerroum, M.; Zegrari, M.; Masmoudi, M.; Berquedich, M. & Elmahjoub, A.A. Machine learning technics for remaining useful life prediction using diagnosis data: a case study of a jaw crusher. *Int. J. Emerging Technol. Adv. Eng*., 2022, **12**(10), 122–135. doi:10.46338/ijetae1022_14.
42. Agustono, I.; Asrol, M.; Budiman, A.S.; Djuana, E. & Gunawan, F.E. State of charge prediction of lead acid battery using transformer neural network for solar smart dome 4.0. *Int. J. Emerging Technol. Adv. Eng*., 2022, **12**(10), 1–10. doi:10.46338/ijetae1022_01.
43. Jain, N. & Singh, P. Binary pattern for copy-move image forgery detection. in handbook of machine vision and augmented intelligence. *In* Lect. Notes electr. Eng. 2023, **1007**. doi:10.1007/978-981-99-0189-0_37.
44. Chana, I. Job migration policies for grid environment. *Wirel. Pers. Commun*., 2016, **89**, 241–269. doi:10.1007/s11277-016-3264-2.
45. Apipawinwongsa, P. & Limpiyakorn, Y. Counterfeit luxury handbag materials image classification using deep learning and local binary pattern. *Int. J. Emerging Technol. Adv. Eng*., 2022, **12**, 41–48. doi:10.46338/ijetae0922_05.
46. Wei, Y.; Machica, I.K.D.; Dumdumaya, C.E.; Arroyo, J.C.T. & Delima, A. P. Liveness detection based on improved convolutional neural network for face recognition security. *Int. J. Emerging Technol. Adv. Eng*., 2022, **12**, 45–53. doi:10.46338/ijetae0822_06.
47. Clarin, J. A. Comparison of the performance of several regression algorithms in predicting the quality of white wine in WEKA. *Int. J. Emerging Technol. Adv. Eng*., 2022, **12**, 20–26. doi:10.46338/ijetae0722_03.
48. Jain N. K. Image forgery detection using biorthogonal wavelet transform. *In* Conference on Machine Vision and Augmented Intelligence (MAI-2022), NIT Jamshedpur, 4-7 March 2022.
49. Abdelhafid, E.; Aymane, E.; Benayad, N.; Abdelalim, S.; Hachem, E.Y. a. M.; Rachid, O.H.T. & Brahim, B. ECG arrhythmia classification using convolutional neural Network. *Int. J. Emerging Technol. Adv. Eng*., 2022, **12**, 186–195. doi:10.46338/ijetae0722_19.
50. Baharun, N.; Faezah, N.; Masrom, S.; Mohamad Yusri, N.A.; Abd Rahman, A.S. Auto modelling for machine learning: A comparison implementation between rapidminer and python. *Int. J. Emerging Technol. Adv. Eng*., 2022, **12**. 15-27. doi:10.46338/ijetae0522_03.
51. Siguas, R.P.; Solis, H.M.; Solis, E.M.; Zamudio, L.M. & Artezano, A.R. application proposal for gastritis diagnosis and treatment applying machine learning. *Int. J. Emerging Technol. Adv. Eng*., 2022, **12**, 32–38. doi:10.46338/ijetae0422_05.
52. Rathore,Neeraj. Report on hierarchical load balancing technique in grid environment. *i-manager's J. Inf. Technol*. 2013, **2**, 21-35. doi:10.26634/jit.2.4.2541.
53. Dylan, C. & Rangkuti, A. H. WhatsApp Chatbot customer service using natural language processing and support vector machine. *Int. J. Emerging Technol. Adv. Eng*. 2022, **12**, 130–136. doi:10.46338/ijetae0222_15.

54. Infusi, M.Z.; Kusuma, G.P. & Arham, D.A. Prediction of local government revenue using data mining method. *Int. J. Emerging Technol. Adv. Eng*. 2022, **12**, 63–74. doi:10.46338/ijetae0122_07.
55. Thakur, M.A. & Kumar, R. Optimizing smart manufacturing with iot integration and leveraging machine learning analysis. *Af. Diaspora J. Math. (Ugc Care Group I)*, *Neuro Quant.*. 2022 **20**, 1620-1629. doi: 10.48047/NQ.2022.20.18.NQ8817.
56. Jain N.K. Binary pattern for copy move image forgery detection. *In* International Conference on Machine Vision and Augmented Intelligence (MAI-2022), NIT Jamshedpur, 4-7 March. 2022.
57. Hasan, K.K.; Hairuddin, M.A.; Mustapa, R.F.; Nordin, S.A. & Ashar, N.D.K. Machine learning approach of optimal frequency tuning for capacitive wireless power transfer system. *Int. J. Emerging Technol. Adv. Eng*. 2022, **12**, 65-71. doi: 10.46338/ijetae1122_07.
58. Kumar, S. & Mishra, S.K. Survey on challenges and techniques for improving energy efficiency IOT network. *Int. J. Emerging Technol. Adv. Eng*. 2019, **9**, 151-155.
59. Agarwal, P.; Rawat, M. P. & Singh, N. Tackling Climate change with the help of Machine Learning. *Int. J. Emerging Technol. Adv. Eng*., 2019, **9**, 163-166.
60. Kumari, J. & Sarwagi, A. An efficient proposed approach to classify the breast cancer dataset using neural network. *Int. J. Emerging Technol. Adv. Eng*. 2019, **9**, 212-217.
61. Rathore, N. Dynamic threshold based load balancing algorithms. *Wireless Pers. Commun*. 2016, **91**, 151-185. doi: 10.1007/s11277-016-3452-0.
62. Agrawal, M.; Khan, A.U. & Shukla, P. Deep long short term memory model for stock price prediction using technical indicators. *Int. J. Emerging Technol. Adv. Eng*. 2019, **9**, 206-210.
63. Jain, N.K. & Mishra, A. An efficient image forgery detection using biorthogonal wavelet transform and improved relevance vector machine. *Wireless Pers. Commun.* 2018, **101**, 1983–2008. doi: 10.1007/s11277-018-5802-6.
64. Teja, U.H. & Choubey, S.B. Electronic nose - A big part of our future. *Int. J. Emerging Technol. Adv. Eng*. 2019, **9**, 93-97.
65. Tiwari, K.; Birthare, M. & Upadhyay, R. Proposal of smart mirror using raspberry PI. *Int. J. Emerging Technol. Adv. Eng*. 2019, **9**, 63-65.
66. Reddy, B.S.; Sathyanarayana, S.K. & Prasad, L.V.R.C. Robust wireless sensor network using cognitive radio. *Int. J. Emerging Technol. Adv. Eng*. 2019, **9**, 123-130.
67. Pande, S. & Purohit, A. Unveiling the impact of extreme learning machine in the defence and military. *Def. Sci. J*. 2024, **74,** 512-517.
68. Thakur, M.A. & Kumar, R. Review of smart manufacturing with IoT integration and leveraging machine learning analysis. *Af. Diaspora J. Math*. 2022, **25**, 88-101.
69. Rathore, N. & Chana, I. Load balancing and job migration techniques in grid: A survey of recent trends. *Wireless Pers. Commun*. **79**, 2089-2125. doi:10.1007/s11277-014-1975-9.
70. Sharma, V. & Kumar, R. Topological broadcasting using parameter sensitivity based logical proximity graphs in coordinated ground-flying Ad Hoc networks. *J. Wirel. Mob. Netw. Ubiquitous Comput*. 2015, **6**, 54-72. doi:10.22667/JOWUA.2015.09.31.054.
71. Bouris, E.; Odugbo, O.P.; Rasheed, H.; Jin, S.; Fei, Z.; Morales, E. & Caprioli, J. A neural network for the detection of glaucoma from optic disc photographs. *Investigative Ophthalmol. & Visual Sci.*, 2024, **65**, 1634.
72. Wiharto, Harjoko, W.T. & Suryani, E. e-LSTM: Efficient net and long short-term memory model for detection of glaucoma diseases. *Int. J. Online Biomed. Eng.,* 2024, **20**, 64. doi: 10.3991/ijoe.v20i10.48603
73. Manghnani, P. & Moghe. A.A. BDIMFs based features fusion and classification for glaucoma prediction. *In* 2024 IEEE International Students' Conference on Electrical, Electronics and Computer Science (SCEECS), Bhopal, India, 2024, pp. 1-6, doi: 10.1109/SCEECS61402.2024.10481851

CONTRIBUTORS

Ms Pooja Manghnani obtainer MTech in Information Technology from RGPV, Bhopal. She is presently working in Govt. Women's Polytechnic College Bhopal as HOD Computer Science Department. Her research interests include: Image processing.
In the current study, she contributed to conception and design, data collection, analysis and interpretation of results.

Dr Asmita A. Moghe obtained PhD Maulana Azad National Institute of Technology Bhopal. She is presently working in University Institute of Technology, RGPV, Bhopal as HOD Information Technology Department. Her research interests include: Image processing.
In the current study she contributed to analysed results, drafted manuscript, reviewed the manuscript.

Defence Science Journal, Vol. 75, No. 1, January 2025, pp. 52-63, DOI : 10.14429/dsj.20107

Finite Field-Based Three-Tier Cryptography Algorithm to Secure the Images

M. Lavanya[#], K. Joseph Abraham Sundar[#,*] and S. Saravanan[$]
[#]*School of Computing, SASTRA Deemed University, Thanjavur - 613 401, India*
[$]*Department of Electronics and Communication Engineering, SASTRA Deemed University, Kumbakonam - 612 001, India*
[*]*E-mail: josephabrahamsundar@it.sastra.edu*

ABSTRACT

Securing the information is an important component in the computer network domain. Image information security is a vital part of the information security. The main process of image cryptography is traversing the image cryptosystem with high processing power, and efficiency. It is in terms of satisfying the cryptography requirements like confidentiality, integrity, and authenticity. A finite field-based image cryptography algorithm called TIEA (Three-tier Image Encryption Algorithm) is proposed in this paper. This algorithm deliberated Shannon's principles of cryptography like confusion and diffusion techniques of the images based on the finite field values. This paper also designed the key stream generation pattern based on the crypto key length. Two subkeys are generated for the purpose of crypto key and the key generation process is used to enhance the permutation of the key. Various benchmark images were tested with this proposed algorithm and also with other existing algorithms. The performance result shows that the proposed algorithm TIEA could be a better candidate algorithm for image security in the network domain.

Keywords: Shannon's principle; Finite field values; Image security; Confusion and diffusion

1. INTRODUCTION

In recent years the information security domain and image security has been a significant research topic. The images may be non-sensitive or very sensitive and healthcare also often transfers personal data[1]. These sensitive data may be prone to various attacks such as interception, fabrication, denial of service, and accessing data in an unauthorized manner. Thus, protecting the information during transmission is a vital process. Unlike the algorithms used to encrypt the text data, algorithms used to encrypt the image data require special features to satisfy the characteristics of image security processing. The existing algorithms like AES, DES, and various public key cryptography algorithms need to be combined with Cipher Block Chaining (CBC) to enhance the security level of image data[2].

Encryption of the images is based on the speed of the algorithm processing. Thus the study of image-based encryption algorithms is more required than the algorithms with fast processing. In[3] an elaborate survey was conducted on the classification of chaotic systems for image encryption algorithms. Numerous chaos-based algorithms were proposed[4-9]. A probabilistic symmetric encryption was proposed using a chaos scheme with suitable random bits in the insertion phase[10]. This method used 4 rounds of 2-staged diffusion which involves exclusive-OR operation. This method also increased the cipher text space and gave more resist to statistical attacks.

A hyper-chaotic system was used to sum the pixels along with different summation processes[11]. The NPCR and UACI were observed. A pathological image encryption method[12] used an external one-time keys method to validate the polynomial multiplication over a Galois field. The results were observed with look-up tables, avalanche effect, and encryption rounds.

Encrypting the image is a big exceptional task than encrypting the text data. The nearby pixel values in the image may have a high correlation and these values are used by the crypt analyzer to analyze the data easily. The generated cipher image must be very random, unpredictable and it should produce distributed histogram results and should satisfy all the statistical tests given by NIST[13]. A shuffling algorithm was proposed to leverage the pseudo-random sequences to enhance the performances of the initial S-Box and verify the image encryption scheme with various RGB color images[14]. Image encryption algorithm SIEA with lightweight processing methodology is shown in the paper [15]. The encryption procedure should be very sensitive and the minor change in the original image should produce a major impact on the cipher image.

In this paper, an encryption algorithm TIEA is proposed. This algorithm follows Shannon's confusion, diffusion logic and finite field in number theory logic. The rest of the paper is designed as follows. The proposed algorithms and the process are highlighted in the section 2. Implementation and results are given in section 3. Performance analysis is discussed in section 4.

2. PROPOSED ALGORITHM

In a network transmission, information security is a vital

Received : 16 April 2024, Revised : 10 September 2024
Accepted : 30 September 2024, Online published : 10 January 2025

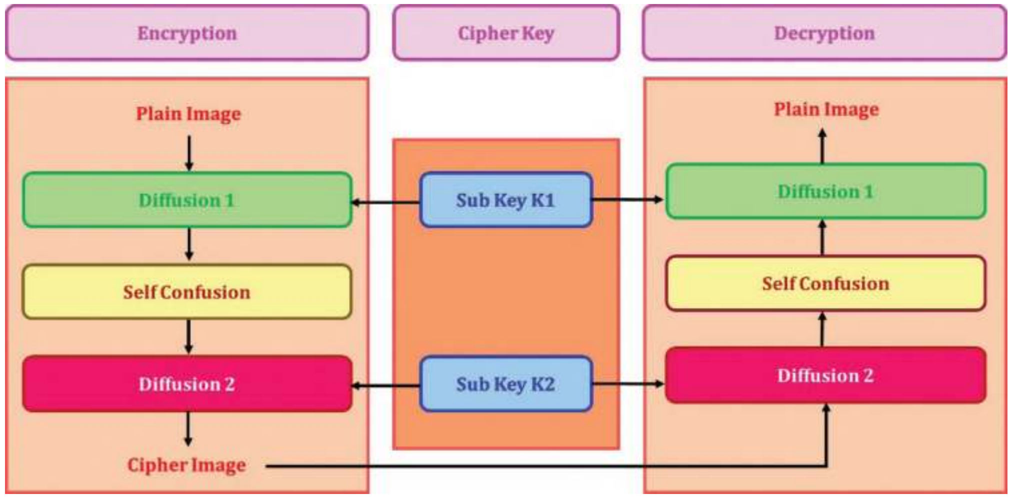

Figure 1. Flow diagram of the proposed algorithm.

process and the algorithm used to secure the data should satisfy the cryptography requirements such as confidentiality, integrity, and availability. It ensures the security of the image data using the proposed TIEA algorithm in this paper. This algorithm is a symmetric model and it has three phases such as key generation, encryption, and decryption. The finite field concept of number theory is used in this algorithm. Initially large prime number is chosen and the cipher key size is dynamically fixed based on the plain image row and column pixel size. Encryption and decryption processes are divided into three phases such as diffusion1, self-confusion, and diffusion 2. The flow diagram of the proposed algorithm is shown in Fig. 1 and the pseudo codes of the modules are given in algorithms 1-4.

2.1 KEY GENERATION

Key generation plays an important role in cryptography. In this proposed algorithm two subkeys k1 and k2 are generated using the cipher key "K". Subkeys are generated as a matrix $K1_{(m,n)}$ and $K2_{(m,n)}$ where m and n are the row and column size of plain image pixel values. The size of K is equal to (m × n). Figure 2 shows the flow diagram of the key generation module. Subkeys k1 and k2 are generated based on the following steps.

- Step 1: Enter cipher key "K" as a input. Choose the random large prime number P
- Step2: Find the factors of the number 'r' where p-1 ≥ r ≥ 3 and form a group for the numbers [i]=F r ={f 1 ,f 2 ,…f K } where i ≥ 1
- Step3: Subkey K1 matrix is formed with G[1] to G[m] as a row seed values (rs)and G[r+1] to G[r+c+1] as a column seed values(cs).
- Step4: Multiplicative inverse of the row seed value by column seed value is calculated if both rs and cs are relatively prime numbers K1(r,c)=(rs -1 mod cs) where 1≤ r≤ m and where 1≤ c≤ n
- Step5: If rs and cs are not relatively prime then both seed values are added and mod with the P value. K1(r,c) =(rs+cs) mod P
- Step6: Subkey K2 matrix is formed with G[last] to G[last-m] as a row seed values (rs) and G[last-m-1] to G[last-m-1-n] as a column seed values(cs).
- Step7: Multiplicative inverse of the row seed value by column seed value is calculated if both rs and cs are relatively prime numbers. K2(r,c)=(rs -1 mod cs) where 1≤ r≤ m and where 1≤ c≤ n
- Step8: If rs and cs are not relatively prime then both seed values are added and mod with the P value. K2(r,c) =(rs+cs) mod P
- Step9: Find the position of the values in the cipher key "K" and place it in the subkey matrix "k1" to form a subkey k1 matrix. K1(r,c)=K[K1(r,c)]

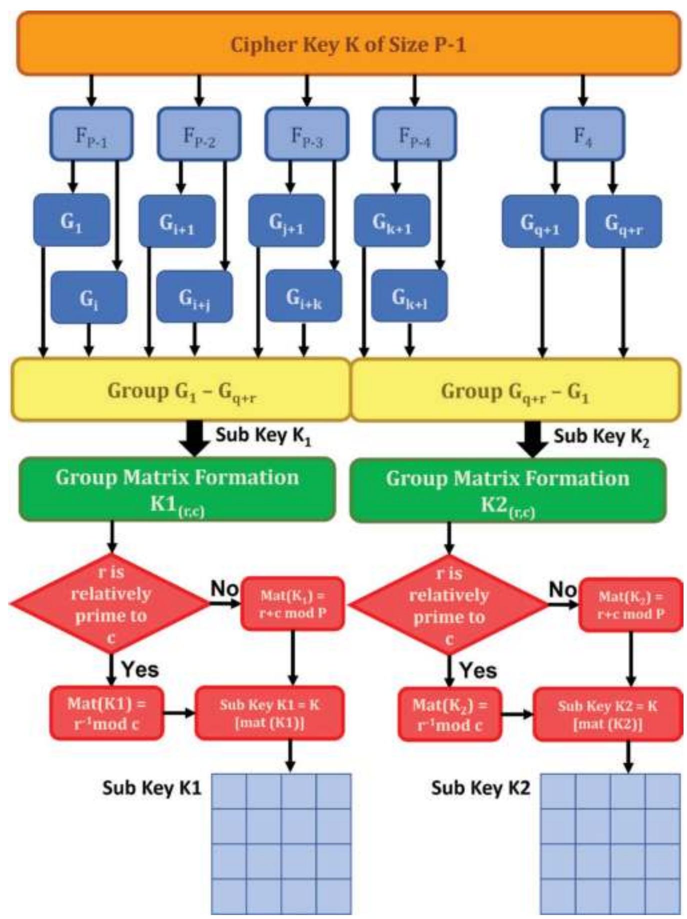

Figure 2. Key generation module.

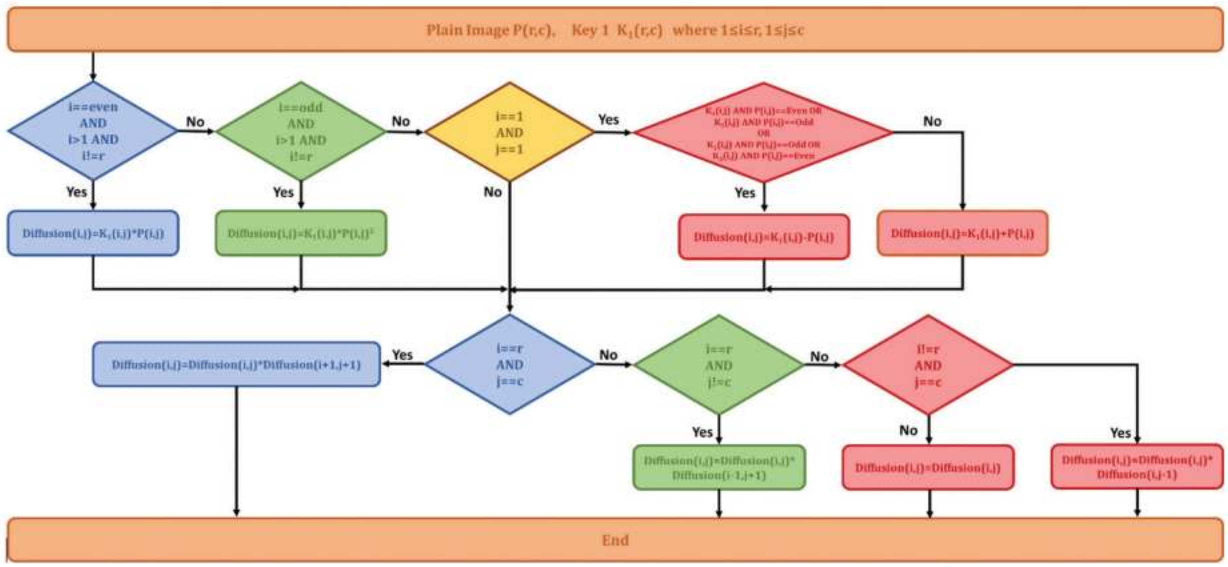

Figure 3. Flow diagram of Diffusion 1.

- Step10: Find the position of the values in the cipher key "K" and place it in the subkey matrix "k2" to form a subkey k2 matrix. K2(r,c)=K[K2(r,c)]

Algorithm 1. Key generation

```
Begin
i← p-1; k ← 1; m ← row; n ← Column;
    r←0 ; c ← 0; j ← 0;
    While i ≥ 4 do
      | Group_k← Factor_p-i
      | k ← k+1
      | i=i+1
    End While
    While r! = m AND c == n do
      | If GCD (Group_j, Group_m+j) ==1
      |     | K1(r,c) ← Group_j  MOD Group_m+j
      |     Else
      |     | K1(r,c) ← (Group_j + Group_m+j) MOD P
      |  Endif
      |   j ← j +1
      |   c ← c+1
      | If c==n AND r == m
      |     |c ← 0
      |     |r ← r+1
      |  Endif
End While

    r←0 ; c ← 0; j ← 1;
    While r != m AND c == n do
      | If GCD (Group_k-j, Group_k-m-j ) ==1
      |    | K2(r,c) ← Group_k-1  MOD Group_k-m-1
      | Else
      |    | K2(r,c) ← (Group_k-1 + Group k-m-1 ) MOD p
      | Endif
      |    j ← j +1
      |    c ← c+1
      | If c==n AND r == m
      |    |c ← 0
      |    |r ← r+1
 Endif
 End While
 End
```

2.2 Encryption

The second module is the encryption module. Plain image is encrypted with the subkey values K1 and K2 based on Shannon's principal diffusion and confusion logic. Encryption process of proposed algorithm in divided in to three modules named as Key1 diffusion, Self-confusion and key2 diffusion. Plain image pixel values are process with K1 and K2 in diffusion modules and in self-confusion no key values are involved.

2.2.1 Key Diffusion 1

Flow diagram of diffusion1 module is given in the Fig. 3.

Algorithm 2. Diffusion 1

```
Begin
   i ← 1; j ← 1; m ← row; n ← column
While i ≤ m do
 | While j ≤ n do
 |      | If i==1 AND j==1
 |      |    | If(K1(i,j) %2==0 AND PI (i,j) %2==0)OR(K1(i,j) %2==1 AND PI (i,j) %2==1)
 |      |    |     | Diffusion1(i,j) ← K1(i,j) + PI (i,j)
 |      |    | Else if(K1(i,j) mod 2==0 AND PI (i,j) %2==1) OR K1(i,j) %2==1)AND PI (i,j)
 |      |    |        %2==0)
 |      |    |     | Diffusion1(i,j) ← K1(i,j) -PI (i,j)
 |      |    | Endif
 |      | Elseif i==m AND j==n
 |      |    | If(K1(i,j) % 2==0 AND PI (i,j) %2==0)  OR (K1(i,j) %2==1)AND PI (i,j)
 |      |    |   | %2==1)
 |      |    |   | Diffusion1(i,j) ← K1(i,j) -PI (i,j)
 |      |    | Elseif(K1(i,j)  %2==0 AND PI (i,j) %2==1) OR K1(i,j) %2==1)AND PI (i,j)
 |      |    |   | %2==0)
 |      |    |   | Diffusion1(i,j) ← K1(i,j) +PI (i,j)
 |      |    | Endif
 |      | Endif
 |      | If(I %2 == 1)
 |      |    |Diffusion1 = K1(i,j) x PI (i,j)
 |      | Elseif(i %2 == 0)
 |      |    |Diffusion1 = K1(i,j) x PI (i,j)
 |      | Endif
 |      | If (i==m AND j==n)
 |      |    | FinalDiff1(i,j) = Diffusion1(i,j) x Diffusion1 (i+1,j+1)
 |      | Elseif(i==m AND j!=n)
 |      |    | FinalDiff1(i,j) = Diffusion1(i,j) x Diffusion1 (i-1,j+1)
 |      | Elseif(i==m AND j==n)
 |      |    | FinalDiff1(i,j) = Diffusion1(i,j) x Diffusion1 (i,j-1)
 |      | Endif
 |      | j=j+1
 |   End while
 |   i=i+1
 End while
End
```

2.2.2 Self-Confusion

Diffusion 1 processed to find the final matrix value which involves plain image matrix and K1 matrix. The output of the diffusion1 module is processed using confusion logic. Flow diagram of self-confusion module is shown in Fig. 4. The final matrix FD1(mxn) follows the following rules to convert the diffused final matrix into self-confused matrix SC(m,n). Number keys are involved in this module.

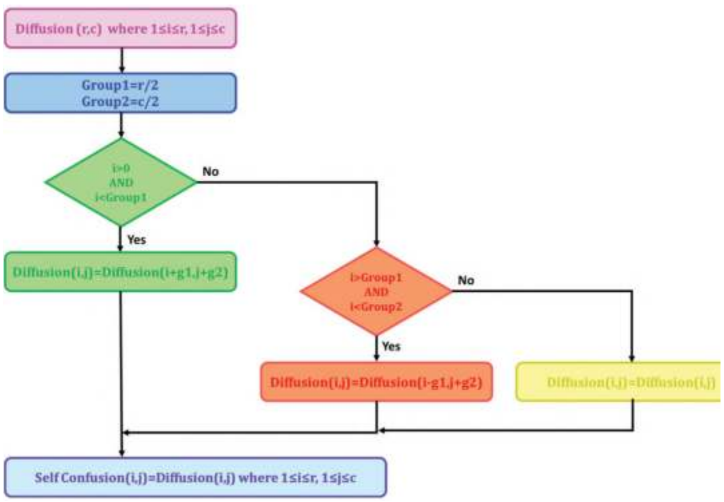

Figure 4. Flow diagram of self-confusion module.

Algorithm 3. Self-Confusion

Begin
$i \leftarrow 1; j \leftarrow 1; m \leftarrow row; n \leftarrow column$
$g1 \leftarrow m/2; g2 \leftarrow n/2$
While $i < m$ **do**
  While $j < n$ **do**
    $Finaldiff1_{(i,j)} \leftarrow Finaldiff1_{(i+g1),(j+g2)}$ where $0 < i < g1$
    $Finaldiff1_{(i,j)} \leftarrow Finaldiff1_{(i-g1),(j+g2)}$ where $g1 < i < g2$
    $selfconfusion_{(i,j)} \leftarrow Finaldiff1_{(i,j)}$
  End While
  j=j+1
End While
i=i+1
End

2.2.3 Key Diffusion 2

- *Step 1:* Self Confusion matrix value SC(mxn) is given as input
- *Step 2:* K2 matrix is converted from hexa to decimal values
- *Step 3:* Calculate the relative prime matrix RP(mxn) by following rules:
- *Step 3.1:* Find the list of relative prime numbers of the value K2(i,j) where 0<i<m+1
- and 0< j <n+1
- *Step 3.2:* Find the mean relative prime value from the list of relative prime numbers of K2(i,j) where 0<i<m+1 and 0< j <n+1
- *Step 4:* Find the modulo inverse matrix MD(m x n) using following equation
- $MD(i,j) = K2(i,j)^{-1} \bmod RP(i,j)$ where 0<i<m+1 and 0< j <n+1
- *Step 5:* Calculate the cipher image matric CM(mxn) multiplying Modulo inverse matrix and Cipher image matrix $CM(i,j) = (MD(i,j) \times SC(i,j)) \bmod 255$.

Flow diagram of diffusion 2 is shown in Fig. 5.

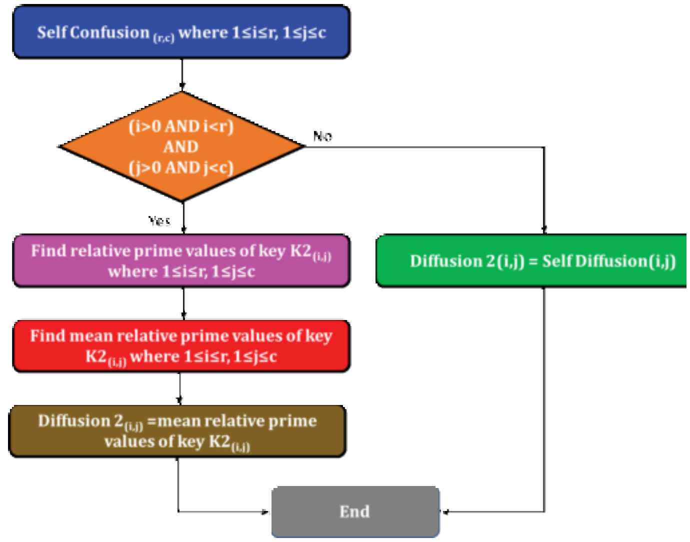

Figure 5. Flow diagram of Diffusion 2.

Algorithm 4: Diffusion 2

Begin
$i \leftarrow 1; j \leftarrow 1; m \leftarrow row; n \leftarrow column; y \leftarrow 0$
While $i \leq m$ **do**
  While $j \leq n$ **do**
    $Rg_y = K2_{(i,j)} \bmod P$
    $y \leftarrow y+1$
    $Mean = ½ \sum Rg_x$
    $RP_{(I,j)} \leftarrow Mean$
    $j=j+1$
  End while
  $i=i+1$
End while
$MD_{(I,j)} \leftarrow KR_{(I,j)} \bmod RP_{(I,j)}$ where $0<i \leq m, 0<j \leq n$
$CM_{(I,j)} \leftarrow MD_{(I,j)}\ X\ SC_{(I,j)} \bmod 255$ where $0<i \leq m, 0<j \leq n$
End

2.3 Decryption

The third module of this algorithm is the decryption process. Cipher image is decrypted with the subkey values K1 and K2 based on Shannon's principal diffusion and confusion logic. Decryption process of proposed algorithm in divided in to three modules named as Key2 diffusion, Self-confusion and key diffusion1. Cipher image pixel values are process with K1 and K2 in diffusion modules and in self-confusion no key values are involved.

2.3.1 Key Diffusion 2

- *Step 1:* Cipher image matrix value CM(4×4) is given as input
- *Step 2:* K2 matrix is converted from hex to decimal values
- *Step 3:* Calculate the relative prime matrix RP(4×4) by following rules:
- *Step 3.1:* Find the list of relative prime numbers of the value K2(i,j) where 0<i<m+1, and 0< j <n+1
- *Step 3.2:* Find the mean relative prime value from the list

of relative prime numbers of K2(i,j) where 0<i<m+1 and 0< j <n+1

- *Step 4:* Find the modulo inverse matrix MI(4×4) using following equation
  MD(i,j) = K2(i,j)$^{-1}$ mod RP(i,j) where 0<i<m+1 and 0< j <n+1
- *Step 5:* Calculate the Self-Confusion matrix SC(i,j) using following Eqn.
  SC(i,j) = MI(i,j)$^{-1}$ × CM(i,j)

2.3.2 Self-Confusion

Diffusion 2 processed to find the self-confusion matrix SC(i,j) which involves cipher image matrix and K2 matrix. The output of the diffusion2 module is processed using confusion logic. The SC matrix follows the following rules to convert the self-confusion matrix into final diffusion 1 matrix. No keys are involved in this module.

- *Step 1:* Self Confusion matrix SC(mxn) is divided based on the calculated value g1 and g2 Where the g1 = m/2 and g2 =n/2
- *Step 2:* Swap the values in SC matrix based on following rules:
  SC(i,j) =SC((i+g1)(j+g2)) where 0<i<g1
  SC(i,j) =SC((i-g1)(j+g2)) where g1<i< g2
- *Step 3*: FD1(i,j)=SC(i,j)

2.3.3 Key Diffusion 1

- Step 1: Diffusion1 final matrix FD1(m × n) is calculated using following rules:
- Step 1.1: D1(i,j) = FD1(i,j) × FD1((i+1)(j+1))$^{-1}$ where i=m and j =n
- Step 1.2: D1(i,j) = FD1(i,j) × FD1((i-1)(j+1))$^{-1}$ where i=m and j !=n
- Step 1.3: D1(i,j) = FD1(i,j) × FD1((i)(j-1)) $^{-1}$ where i!=m and j =n
- Step 2: Diffusion1 matrix D1(mxn) is calculated based on following rules
- Step 2.1: if K1(i,j) mod 2 =0 AND D1(i,j) mod 2 = 0 OR K1(i,j) mod 2 =1 AND Pt(i,j) mod
  2 = 1, Pt(i,j) = D1(i,j) - K1(i,j) + where i = 1 and j = 1
- Step 2.2: if K1(i,j) mod 2 =0 AND D1(i,j) mod 2 = 1OR K1(i,j) mod 2 =1 AND Pt(i,j) mod
  2 =0, Pt(i,j) = D1(i,j) + K1(i,j) where i = 1 and j = 1
- Step2.3: if K1(i,j) mod 2 =0 AND D1(i,j) mod 2 = 0 OR K1(i,j) mod 2 =1 AND Pt(i,j) mod
  2 = 1, Pt(i,j) =D1(i,j) + K1(i,j) where i =m and j = n
- Step 2.4: if K1(i,j) mod 2 =0 AND Pt(i,j) mod 2 = 1OR K1(i,j) mod 2 =1 AND Pt(i,j) mod 2 =0 Pt(i,j) = D1(i,j) - K1(i,j) where i =m and j = n
- Step 2.5: ifi mod 2 =1 Pt(i,j) = D1(i,j) × K1(i,j)$^{-1}$ where 1<i<m and 1<j<n
- Step 2.6: if i mod 2 =0 Pt(i,j) = (D1(i,j) × 2^{-1}) * K1(i,j)$^{-1}$ where 1<i<m and 1<j<n

3. IMPLEMENTATION AND EXPERIMENTAL RESULTS

The proposed TIEA algorithm modules are implemented

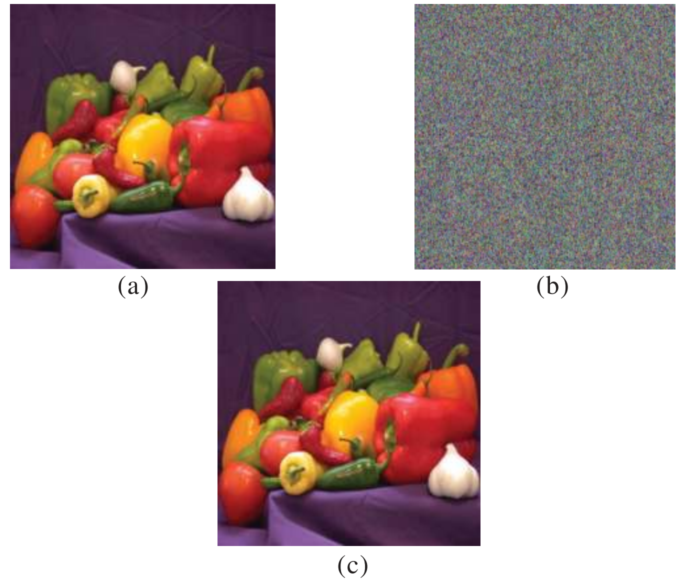

Figure 6. Color image vegetables; (a) Original image; (b) Encryption image; and (c) Decryption image.

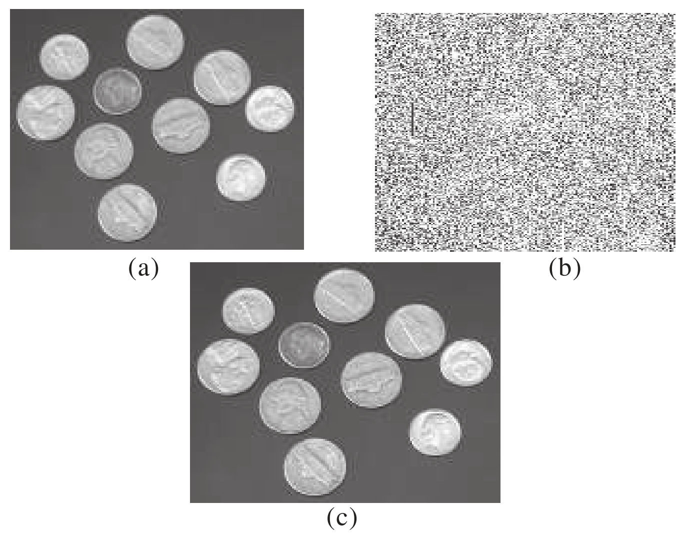

Figure 7. Dollar image; (a) Original image; (b) Encryption image; and (c) Decryption image.

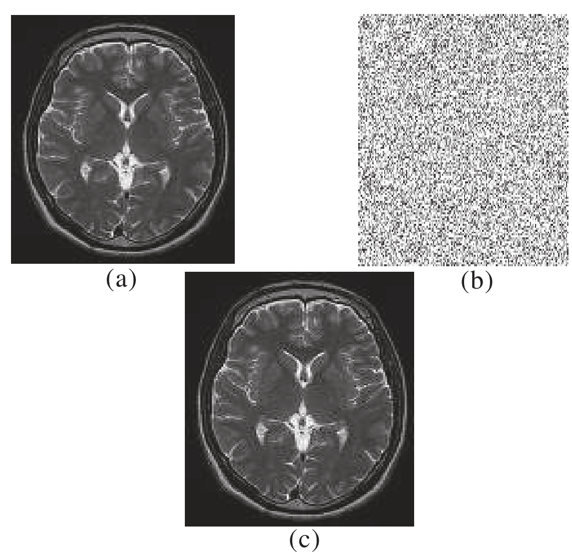

Figure 8. CT image Harns; (a) Original image; (b) Encryption image; and (c) Decryption image.

on MATLAB 2019b software with core i3, 2GB graphics card, and 8 GB RAM. Three bench mark images are taken from the MATLAB database of different scales such as gray, RGB color and medical image Harns Computed Tomography (CT)[18-20] involved in the testing process of the algorithm. Different dimension images are used to check the scalability of the algorithm. Figure 6 to Fig. 8 shows the plain image and cipher image of bench mark data.

4. PERFORMANCE ANALYSIS

To verify and prove the achievement ability and the security level of the proposed TIEA algorithm numerous trails have been processed to validate the qualitative and quantitative measures. The proposed algorithm is resistant to the exhaustive search analyze and it strictly follows diffusion and confusion technique. Existing DES algorithm key size is 56 bit and AES key size is 128 bits fixed. Compare with these existing algorithms the TIEA algorithm key size is dynamic in nature based on the image pixel size. Proposed TIEA algorithm was compared with the standard algorithms AES[16] and holomorphic encryption[17]. Numerous procedures are followed to perform the analyzation of the algorithms such as Differential analysis, Correlation analysis, Histogram analysis, key sensitivity analysis[19] and the results and cipher outputs shows the randomness of the encrypted images.

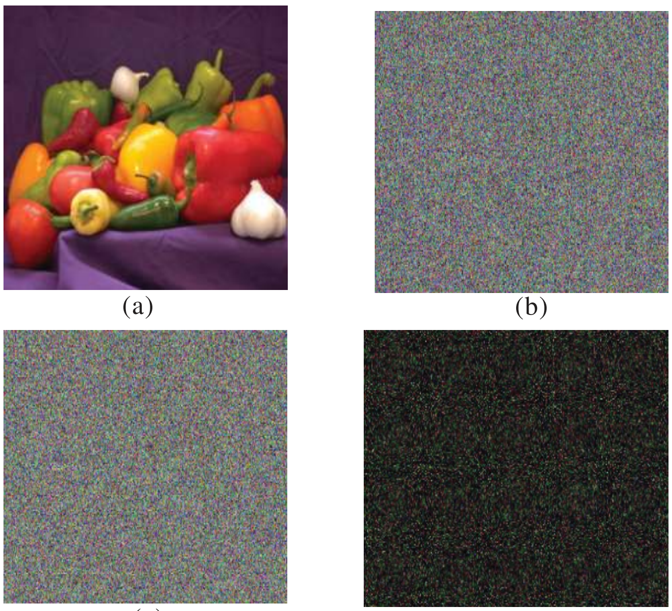
(a) (b) (c) (d)

Figure 9. Color image vegetables; (a) Original image; (b) Encryption 1; (c) Encryption 2; and (d) Difference between 12a and 12b.

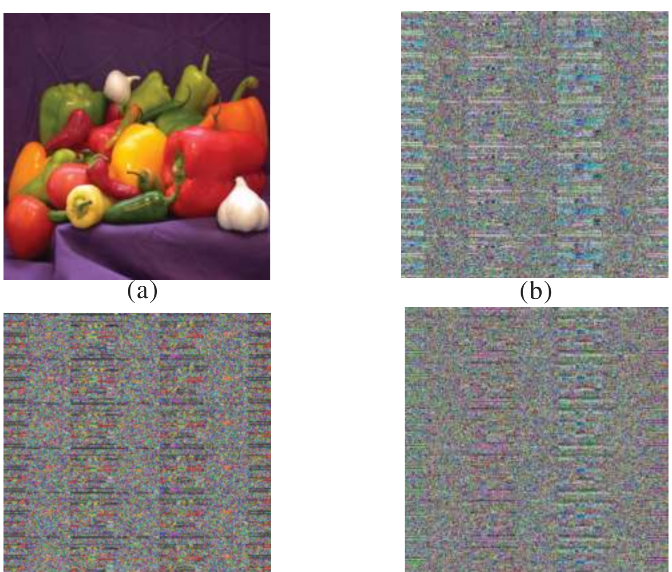
(a) (b) (c) (d)

Figure 10. Color image Vegetables; (a) Decryption with the correct key; (b) Decryption with a 2-bit modified Key; (c) Decryption with a 4-bit modified Key; and (d) Decryption with 8-bit modified Key.

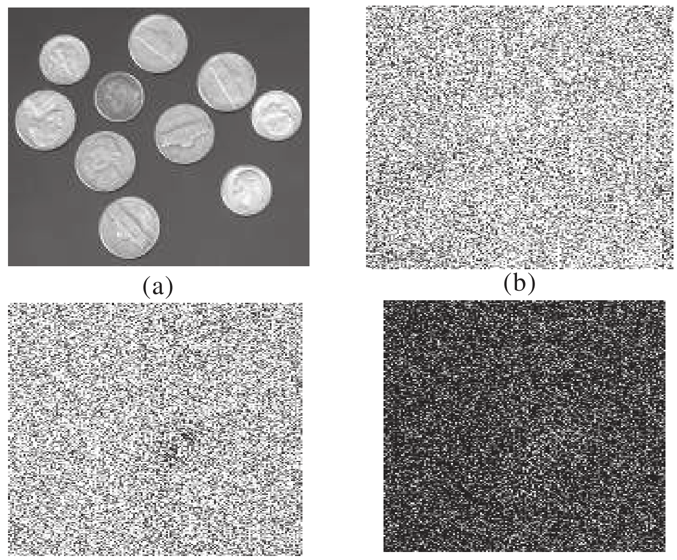
(a) (b) (c) (d)

Figure 11. Dollar image; (a) Plain image; (b) Encryption 1; (c) Encryption 2; and (d) Difference between 14b and 14c.

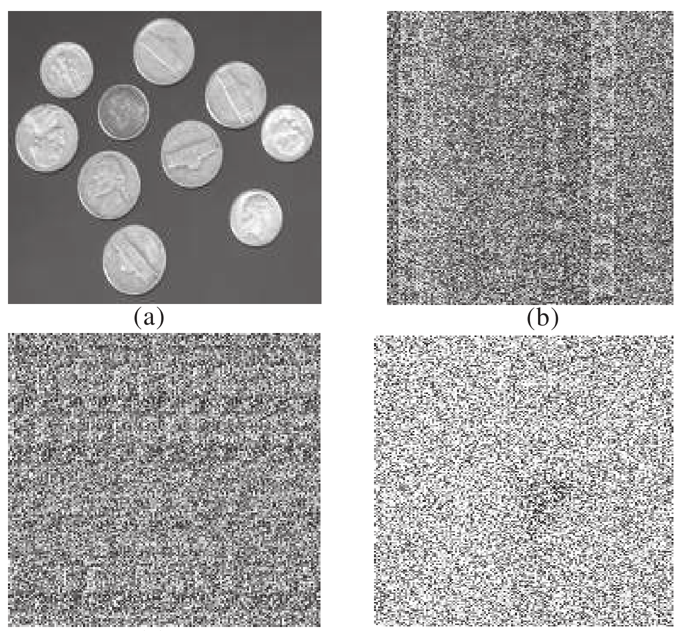
(a) (b) (c) (d)

Figure 12. Dollar image; (a) Decryption with the correct key; (b) Decryption with a 2-bit modified key; (c) Decryption with a 4-bit modified key; and (d) Decryption with an 8-bit modified key.

4.1 Key Sensitivity Analysis

The key sensitivity analysis is the vital procedure to validate the proposed algorithm in terms of the randomness of the results with respect to the key and the avalanche effect of the algorithm. Various scale images are considered to test and perform key analyzation. Cipher key is slightly modified and the sub keys K1 and K2 are generated to test the cipher image randomness. The figure 9-14 Shows and prove that the proposed algorithm provides the random outputs and there is no similarity between the cipher images. For each and every different key the random cipher image is generated. Hence it is proved that the proposed TIEA algorithm performs well in terms of key sensitivity and provides the adequate security to the image data while transmission.

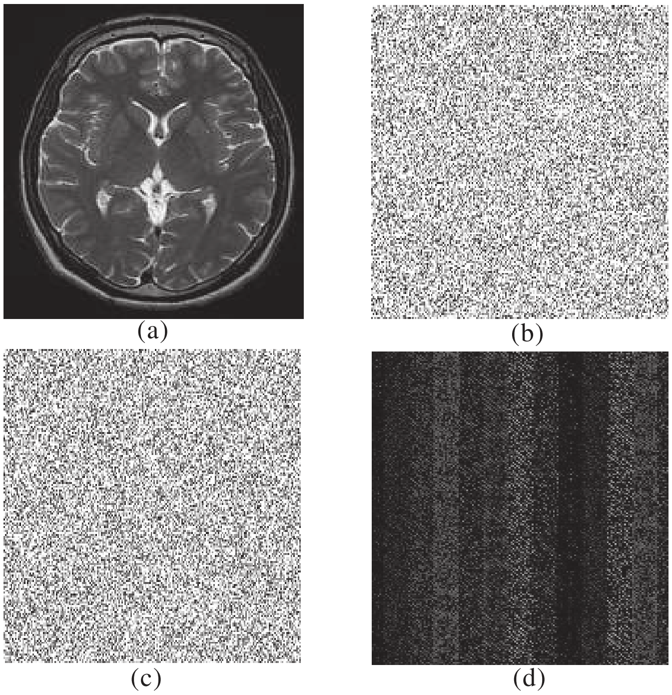

Figure 13. CT image Harns; (a) Plain image; (b) Encryption 1; (c) Encryption 2; and (d) Difference between 16b and 16c.

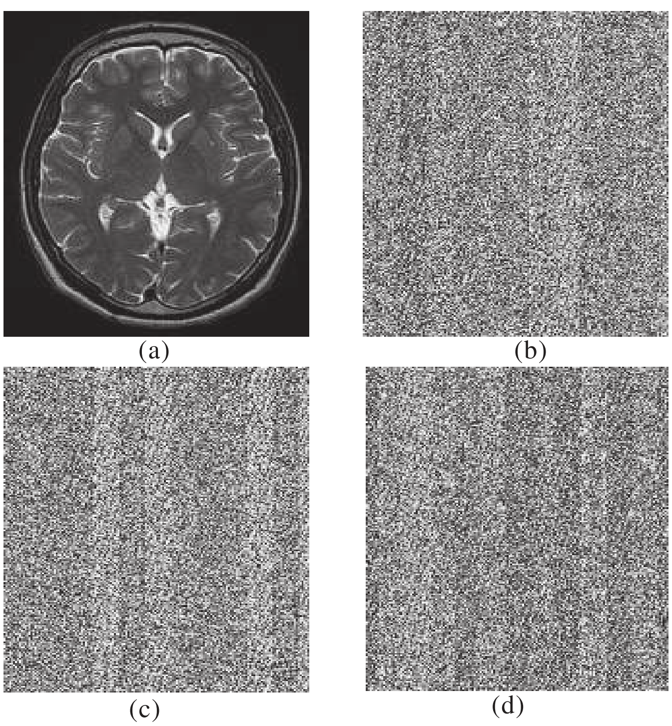

Figure 14. CT image Harns; (a) Decryption with the correct key; (b) Decryption with a 2-bit modified key; (c) Decryption with a 4-bit modified key; and (d) Decryption with 8-bit modified key.

4.2 Histogram Analysis

Plain images and encrypted images are differentiated with the pixel values. The pixel value positions of these images are examined and verified using the histogram analysis. Pixel values of the original image are in non-uniform and random positions in histograms[20]. To overcome the statistical attack the position of pixel values in cipher image is very important. Image balancing and placing the pixels in distributed and decentralized manner is essential to prove the randomness of the pixel positions. The pixel values are uniformly distributed in the histogram analysis diagram shown in Fig. 15- Fig. 17.

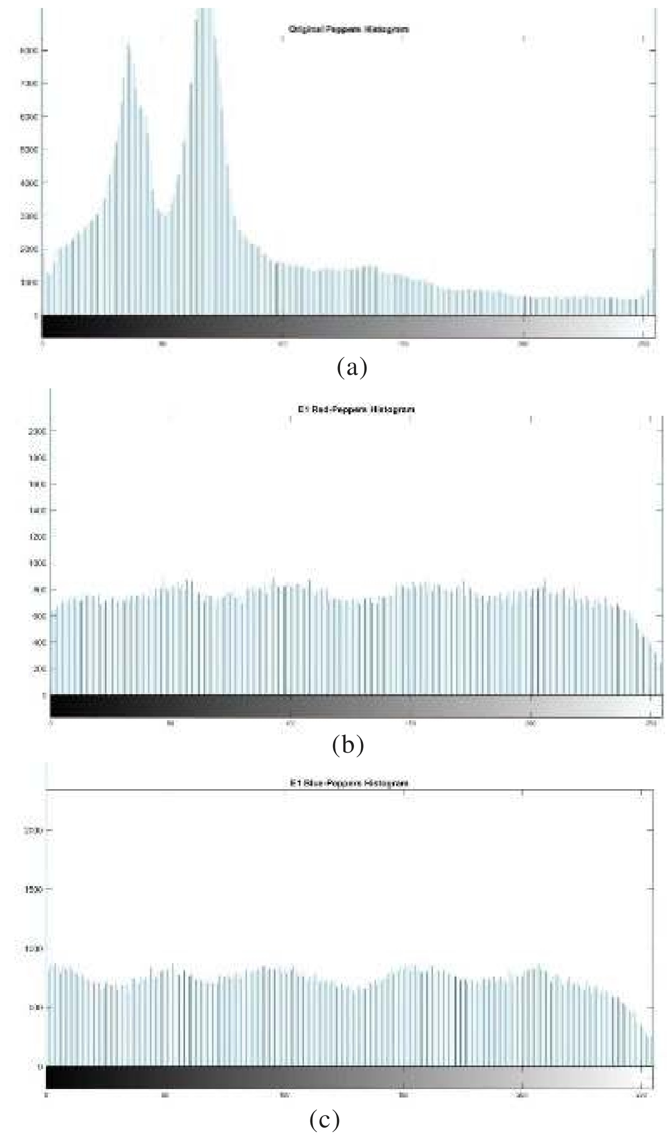

Figure 15. Histogram; (a) Vegetables plain image; (b) Encryption 1; and (c) Encryption 2.

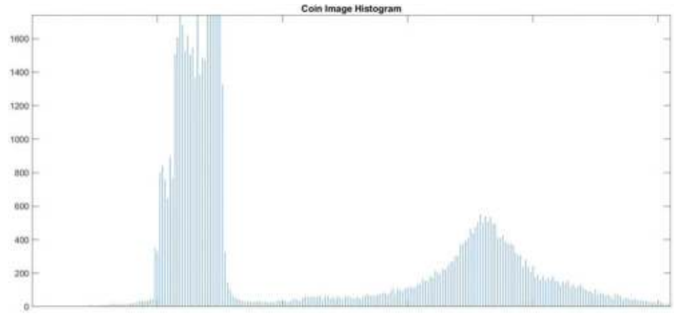

(a)

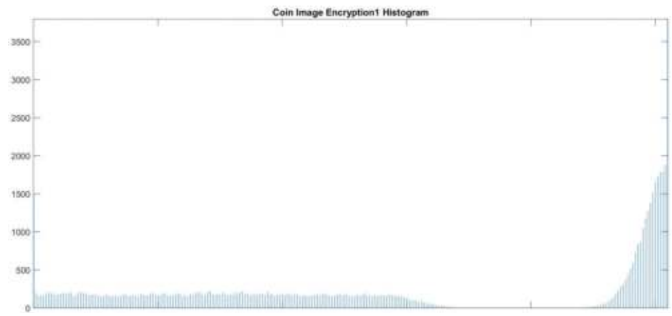

(b)

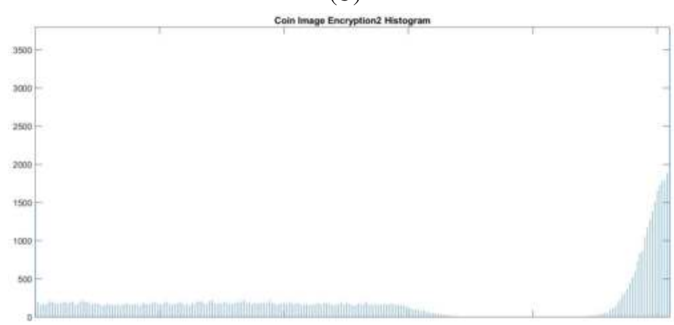

(c)

Figure 16. Histogram; (a) Dollar plain image; (b) Encryption 1; and (c) Encryption 2.

4.3 Correlation of Adjacent Pixels

The plain image pixel values have the high and close correlation with the neighboring pixel values. These high correlation increases the chances of statistical attack by the analyst. Hence the encryption process focuses on reducing the correlation values among the neighboring pixel values in the encrypted image to reduce the possibilities of the attacks. Eqn. 1 shows the correlation coefficient values of the encrypted image.

$$ek(i) = \frac{1}{n}\sum_{l=1}^{n} i_l$$

$$dk(i) = \frac{1}{n}\sum_{l=1}^{n} (i_l - ek(i))^2 \qquad (1)$$

$$c(i, j) = \frac{1}{n}\sum_{l=1}^{n} (i_l - ek(i)) - (j_l - ek(j))$$

Gray measurements of two nearby pixels are denoted by i and j values. Figure 18 - Fig. 24, shows the outputs of the correlation values of the plain and cipher images with respect to the coefficient values of Horizontal (H), Diagonal (D) and vertical (V). The output figures shows that the correlation values are decreased in the cipher images compared with the plain images. The correlation analysis output shown is shown in the Table 1.

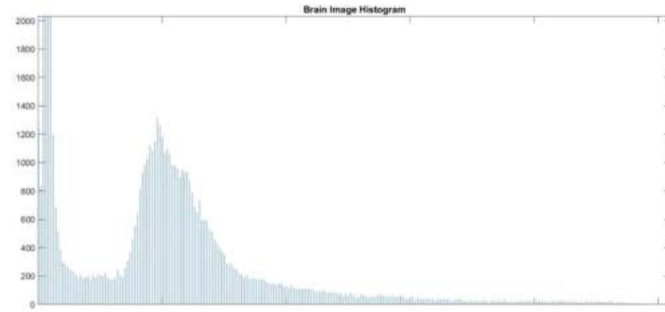

(a)

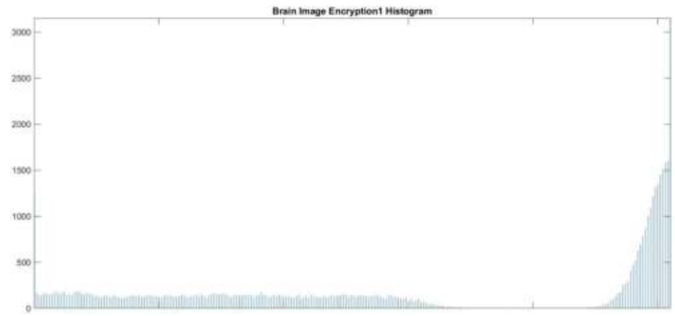

(b)

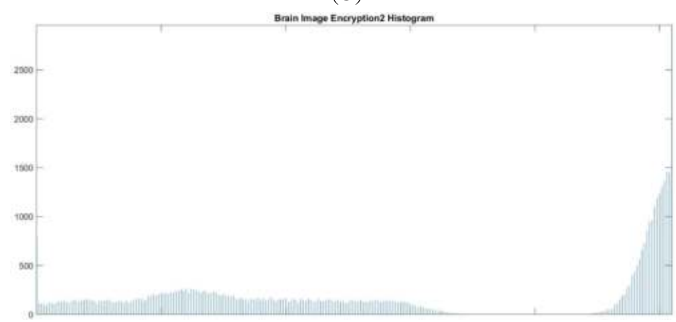

(c)

Figure 17. Histogram; (a) Harns plain image; (b) Encryption 1; and (c) Encryption 2.

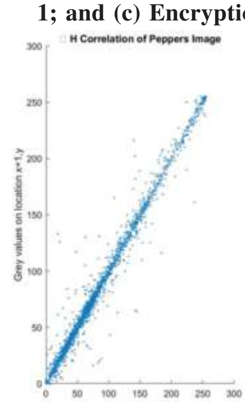

(a)

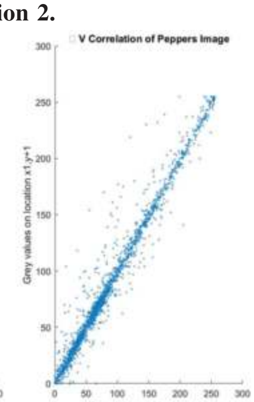

(b)

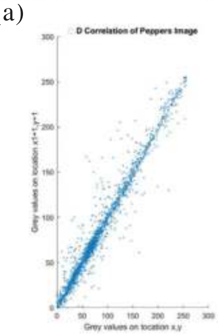

(c)

Figure 18. Vegetables plain Image; (a) H_Correlation; (b) V_Correlation; and (c) D_Correlation.

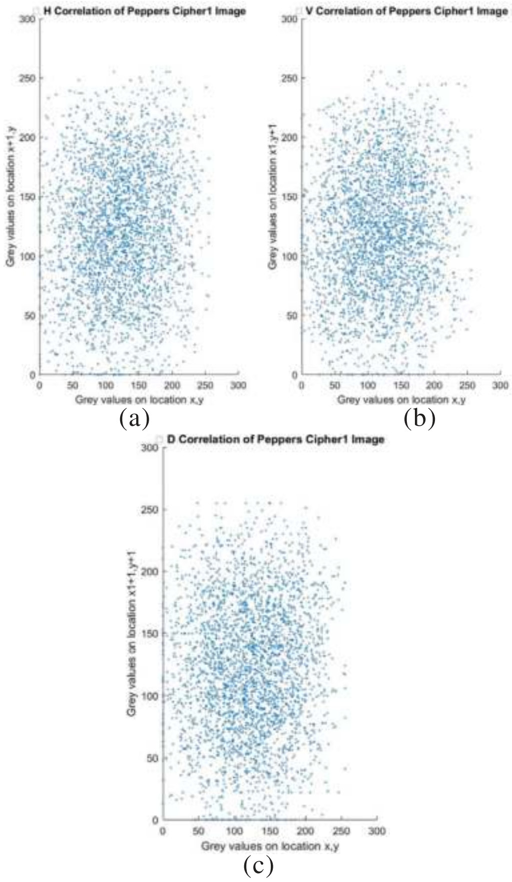

Figure 19. Vegetables cipher Image; (a) H_Correlation; (b) V_Correlation; and (c) D_Correlation.

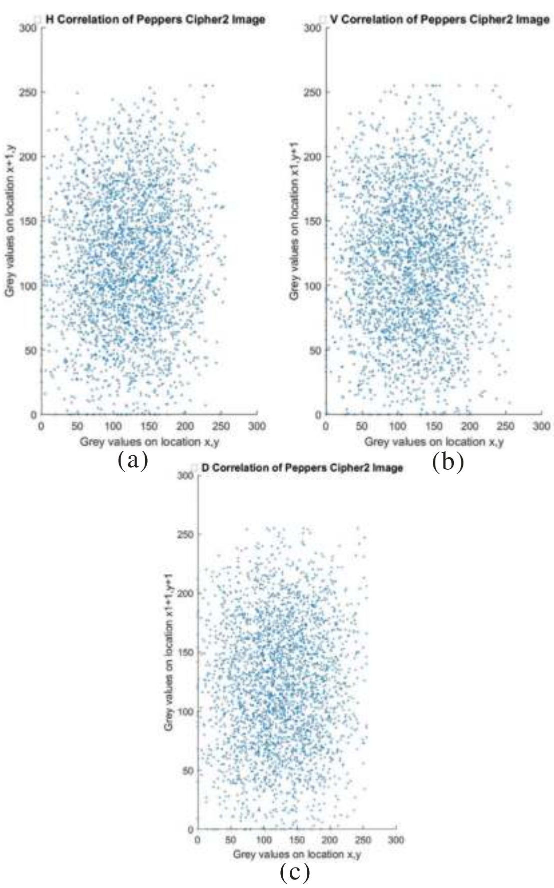

Figure 20. Vegetables cipher image 2; (a) H_Correlation; (b) V_Correlation; and (c) D_Correlation.

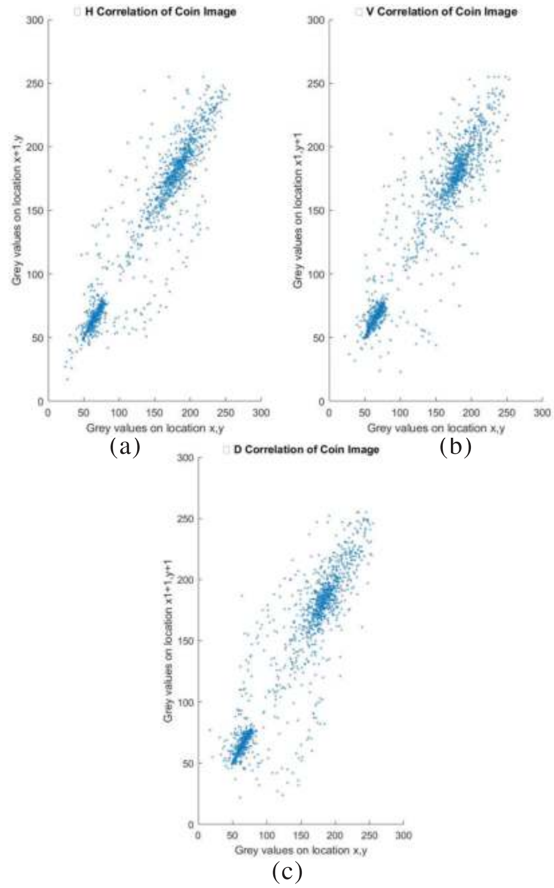

Figure 21. Dollar plain image; (a) H_Correlation; (b) V_Correlation; and (c) D_Correlation.

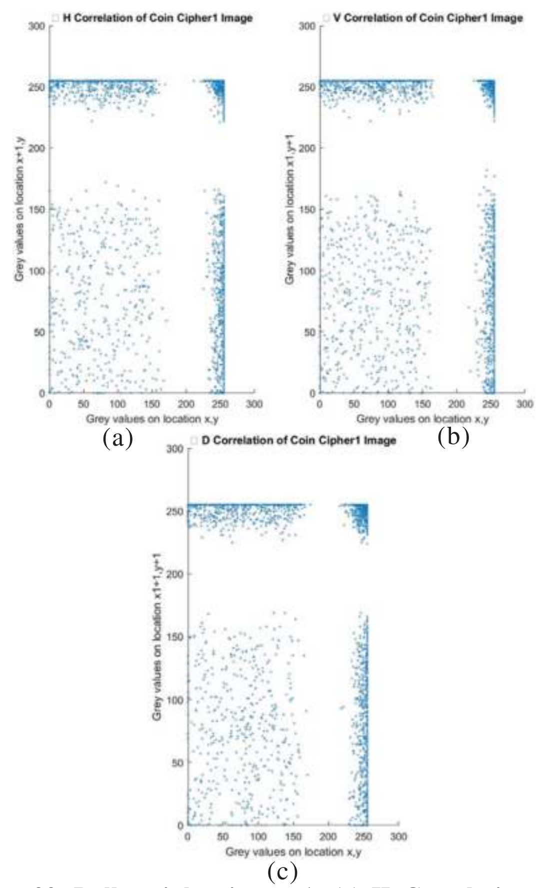

Figure 22. Dollar cipher image 1; (a) H_Correlation; (b) V_Correlation; and (c) D_Correlation.

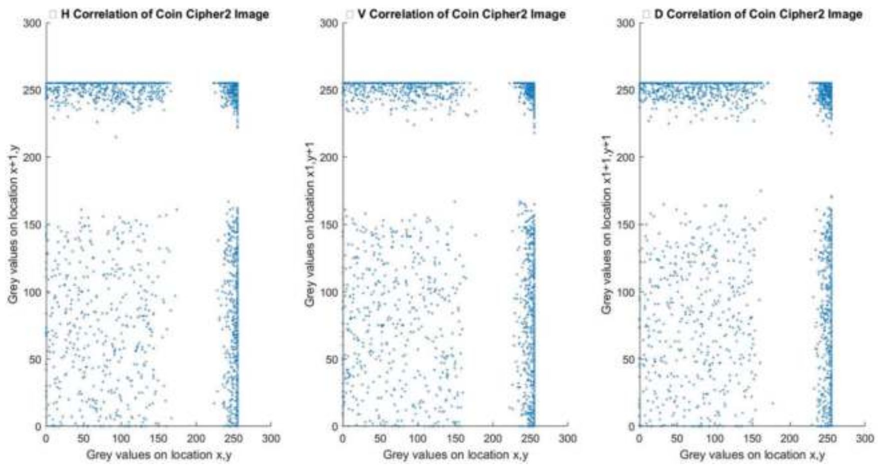

(a) (b) (c)

Figure 23. Dollar cipher image 2; (a) H_Correlation; (b) V_Correlation; and (c) D_Correlation.

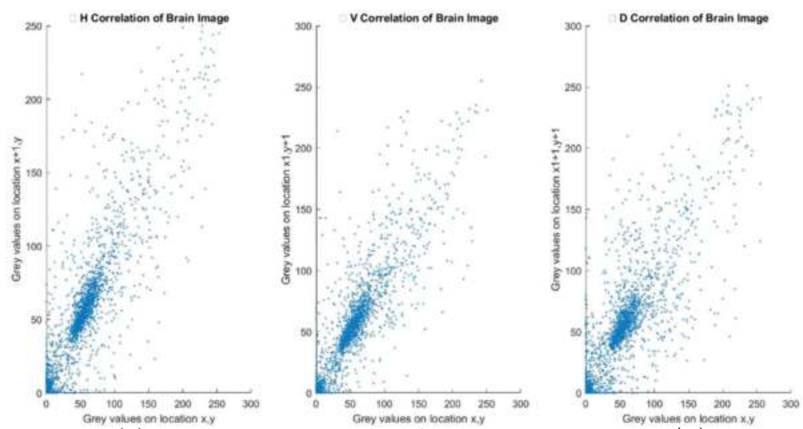

(a) (b) (c)

Figure 24. Harns plain image; (a) H_Correlation; (b) V_Correlation; and (c) D_Correlation.

Table 1. Results of correlation analysis

Image	Vegetables (512 x 512) color image			Dollar (1024 x 1024) gray scale image			Harns (220 x 275) CT image		
	Plain	**Cipher 1**	**Cipher 2**	**Plain**	**Cipher 1**	**Cipher 2**	**Plain**	**Cipher 1**	**Cipher 2**
Horizontal	0.9922	0.0510	0.2486	0.9752	-0.0056	-0.0292	0.8997	-0.0324	-0.0088
Vertical	0.9906	0.1166	0.2465	0.9716	0.0202	-0.0213	0.9078	-0.0096	-0.0023
Diagonal	0.9819	0.0763	0.4672	0.9571	0.0468	0.0165	0.8338	-0.0191	-0.0199

4.4 Information Entropy Analysis

The qualitative measures the cipher image randomness. The information entropy is used to find the randomness of the encrypted image. Eqn. 2 shows the formula used to calculate the information entropy value.

$$IE(r) = \sum_{i=0}^{2^n-1} l(r_x)\log_l \frac{1}{r_i} \qquad (2)$$

The images have 8 as an entropy value. Table 2 shows the information entropy values of the encrypted images. The values of the cipher images are close to their plain image entropy values that show the pixel loss of the cipher image is reduced and the Table 3 shows the efficiency of the proposed algorithm with respect to the information entropy.

Table 2. Information entropy

Image	Information entropy
Vegetables_Original	7.37
Vegetables_Encryption1	7.73
Vegetables_Encryption2	7.74
Dollar_Original	6.33
Dollar_Encryption1	5.66
Dollar_Encryption2	5.68
Harns_ Original	6.27
Harns_Encryption1	5.59

4.5 Differential Attack Analysis

The efficient cryptography algorithms have the features that the cipher images pixel values are sensitive to the plain images. Minor changes in the plain images must make the major changes in the cipher images in the efficient algorithm. The Unified Average Change Intensity (UACI) and Pixel Change Rate (NPCR) are the two parameters used in the differential analysis to identify and prove the efficiency of the proposed

Table 3. Differential attack analysis

Image	NPCR_Score	NPCR_dist	UACI_Score	UACI_dist
Vegetables	0.9941	0.9961	0.2317	0.3347
Dollar	0.8916	0.9961	0.3772	0.3346
Harns	0.8944	0.9961	0.3728	0.3346

Table 4. Comparison of the proposed method with other methods

Algorithm	Correlation analysis			Information entropy	Differential attack analysis	
	H	V	D		NPCR	UACI
M-AES[17]	-0.0039	0.0058	0.0023	6.5653	99.59	31.06
Holomorphic encryption[17]	-0.0007	0.0029	0.0020	6.5791	99.60	31.13
SIEA[15]	0.02728	0.03793	0.0709	6.6919	99.61	33.46
Proposed TIEA	-0.0347	-0.0231	-0.0109	7.00	99.61	33.46

algorithm in terms of the differential analysis. Eqn. 3 and Eqn. 4 shows the formula to find the NPCR and the UACI values.

$$N = \frac{\sum dk(i,j)}{m*n} \tag{3}$$

$$U = \frac{1}{m*n}\left(\sum \frac{ek1(i,j) - ek2(i,j)}{255}\right) \tag{4}$$

Plain images are encrypted with two different keys and the ek1 and ek1 are the different encrypted images. The row and column values are denoted by m and n. The results must be close to 1 to prove the efficiency of the algorithms. The proposed algorithm is resistant to the differential attack shown in the table 3. Quantitative measures are defined by the NPCR Score with almost 1 is good. Qualitative measure is calculated with the NPCR_pval value and Mean average is denoted with the NPCR_dist. In the other end UACI score should give very low value close to 0 and mean of UACI is denoted by UACI_dist.

The proposed TIEA algorithm performance is compared with M-AES[1], Holomorphic Encryption[17] and SIEA[15] and the results were tabulated in Table 4. The values in the table gives the clear ideas that the proposed algorithm performance is better and efficient compare with the existing algorithms. The TIEA algorithm is designed with the finite field concepts in the number theory and the dynamic cipher key generation model. Also, the algorithm processing time is less and the light weight procedures are followed compare with the standard algorithms.

5. CONCLUSION

The proposed TIEA algorithm is used to transfer the image data securely. During transmission, sensitive images such as medical-related scan images or X-Ray images security is very essential and data loss also to be reduced to assure the receiver that he received the correct image. To ensure the correctness of the image and to increase the randomness of the cipher image the proposed algorithm is designed efficiently. The algorithm performance is tested with various methods with variations in the input images such as black and white, grayscale, color, and CT Images. The algorithm follows the confusion and diffusion techniques to increase the randomness and complexity of an algorithm. The experimental results show that the proposed algorithm is performing well with various dimensions of images. The cipher key is given by the sender with dynamic size and the subkeys K1 and K2 are generated with fixed size which helps the encryption process to become lightweight. The complexity of the proposed algorithm is $O(n^2)$. The performance analysis shows the benefits of the proposed TIEA algorithm. Even though it is proposed for image encryption still the text data can be used by the sender to send the data securely.

REFERENCES

1. Alawida, M.; Samsudin, A. & Teh, J.S. A new hybrid digital chaotic system with applications in image encryption. *Signal Process*., 2019, **160**, 45–58. doi:10.1016/j.sigpro.2019.02.016
2. Paar, C. & Pelzl, J. Understanding cryptography: A textbook for students and practitioners. Springer, Heidelberg, 2009, 292p.
3. Pengfei, Fang.; Han, Liu. & Chengmao, Wu. A survey of image encryption algorithms based on chaotic system. *Vis Comput*., 2023, **39**, 1975–2003. doi:10.1007/s00371-022-02459-5
4. Zahmoul, R.; Ejbali, R. & Zaied, M. Image encryption based on new beta chaotic maps, *Opt. Lasers Eng*., 2017, **96**, 39-49. doi:10.1016/j.optlaseng.2017.04.009
5. Liu, H. & Wang, X. Colour image encryption using spatial bit-level permutation and high-dimension chaotic system. *Opt. Commun*. 2011, **284**(16), 3895–390. doi:10.1016/j.optcom.2011.04.001
6. Guan, Z.H.; Huang, F. & Guan, W. Chaos-based image encryption algorithm. *Phys. Lett. A*. 2005, **346**(1), 153–157. doi:10.1016/j.physleta.2005.08.006
7. Norouzi, B.; Mirzakuchaki, S.; Seyedzadeh, S.M. & Mosavi, M.R. A simple, sensitive and secure image encryption algorithm based on a hyper-chaotic system with only one round diffusion process. *Multimedia Tools App*., 2012, **71**(3), 1469–1497. doi:10.1007/s11042-012-1292-9

8. Guodong, Ye. & Kwok-Wo, Wong. An efficient chaotic image encryption algorithm based on a generalised Arnold map. *Nonlinear Dyn*. 2012, **69**(4), 2079–2087. doi:10.1007/s11071-012-0409-z
9. Alireza, Arab.; Mohammad, Javad, Rostami. & Behnam, Ghavami. An image encryption method based on chaos system and AES algorithm. *J. Supercomput*. 2019, **75**(10), 6663–6682. doi:10.1007/s11227-019-02878-7
10. Dhall, S.; Pal, S.K. & Sharma, K. A chaos-based probabilistic block cipher for image encryption. *J. King Saud Univ. - Comput. Inf. Sci.,* 2022, **34**(1), 1533-1544. doi:10.1016/j.jksuci.2018.09.015
11. Norouzi, B.; Mirzakuchaki, S.; Seyedzadeh, S.M. & Mosavi, M.R. A simple, sensitive and secure image encryption algorithm based on hyper-chaotic system with only one round diffusion process. *Multimedia Tools App*., 2014, **71**(3), 1469–1497. doi:10.1007/s11042-012-1292-9
12. Liu, H.; Kadir, A. & Liu, J. Color pathological image encryption algorithm using arithmetic over Galois field and coupled hyperchaotic system. *Opt. Lasers Eng*., 2019. **122**, 123–133. doi:10.1016/j.optlaseng.2019.05.027
13. Rukhin, A.; Soto, J.; Nechvatal, J.; Smid, M. & Barker, E. A statistical test suite for random and pseudorandom number generators for cryptographic applications, NIST Special Publications, Va, USA, 2010. 71p.
14. Dougherty, S.T.; Klobusicky, J. & Şahinkaya, S. An S-Box construction from exponentiation in finite fields and its application in RGB colour image encryption. *Multimedia Tools App*., 2023, **83**(14), 1-29. doi:10.1007/s11042-023-17046-6
15. Lavanya, M.; Joseph, Abraham.; Sundar, K. & Saravanan, S. Simplified Image Encryption Algorithm (SIEA) to enhance image security in cloud storage, *J. Multim. Tools and Appl.*, 2024, 1573-7721. doi:10.1007/s11042-023-17969-0
16. Adeniyi, A.E.; Abiodun, K.M. & Awotunde, J.B. Implementation of a block cipher algorithm for medical information security on cloud environment: Using modified advanced encryption standard approach. *Multimed Tools Appl*., 2023, **82**(10), 1-5. doi:10.1007/s11042-023-14338-9
17. Anushiadevi, R. & Amirtharajan, R. Design and development of reversible data hiding-homomorphic encryption & rhombus pattern prediction approach. *Multimed Tools Appl*., 2023, **82,** 46269–46292. doi:10.1007/s11042-023-15455-1
18. Ratan, R. & Yadav, A. Security analysis of bit plane level image encryption schemes. *Def. Scie. J*., 2021, **71**(2), 209-221. doi: 10.14429/dsj.71.15643
19. Teng, L.; Wang, X. & Xian, Y, Image encryption algorithm based on a 2D-CLSS hyperchaotic map using simultaneous permutation and diffusion. *Inf. Sci*., 2022, **605**, 71–85. doi:10.1016/j.ins.2022.05.032
20. Wei, Song.; Chong, Fu.; Ming, Tie.; Chiu-Wing, Sham. & Jun, Liu. A fast parallel batch image encryption algorithm using intrinsic properties of chaos. *Signal Process. Image Commun*., 2022, **102**, 116628. doi:10.1016/j.image.2021.116628

CONTRIBUTORS

Dr M. Lavanya is presently working as an Assistant Professor at School of Computing, SASTRA Deemed University, Thanjavur, Tamil Nadu. Her research interest focuses in Cryptography, cloud resource allocation, cloud security and operating system principles.
In this paper she has contributed in development of the encryption and decryption algorithm. She has been the content writer of this paper.

Dr K. Joseph Abraham Sundar is currently working as an Assistant Professor at the School of Computing, SASTRA Deemed University, Thanjavur, Tamil Nadu. He obtained his PhD in Computer Science Engineering from SASTRA Deemed University. His areas of interests are super resolution image reconstruction, text and object detection, image cryptography. In the current study he has carried out the performance analysis of the encryption and decryption algorithms. He has contributed significantly in the image processing aspects of the paper.

Dr S. Saravanan is presently working as an Assistant Professor at Department of Electronics and Communication Engineering, Srinivasa Ramanujan Centre, SASTRA Deemed University, Kumbakonam, Tamil Nadu.
In the current study he has done extensive literature survey in order to identify the merits and demerits of various encryption methods which has been a great support in this research work.

Defence Science Journal, Vol. 75, No. 1, January 2025, pp. 64-75, DOI : 10.14429/dsj.19180

A Study of Various Mitigation Strategies For RF Communications Blackout Phenomenon

S. Shankari[#,*], CH. N.P.V. Chandra Shekhar[#] and Gande Arun Kumar[$]
[#]*DRDO-Advanced Systems Laboratory, Hyderabad – 500 058, India*
[$]*Department of ECE, National Institute of Technology, Warangal - 506 004, India*
[*]*E-mail: shankaris.asl@gov.in*

ABSTRACT

In any aerospace application, the vehicle travelling in space, upon re-entry is subjected to high temperatures and high pressures. The matter surrounding the re-entry vehicle due to high temperature and pressure gets converted into the plasma state and results in high attenuation of electromagnetic signals. This phenomenon is called a Radiofrequency (RF) blackout. Radiofrequency blackout has critical implications during the reentry phase of space vehicles or missiles. In this paper, the RF blackout phenomenon is discussed with an emphasis on mitigation techniques. Shapes of the re-entry vehicle, higher frequency communication, electrophiles, magnetic windowing, and metamaterials have been discussed and compared. The comparison is performed with respect to weight, complexity, cost, and attenuation performance. Metamaterial-based mitigation technique has low design complexity, weight, cost, and attenuation performance and can provide minimum RF blackout time.

Keywords: ICBM; Telemetry; Mach; Metamaterials; RF blackout; Plasma

NOMENCLATURE

N : Nitrogen
O : Oxygen
H : Magnetic field intensity
E : Electric field intensity
j : Imaginary part of a component
ω : Angular frequency
Hz : Hertz
μ : Magnetic permeability
ε : Electric permittivity

1. INTRODUCTION

Humans have been using reusable re-entry vehicles for aerospace missions since 1969. Ever since then, scientists have encountered and have been battling the RF blackout hurdle during the re-entry phase of the flight. Specifically, when a re-entry vehicle penetrates the earth's atmosphere with high speeds such as Mach 19, the atmosphere around it, especially in front of the vehicle experiences high pressures and gets highly compressed, forming a shock wave around it[1]. The highly compressed gas also experiences high temperatures resulting from the altitude of the atmosphere and friction against the re-entry vehicle. This results in the generation of high heat around the vehicle. The high heat and compression will ionize the gases in the atmosphere within the shock region eventually forming electron plasma as shown in Fig.1[2].

The electron plasma has a characteristic which is extremely disadvantageous to the re-entry vehicle. The electron plasma attenuates electromagnetic signals propagating through it[3]. These electromagnetic signals consisting of various radio frequencies which have the data of copious systems such as tracking, telemetry, voice communications, and Global Positioning Systems. The attenuation of the RF signals is directly proportional to the thickness of the plasma sheath. As the density increases, attenuation increases. An illustration is shown below which helps in understanding the gravity of the problem.

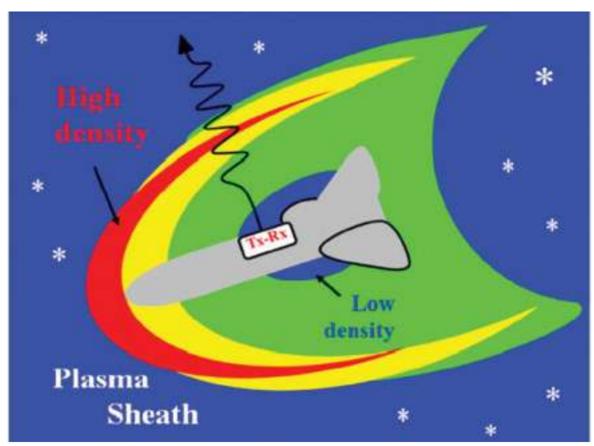

Figure 1. Plasma sheath during re-entry phase.

It can be observed that the density of the plasma sheath encompassed around the re-entry vehicle increases as the thickness increases. The electron plasma affects the RF signals in an adverse manner resulting in a complete loss of communication with the re-entry vehicle and even a loss of GPS acquisition.

Received : 13 September 2023, Revised : 23 August 2024
Accepted : 21 October 2024, Online published : 10 January 2025

The RF blackout can last from 50 sec. to 12 min. depending upon the speed and flight trajectory of the re-entry vehicle[4]. Various approaches to reduce the RF blackout issue have been proposed resulting in varying magnitudes of success. Specifically, modifying or reshaping the nose of the re-entry vehicle to generate less friction while penetrating the atmosphere; switching to higher frequencies of operation which can perforate through the electron plasma; instead of directing the RF signals from the vehicle to the ground station, communication is established with re-entry vehicle using a satellite as an intermediary. Another approach is the use of coolants. Decreasing the outer layer temperature of the vehicle using coolants prevents the atmosphere in the shock wave region from undergoing high temperatures, eventually restraining the formation of plasma or ionization of gases into plasma[5].

The paper presents the plasma formation during re-entry phase of the vehicles, it also discusses various re-entry vehicles and their advantages and disadvantages, various mitigation techniques have been discussed. The mitigation techniques are based on shaping, using higher frequencies, electrophiles liquid quenchants, magnetic windows, and metamaterials. The paper compares the different mitigation techniques with respect to RF attenuation, RF blackout time, payload weight and complexity.

2. PLASMA SHEATH FORMATION ON THE RV

The re-entry phase of every flight trajectory is the most crucial and nail-biting phase. During this phase, the vehicle descending from space pierces through the atmosphere possessing high kinetic energy levels. This kinetic energy compels the re-entry vehicle to radiate heat energy in inordinate proportions. These high energy levels of enthalpy excite the air around the vehicle to ionize. Ionization converts air into plasma and forms a thick plasma sheath around the re-entry vehicle. This very plasma sheath attenuates the RF signals emerging out or entering the re-entry vehicle. Not only during the re-entry phase, but also during the entry (take off) and landing approach. The vehicle inevitably experiences an RF blackout phenomenon during re-entry, which leads to complete communications, telemetry and tracking, and GPS acquisition loss[6].

To overcome the RF blackout issue, the properties of the plasma must be comprehensively studied. At atmospheric pressure, the nitrogen and oxygen molecules start to dissociate at 4000K and 2000K respectively, and at temperatures 9000K and above, nitrogen and oxygen undergo the ionization effect. In between 4000 K, and 6000 K, the *NO* gets ionized to form NO^+. Such ionization of different atmosphere elements tends to form a plasma envelop around the re-entry vehicle. At higher altitudes, the atmospheric pressure drops, consequently, the temperatures of ionization and dissociation also decrease. The following reactions take place to ionize the atmospheric elements[7].

$N_2 + M \rightleftharpoons N + N + M$

$N_2 + e^- \rightleftharpoons N + N + e^-$

$O_2 + M \rightleftharpoons O + O + M$

$NO + M \rightleftharpoons N + O + M$

$NO + O \rightleftharpoons N + O_2$

$N_2 + O \rightleftharpoons NO + N$

$N + N \rightleftharpoons N_2^+ + e^-$

$O + O \rightleftharpoons O_2^+ + e^-$

$N + O \rightleftharpoons NO^+ + e^-$

$N + e^- \rightleftharpoons N^+ + 2e^-$

$O + e^- \rightleftharpoons O^+ + 2e^-$

$NO^+ + O \rightleftharpoons N^+ + O_2$

$O_2^+ + N \rightleftharpoons N^+ + O_2$

$O^+ + NO \rightleftharpoons N^+ + O_2$

$O_2^+ + N_2 \rightleftharpoons N_2^+ + O_2^+ + N_2 \rightleftharpoons N_2^+ + O_2 O_2$

$O_2^+ + O \rightleftharpoons O^+ + O_2$

$NO^+ + N \rightleftharpoons O^+ + N_2$

$NO^+ + O_2 \rightleftharpoons O_2^+ + NO$

$NO^+ + O \rightleftharpoons O_2^+ + N$

$O^+ + N_2 \rightleftharpoons N_2^+ + O$

$NO^+ + N \rightleftharpoons N_2^+ + O$

$N_2 + N^+ \rightleftharpoons N_2^+ + N$

$M = N_2, O_2, NO, N_2^+, O_2^+, NO^+, N^+, O^+, N, O$

As these reactions occur, the atmospheric air is converted into ion-dense plasma filled with N_2^+, O_2^+ ions. The concentration of these ions is very low, but the density of free electrons liberated due to the chemical reactions is sufficiently high enough to attenuate the incoming or outgoing RF communications signals. But contrary to popular belief, the blackout is not caused by the factor of high-density electron plasma; instead, it is caused by high frequency of oscillations of the electrons. This concept can be thoroughly understood by studying Maxwell's Eqn. describing the propagation of electromagnetic waves in free space and the interaction of an electromagnetic wave with plasma governed by Maxwell's Eqn.[8]:

$$\nabla \times H = j\omega\varepsilon_v E + Nev \quad (1)$$

$$\nabla \times E = -j\omega\mu_v H \quad (2)$$

$$\nabla \cdot E = \frac{ne}{\varepsilon_\upsilon} \quad (3)$$

$$\nabla \cdot H = 0 \quad (4)$$

After solving the above four Eqn., the following expression is obtained which represents plasma by a dielectric permittivity.

$$\varepsilon = \varepsilon_\upsilon \left(1 - \frac{\omega_P^2}{\omega^2}\right) \quad (5)$$

This Eqn. can also be written as:

$$\frac{\varepsilon}{\varepsilon_\upsilon} = K_o = 1 - X$$

where

$$7X = \frac{\omega_P^2}{\omega^2}$$

The above Eqn. demonstrate that, in a plasma, the wave propagation is similar to that in any ordinary dielectric medium, provided X is less than unity i.e., $\omega > \omega_p$. But if the X is more than unity i.e., $\omega < \omega_p$ then plasma offers attenuation to the electromagnetic signals.

However, the concepts of plasma sheath formation as a combination of chemical reactions and thermodynamic processes are still complex to understand. Furthermore, the rate at which these thermodynamic and chemical reactions take place changes abruptly in a continuous manner, making it very hard to find a pattern to study systematically. Therefore, a comprehensive study of plasma characteristics using analytical techniques is not possible. Hence, plasma parameters are evaluated experimentally using different sensors on board at the re-entry flights.

The plasma sheath enveloping a typical ICBM re-entry vehicle has four flow regions, as shown in Fig. 2[9]. The stagnation region is the first region where the impact from the angle of attack takes place. This region comprises high-temperature and high-pressure gases and is bounded by a thin boundary layer and shock region.

Consequently, extreme plasma conditions arise in this region. Therefore, antennas are usually not mounted near the stagnation region. Instead, they are placed in the aft body region, where the environmental conditions are comparatively tolerant.

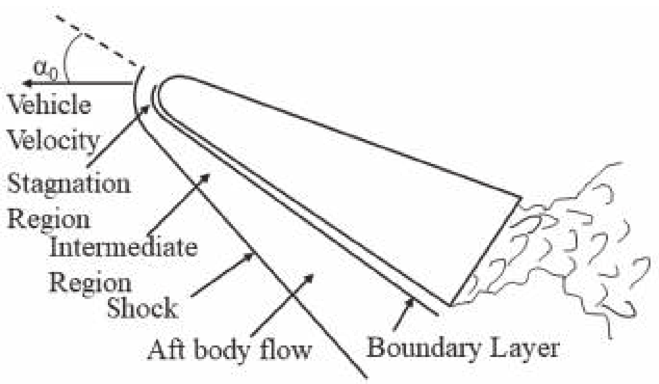

Figure 2. Flow regions of ICBM payload during re-entry phase.

The Intermediate region consists of gases in a non-equilibrium state. The plasma conditions in this region are not as strong as in the earlier region but dire enough to cause total RF blackout from the antennas situated on the aft body.

The aft body region consists of gases that get ionized by entering through the boundary of the shock region. Factors such as the shape of the re-entry vehicle and the angle of attack determine the electron density of the plasma. The conditions of plasma in the aft body region are not as extreme as in the region of the intermediate stage. The boundary layer is just below the aft body flow region. Generally, this layer is very important in terms of ionization. The typical plasma formation starts to take place along the surface of the re-entry vehicle i.e., along the boundary layer region. The ionization in this region begins to take place at the altitude of 80 km and starts to rapidly grow along the surface of the re-entry vehicle.

The region behind the re-entry vehicle is called the wake region, where a prominent rate of recombination of ions and electrons takes place. Generally, the region is not affected by plasma and does not experience RF communications blackouts.

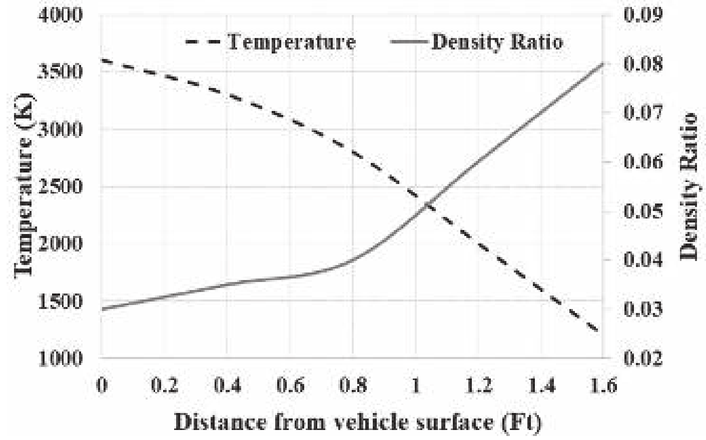

Figure 3. Variation of temperature and relative air density at antenna location.

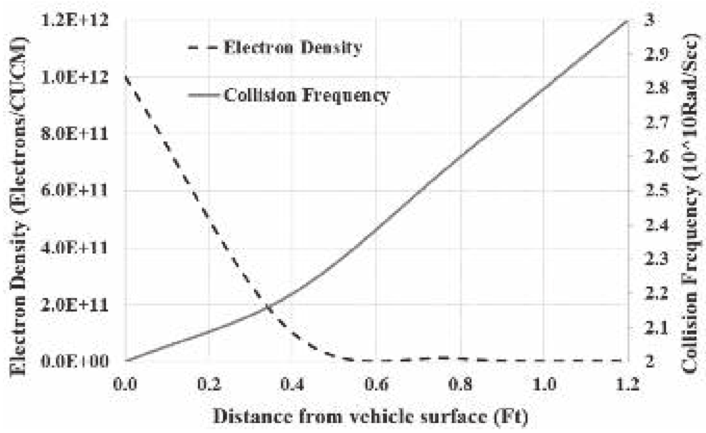

Figure 4. Variation of electron density and collision frequency at antenna location.

As the re-entry vehicle descends from outer space into the earth's atmosphere, the air surrounding the re-entry vehicle gradually turns into plasma as the re-entry vehicle pierces the atmosphere. The plasma attains the highest frequency of oscillation and density somewhere around the middle of the descent journey. Consequently, due to the decreasing velocity of the re-entry vehicle and the high electron densities at lower altitudes, the plasma again gradually gets converted back into air gradually. The conversion of plasma back to air occurs as the electrons of the plasma collide with neutral particles of air. A graphical representation of the changes in temperature during the descent phase and the relative air density at the antenna location forming radially outwards against the distance from the re-entry vehicle surface is shown in Fig. 3 while Fig. 4 shows the graphical representation of the changes in the electron density of the plasma and collision frequency rate of electrons with neutral particles against the distance from the re-entry vehicle surface[10].

3. TYPES OF RE-ENTRY VEHICLES

This section discusses different re-entry vehicles, which form a pre-requite for mitigation approaches.

3.1 Ballistic Re-entry Vehicles

The ballistic re-entry vehicle, as shown in Fig. 5[11], is

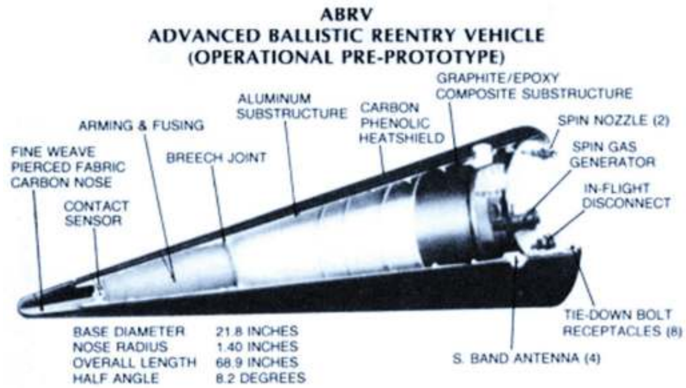

Figure 5. Typical re-entry vehicle.

Figure 6. NASA space shuttle orbiter re-entering Earth with a 40° angle of attack.

categorised into two types, i.e., Blunt nose and sharp nose, based on the physical appearance and the construction of the re-entry vehicle. A blunt nose re-entry vehicle is surrounded by a strong shock wave with a large circumference, which can convert large volumes of air flowing and present within the shock region into a large volume of plasma upon which the sheath properties are characterized. Whereas the sharp-nose re-entry vehicle is enveloped by a weak, thin shock wave which can convert the air into a plasma medium only along the boundary layer region by viscous dissipation of the atmosphere engulfed inside the shock wave, which determines the sheath properties.

Another fascinating characteristic of the blunt-nosed and sharp-nosed re-entry vehicles is that the blunt-nosed re-entry vehicle has the potential to produce high levels of electron densities and a large thickness of plasma sheath on the re-entry vehicle, whereas the sharp-nosed re-entry vehicle has a void between the shock wave region and boundary layer along the surface of the re-entry vehicle.

3.2 Blunt Re-entry Vehicles

This class of re-entry vehicles is studied by taking two subjects into consideration. The first subject is the NASA shuttle orbiter, as shown in Fig. 6[12]. The shuttle orbiter leaving the international space station, re-enters the atmosphere at very high altitudes with high angles of attack with an intent to decelerate and not get affected by the aerodynamic heating. A 40° angle of attack is maintained by the shuttle orbiter during the re-entry phase. After a calculated descent, the shuttle is levelled back into normal flight mode for landing operation

The second subject under study is RAM C – III, as shown in Fig. 7[13]. The RAM C – III vehicle is the payload of spacecraft Project RAM. A series of tests were conducted by NASA in 1972 using a RAM C – III vehicle to understand the RF blackout phenomenon. This re-entry vehicle recorded the beginning of the blackout phenomenon for the S-Band antenna at 77 km from the ground and recorded the dissipation of the phenomenon at 24 km from the earth's surface.

During this descent, the antenna was placed in the re-entry vehicle at 0.22 meters from the tip of the nose. Another test was carried out by varying the frequency bands of operation of the antenna in the re-entry vehicle[14].

S, X and K_a bands are subjected to the blackout phenomenon and are carefully studied. An antenna positioned

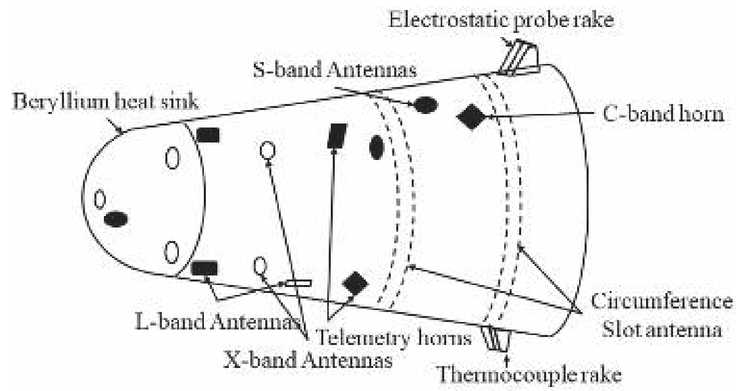

Figure 7. Various antennas on the surface of a re-entry vehicle.

at 0.22 mtr from the tip of the nose of the re-entry vehicle, experienced the onset of 20 % attenuation of the RF signals from 77 km to 69 km when X band frequency of operation is used. Whereas the K_a band frequency of operation realized the onset of 20 % attenuation at 38 km, thus, giving an advantage of 39 km difference when compared with S-Band This shifting of frequency from SS-band to K_a band reduced the duration of this phenomenon to only 4 sec. instead of 28 sec.[15].

3.3 Sharp–Tipped Slender Cones

In a sharp-nosed re-entry vehicle, as shown in Fig. 8[16], when descending from space, the air offers friction and heats up the re-entry vehicle, causing the heat shield to erode and introduce these impurities into the atmospheric flow. A weak, oblique shock wave is formed around the re-entry vehicle during the descent and the air engulfed in between the shock wave and the boundary layer doesn't get ionized due to insufficient temperatures[17]. A laminar flow is formed and maintained on the boundary layer at very high altitudes and is thin when compared with the RF wavelength which beneficially decreases the attenuation[18].

At 22 km altitude, a transition takes place from laminar flow to turbulent flow at the boundary layer, causing the air temperature to increase to its peak value and also extending the thickness of the boundary layer region by fourfold. This results in the rapid increase of the attenuation of RF communications to a maximum extent over the entire flight path[19].

3.4 Unpowered Lifting Glide Vehicle

To study this class of re-entry vehicles, an Apollo

Figure 8. Sharp tipped re-entry vehicle.

Figure 9. Re-entry of Apollo capsule.

Figure 10. X – 43 re-entry flight.

capsule as shown in Fig. 9[20], during descent phase is taken into consideration. After a series of flight tests, NASA arrived at the conclusion that, at an altitude of 80 km, the blackout phenomenon turned up and lasted to 49 km, resulting in 16 min. of total blackout. The capsule that re-entered with a 40-degree angle of attack and sustained blackout for S-band antennas that are mounted on the belly of the re-entry vehicle at high altitudes are subjected to strong degrees of ionization. A pragmatic solution to counter the blackout and keep the communications without any interruptions is by employing the antennas located above the crew compartment to transmit to the satellite constellations and relay back those signals to ground stations by means of Tracking & Data Relay Satellite System (TDRSS)[21]. After successive flight tests, NASA was able to decrease the blackout duration to 15 min. i.e., by 1 min. by decreasing the angle of attack from 40° to 20°[22].

3.5 Powered Air Breathing Lifting Vehicle

In 2004, NASA test launched an air breathing propulsion vehicle having capability of hypersonic cruising under X – 43 programs. The X – 43 as shown in Fig. 10[23], was launched prior to engine ignition at hypersonic speeds from the nose of the Pegasus rocket. The X – 43 A achieved speed of Mach 7 at 30 kms. The X – 43 had sharp edges and drifts with zero angle of attack, making it almost immune to the blackout problem. If the vehicle achieves higher Mach numbers, there is a possibility of the blackout problem[24].

3.6 Commercial Cargo "Slightly Lifting" Ballistic Re-entry Vehicle

An example of this class is K – 1 fully recoverable two stage vehicle is shown in Fig. 11[25]. Upon launch, after the first stage separation, the second stage enters the orbit, delivers the payload, re-enters the earth's atmosphere and is eventually recovered by employing parachutes at Mach 2.5. The re-entry vehicle is blunt nosed cylinder, terminated with a large flare. During re-entry, no flow fields were formed and detected, hence no studies have been made about the ionization distribution[26].

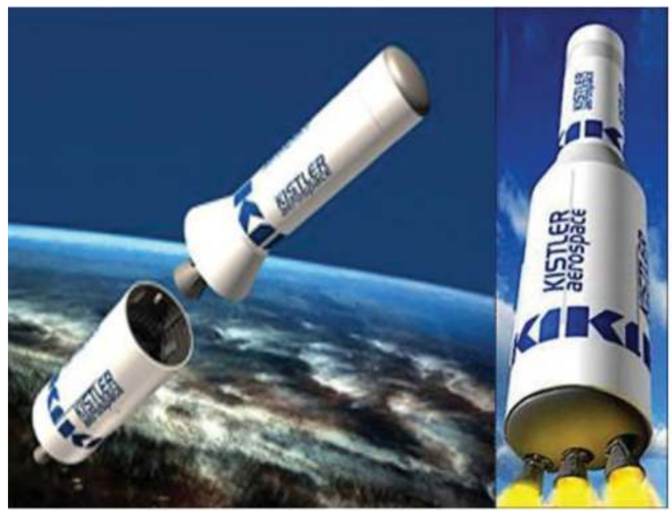

Figure 11. K–1 rocket booster lauch and seperation.

3.6.1 Comparison of Blackout Trajectories for Four Re-entry Vehicle Classes

Comparison of trajectories encompassing the blackout phase for four re-entry vehicle class is illustrated in Fig. 12[27]. They are space shuttle orbiter, RpK OV, RAM C and sharp-tipped RVs. The trajectory of sharp RV which lacks blackout phase is an ideal condition. After multiple flight tests, it has been observed that blackout is inevitable, irrespective of the vehicle class. The zone of interest in this comparison is the difference in the trajectories of RpK OV and Space shuttle, which projects that the OV maintains comparatively higher speeds at each consecutive altitude. The space shuttle experiences an inordinate amount of blackout time (16 min.) when compared with RpK OV (1 min.), which arises from the fact that the space shuttle travelling in space re-enters into the earth's atmosphere maintaining a 40° angle of attack to decelerate at high altitudes, reduce the heat transfer and protect itself from thermal ablation effects. Meanwhile K – 1 predominantly follows a supersonic ballistic trajectory, resulting in only one min. of re-entry phase where blackout recovery is possible.

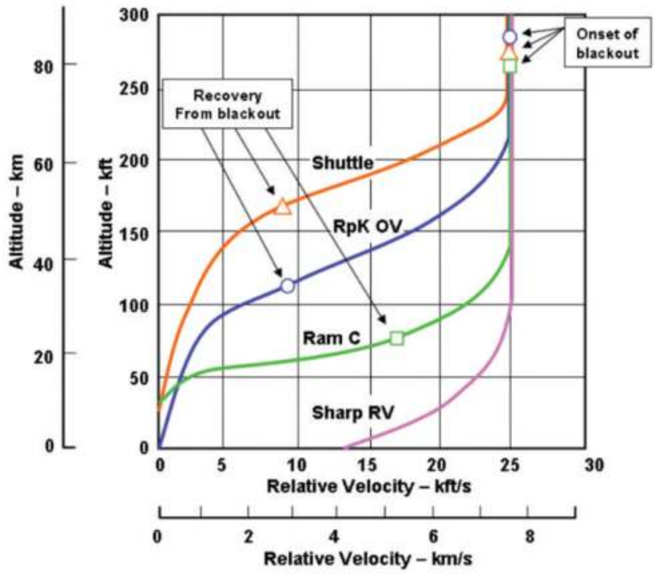

Vehicle	Blackout duration, minutes
Shuttle	16
RpK OV	1
Ram C	0.5
Sharp RV	0

Figure 12. Blackout trajectories for four class re-entry vehicles.

Although onset of the blackout for all vehicles under consideration starts at almost equal altitudes, but the offset is different for each vehicle depending on the re-entry vehicle's aerodynamic shape, re-entry velocity and angle of attack. The factors that determine the blackout are all interdependent such as, the temperature of the flow field depends on the re-entry velocity, and the degree of ionization in the flow depends on the temperature[28].

4. BLACKOUT MITIGATION TECHNIQUES

Ever since Yuri Gagarin in 1961 circled the earth and re-entered, humans have been trying numerous strategies to eliminate or mitigate the blackout effect on the re-entry vehicle. There are eight mitigation techniques that have been identified, studied, simulated and tested as potential solutions for the blackout phenomenon. These mechanisms are switching to aerodynamic shaping of the re-entry vehicle, higher frequencies, electrophilic liquid quenchants injection into plasma sheath, magnetic field application, communicating with a satellite and metamaterial antennas. These approaches will be discussed in detailed manner in the next section[29].

4.1 Aerodynamic Shaping

To reduce the thickness of the plasma sheath as much as possible, the aerospace R&D and defence organisations have espoused aerodynamic shaping designs. The plasma sheath forming around a sharp tipped re-entry vehicle is very thin when compared with blunt nose re-entry vehicle. But the disadvantage of sharp tipped vehicle is that, reduced payload capacity, however it gives a relief to the aerodynamic heating problem[30].

A potential design of this technique is shown in Fig.13[31]. In this prototype, an antenna located on top of a slender, sharp probe protrudes from the front of the re-entry vehicle and extends outside of the shock wave region of the blunt

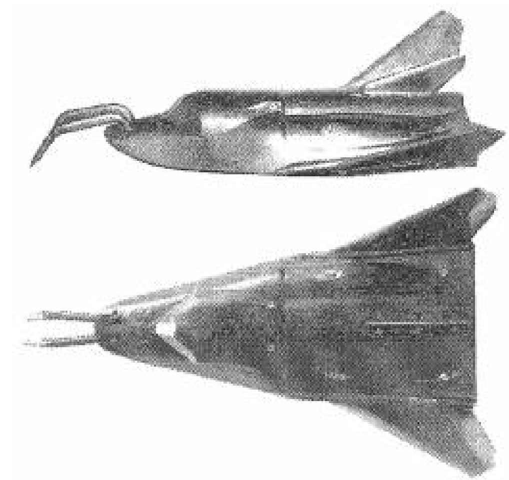

Figure 13. Sharp probe projecting ahead of the blunt nose vehicle shock bow region.

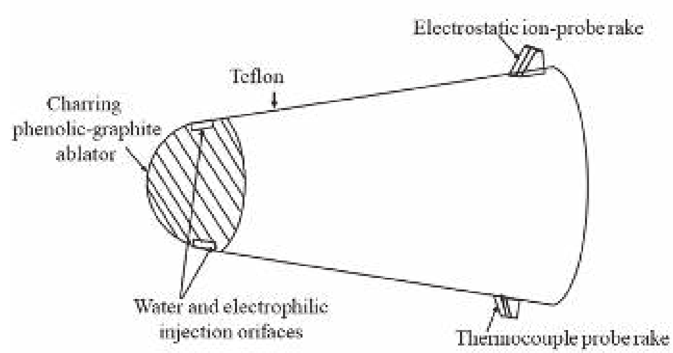

Figure 14. RAM C – III flight re-entry vehicle.

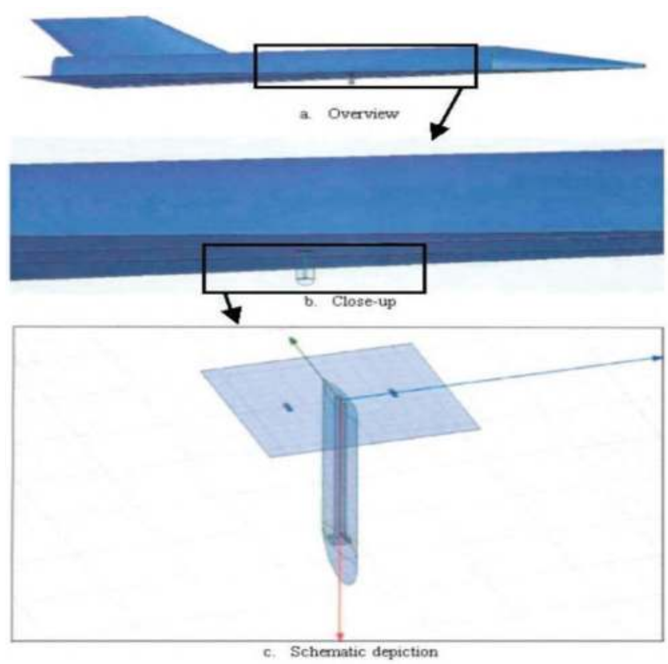

Figure 15. Blade configuration.

nose re-entry vehicle. Experimental evaluation and Finite Element Analysis (FEA) of the re-entry vehicle, pertaining to heat transfer conditions, structural simulations, aerodynamic studies and location of the antenna on the re-entry vehicle, for obtaining adequately low electron density plasma flowing aft. The probe is intentionally manufactured with porous sintered metal that can store cold gas for survival and is designed to be a sharp-nosed cone. Another example of aerodynamic shaping, as shown in Fig.14 and Fig.15[32], is done with RAM C. In 1970, NASA has tested this approach on RAM C-III. Two blades were attached on the either side of the re-entry vehicle. These blades contain electrodes for measurement purposes. One blade contains electrostatic ion probes, that are used to measure the electron density of the plasma and another blade contains thermocouple which measures temperature in the boundary layer. The blades are designed in such a manner that they did not disturb the laminar flow distribution. The blade was also designed to bear a slot antenna at the end of the blade or in the either of the two faces. When the plasma sheath is formed around the re-entry vehicle, the blades are protruded out of the re-entry vehicle and extended beyond to extent that the electrodes measure negligible electron density. Once the tip of the blade which contains a slot antenna or a microchip antenna, is protruded outside the plasma sheath, which essentially reduces attenuation of the RF signals[33].

When the re-entry vehicle reaches lower altitudes, due to the increased electron neutral collisions, the blackout phenomenon gradually perishes. As the attenuation is decreased, the blades are retracted back into the re-entry vehicle. According to the tests conducted by NASA using RAM C III, at 47 Kms the tip of the blades were only 6 centimetres away from the surface of the re-entry vehicle and at 30 Kms, the plasma sheath started to perish gradually due to the electron neutral collisions.

4.2 Higher Frequencies

The attenuation of the RF signals takes place when the operating frequency is less than the plasma frequency. To decrease the attenuation and resume the communications, the operation must be switched to a higher frequency mode which is greater than the peak plasma frequency. This concept is better expressed using the below expressions[34].

$f_o < f_P$ ⇒ Exponential decay in the transmission of the signal

$f_o = f_P$ ⇒ 100 % reflection of the signal

$f_o > f_P$ ⇒ 100 % transmission of the signal

The following graphs are the simulated results of the plasma frequency along the re-entry phase, against the operating frequency to calculate the attenuation offered by the plasma.

It can be comprehended from the graphs as shown in Fig. 16, Fig. 17, and Fig. 18[35] that as the operating frequency band is shifted to a higher mode, the attenuation offered by the plasma is decreased. Although the attenuation is reduced, this does not imply that the RF communications are resumed[36]. It can be only perceived that the communications are still distorted beyond recognition. For the RF communications to be completely restored with good quality, it is necessary that the operating frequency should be higher than the plasma frequency. However, this method of opting for higher frequencies introduces a snag[37]. As the operation mode is switched to higher frequencies, the power requirement is also increased. Consequently, the cost of securing and installing huge batteries in large quantities and other various equipment makes this technique prohibitively expensive. Another disadvantage is that by increasing the number of equipment, the weight of the payload is increased, decreasing the vehicle's range.

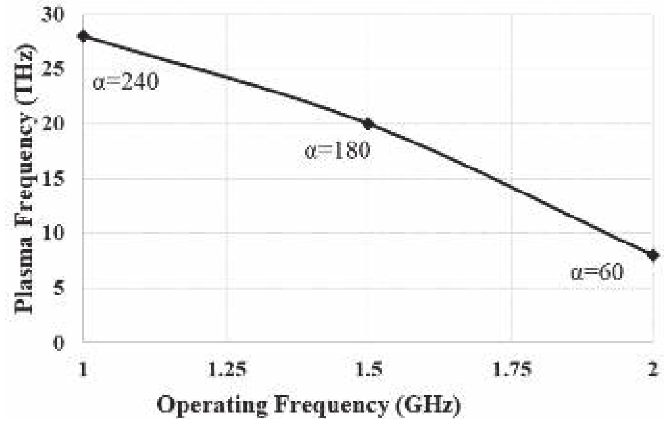

Figure 16. L–Band operating frequency (vs) Plasma frequency.

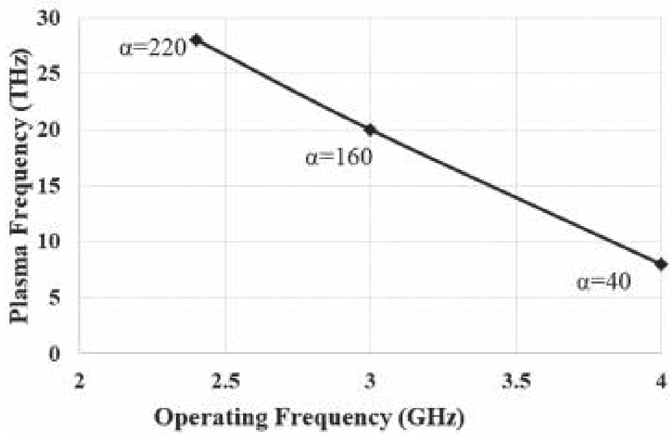

Figure 17. S–Band operating frequency (vs) Plasma frequency.

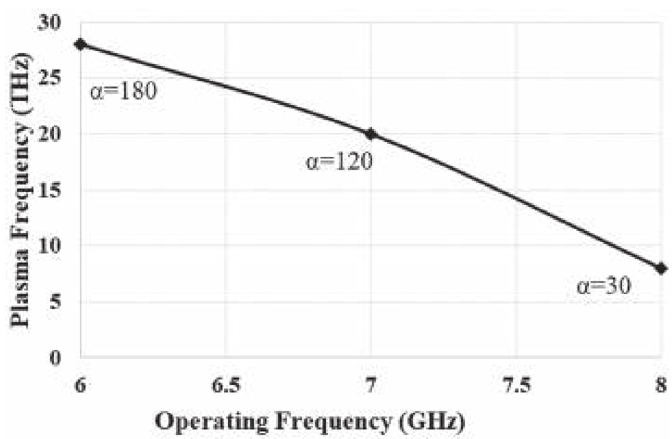

Figure 18. C–Band operating frequency (vs) Plasma frequency.

4.3 Quenchants/Electrophiles

The high temperature produced by the friction on the surface of the re-entry vehicle ionizes the air and converts it into plasma. By decreasing this temperature, the blackout issue can be brought under control. Releasing electrophilic molecules into the atmosphere which immediately combine with the free electrons of the plasma and form negative ions. This process significantly lowers the temperature of the atmosphere, thus resulting in a decrease in the plasma frequency. Theoretical research suggests that injecting a foreign dust particle of the size of a micrometer into the plasma would result in lowering the electron density and, consequently, the plasma frequency. Experiments in the laboratories have proven that sulfur hexafluoride, carbon dioxide, molecular oxygen, and nitrous oxide are useful electrophiles[38].

Now the question arises, as to which kind of matter to release as the electrophile and three cases come up. The injection of quenchants as a gas into the plasma sheath is not physically possible since there is no method that can facilitate a gas to penetrate through an ionized layer of plasma, at least beyond the boundary layer of the re-entry vehicle. Correspondingly, injection of solid particles is also impractical, because solid particles tend to reach higher temperatures at a rapid rate. Eventually, this leaves liquid as the only option[39].

Upon experiments, the injection of liquid electrophiles was found to be the most reasonable and physically possible method because liquids injected at high jet speeds can easily penetrate through the plasma which is forming around the re-entry vehicle, travelling at hypersonic speeds. The nozzles through which the quenchants are injected have a throat diameter of 0.05 mm and is situated near the antenna in an upstream direction.

At first, water was extensively investigated as the first liquid quenchant and was found to be reducing the electron density significantly. But later on, several chemical compounds developed in laboratory such as carbon tetrachloride, boron tribromide, acetone and freon were found to be more effective than water in reducing the electron density.

The effectiveness of various electrophilic quenchants was tested using RAM C-III during multiple re-entry flight tests. The graph illustrated by Fig. 19[40] describes the effect of quenchants on different antennas. The dark region within the attenuation bar indicates the injection effects observed on the antenna.

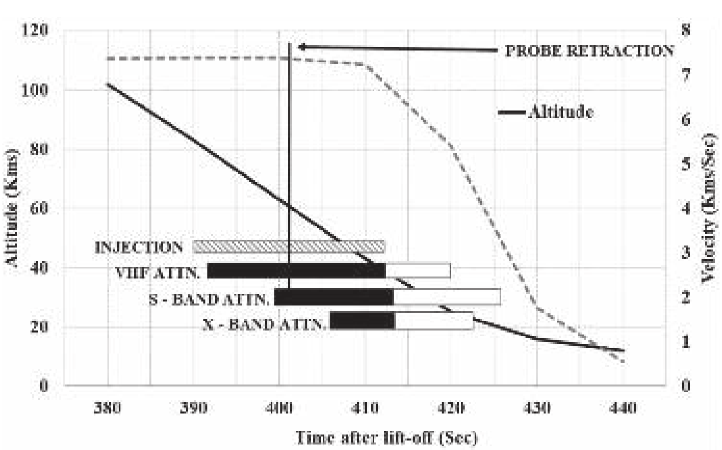

Figure 19. Electrophilic quenchants injection effects on different band antennas.

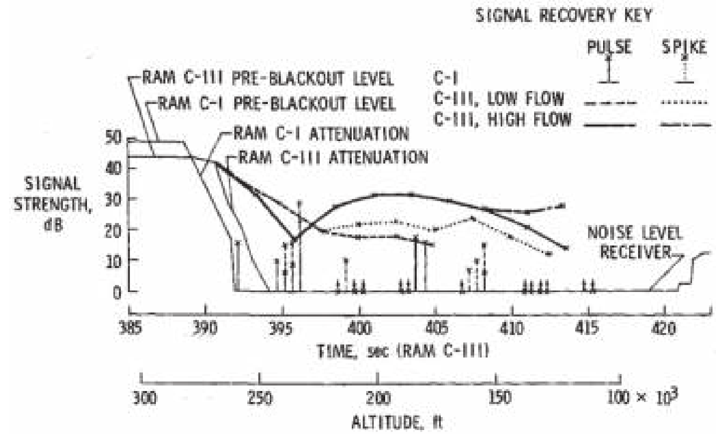

Figure 20. Comparison of RAM C-I & RAM C-III flight's blackout alleviation technique using water injection.

The signal recovery after overcoming blackout using the electrophilic quenchants in two different flight trails with RAM C-I and RAM C-III is demonstrated in the graph illustrated by Fig. 20[41]. The graph conveys that, the original signal which is at 45 dB will undergo attenuation due to blackout and gets decreased to 0 dB; but by using electrophilic quenchants, the signal can be recovered up to 30 dB[42].

It was proven that the injection of the quenchants, was the most reliable technique to mitigate the blackout problem. But this technique comes with its own disadvantages. Firstly, a thorough knowledge about the plasma properties is required to decide which chemical compound is required to be used as a quenchant. To study the plasma properties, high precision electromagnetic sensors are required to be placed on the surface of the re-entry vehicle. Even so, the characteristic of the plasma is such that it rapidly changes it properties, eventually making it difficult to find a pattern in the properties of the plasma[43].

Secondly, the required mechanism to carry and inject the quenchants by the re-entry vehicle increases the payload weight and cost, eventually decreasing the range of the vehicle. Hence, to use this technique, certain aspects must be compromised[44].

4.4 Magnetic Window

The strong electron-dense plasma attenuates or reflects back the entire RF signals emitting from the re-entry vehicle. To counter this strong electron-dense sheath, if equally strong magnetic field lines are oriented in such a way that the electrons are attracted to the magnetic field lines and are tightly bound to the magnetic field lines through gyration and do not influence their electric charge on the RF signals coming through them, then there is a chance that a window generated by the magnetic field can provide a path for the RF signals so that they can pass through[45].

The simulation results shown by Fig. 21[46] of the discussed hypothesis prove that when the plasma is subjected to a force generated by a magnetic field intensity, there is, not only a significant reduction in the attenuation offered by the plasma but also the rate of reduction is increased.

However, the drawback that comes by employing this technique is, again, the additional weight of the equipment,

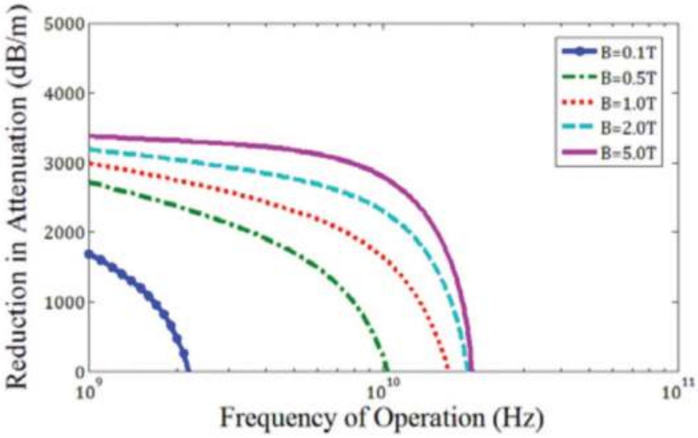

Figure 21. Reduction in attenuation (vs) operating frequency.

required to generate magnetic field lines that will significantly increase the weight of the payload, hence decreasing the range of the flight vehicle[47].

4.5 Employing Satellites

As discussed earlier, there are five regions of the re-entry vehicle, out of which four regions are influenced by the plasma. The wake region is the only region that is not affected by the plasma because it is not directly exposed to the air, which is converted in the shock bow region. Hence this area can be used for communications. Antennas can be flushed on the surface of the wake region and could be used for communications as shown in Fig. 22[48]. However, the signals emerging from the antenna are highly directional and are directed in the opposite direction of the descent, making it difficult for the ground stations to receive those signals. To receive these signals, satellites must be used to receive these signals, amplify and relay them back to the ground stations. This process is arduous, involving many equipment such as satellites, relays, etc. Hence, employing this technique is tedious, time-consuming, and not optimum.

Figure 22. Employing satellite from payload antenna.

4.6 Metamaterials

Metamaterial is not some rare earth materials or something made out of different chemicals. The properties of a metamaterial are not defined by its chemical composition, rather it is defined by its physical structure. A material becomes meta by the difference in its physical structure[49].

Metamaterials are the kind of materials that exhibit abnormal behavior when compared with normal materials. This abnormal behavior is very useful for several applications such as super lenses, cloaking, negative thickness, etc. One of the applications is in antennas. Metamaterials produce a negative permeability magnetic field that is analogous to the negative permittivity electric field of the plasma sheath. Basically, the application of metamaterials is a derivative of the magnetic window. When both permittivity and permeability of the atmosphere is negative, it allows the RF signals to pass through. If the former or the latter is different from one another, RF signals will be attenuated completely. Hence, metamaterial has a significant application in antennas, which can operate in the presence of highly dense electron plasma[50].

The advantages of this technique are that metamaterial is easy to procure and manufacture, lightweight, and easy to install and operate. If this technique is practically proven, metamaterials will become the prime solution for the RF communications blackout issue.

5. COMPARISON OF DIFFERENT MITIGATION TECHNIQUES

As discussed in the earlier sections, there are numerous approaches to counter the RF communications blackout problem, out of which six approaches have high probability of success. But each approach has its own advantages and disadvantages. Comparing each technique with one another will bring out the best strategy.

By comparing the techniques, aerodynamic shaping and satellite communication counters the blackout issue, but the former compromises the payload capacity, and the latter increases the complexity. Now, when other strategies are compared, such as switching to higher frequencies, injection of quenchants, creating a magnetic window, and employing a higher power source, it is observed that all these techniques were able to counter the blackout problem except the technique involving the employment of the high-power source. But all these techniques come with the disadvantage of decreased range, which is not desirable. The only solution that does not offer any disadvantage but also counters the blackout issue without compromising any aspects of a typical re-entry vehicle is the application of metamaterial in antennas. Although this solution is only theoretically hypothesized, metamaterial will be a revolutionary solution to the RF communications blackout phenomenon if proven practically[49-50].

6. CONCLUSION

Multiple rockets and flights have been flown into space and brought back to earth, to study and solve the blackout issue. To study the blackout issue, firstly, it is required to study the physical and chemical properties of the plasma sheath. To study these properties, high-precision electromagnetic sensors are to be installed on the surface of the re-entry vehicle to record the data of various parameters. Once the plasma's behaviour is understood, any mitigation should be adopted which is suitable for the application. For instance, a ballistic flight vehicle containing a re-entry vehicle will undergo the blackout phenomenon during the re-entry phase

Table 1. Comparison of different mitigation techniques

Factors→ Techniques↓	**Signal recovery time (Sec)**	**Attenuation experienced (dB)**	**Efficiency**	**Additional payload weight**
Aerodynamic shaping 40° AoA to 20° AoA	900	NIL	Very low	No
Higher frequencies VHF to X band	9.4	14	Very high	Yes
Quenchants (water)	300	20	Moderate	Yes
Magnetic window 0.075 Tesla	NIL	40	Moderate	Yes
Satellite communication	NIL	NIL	Very high	Yes
Metamaterial	NIL	5-10	Very high	No

of the trajectory. The appropriate mitigation method that must be used that does not increase the payload weight, cost, and complexity is metamaterials in the antenna.

REFERENCES

1. Anderson, J.D. Compressible flow: Some preliminary aspects. In fundamentals of Aerodynamics, 3rd de.; McGraw-Hill Education: New York, NY, USA, 2001; pp. 456-457.
2. Webb, Bruce A. & Richard, W. Ziolkowski. A metamaterial-inspired approach to mitigating radio frequency blackout when a plasma forms around a reentry vehicle. *Photonics*, 2020, **7**(4). doi: 10.3390/photonics704008
3. Takahashi, Y.; Enoki, N.; Takasawa, H. & Oshima, N. Surface catalysis effects on mitigation of radio frequency blackout in orbital reentry. *J. Physics D Appl. Physics*, 2020, **53**(23). doi:10.1088/1361-6463/ab79e0.
4. Jordan, E.C. & Balmain, K.G. Electromagnetic waves and radiating systems. Prentice-Hall, Inc., Englewood Cliffs, 1968.
5. Rybak, J.P. & Churchill, R.J. Progress in reentry communications. *In* IEEE Transactions on Aerospace and Electronic Systems, AES-7, 1971, **5**, pp. 879-894. doi: 10.1109/TAES.1971.310328.
6. Hartunian, R.A. Causes & mitigation of radio frequency blackout during re-entry of reusable launch vehicles. Aerospace corporation, Report Number: ATR-2007(5309)-1; DOT-VNTSC-FAA-06-23; January 2007
7. Hartunian, R.; Seibold, R. & Shome, P. Implications and mitigation of RF blackout during reentry of RLVs, 2007 doi: 10.2514/6.2007-6633
8. Zhou, Hui.; Xiaoping, Li.; Kai, Xie; Yanming, Liu & Yuanyuan, Yu. Mitigating reentry radio blackout by using a traveling magnetic field. *AIP Advances,* 2017, **7**(10), 105314. doi: 10.1063/1.4999039
9. Schroeder, L.C. & Akey, N.D. Material injection alleviation during the RAM C-III Flight. *J. Spacecraft and Rockets,* 1973, **10**(3), 170-174. doi: 10.2514/3.61866
10. Joerger, C.D. & Glatt, M.A. Analysis of plasma generators for testing reentry communications systems. Proc. 3rd Symp. Plasma Sheath-Plasma electromagnetics of hypersonic flight, 3, USAF Cambridge Research Labs., Rept. AFCRL-67-0280, p. 1, 1967.
11. Advanced ballistic re-entry vehicle. https://up-ship.com/blog/?p=43154 (Accessed on 01 September 2023).
12. NASA–Spacecraft design. https://www.nasa.gov/centers/ames/research/2007/faq-shuttlereentry.html (Accessed on 01 September 2023).
13. Airforce times. https://www.airforcetimes.com/news/your-air-force/2015/08/19/air-force-test-launches-unarmed-missile-from-california/ (Accessed on 01 September 2023).
14. Fire-resistant reinforcement makes steel structures sturdier. https://spinoff.nasa.gov/Spinoff2006/ps_3.html (Accessed on 01 September 2023).
15. X – 43A flight (Hyper – X). https://www.nasa.gov/centers/armstrong/history/experimental_aircraft/X-43A.html (Accessed on 01 September 2023).
16. The reentry plasma sheath. Space/Aero., **41**, p. 53, May 1964.
17. Fuhs, A.E., Flight instrumentation for reentry plasma sheath. AIAA/Northwestern University Fifth Biennial Gas Dynamics Symposium, AIAA Paper No. 1963-379, 1963, 14-16. doi: 10.2514/ 6.1963-379
18. Steiger, M.; Glatt, L.; Fernandez, F.; Fedele, J. & Golden, K. Reentry communication: Theoretical analysis and flight test results. AIAA 8th Aerospace Sciences Meeting, AIAA Paper No. 70-220, Jan 19-21, 1970. doi: 10.2514/6.1970-220.
19. Dunn, M. G. & Kang, S.W. Theoretical and experimental studies of reentry plasmas. NASA CR-2232, Apr 1973.
20. Schexnayder, C.J.; Evans, J.S. & Huber, P.W. Comparison of theoretical and experimental electron density for RAM C Flights. Proceedings of The Entry Plasma Sheath and its Effects on Space Vehicle Electromagnetic Systems, I, NASA SP-252, NASA Langley Research Center, Oct 13-1970, **15**, pp. 277-303.
21. Jones, Jr. W.L. & Cross, A.E. Electrostatic probe measurements of plasma surrounding three 25,000 foot per second reentry flight experiments. Proceedings, The Entry Plasma Sheath and its Effects on Space Vehicle Electromagnetic Systems, I, NASA SP-252, NASA Langley Research Center, 1970, Oct 13-15, pp. 109-136.
22. McCabe, W.M. & Stolwyk, C.F. Electromagnetic propagation through shock-ionized air surrounding glide re-entry spacecraft. *IEEE Trans. Space Electron. Telemetry*, SET-8, 1962, **257**. doi: 10.1109/IRET-SET.1962.5008850
23. Schroeder, L.C. & Russo, F.P. Flight investigation and analysis of alleviation of communications blackout by

water injection during Gemini 3 Reentry. NASA TM X-1521, pp. 1–56, 1968.
24. Usui, H.; Matsumoto, H.; Yamashita, M.; Yamane, F. & Takenaka, S. Computer experiments on radio blackout of a reentry vehicle. *In* Proceedings of 6th Spacecraft Charging Technology Conference, AFRL-VS-TR-20001578, European Space Agency, the NASA Astrophysics Data System, September 2000, pp. 107–110.
doi: 10.1016/S0273-1177(99) 00560-8
25. Kim, M.; Keidar, M. & Boyd, I.D. Analysis of an electromagnetic mitigation scheme for reentry telemetry through plasma. *J. Spacecraft and Rockets*, 2008, **45**(6), 1223–1229.
doi: 10.2514/1.37395
26. Belov, I.F.; Borovoy, V.Y.; Gorelov, V.A.; Kireev, A.Y.; Korolev, A.S. & Stepanov, E.A. Investigation of remote antenna assembly for radio communication with reentry vehicle. *J. Spacecraft and Rockets*, 2001, **38**(2), 249–256.
doi: 10.2514 /2.3 678
27. Takahashi, Y.; Yamada, K. & Abe, T. Examination of radio frequency blackout for an inflatable vehicle during atmospheric reentry. *J. Spacecraft and Rockets*, 2014, **51**(2), 430–441.
doi: 10.2514/1.A32539
28. Jung, M.; Kihara, H.; Abe, K. & Takahashi, Y. Numerical simulation of plasma flows and radio-frequency blackout in atmospheric reentry demonstrator mission. AIAA, 2017, pp. 3308.
doi: 10.2514/6.2017-3308
29. Takahashi, Y. Advanced validation of CFD-FDTD combined method using highly applicable solver for reentry blackout prediction. *J. Physics D: Appl. Physics*, 2016, **49**(1), 015201.
doi: 10.1088/0022-3727/49/1/015201
30. Tran, P.; Paulat, J.C. & Boukhobza, P. Re-entry flight experiments lessons learned: The atmospheric reentry demonstrator ARD. Nato Report, RTO-EN-AVT-130-10, 2007, pp. 10–46.
31. Takahashi, Y.; Yamada, K.; & Abe, T. Prediction performance of blackout and plasma attenuation in atmospheric reentry demonstrator mission. *J. Spacecraft and Rockets*, 2014, **51**(6), 1954–1964.
doi: 10.2514/1.A32880
32. Jung, M.; Kihara, H.; Abe, K.i. & Takahashi, Y. Reentry blackout prediction for atmospheric reentry demonstrator mission considering uncertainty in chemical reaction rate model. *Physics of Plasmas*, , 2018, **25**(1), 013507.
doi: 10. 1063/1.5010713
33. Schroeder, L.C. RAM flight test results & conclusions, NASA SP-52, 1964.
34. Akey, N.D. & Cross, A.E. Radio blackout alleviation and plasma diagnostic results from a 25,000 foot-per-second blunt body reentry, TN D-5615, 1970, NASA.
35. Grantham, W.L. Flight results of a 25,000 foot-per-second reentry experiment using microwave reflectometers to measure plasma electron density and standoff distance, TN D-6062, 1970, NASA.
36. Kang, S.-W.; Jones, W.L.; Jr. & Dunn, M.G Theoretical and measured electron density distributions for the RAM vehicle at high altitudes. *AIAA Journal*, 1973, **11**(2), 141-149.
doi: 10.2514/6.1972-689
37. Kurzius, S.C. & Ellison, R. Effect of water droplets on reentry plasma sheaths. CR-66149, 1965, NASA.
38. Kurzius, S.C.; Raab, F.H. & Revolenski, R.L. lonization suppression in high temperature, low pressure plasma by electrophilic vapors and sprays. CR-1701, 1970, NASA.
39. Cuddihy, W.F.; Beckwith, I.E. & Schroeder, L.C. Flight test and analysis of a method for reducing radio attenuation during hypersonic flight. TM X-1331, 1967, NASA.
40. Schroeder, L.C. & Russo, F.P., Flight investigation and analysis of alleviation of communications blackout by water injection during gemeni 3 reentry. TM X-1521, 1968, NASA.
41. Crowe, R.W. & Kilpatrick, W.D. A fundamental study of electrophilic gasses and plasma quenching. CR-66206,1968, NASA.
42. Schroeder, L.C.; Jones, W.L.; Jr., Swift, C.T. & Cross, A.E. Radio blackout alleviation by fluid injection and plasma measurements during the RAM C-III re-entry at 25,000 Ft/Sec," TM X-2563, 1972, NASA.
43. Joerger, C.D. & Glatt, M.A. Analysis of plasma generators for testing reentry communications systems. Proc. 3rd Symp. plasma sheath-plasma electromagnetics of hypersonic flight, 3, USAF Cambridge Research Labs., Rept. AFCRL-67-0280, 1967, p. 1.
44. Friel, P.J. & Rosenbaum, B. Propagation of electromagnetic waves through reentry-induced plasmas in advances in the astronautical Sciences, 11, H. Jacobs, Ed. New York: American Astronautical Soc., 1963, p. 399.
doi: 10.1109/IRET-SET.1962. 5008850.
45. Plonsey, R. & Coffin, R.E. Principles & applications of electromagnetic fields. New York: McGraw-Hill, 1961.
46. Tanenbaum, B.S. Plasma Physics. New York: McGraw-Hill, 1967.
47. Spitzer, L.; Jr. Physics of fully ionized gases. New York: Interscience, 1956.
48. Epstein, M. Antenna breakdown in a hypersonic re-entry environment. Proc. 3rd Symp. plasma sheath. Plasma electromagnetics of hypersonic flight, 2, USAF Cambridge Research Labs., Rept. AFCRL-67-0280, 1967, p. 169.
49. Jacavanco, D.J. Electron reduction in the reentry plasma sheath. USAF Cambridge Research Labs., Rept. AFCRL-69-0154.
50. Lehnert, R. & Rosenbaum, B. Plasma effect on Apollo reentry communications. NASA Tech. Note TN D-2732, 1965.

CONTRIBUTORS

Ms S. Shankari obtained her MS in Embedded Systems Design from Manipal University. She is working as Scientist 'F' at DRDO-ASL. She worked in the area of new set of technologies in missile system leading to weight and space optimisation.
In the current study, she did the literature survey and collected information on the blackout phenomenon and various mitigation techniques, comparing strategies and converging to an optimal solution.

CH. N.P.V. Chandra Shekhar obtained his BE in Electronics and Communications from MVSR Engineering College, Osmania University. He is working as a Research Engineer at DRDO-ASL. In the current study he did a literature survey and collected information about the different classes of re-entry vehicles.

Dr G. Arun Kumar obtained his PhD degrees in Electronics and Telecommunications Engineering from Jadavpur University. He is working as a Assistant Professor at Department of Electronics and Communication Engineering, National Institute of Technology Warangal.
In the current study he guided the authors and supervised the literature survey and took the responsibility of editing the paper.

Defence Science Journal, Vol. 75, No. 1, January 2025, pp. 76-83, DOI : 10.14429/dsj.19289

Ku Band Diplexer Antenna for Data Relay Satellite Uplink in ITU-R

Anand Swaminathan[#,*] and Preethi Elizabeth Navamani[$]

[#]*Department of ECE, Mepco Schlenk Engineering College, Sivakasi - 626 005, India*
[$]*Department of ECE, Saranathan College of Engineering, Tiruchirappalli - 620 012, India*
[*]*E-mail: sanand@mepcoeng.ac.in*

ABSTRACT

This work describes a substrate-integrated waveguide (SIW) based Ku band diplexer antenna (DA) for data relay satellite (DRS) low and medium data rate uplink. Designing diplexers that operate at closely spaced frequencies is difficult. The DA's bandwidth (BW) in the proposed design ranges from 12.6 to 15.2 GHz. According to the ITU-R standard, one of the DA's ports operates between 12.75 and 13.25 GHz, while the other operates between 14.5 and 14.75 GHz. The proposed antenna achieves both high gain and wide BW concurrently, which is challenging to do in DA. The radiation caused by the coupling between the proximity modes is excited using a back-to-back triangular SIW and square slots. This SIW DA radiates with 25 dB port isolation and linear polarisation at broad frequencies. It is small, and the slot-loading effect reduces the antenna size. It is suitable for DRS's low and medium data rate uplink multiplexing applications since both ports obtain a wide BW of 20.14 percent at frequencies between 12.6 and 15.2 GHz and a gain of 4.5 dBi. The smaller ECC (less than 0.4) ensures mutual coupling between ports and improves performance and data transmission.

Keywords: Diplexing antenna; Substrate-integrated waveguide; Ku band; Data relay satellite

NOMENCLATURE

BW	: Bandwidth
CP	: Circularly polarized
DA	: Diplexer antennas
ϵ_r	: Relative permittivity
dBi	: Decibels relative to isotropic
DR	: Data relay
GHz	: Gigahertz
ITU-R	: International telecommunication union radio communication sector
LHCP	: Left hand circularly polarised
RHCP	: Right hand circularly polarized
SD	: Self-diplexing
SIW	: Substrate integrated waveguide
tan δ	: Loss tangent
VNA	: Vector network analyser
VSWR	: Voltage standing wave ratio

1. INTRODUCTION

In satellite transmission systems, antenna[1-2] is a very important part. They allow stations on Earth and satellites in space to send and receive signals. Compact Diplexer Antennas (DA) have recently received a lot of attention due to the rapid development of satellite communication system requirements. DA is a passive device that uses two ports to broadcast frequency-multiplexed signals. Both ports' signals operate in separate frequency ranges and coexist without interfering with each other. The signal on port 1 will typically occupy one frequency range, while the signal on port 2 will occupy another. The diplexer in this case is comprised of band pass filters (ideally a low-pass and a high-pass filter) that connect to suitable ports to pass the frequencies. DA can be categorised into two types based on the duplexing frequencies: (i) in-band diplexers and (ii) out-of-band diplexers. The in-band diplexer resonates at two frequencies inside the same band, while the out-of-band diplexer resonates at two different bands. Out-of-band DAs are comparatively simple to construct because of the large frequency separation and high degree of port isolation. An antenna that diplexes the in-band frequencies, such as DR satellite low and medium data rates, for uplink in the Ku band is crucial. The typical frequency requirement of the ITU-R recommendation of DR satellite low and medium data rates for uplink is shown Fig.1(a), and the functions of duplexing antennas are shown Fig. 1(b). The challenge of this research is to diplex the two frequency ranges (i) 12.75–13.25 GHz and (ii) 14.5–14.75 GHz with a guard band of 1.2 GHz in the Ku band. Four aspects of prior research work have been reviewed: SIW[3-4] antenna, diplexer antenna, and diplexer antenna based on SIW and Ku band applications. As a planar waveguide, SIW retains most of the advantages of classic waveguides, such as low loss, a high Q factor, and high power capacity. Due to their superior performance, such as high gain, low profile, wide BW, frequency reconfigurability, and low cross polarisation, SIW cavity antennas have attracted interest[5-10]. Self-Diplexing (SD) antenna eliminates the requirement for a higher-order diplexer network, resulting in a more compact and efficient RF

Received : 07 July 2023, Revised : 05 June 2024
Accepted : 05 August 2024, Online published : 10 January 2025

front-end system. Low-cost wireless transceiver applications, on-chip active antennas, retro directive antennas, and other applications greatly benefit from these circuits. A two-port planar SD SIW slot antenna[11] was the subject of investigation, where researchers done the various analysis.

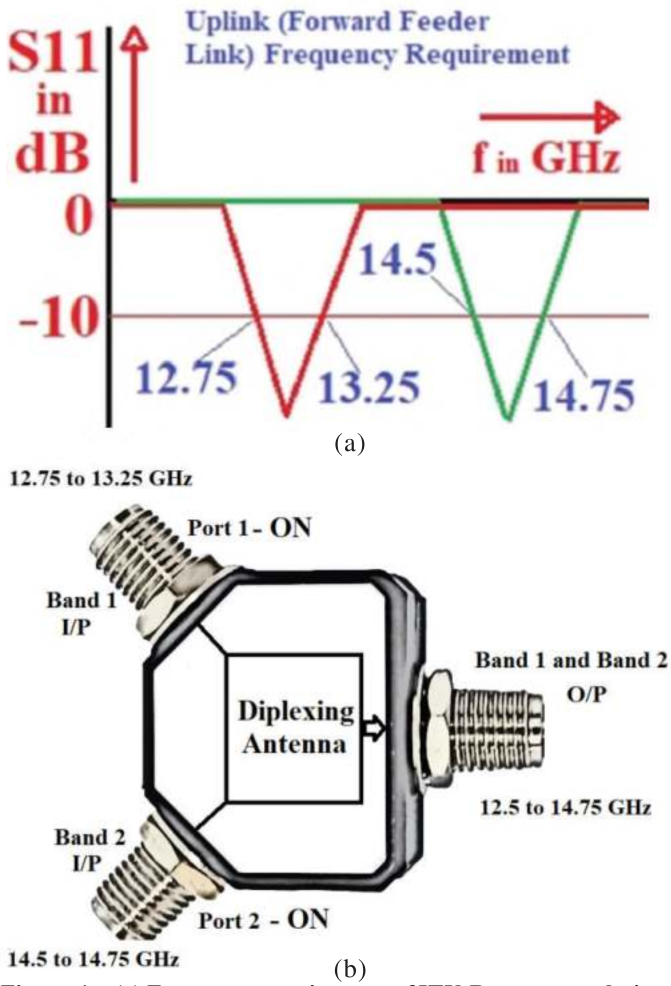

Figure 1. (a) Frequency requirement of ITU-R recommendation of DR satellite low and medium data rate for uplink; and (b) Diplexing antenna operation.

Two distinct feed lines excite a bowtie-shaped slot with a SIW cavity backing to resonate at two different frequencies in the X-band (8–12 GHz). For radiation at 8.97 GHz and 11.3 GHz, the two HMSIW resonators are placed together in a shared slot. There is around 20 dB of isolation between the two ports, which offer gains of 4.3 and 4.2 dBi at their respective resonance frequencies. Over a frequency range of 2.5–2.7 GHz, a 12 patch dual-polarized antenna array[12] is described. In order to optimize the radiation performance, it has an artificial periodic structure as well as a pair of cavities that are located below the radiating elements. It provides good isolation between its two ports while operating at two different frequencies. In addition, the literature describes a mode-based design method for dual-band and self-diplexing antennas[13] with double T-stubs loaded apertures. The authors describe a dual-fed, self-diplexing planar inverted 'F' antenna[14] and its related RF front-end. It is demonstrated that co-designing the antenna and front-end may be used to double the operational BW without sacrificing substantial size or performance.

A dual-band, dual-sense Circularly Polarized (CP) antenna[15] array with SD aperture sharingis used for transmitting and receiving applications in X-band satellite communication systems. The antenna can receive and transmit left-handed CP (LHCP) signals in the low band while receiving and sending right-handed CP (RHCP) signals in the high band. SIW technology, which works as a bridge between planar and non-planar technology, is an excellent choice for the creation of microwave diplexers. Due to this, SIW diplexer antennas[16-19] take advantage of the high gain, high power capacity, low cross polarization, and high selectivity, of planar diplexer antennas. Certain SIW-based triplexing[20] and quadruplexing[21-22] antennas have also been reported in the literature. Recently, there has been a lot of interest in antenna research and applications for usage in the Ku band, as well as an increasing number of antenna systems to provide various services[23-26].

Satellite communication systems use a variety of DAs. Some of these antennas are SIW cavity-backed slot antennas intended for wideband, S-band, and C-band use. These include DA with high port isolation, polarized antennas, low-profile Ku-Band antennas, and double-layer Ku/K dual-band antennas. These antennas are intended to provide a wide BW, multi-band operation, high efficiency, and low profile designs. However, designing DAs for closely spaced frequencies is challenging. The proposed DA provides useful gain for Ku band DA while also providing a wide BW. Moreover, this antenna is specifically developed for data relay satellite uplink in ITU-R.

In this work, a compact, wide BW, SIW DA is proposed to multiplex the low and medium data rates for uplink in DR satellites. It is made up of square slots with orthogonal feed lines and a back-to-back triangular SIW. This structure closes the distance between the two modes, allowing them to merge. The orthogonal feed with square slots improves the transmission zeros, leading to higher port isolation, and the coupling of two modes creates ultra-BW. This proposed antenna is unique because it has (i) back-to-back triangular SIW, (ii) leading diagonal square slots, (iii) operation of both ports in the same band, (iv) wide band in all port operating conditions, and (v) diplexing the low and medium data rates for DR satellite uplink. Better performance in many antenna parameters like gain, return loss, VSWR, current distribution, power matching, polarization etc. are the advantages of the proposed DA.

2. DESIGN OF DIAGONAL SIW SQUARE CAVITY DIPLEXER ANTENNA

The DA has gained interest in many multi-communication systems. This section describes the diagonal SIW square cavity DA in detail, with the required reflection analysis and radiation characteristics. Due to its diplexing characteristics, DA reduces the requirement for additional antennas and improves the compactness and efficiency of the overall RF front end. In the designed SIW structure, holes are placed at the corner of the cavity, called a diagonal SIW antenna. The folded SIW at four corners forms walls, and this antenna has a square slot cut at leading diagonals. The cavity formation reduces the antenna size and provides good reflection coefficients. The designed

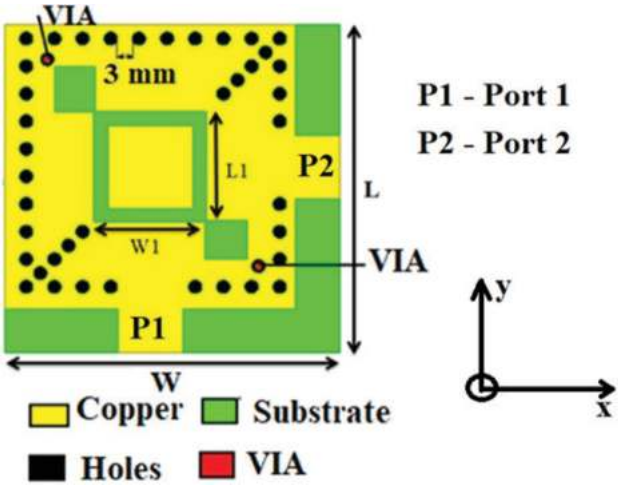

Figure 2. Geometry of the proposed SIW based diplexing antenna.

SIW DA with a diagonal rectangular slot is etched on the top (Fig. 2).

From the direction of the electric fields on the port, the mode of excitation is identified. The TE10 mode, for instance, denotes the direction of the electric field that is resonating in the first mode when one port is excited. Similarly, in dual port excitation, directions of electric fields are excited in two modes. A h=1.6 *mm* thick FR4 substrate ε_r=4.4 and tan δ =0.02 and the Ansoft's HFSS full-wave simulator are used for analysis. The size parameters of the diagonal SIW square cavity DA are given in Table 1. In addition to having

Table 1. Design parameter of proposed DA

h (mm)	L (mm)	W (mm)	L1 (mm)	W1 (mm)	P (mm)	D (mm)
1.6	35	35	11.78	11.78	3	2

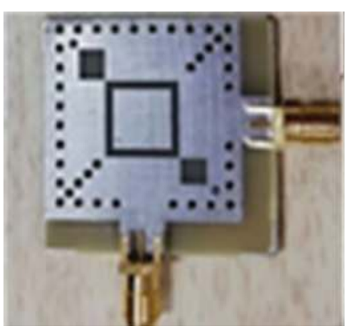

(a)

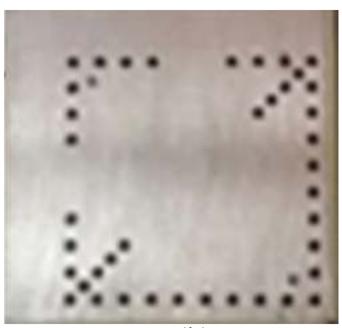

(b)

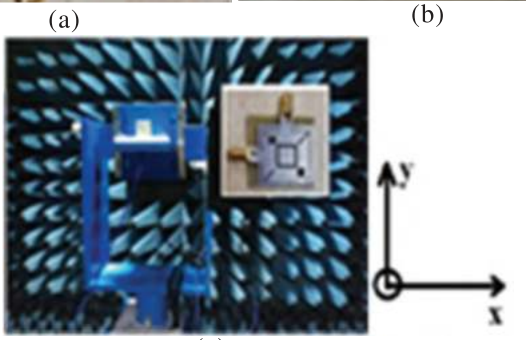

(c)

Figure 3. Designed fabricated prototype antenna, (a) top view; (b) bottom view; and (c) measurement setup of antenna parameters in Anechoic chamber.

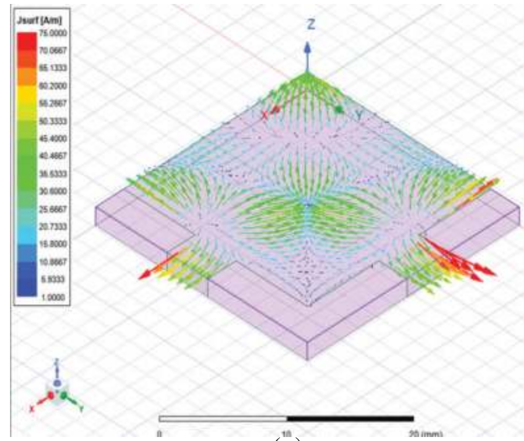

(a)

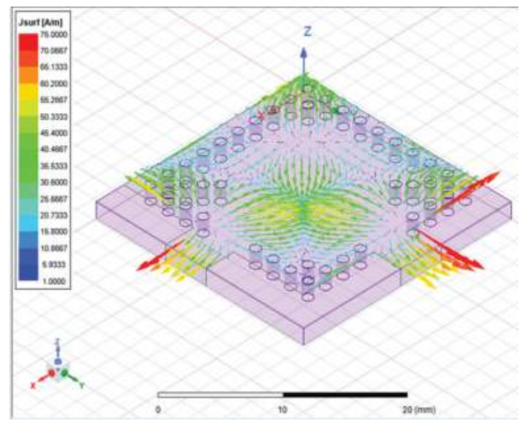

(b)

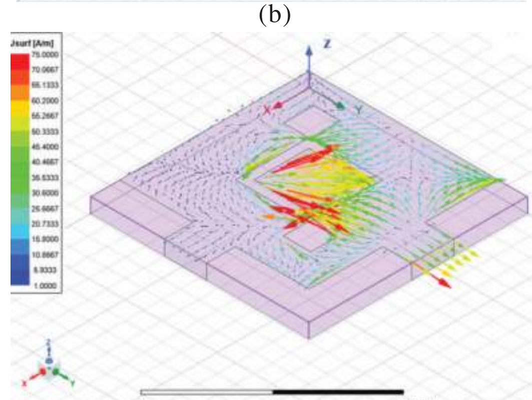

(c)

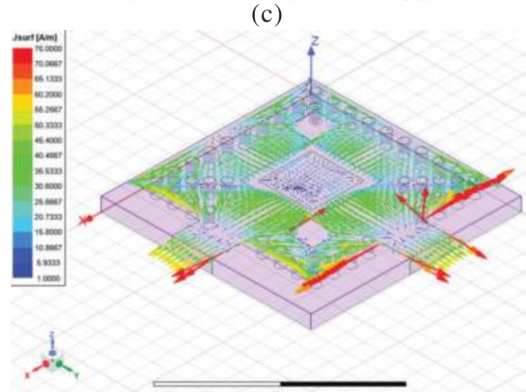

(d)

Figure 4. Current distributions of development steps of proposed antenna design, (a) Step-1: Antenna without SIW: and slots (b) Step-2: Antenna with SIW; (c) Step-3: Antenna with slots; and (d) Step-4: Antenna with SIW and slots (proposed).

the high isolation between the ports, two different feed lines in resonant modes provide high gain. The DA has a diagonal SIW square cavity slot on the top of the patch, and the corner cavity is extended through via holes.

This overall structure reduces the antenna size and provides improved radiation characteristics. A patch is connected to the feed for excitation, and the holes act as the electric sidewalls or fences of SIW, and they are also used to increase the electric path and BW of the antenna. The holes couple the energy from the feeding network, and the smooth transition between the substrate and the dielectric 'via' further enhances the BW of the antenna and the isolation between the ports above 20 dB. The overall view of the designed antenna and the fabricated prototype of the designed antenna are shown Fig. 3.

The SIW and diagonal slots help to increase isolation between the two ports. The proposed design consists of four main steps: (i) microstrip patch; (ii) SIW inclusion in patch; (iii) diagonal slot inclusion in patch; and (iv) a combination of all three steps. The current distributions of all steps are shown Fig. 4 to demonstrate the isolation effectiveness of the proposed antenna design. Inserting the SIW fence step 2 into a plain microstrip patch improves the current length, as seen in Fig. 4(b). Additional slots in the microstrip patch's diagonals (step 3) enhance the current distribution closer to the antenna's center, as seen Fig. 4(c). In step 4, both SIW walls and diagonal slots lengthen the currents while also changing their phase, as shown Fig. 4(d). The current phase's adjustment increases the isolation properties.

The improvement in isolation can be seen Fig. 5, which displays the isolation of each step and how the proposed antenna design performs better. High isolation ensures that the signals from one port do not significantly affect the signals on another port, which is particularly important in applications like DA, where multiple signals are transmitted and received simultaneously.

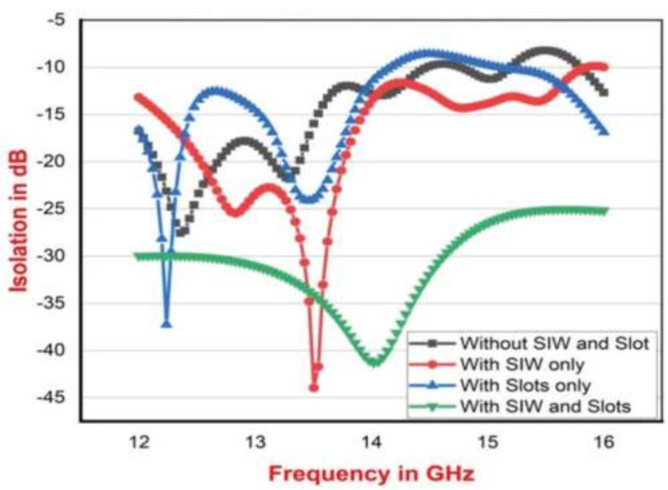

Figure 5. Isolation parameter of development steps (step1 to step 4) of proposed antenna design.

An isolation value of less than -20 dB is generally considered a satisfactory standard. The proposed antenna achieved this at the required frequency (12.6 GHz to 15.2 GHz). The SIW structure in the proposed DA confines electromagnetic waves, which helps reduce unwanted coupling between ports.

3. EXPERIMENTAL AND SIMULATION RESULTS

3.1 Scattering and Radiation Performance

The simulation results are analysed using finite element analysis in ANSYS HFSS (2021R2). The reflection parameters of the designed antenna are measured using an Agilent VNA with frequency coverage of 30 kHz to 20 GHz. The radiation and scattering performances of the designed antenna are tested in the anechoic chamber, as shown Fig. 3(c). The radiation and scattering characteristics of the two ports of this DA are studied separately as well as together. The simulated results of the S11 parameter for two ports are depicted in Fig. 6. The desired frequency range is in the Ku band, between 12 and 17 GHz. S11 coefficients are described, only when port 1 is 'ON' and only when port 2 is 'ON'. The 'ON' means that the signal feed is given to a particular port. The status of the ports and their significance are given in Table 2.

Table 2. Diplexing antenna (DA) port's status and its operation

Ports	State		
Port 1	On	Off	On
Port 2	On	On	Off
Operation	Diplexer	--	--

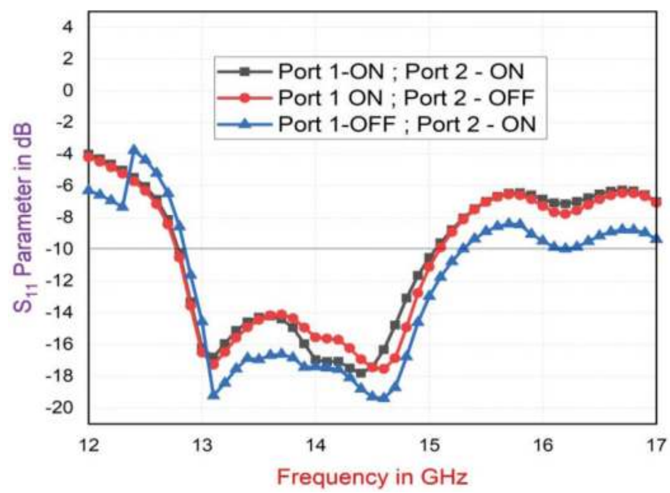

Figure 6. Reflection coefficients of proposed DA corresponding port 'ON'.

In addition, the S11 parameter when both ports are 'ON' is shown in Fig. 6. S11 refers to the reflection coefficient, a parameter used to characterize how well a device reflects radio waves. In the case of an antenna, a low S11 value indicates good impedance matching. The designed antenna resonates with good matching from almost 12.6–15.2 GHz in both ports separately and together, and a wide BW of 20.14 % is achieved (Fig. 6). In addition, S11 performances are well supported by studying the VSWR plot (Fig. 7) in the desired frequency range. The obtained VSWR within the range of 1–1.8 ensures that the designed antenna is well matched to the operating frequency conditions. The gain of the designed DA for an interested frequency range from 12 GHz to 17 GHz is shown (Fig. 8). It refers to the amount of signal a given antenna can radiate or receive in a given direction in a specified frequency range. Slots and SIW, which add more current paths to the antenna element, are the reasons for these improvements. Such

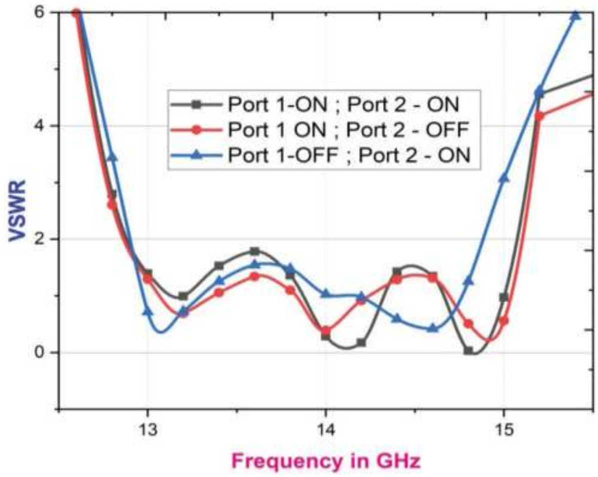

Figure 7. VSWR of proposed diplexing antenna (DA).

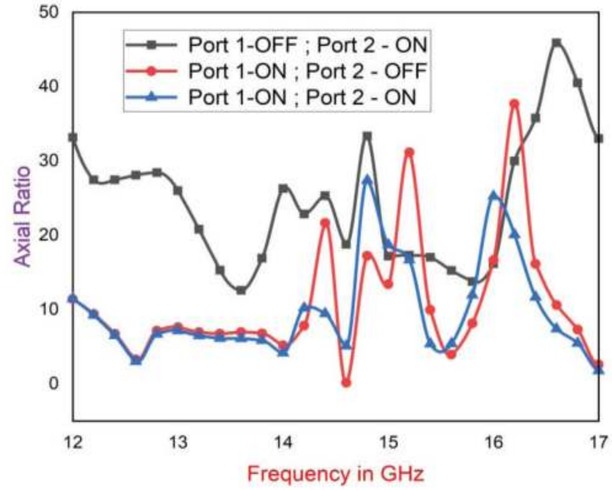

Figure 9. Axial ratio of proposed diplexing antenna.

paths may alter the overall current distribution, which could improve the antenna's S11 and VSWR.

The gain of the proposed antenna is computed by comparing the observed power transmitted/received by the proposed DA. The proposed DA has a moderate gain within the required frequency range. The proposed DA operates from 12.6-15.2 GHz with gains ranging from 4.5 to 3.5 dBi. The frequency vs. gain of the proposed DA with port 'ON' conditions are described (Fig.8). Antenna gain in a particular direction can be increased by gathering more signal energy and confining it in that direction using a larger effective aperture area of the proposed DA. DRS typically requires stronger received signals, and the proposed DA with a higher gain ensures sufficient signal strength.

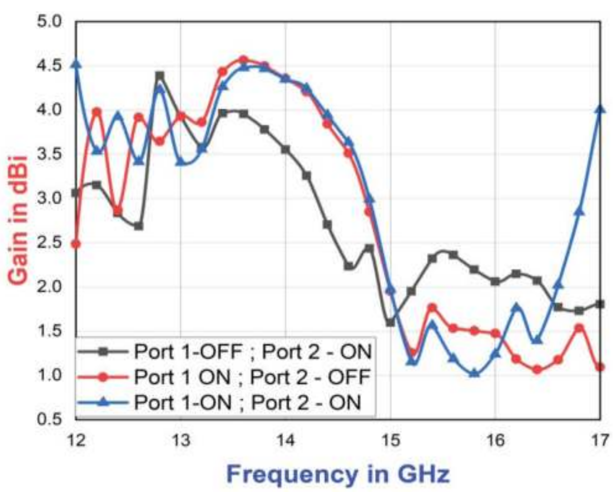

Figure 8. Gain vs frequency of the proposed self-diplexing antenna.

The axial ratio is a fundamental parameter used to characterize the polarisation purity of an antenna. The axial ratio of the proposed antenna is shown (Fig. 9) and the designed DA works well at the specified operating frequency when ports are excited. Within 12.6–15.2 GHz, the axial ratio is almost steady in the proposed antenna. This is because the plane of the patch, specifically the square patch antenna on a grounded substrate, stimulates currents that primarily flow along the patch's length or width.

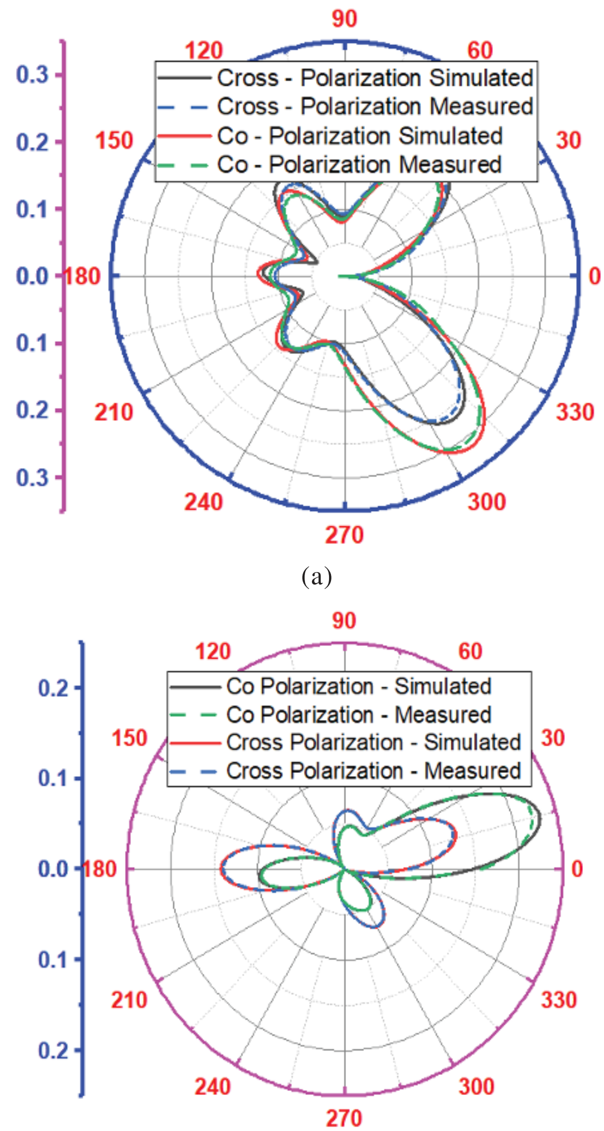

Figure 10. E Plane and H Plane radiation pattern, Co polarization and cross polarization pattern (both simulated and measured) of proposed DA, (a) at 13 GHz; and (b) 14.625 GHz.

The E-plane (xz-plane) and H-plane (xy-plane) radiation patterns at two frequencies of 13 GHz and 14.625 of the proposed DA are shown in Fig. 10. The measured and simulated results agree well with each other in the angular range around the broadside direction. The proposed DA's performance at the two frequencies is consistent with the design objectives in terms of gain, directionality, and minimal interference, as determined from the radiation pattern analysis and the measured pattern closely matches the simulated results.

3.2 Current Distribution Analysis

The electric field distribution is changed based on the port conditions. The electrons on the patch surface get excited and move around the port.

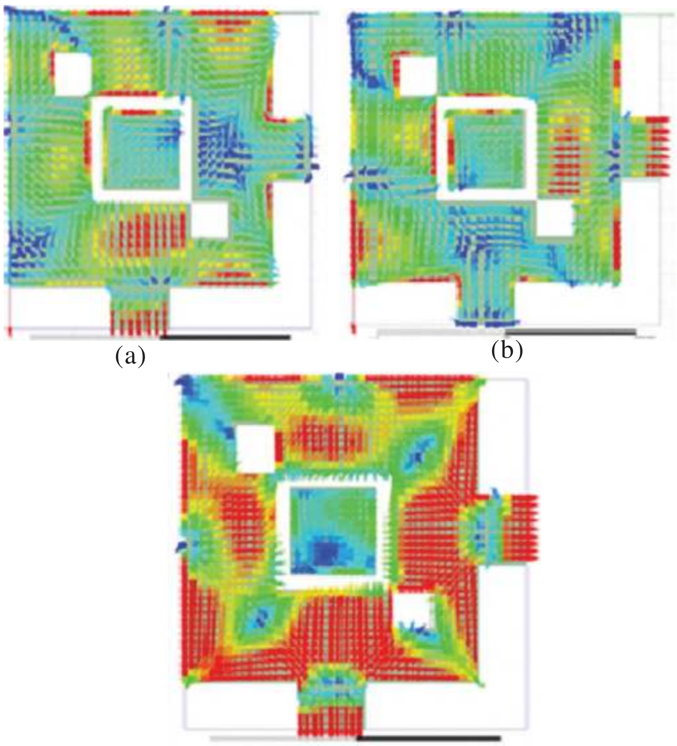

(a) (b)

(c)

Figure 11. Current distributions of proposed antenna, (a) Port 1 feed (13GHz) 'ON'; (b) Port 2 feed (14.62GHz) 'ON'; and (c) Port 1 feed (13GHz) 'ON' and port 2 feed (14.62GHz) 'ON.

Some imbalanced surface impedance is present along with the patch, which can weaken the current along the y-direction. When port 2 is 'ON', the EM waves incident around port 2's surface and other surfaces have an imbalanced impedance. The red colour indicates a strong electric field, and the blue color indicates a weak electric field. When port 1 is turned on, EM waves collide with port 1's surface. When both ports receive feeds, the current distribution near the ports increases (Fig. 11). In addition, the current distributions are symmetrical with their orthogonal ports. The proposed DA shows the overall radiation performance (Fig. 12) in terms of peak directivity, beam area, incident power, accepted power, radiated power, and radiation efficiency.

Each parameter's results reveal that the proposed DA has good radiation characteristics and is capable of performing the necessary purpose. The results of the proposed DA's simulated reflection coefficient are displayed (Fig. 13). A smaller discrepancy between simulated and measured scattering coefficients ensures that the developed DA can be used in practice. Table III shows the comparison of the proposed DA with other reported works found[11-13,15-18]. This comparison mainly focuses on size, frequency, BW, gain, radiation efficiency, and isolation. The antenna[11] has a lower profile than the proposed DA. At the same time, the frequencies are well separated. Despite the fact that isolations are high[12-13], they are relatively larger in size. The proposed DA has a low profile, is restricted to the Ku band, and sticks to the ITU recommendation with moderate isolation.

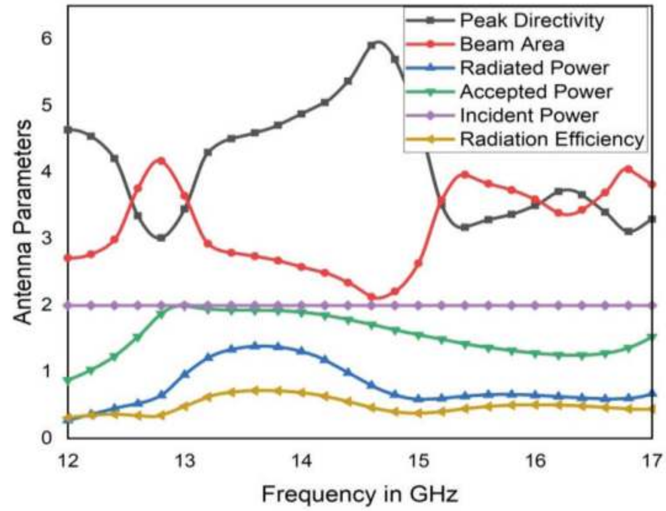

Figure 12. Performance of other antenna parameters.

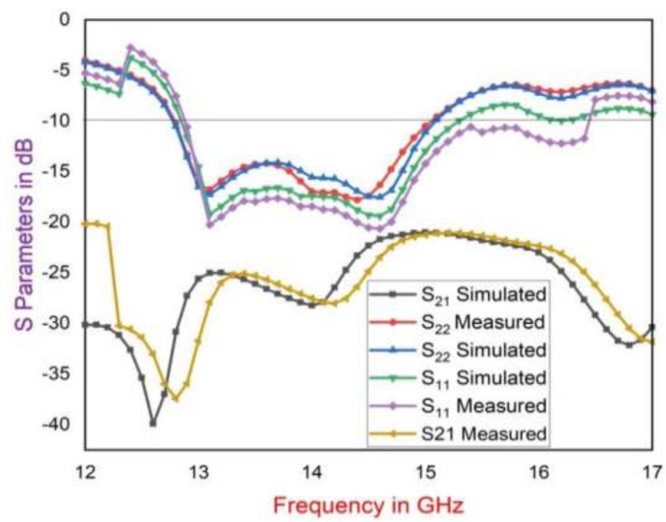

Figure 13. Simulated and measured reflection coefficients.

Mutual coupling between ports in a DA refers to the mutual interaction of signals at several ports. Mutual coupling in a diplexer, which commonly combines or separates signals across many frequency bands, can have an impact on antenna system isolation and performance. To avoid signal interference between ports, restrict mutual coupling. Understanding port interdependence is necessary when measuring mutual coupling with the Envelope Correlation Coefficient (ECC).

Table 3. Performance comparison of proposed DA

Ref.	Size (mm^3)	Frequency (GHz)	BW (GHz)	Gain (dBi)	Rad. Eff. (%)	Isolation (dB)
[11]	18.8×17×0.787	9.0 - 11.2	1.2	4.3	78	27
[12]	120×120×1.6	2.4-2.8	0.4	8.5 to9.1	NR	45
[13]	50×50×1.6	2.5,5.5	3	1.9	87	40
[15]	14.4x14.4x2.7	7.3-8.3	1.0	8	NR	27
[16]	12.5x14x1.5	11-12	1.78	6	NR	14.7
[17]	20.72x0.72x1.58	10.5	1.32	5.95	NR	29
[18]	20.7×9.7x1.524	3.6-5.4	1.8	5.34	>90	>32.5
This Work	35x35x1.6	12.6-15.2	2.6	4.5	74	25

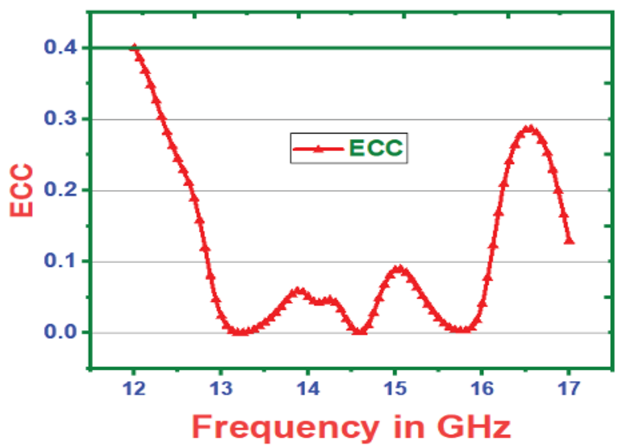

Figure 14. ECC of the proposed diplexer antenna.

It is an important metric to measure the performance of multi-frequency and multiport antenna systems, such as those that include diplexers. Lower ECC values (<0.4) recommend improved isolation and diversity performance in diplexer systems. The frequency versus ECC of the proposed DA is shown (Fig. 14), and it is found that mutual coupling is within the stipulated limit in the desired frequency range. By integrating advanced switching mechanisms and exploring new materials and design techniques, researchers can significantly improve the performance and functionality of Ku band diplexer antennas for future data relay satellite applications.

4. CONCLUSION

A Ku band SIW based Diplexer Antenna (DA) for low and medium data rate Data Relay Satellite (DRS) uplink is presented. It overcomes a diplexer's design constraint of working at closely spaced frequencies. According to the ITU-R guideline, one of the DA's ports operates between 12.75 and 13.25 GHz, while the other operates between 14.5 and 14.75 GHz. The triangular SIW is used inconjunction with square slots to trigger proximity modes and radiation caused by mode coupling. This compact SIW DA radiates with 25 dB port isolation and linear polarization. Its BW in both ports is 20 %, making it appropriate for DRS low and medium data rate uplink multiplexing applications. The lower ECC (below 0.4) between the ports results in decreased mutual coupling, which improves the performance and data transmission capabilities of data relay satellites in Ku band applications.

REFERENCES

1. Verma, Akhilesh.; Arya; Ravi Kumar & Srinivasa, N.R. Monopole cavity resonator antenna with AMC and superstrate for 5G/WiMAX applications. *Def. Sci. J.*, 2023, **73**(1).
doi: 10.14429/dsj.73.17759
2. Shankar, M.R.; Niranjanappa, A.C.; & Dattaguru, B. Aero structural and electromagnetic design optimisation of maritime patrol aircraft radome using direct search algorithms. *Def. Sci. J.*, 2023, **73**(4), 394-401.
doi: 10.14429/dsj.73.17889
3. Saravanakumar.; Murugeshwari.; Kumar, Arvind & Raghawan, S. Substrate integrated waveguide-fed wideband circularly polarised antenna with parasitic patches, *Def. Sci. J.,* 2019, **69**(1).
doi: 10.14429/dsj.69.13049
4. Pelluri, Sambaiah.; Anmol, Jain & Kartikeyan, M.V. Novel dual-band SIW filter using Quad mode cavity. *Def. Sci. J.,* 2019, **69**(5), 453-57.
doi:10.14429/dsj.69.14950
5. Yang, T.; Zhao, Z.; Yang, D. & Nie, Z. Low Cross-polarization SIW slots array antenna with a compact feeding network. *IEEE Ante. and Wire Propa. Lett.*, 2020, **20**(2), 189-193.
doi: 10.1109/LAWP.2020.3043774
6. Li,W.; Liu, S.; Deng, J.; Hu, Z. & Zhou, Z. A Compact SIW Monopulse antenna array based on microstrip feed. *IEEE Ante and Wire Propa Lett.,* 2021, **20** (1), 93-97.
doi: 10.1109/LAWP.2020.3041485
7. Cai, S.; Liu, J.; & Long, Y. Investigation of SIW cavity-backed slot and patch antennas with conical radiation patterns. *IEEE Trans on Ante and Propa.,* 2020, **68** (8), 5978- 88.
doi: 10.1109/TAP.2020.2990312
8. Fan, C.; Wu, B.; Wang, Y.L.; Xie, H.Y. & Su, T. High-gain SIW filtering antenna with low H-plane cross polarization and controllable radiation nulls. *IEEE Trans on Ante and Propa.,* 2020, **69**(4), 2336-40.
doi: 10.1109/TAP.2020.3018595
9. Yi, X.; & Wong, H.; A wideband substrate integrated waveguide-fed open slot antenna. *IEEE Trans on Ante. and Propa.*, 2020, **68**(3), 1945-1952.
doi: 10.1109/TAP.2019.2948680
10. Qin, J.; Fu, X.; Sun, M.; Ren, Q. & Chen, A. Frequency reconfigurable antenna based on substrate integrated

waveguide for S-band and C- band applications. *IEEE Access,* 2021, **9**, 2839-2845.
doi: 10.1109/ACCESS.2020.3047540

11. Mukherjee, S. & Biswas, A. Design of self-diplexing substrate integrated waveguide cavity-backed slot antenna, *IEEE Ante and Wire Propa Lette*, 2016, **15**, 1775-78.
doi: 10.1109/LAWP.2016.2535169
12. Li, J.; Yang, S.; Gou, Y.; Hu J. &. Nie, Z. Wideband dual-polarized magnetically coupled patch antenna array with high port isolation. *IEEE Trans on Ante and Propa*, 2016, **64**(1), 117-125.
doi: 10.1109/TAP.2015.2502264
13. Lu Y.; & Lin, Y. A mode-based design method for dual-band and self-diplexing antennas using double T-stubs loaded aperture. *IEEE Trans on Ante and Propa*, 2012, **60** (12), 5596-5603.
doi: 10.1109/TAP.2012.2211852
14. Boyle, K.R.; Udink, M.; de Graauw A. & Ligthart, L.P. A dual-Fed, self-diplexing PIFA and RF front-end. *IEEE Trans on Ante and Propa*, 2007, **55**(2), 373-382.
doi: 10.1109/TAP.2006.889852
15. Mao, C.; Jiang, Z. H.; Werner, D. H.; Gao S.S. & Hong, W. Compact self-diplexing dual-band dual-sense circularly polarized array antenna with closely spaced operating frequencies. *IEEE Trans on Ante and Propa*, 2019, **67**(7), 4617- 25.
doi: 10.1109/TAP.2019.2911274
16. Priya, S.; Kumar, K.; Dwari, S. & Mandal, M.K. Circularly polarized self-diplexing SIW cavity backed slot antennas. *IEEE Trans on Ante and Propa*, 2020, **68**(3), 2387-92.
doi: 10.1109/TAP.2019.2938576
17. Khan A.A. & Mandal, M.K. Compact Self-diplexing antenna using dual-mode SIW square cavity. *IEEE Ante and Wire Propa Lette*, 2019, **18**(2), 343-47.
doi: 10.1109/LAWP.2018.2890790
18. Iqbal, A.; Al-Hasan, M.; Mabrouk I.B. & Nedil, M. Ultracompact quarter-mode substrate integrated waveguide self-diplexing antenna. *IEEE Ante and Wire Propa Lette*, 2021, **20**(7), 1269-73.
doi: 10.1109/LAWP.2021.3077451
19. Iqbal, A.; Tiang, J.J.; Lee, C.K & Mallat, N.K. SIW cavity backed self-diplexing tunable antenna. *IEEE Trans on Ante and Propa*, 2021, **69**(8), 5021-25.
doi: 10.1109/TAP.2021.3060024
20. Dash, S.K.K.; Cheng, Q.S.; Barik, R.K.; Pradhan, N. C. & Subramanian, K.S. A Compact triple-fed high-isolation SIW-based self- triplexing antenna. *IEEE Ante and Wire Propa Lette*, 2020, **19**(5), 766-70.
doi: 10.1109/LAWP.2020.2979488.
21. Iqbal, A.; Al-Hasan, M.; Mabrouk I.B. & Nedil, M.; Compact SIW-based self-quadruplexing antenna for wearable transceivers, *IEEE Ante and Wire Propa Lette*,, 2021, **20**(1), 118-122.
doi: 10.1109/LAWP.2020.3043258
22. Kumar, K.; Priya, S.; Dwari, S. & Mandal, M.K. Self-quadruplexing circularly polarized SIW cavity-backed slot antennas. *IEEE Trans on Ante and Propa*, 2020, **68**(8), 6419-23.
doi: 10.1109/TAP.2020.2970101
23. Li, M.Y.; Ban, Y.L. & Yan, F.Q. Wideband low-profile Ku-band transmitarray antenna. *IEEE Access*, 2021, **9**, 6683-88.
doi: 10.1109/ACCESS.2020.3048346
24. El-Hameed, A.S.A. & Sato, M. Antenna array for Ku-band MIMO GB-SAR. *IEEE Access*, 2021, **9**, 29565-572.
doi: 10.1109/ACCESS.2021.3058004
25. Cai, M.; Yan, Z.; Fan, F.; Yang S. & Li, X. Double-layer Ku/K dual- band orthogonally polarized high-efficiency transmitarray antenna. *IEEE Access*, 2021, **9**, 89143-89149.
doi: 10.1109/ACCESS.2021.3089489
26. Abdollahvand M.; Forooraghi K.; Encinar J.A.; Atlasbaf Z.; & Martinez-de-Rioja V. A 20/30 GHz reflectarray backed by FSS for shared aperture Ku/Ka-band satellite communication antennas. *IEEE Ante and Wire Propa Lett*, 2020, **19**(4), 566-570.
doi: 10.1109/LAWP.2020.2972024

CONTRIBUTORS

Dr Anand Swaminathan obtained his PhD in Information and Communication from Anna University, Chennai and working as Professor in ECE, Mepco Schlenk Engineering College, Sivakasi, India. His areas of interest are: Antenna design, AI & computer vision.
In the current study he has contributed in the design and development of diplexer antenna, laboratory tests, and simulation model design results.

Dr Preethi Elizabeth Navamani obtained her PhD in Information and Communication (Antenna Design) from Anna University, Chennai and working as Assistant Professor, Department of ECE, Saranathan College of Engineering, Tiruchirappalli, India. Her areas of interest include: Microstrip patch antenna design and optimisation.
In the current study she has contributed in the design and simulation model to improve the proposed method.

Defence Science Journal, Vol. 75, No. 1, January 2025, pp. 84-89, DOI : 10.14429/dsj.19950

Taking Control of Dead Zone of Radiolocation Station by the Automatic Acting Electro-Optic System

Elshan G. Hashimov[#,*] and Roman R. Maharramov[$]

[#]*Azerbaijan Technical University, Baku, Azerbaijan*
[$]*Military Scientific Research Institute, Baku, Azerbaijan*
[*]*E-mail: hasimovel@gmail.com*

ABSTRACT

In the article, in order to effectively detect unmanned aerial vehicles and create an effective radar location, a mathematical model of covering the dead zone of radiolocation stations with an electro-optical system installed on an automatically operating bench placed on a visual observation post, opened in the direction of the likely flight of the enemy, was built and a comparison was made on concrete examples. The aim of the research work is to build a mathematical model of the monitoring of the dead zone of the radiolocation station with the help of an electro-optical system mounted on an automatically operating bench placed on a visual observation post. The following problems are solved in the article: analysis of the characteristics of the radiolocation area; development of a mathematical model for evaluating the dead zone of radiolocation stations with an automatically operating electro-optical system mounted on a bench; assessment of the probability of the unmanned aerial vehicle passing through the field of view of the electro-optical system without detection. The following research methods are used to solve problems: synthesis, theoretical analysis, mathematical modeling, comparative analysis. The following results were obtained: an electro-optical system automatically operating with a rotation period of T=10 [sec] mounted on a bench will detect the UAV traveling a distance of 27 km, for 138 times in 23 minutes , with a rotation period of T=20 [sec] mounted on a bench will detect the UAV covering a distance of 18 km, for 27 times in 9 minutes , with a rotation period of T=20 [sec] mounted on a bench will detect the UAV covering a distance of 3 km 3 times in 1 min. From the comparison of the obtained numbers and the reports made on the basis of the obtained mathematical algorithm, it can be concluded that it is possible to detect unmanned aerial vehicles by means of 1 automatically operating electro-optical system installed on the bench.

Keywords: Unmanned aerial vehicle; Dead zone; Radiolocation field; Automatically operating bench; Radiolocation station; Electro-optical system

1. INTRODUCTİON

Due to the increased demand for UAVs that have been successfully tested in modern local conflicts and wars, the Patriotic War, Local anti terrorist operations in 2023, and the ongoing Russia-Ukraine war, the world's well-known scientific institutions and companies in this field are constantly developing new types of UAVs are working towards the creation and improvement of UAVs. UAVs differ from each other in terms of purpose, size, function, flight distance, level of autonomy, design and a number of other features.

The development of UAVs for Air defense systems has become one of the main problems. Air defense systems cannot timely detect UAVs that are small in size, relatively silent and flying at low altitudes. At the same time, special colors and protective layers are used in the manufacture of UAVs, which makes it difficult to detect them with the eye or vision devices.

With the emergence of UAVs, the task of combating them has become significantly more relevant. After detecting and identifying UAVs by radar stations, it is necessary to take measures for its neutralisation.

The conducted analyzes show that the use of air defense and radioelectronic warfare systems is considered effective for the application of all types of UAVs. Countermeasures against unmanned aerial vehicle based on the joint use of radioelectronic warfare and air defense systems are already actively used in the practice of local combat operations, as well as for the protection of strategic objects[1-8]

An important aspect of effective countermeasures to UAVs by air defense units is their early detection. Early detection of a drone helps save time and make the right decision against it.

Based on the conducted analyzes and current armed conflicts, we can note that many methods are effectively used to detect UAVs. One of the most effective methods used is the detection of UAVs through RLSs[9].

Radar stations, other types of troop detection means, in interaction with visual observation posts are effectively used means to control the airspace. In local anti-terrorist measures that took place in 2023, RLSs were also effectively used to control the airspace. Based on the analysis of the Patriotic

Received : 18 March 2024, Revised : 11 November 2024
Accepted : 14 November 2024, Online published : 10 January 2025

War in 2020, Local anti-terrorist measures in 2023, and many armed conflicts, it remains a problem to effectively detect and identify UAVs through RLSs, especially UAVs with a small effective reflection area[10].

The large number of applications of UAVs by the enemy requires the establishment of an anti-UAV system in every aviation and air defense unit of the Air Force. The issue of detecting and countering UAVs should be taken into account when building the system. In order to more effectively combat UAVs within the system, their rapid long-range detection as well as dead-cannon detection is an important factor[11].

A dead gap is a part of space above the head of a radar station that cannot be seen by RLS (Fig. 1). The presence of the part located above the head of the radar station is conditioned by the appropriate selection of the orientation diagram in the vertical plane, which depends on the relief of the area in the zone of influence of the station, the nature of the position, the height of the antenna and the technical parameters of the RLS. It is impossible to detect and track air targets in the space above the head of the radar station[12].

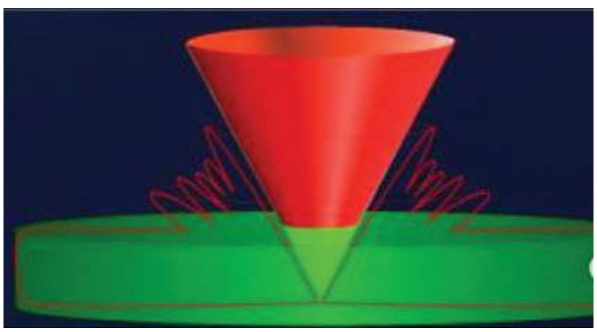

Figure 1. Dead zone (Zone on RLS).

1.1 Analysis of the Latest Studies and Publications

A literature review and analysis of other authors' articles and studies help provide more information and context on the issue. Below are examples of literature review results. Feasibility analysis of long-range detection of unmanned aerial vehicles using robotic telescopes was investigated[13]. In[14], the results obtained in the field tests of detection and tracking of UAVs operating at low altitude with a small effective reflection area and simultaneous detection of several UAVs using a sensor network were discussed, in[15] an efficient algorithm for detecting UAVs using cameras was presented. However, in none of these works, the issue of detection of UAVs in the dead zone was not investigated. In[16] the detection and tracking of small UAVs flying at low altitude, and at the same time the results obtained in the field tests of the detection of several UAVs using a sensor network consisting of acoustic antennas, small radar systems and optical sensors are discussed. In[17] is analyzed an autonomous drone detection and tracking system using a static wide-angle camera and a low-angle camera mounted on a rotating tower, proposed a combined multi-frame deep learning detection technique in which a frame from a zoomed-in tower camera is overlaid on a frame from a wide-angle static camera to make efficient use of memory and time. In[18], the problem of classification according to belonging to objects is solved by determining the spatial coordinates of the images of point objects found in the optical receiver system. An algebraic approach to solving this problem based on solving systems of linear equations with consideration of measurement noise is proposed.

The "Drone-Bird Detection Problem" was analysed to detect a drone appearing at a point in the video where birds may also be present[19]. A UAV detection framework based on video images was proposed. Depending on whether the video images are recorded by static cameras or moving cameras, it initially detects the regions containing the object by median background subtraction or deep learning-based object proposal method, respectively[20].

Problems encountered when using rapid test models are discussed in detail in the investigation of radars for air-fire control for operations[21].

The capabilities of special objects subjected to UAV attacks operating in a swarm are determined[22]. A countermeasure system against swarming UAVs is being discussed to protect specific objects from swarming UAV attacks. Currently used detection systems are analyzed and their application against swarming UAVs is revealed.

A sensor system is developed for high-energy lasers that will include detection using a single detector[23].

A literature review helps to understand the trends and progress for the detection of UAVs using an automatically acted bench-mounted electro-optical system. The use of samples helps to flesh out these approaches and technologies used by researchers to achieve the goal of detecting UAVs in a dead zone using mounted on an automatically operating bench electro-optical system.

The article considers the creation of an effective radiolocation area to increase the probability and effectiveness of the detection of UAVs. Thus, the detection of the UAV in the dead valley of the radar station through the electro-optical system installed on the automatically operating bench was considered and the evaluation results are being compared.

1.2 Purpose of the Research Work

To detect a UAV flying at a certain speed through how much electro-optical systems installed on an automatically operating bench, and is the calculation of the probability of passing without detection.

2. PERFORMİNG RESEARCH

2.1 Setting Issue of Evaluating the Invisible Zone Above the Head of the Radar Station by Means of Automatic Cameras Placed at the Visual Observation Post

Detection of UAVs and creation of an effective radar field, using an automatically operating camera placed on a visual observation post, control of the RLS dead gap can be organized in different ways. These methods differ from each other mainly depending on the rotation speed of the automatically operating camera placed on the visual observation post, the detection distance of the RLS, how the camera is directed and its viewing angle. It is clear that the implementation of an automatically operating camera placed in a visual observation post will reduce the dead gap of RLS.

The issue raised within the framework of this study is the development of a mathematical model of the detection of UAVs in a dead ravine depending on the number and speed of rotation of the camera.

2.2 Investigating of Problem Solving

The target detection distance of the RLS operating in the position d, and the characteristic angle of the dead zone (sector left out of observation) by α. It is clear that the radar station's unobserved zone can be described as a truncated cone, and the height of this cone is calculated by the Eqn.

$$h = dctg\frac{\alpha}{2} \tag{1}$$

It is assumed that near the radiolocation station (at a distance of $(10 \div 20[m])$ N number of electro-optical systems are placed on a rotary table to detect UAVs entering its unobserved sector (Fig. 2). Compared to the dimensions of the observation coverage of RLS, the distance between the camera placed on the visual surveillance post and the station operating in the position is very close, it can be considered with a fairly large accuracy that the point where the bench is located coincides with the point where the RLS is located. It is assumed that the bench rotates at a constant speed and its period of rotation T [m] is known.

It is also assumed that all electro-optical systems are of the same type and their viewing angle φ is known. Electro-optical systems are oriented so that their angle of view allows detection of UAVs that may enter the RLS's dead zone (to the unobserved zone).

A cross-section of an electro-optical system's viewing angle along the vertical plane can be described as the triangle OAB shown in Fig. 2. The passing of the UAV the distance AB at such plane can be considered as passing it from the control zone of the electro-optical system. Rotation of bench causes the formation of an annular viewing line around the RLS at the viewed altitude whose width is equal to $f \equiv |AB|$. If we consider the Eqn. (1), the distance f from the triangle OAB can be calculated as follows[24]:

$$|BC| = htg\left(\frac{\alpha}{2} - \varphi\right) \tag{2}$$

$$|AB| = d - |AB| = d - htg\left(\frac{\alpha}{2} - \varphi\right) = d - d\frac{\text{tg}\left(\frac{\alpha}{2} - \varphi\right)}{\text{tg}\frac{\alpha}{2}}, \tag{3}$$

$$f = d\left(1 - \frac{\text{tg}\left(\frac{\alpha}{2} - \varphi\right)}{\text{tg}\frac{\alpha}{2}}\right). \tag{4}$$

Let us estimate the probability that a UAV flying at a certain speed V will go undetected by the camera, depending on the number of cameras placed on the visual observation post.

It is clear that the time $\Delta t = f / V$ is required for the UAV flying at the speed V to cover the distance f müddəti tələb olunur and if the condition $\Delta t \geq T / N$ or

$$N\Delta t \geq T \tag{5}$$

is met, such UAV cannot cross the viewing line, avoiding the control of this or that electro-optical system. The Eqn. (5) allows to determining the maximum cycle time for the detection of UAVs moving at the considered speed by the N number electro-optical systems.

However, the speed of rotation of the used bench can increase due to various technical reasons. Suppose that inequality (5) is not satisfied, in other words,

$$N\Delta t < T \tag{6}$$

In this case, let's estimate the probability that the UAV will pass through the viewing zone of the electro-optical system without being detected.

Each electro-optical system rotates on the bench and reaches the location of the other electro-optical system relative to the Earth in T / N time. If condition (6) is satisfied, this period can be divided into 2 parts: $(0, \Delta t)$ and $(\Delta t, T/N)$. If we apply the geometric probability Eqn., the probability of the UAV passing through the viewing zone of the electro-optical system without detection is calculated as follows[25]:

$$P = \frac{\frac{T}{N} - \Delta t}{\frac{T}{N}}, \tag{7}$$

or

$$P = 1 - \frac{N\Delta t}{T}. \tag{8}$$

As can be seen from the Eqn. (8), as the cycle time of the bench increases, the probability of the UAV passing through the viewing area without being detected increases.

3. EVALUATİON OF LAYOUT SCHEMES (OPTIONS)

3.1 Option 1

Suppose that the characteristic invisible zone above the head of the station is α=120°, flight speed of dangerous UAV v=70[km/h], detection distance of a radiolocation station d=35[km]. One electro-optical system is installed on an automatically rotating bench located near the radiolocation station (Fig. 2). Let's accept that the rotation period of the bench is T=10[san], the distance seen by the camera L_v=40[km], angle of view is $\varphi = 40°$. In this case, to determine the number of automatically operating electro-optical systems installed on the bench, let's evaluate the considered variant (scheme) of the detection of the UAV in the dead zone:

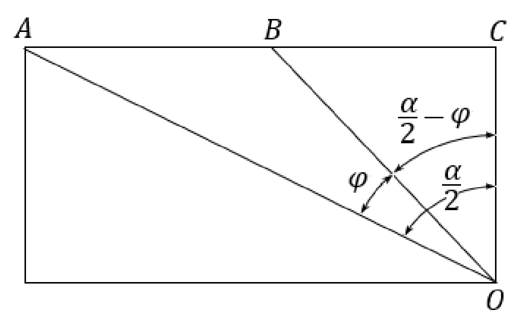

Figure 2. Calculation of the width of the annular control zone.

$$f = d\left(1 - \frac{\text{tg}\left(\frac{\alpha}{2} - \varphi\right)}{\text{tg}\frac{\alpha}{2}}\right); \tag{9}$$

$$f = 35\left(1 - \frac{\text{tg}\left(\frac{120°}{2} - 40°\right)}{\text{tg}\frac{120°}{2}}\right) = 35\left(1 - \frac{\text{tg}20°}{\text{tg}(60°)}\right) = 27,64516\,km \tag{10}$$

$$\Delta t = f / V = \frac{27,64516}{70} \approx 23\text{min} = 1380\,sec \tag{11}$$

$$N \geq \frac{T}{\Delta t}\frac{10\,sec}{1380\,sec} = 0,00725 \tag{12}$$

Since the condition N≥0,00725 is satisfied we can conclude that to detect the unmanned aerial vehicle flying at a speed of *v*=70[*km*/*h*] one electro-optical system should be installed on the rotary bench. Based on the obtained numbers, we can say that the UAV will cover the distance AB in 23 minutes. This means that the electro-optical system automatically operating with a rotation period of *T*=10[*sec*] mounted on the bench will detect the UAV 138 times in 23 min., covering a distance of 27,64516 km.

3.2 Option 2

Suppose that the characteristic invisible zone above the head of the station is α=120°, flight speed of dangerous UAV is *v*=120[*km*/*h*], detection distance of a radiolocation station is *d*=35[*km*]. One electro-optical system is installed on an automatically rotating bench located near the radiolocation station (Fig. 2). Let's accept that the rotation period of the bench is *T*=20[*sec*], the distance seen by the camera L_v=40[*km*], angle of view is $\varphi = 20°$. In this case, to determine the number of automatically operating electro-optical systems installed on the bench, let's evaluate the considered variant (scheme) of the detection of the UAV in the dead zone:

$$f = d\left(1 - \frac{\text{tg}\left(\frac{\alpha}{2} - \varphi\right)}{\text{tg}\frac{\alpha}{2}}\right); \tag{13}$$

$$f = \left(1 - \frac{\text{tg}\left(\frac{120°}{2} - 20°\right)}{\text{tg}\frac{120°}{2}}\right) \tag{14}$$

$$f = 35\left(1 - \frac{\text{tg}40°}{\text{tg}(60°)}\right) \approx 18\,km; \tag{15}$$

$$\Delta t = f / V = \frac{18}{120} = \frac{18}{120} \approx 9 = 540\,sec \tag{16}$$

$$N \geq \frac{T}{\Delta t} = \frac{20\,sec}{540\,sec} = 0,03704; \tag{17}$$

Since the condition $N \geq 0,03704$ is satisfied we can conclude that to detect the unmanned aerial vehicle flying at a speed of *v*=120[*km*/*h*] one electro-optical system should be installed on the rotary bench. Based on the obtained numbers, we can say that the UAV will cover the distance AB in 9 min. This means that the electro-optical system automatically operating with a rotation period of *T*=20[*sec*] mounted on the bench will detect the UAV 27 times in 9 min., covering a distance of 18 km.

3.3 Option 3

Suppose that the characteristic invisible zone above the head of the station is α=120°, flight speed of dangerous UAV is *v*=150[*km*/*h*], detection distance of a radiolocation station is *d*=10[*km*]. One electro-optical system is installed on an automatically rotating bench located near the radiolocation station (Fig. 2). Let's accept that the rotation period of the bench is *T*=20[*sec*], the distance seen by the camera L_v=40[*km*], angle of view is $\varphi = 10°$. In this case, to determine the number of automatically operating electro-optical systems installed on the bench, let's evaluate the considered variant (scheme) of the detection of the UAV in the dead zone:

$$f = d\left(1 - \frac{\text{tg}\left(\frac{\alpha}{2} - \varphi\right)}{\text{tg}\frac{\alpha}{2}}\right); \tag{18}$$

$$f = 10\left(1 - \frac{\text{tg}\left(\frac{120°}{2} - 20°\right)}{\text{tg}\frac{120°}{2}}\right) = 10\left(1 - \frac{\text{tg}50°}{\text{tg}(60°)}\right) \approx 3\,km; \tag{19}$$

$$\Delta t = f / V = \frac{3}{150} \approx 1\text{min} = 60 \text{ sec}; \tag{20}$$

$$N \geq \frac{T}{\Delta t} = \frac{20}{60} = 0,33\,sec. \tag{21}$$

Since the condition $N \geq 0,33$ is satisfied we can conclude that to detect the unmanned aerial vehicle flying at a speed of *v*=150[*km*/*h*] one electro-optical system should be installed on the rotary bench. Based on the obtained numbers, we can say that the UAV will cover the distance AB in 1 min. This means that the electro-optical system automatically operating with a rotation period of *T*=20[*sec*] mounted on the bench will detect the UAV 3 times in 1 min, covering a distance of 3 km.

4. CONCLUSİON

In this work, the issue of keeping the invisible zone on the head of the RLS under control by means of cameras placed on the visual surveillance post was investigated. Taking into account the angle of view of the camera, the distance it can see, the invisible zone above the head of the RLS, the height at which the drone can enter the invisible zone above the head of the RLS, the number of cameras placed on the visual reconnaissance post and the distance between the stations, according to the reports made, the invisible zone above the head of the station it is possible to detect UAVs in the zone through cameras placed at the visual observation post.

As a result, we can note that according to the reports made on the basis of the obtained mathematical algorithm, it is possible to detect unmanned aerial vehicles by means of 1 automatically operating electro-optical system installed on the bench.

REFERENCES

1. Brzozowski, M.; Pakowski, M.; Nowakowski, M.; Myszka, M. & Michalczewski, M. Radiolocation devices for detection and tracking small high-speed ballistic objects - features, applications, and methods of tests,

Sensors, 2019, **19**(24), 5362.
doi:10.3390/s19245362

2. Makarenko S.I., Timoshenko, A.V. & Vasilchenko, A.S. Counter unmanned aerial vehicles. Part 1. Unmanned aerial vehicle as an object of detection and destruction. *Syst. Control, Commun. and Security*, 2020, 109-146.
doi: 10.24411/2410-9916-2020-10105.
3. Hashimov E.G. & Huseynov B.S. Some aspects of the combat capabilities and application of modern UAVs , *National Sec. Military Knowl.,* 2021. **3**(7). https://mod.gov.az//images/pdf/7440712d93276d13d09990c7a1e203ea.pdf
4. Fioranelli, F.; Ritchie, M.; Griffiths, H. & Borrion H. Classification of loaded/unloaded micro-drones using multistatic radar, *Elect. lett*, **51**(22), 1813-1815.
doi: 10.1049/el.2015.3038
5. Bayramov, A. & Hashimov, E. Application SMART for small unmanned aircraft system of systems. In Shmelova, T., Sikirda, Y. & Sterenharz, A. (eds.) Handbook of Research on Artificial Intelligence Applications in the Aviation and Aerospace Industries, 2019, **8**, pp. 193–213.
doi: 10.4018/978-1-7998-1415-3.ch008
6. Hashimov, E.G. & Maharramov R.R. Prospects for the creation of automatic control systems to counter UAVs in air defense systems. Applied aspects of scientific activity in the field of defense and state security. *In* International Military Scientific Conference, Minsk, 29 April, 2021, pp.53-54
7. Bayramov, A.A.; Hashimov, E.G. & Nasibov, Y.A. Unmanned aerial vehicle applications for military GIS task solutions. Research anthology on reliability and safety in aviation systems, spacecraft, and air transport, 2020, 1092–1115.
doi: 10.4018/978-1-7998-5357-2.ch044
8. Hashimov, E.G. & Maharramov, R.R. Prospects for the development of air defense systems against UAVs : Modern directions of development of information and communication technologies and management tools. *In* Abstracts of reports of the 11th international scientific and technical conference, April 8-9, 2021, **1**, pp. 31-32. https://repository.kpi.kharkov.ua/server/api/core/bitstreams/2fa5a5f5-b105-40b8-a06c-46b24149434e/content
9. Angelo, Coluccia; Gianluca, Parisi & Alessio, Fascista. Detection and classification of multirotor drones in radar sensor networks: A review. *Sensors*, 2020, **20**(15), 4172.
doi: 10.3390/s20154172
10. Zhang Chi.; Zhang, C.; Kong, R.; Xing, S. & Zhang, Jiao. An overview of countermeasures against low-altitude, slow-speed small UAVs *In* International Symposium on Advanced Launch Technologies (ISALT 2022), – Journal of Physics: Conference Series.
doi: 10.1088/1742-6596 / 2460/1/012164
11. Yeremin, G.V.; Gavrilov, A.D. & Nazarchuk, I.И. Small-sized unmanned aerial vehicles are a new problem for air defense. Courage [Electronic resource]. 29.01.2015, **6**(14). http://otvaga2004.ru/armiya-i-vpk/armiya-i-vpkvzglyad/malorazmernye-bespilotniki/
(Accessed on 11 December 2019)
12. Hashimov, E.G.; Maharramov, R.R.; Muradov, S.A. & Katexliyev, V. Methods of detection of UAVs operating in the dead canyon through RLS // Patriotic war: 44-day victory chronicle. Materials of the republican scientific-practical conference dedicated to the 2nd anniversary of the victory in the 44-day Patriotic war, November 2-3, 2022. 176-178. https://mod.gov.az//images/pdf/029381d6e12e305ad5765d068086f6ac.pdf
(Accessed on 11 December 2019)
13. Sudenko S.A. What is a radar detection dead zone and how to determine it? https://studfile.net/preview/8961005/page:11/.
(Accessed on 21 December 2019)
14. Denis, O. Feasibility analysis of optical uav detection over long distances using robotic telescopes /O. Denis, S. Andreas, N. Christopher, S. Georg. *IEEE Trans. on Aero. and Elect. Systs,* 2023, **59**, 1-10.
doi:10.1109/TAES.2023.3248560
15. Wee, Kiong, Ang; Wei, S.T. & Yakimenko, O.A. Enabling an EO-sensor-based capability to detect and track multiple moving threats onboard suas operating in cluttered environments. A. Weekiong, S.T. Wei, O.A. Yakimenko . *In* Proceedings of the 2019 2nd International Conference on Control and Robot Technology, 2019, pp. 115-124.
doi: 10.1145/3387304.3387305
16. Thomas, Muller. Robust drone detection for day/night counter-UAV with static VIS and SWIR cameras, Karlsruhe. *In* Proc. of SPIE, 10190, 2017, 1-12.
doi:10.1117/12.2262575
17. Martin, L.; Sebastien, H.; Hommes, A.; Kloeppel, F.; Shoykhetbrod, A.; Thomas, G.; Winfried, J.; Naz, P. & Christnacher, F. Multi-sensor field trials for detection and tracking of multiple small unmanned aerial vehicles flying at low altitude. – may 2017. *In* Proc. of the SPIE, **10200**, pp. 13.
doi: 10.1117/12.2261930
18. Eren, U.; Emmanuel, Z.; Nicolas, R. & Paul-Edouard, D. Deep learning-based strategies for the detection and tracking of drones using several cameras. *IPSJ Trans. on Comp. Vision and Appl*., 2019, 2-13.
doi:10.1186/s41074-019-0059-x
19. Klochko, V.K. Processing moving object images in the optical receiver positioning system. *In* Proc. of the Int. Conference on Computer Graphics and Vision Graphicon, 2022, pp. 518-527. https://www.graphicon.ru/html/2022/papers/paper_053.pdf
20. Angelo, C.; Marian, G.; Tomas, P.; Geert, D.C.; Arne, S.; Lars, S.; Johannes, K.; Tobias, S.; Juergen, B.; IOSB; Mohammad, F.; Ruhallah, A.A.; Cemal, A.; Sinan, K.; Muhammad, S.; Nabin, S.; Sultan, D.K.M. & Michael, B. Drone-vs-bird detection challenge. *In* IEEE AVSS 2017. Lecce, 2017, pp. 1-6.
doi:10.1109/AVSS.2017.8078464
21. Arne, S.; Lars, S.; Johannes, K.; Tobias, S. & Jürgen, B. Deep cross-domain flying object classification for robust UAV detection. *In* 14th IEEE International Conference on Advanced Video and Signal Based Surveillance, - Lecce, 2017, **23**.
doi: 10.1109/AVSS.2017.8078558
22. Basha, M. & Ware, N.R. Design validation and reliability assurance of electronic systems using the next generation

RGT models. *Def. Sci. J.*, 2023, **73**(5), 594-601. doi:10.14429/dsj.73.18798
23. Nallamalli, R.; Singh, K. & Kumar, I.D. Technological perspectives of countering UAV Swarms. *Def. Sci. J.*, 2023, **73**(4), 420-428. doi:10.14429/dsj.73.18695
24. Gogoi, T. & Kumar, R. Design and development of a laser warning sensor prototype for airborne application. *Def. Sci. J*, 2023, **73**(3), 332-340. doi:10.14429/dsj.73.18662
25. Merzlyak, A.G.; Polonsky, V.B. & Yakir M.S. Geometry. Textbook for 9th grade of general education institutions. Kh.: Gymnasium, 2009, − 272.
26. Bronshtein, I.N.; Semendyayev, A.K.; Musiol, G. & Muehlig H. Probability theory and mathematical statistics. *In* Handbook of Mathematics. Springer, Berlin, Heidelberg. doi:10.1007/978-3-540-72122-2_16

CONTRIBUTORS

Dr Elshan Hashimov obtained his Doctor of Philosophy in National Security and Military Sciences from the National Defense University. Currently, he is working as a Professor at National Defense University, Technical University and Military Scientific Research Institute. His areas of interest are: Military education and military science, geographic information systems, UAVs, target detection, analysis of modern warfare.
In the current study, the author carried out the work related to the formulation of the problem, the investigation of the problem, and the preparation of the reports.

Mr Roman Maharramov is an adjunct at the Military Scientific Research Institute. His areas of interest are: UAVs and application of air defense system against UAVs.
In the current study, the author was involved in the preparation of the introduction, conducting research and reports, and reviewing the literature.

Defence Science Journal, Vol. 75, No. 1, January 2025, pp. 90-99, DOI : 10.14429/dsj.20106

Defence Locator Beacon: Integrating SHF Body-Wearable Antenna with Multifunctional Frequency Selective Surface

Pooja Bhatt[#,*], Rashmi Pandhare[$] and Saurabh Shukla[!]

[#]*IPS Academy, Institute of Engineering & Science, Indore - 452 009, India*
[$]*Indian Institute of Information Technology, Nagpur - 441 108, India*
[!]*DRDO-Directorate of PARO&M, Delhi-110 011, India*
[*]*E-mail: poojabhatt2505@gmail.com*

ABSTRACT

The integration of a Super High Frequency (SHF) on-body antenna with Frequency Selective Surfaces (FSS) marks a significant advancement in defense beacon technology. This study presents a unique, wearable, apple-shaped SHF antenna incorporating a multifunctional FSS for use as a Defense Locator Beacon (DLB). Key features include high gain, highly directional radiation pattern, low Specific Absorption Rate (SAR), reduced Radar Cross Section (RCS), and compact dimensions. The antenna, made on denim fabric, operates across the entire SHF band. With a 9-cell FSS array on a semi-flexible RT Duroid substrate, the structure is both simulated and fabricated, showing enhanced performance: peak gain increased from 7.14 to 11.1 dBi, FBR from 3.58 dB to 19.87 dB, and RCS reduced from -25 to -50 dB. Link Budget Analysis confirms effective communication, with ranges of 67 m and 64 m for 100 Mbps and 200 Mbps. The proposed antenna ensures high-speed communication and accurate location identification for military personnel.

Keywords: Compact; Defence; Flexible; FSS; Link margin; RCS; SAR

NOMENCLATURE

ε_r	: Relative permittivity
f_L	: Lower frequency
$P_{backward}$	: Backward power
ΔT	: Change in temperature
$P_{forward}$	: Forward power
Σ	: Tissue's conductivity (S/m)
β	: Propagations Constant
φ_{fss}	: Reflection phase of FSS
E	: Electric field (V/m)
ρ	: Tissue's mass density (kg/m^3)

1. INTRODUCTION

In modern defence operations, the seamless exchange of information and precise location identification are pivotal for mission success and the safety of deployed personnel. High gain antennas stand as indispensable assets within the arsenal of military communication systems, facilitating rapid data transmission and accurate positioning across diverse operational environments. High-speed communication enables seamless integration of location information into command and control systems, allowing commanders to monitor the location of individual soldiers, units, or assets in real-time. This enhances situational awareness, enables more effective decision-making, and supports mission planning and execution by ensuring that personnel are properly positioned and deployed according to operational requirements[1-4]. In the dynamic and often challenging landscapes of Defence operations, these antennas ensure reliable connectivity, even amidst obstacles, interference, or GPS limitations. When integrated into wearable communication systems, high gain antennas empower soldiers with the ability to transmit and receive critical data swiftly; fostering enhanced situational awareness and informed decision-making on the battle-field[7-9].

Existing defence locator beacons utilise technologies such as GPS, satellite communication, and radio frequency transmissions to broadcast distress signals and facilitate search and rescue efforts. While these beacons have proven effective in many scenarios, they often face challenges such as large, bulky, susceptibility to jamming, and inadequate transmission range in certain environments. Despite their utility, current defence locator beacons suffer from several limitations that hinder their effectiveness in demanding military operations. The proposed next-generation defence locator beacon addresses these challenges through innovative design features and advanced technologies.

The linch pin of location identification lays in the excellent quality of gain and highly directional radiation patterns. The main objective of DLB is to send a distress signal. Integration of SHF on-body wearable antenna, augmented with FSS presented here is a groundbreaking advancement in defence beacon technology. The result is a substantially enhanced gain and highly directional radiation signatures, rendering the defence personnel more resilient to location surveillance. Long range communication reliability is paramount in mission scenarios

Received : 16 April 2024, Revised : 11 July 2024
Accepted : 12 August 2024, Online published : 10 January 2025

and is conferred by the Link Margin Analysis presented here. The set-up involves the incorporation of 3×3 array. Antenna is fabricated on denim which is completely flexible material and FSS is fabricated on RT-Duroid that is again a semi-flexible material. A very low value of SAR ensures soldier's safety. All these qualities make the proposed next-generation defence locator beacon perfect for seamless integration into existing military infrastructure, including communication networks, satellite systems, and search and rescue protocols.

2. LITERATURE REVIEW

To comprehend to the multifunctional capabilities of the antenna proposed in this paper, it is compared with some similar work done in previous literatures. Table 3 displays some important attributes and depicts how the proposed design is better than the rest.

The work done in the literature suffices some attributes but not all. The studies are more or less showing similar work done with non-flexible material using FSS to enhance gain[3-5]. The values are good however, not body-wearable. The designs have used semi-flexible materials and does not ensure human safety as SARs are not calculated[4,6]. Work done has computed RCS of 10 dB, that is again far less than the 25 dB achieved by the proposed design[10]. Work display good values of SAR however the gain achieved are very less[11-12]. All the above literature does not show link budget analysis hence cannot be said to have accurate and high speed data rate needed for defence or military location identification systems.

It is evident that the proposed design is a mixed study that covers all the necessary aspects that are essential in successful application and demonstration of a Defence Locator Beacon. Such collaborative work is not to be seen in literature till date. This makes the design inevitably novel and highly beneficial for the said applications.

The synergy of these elements in a single design represents a significant advancement in the field. This novel approach not only pushes the boundaries of antenna design but also offers substantial practical benefits for Defence Locator Beacon applications. The comprehensive nature of this work, combining multiple optimisations that are typically addressed separately, makes it a unique and valuable contribution to the field.

3. ANTENNA FORMATION AND CHARACTERISTICS

This section delivers the formation of proposed antenna. The geometric configuration of the proposed architecture is shown in Fig. 1(a) displaying the front and back view of the proposed antenna. The antenna is designed on denim fabric

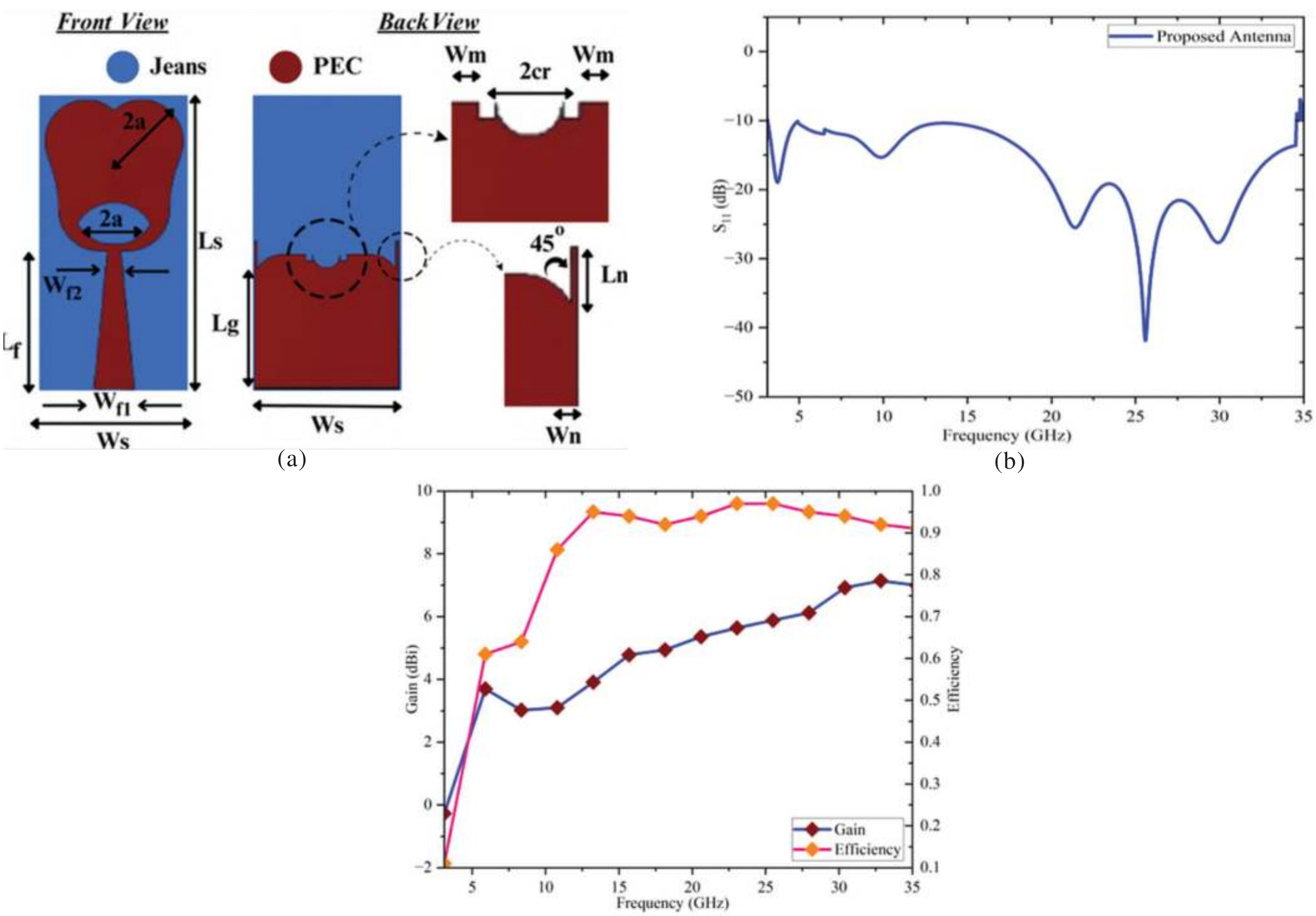

(c)

Figure 1. (a) Proposed Apple-Shaped Antenna (a) S_{11} (b) Gain (Left Y); and (c) Efficiency (Right Y) v/s Frequency.

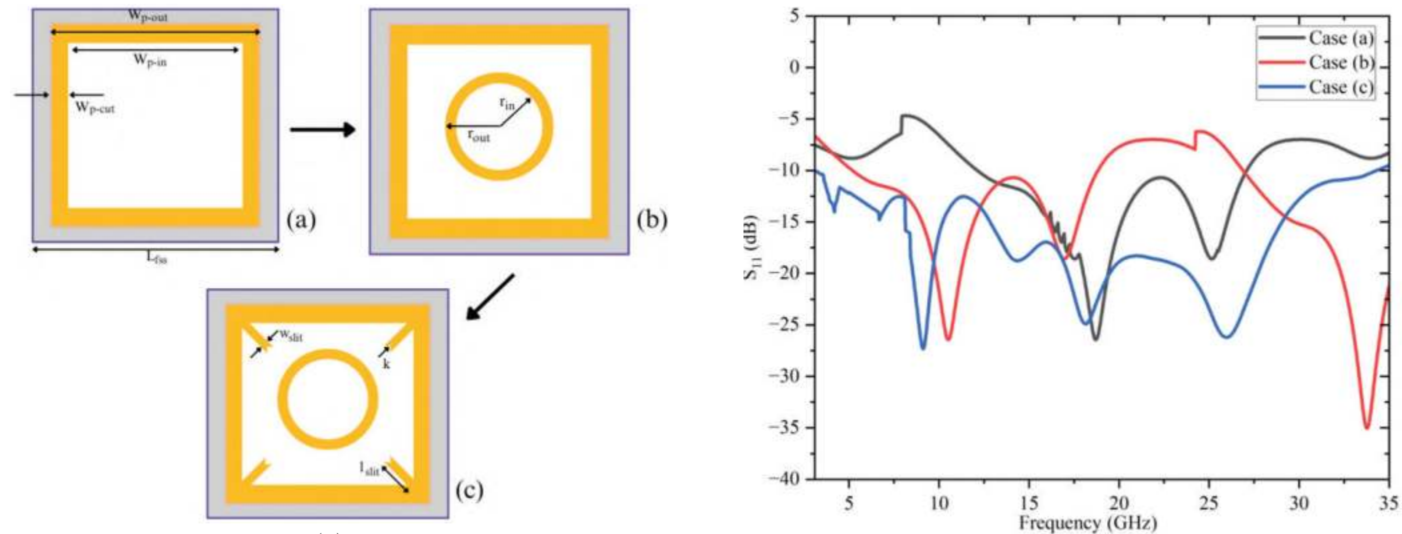

(a) (b)

Figure 2. (a) Stepwise formation of unit cell; and (b) S_{11} characteristics.

Table 1. Designed parameters of antenna and FSS

Designed parameters of antenna			Designed parameters of FSS		
Elements	**Description**	**Values (mm)**	**Elements**	**Description**	**Values (mm)**
L_s	Substrate length	21.5	L	Array length	45
W_s	Substrate width	10.5	L_{fss}	Unit length	15
a	Patch radius	3	$W_{p\text{-}in}$	Inner square length	12.3
W_{f1}/ W_{f2}	Feedline width	3,1	$W_{p\text{-}out}$	Outer square length	14
L_f	Feedline length	10.15	$W_{p\text{-}cut}$	Border width	1.7
L_g	Ground length	9.75	r_{in}	Inner circle radius	3
L_n	Notch length	2	r_{out}	Outer circle radius	4
W_n	Notch width	0.25	l_{slit}	Notch length	8.5
W_m	Square-slit width	0.5	w_{slit}	Notch width	0.5
cr	Circular slit radius	1	k	Cut	0.1

with relative permittivity of 1.65, loss tangent of 0.0009 and thickness 1 mm. The various parameters optimized are given in Table 1. The complete design consists of an apple-shaped patch with tapered feed and a leaf-shaped slot. The defected ground structure is used to obtain the maximum bandwidth and is achieved with circular and rectangular slits and notches introduced on the partial bent ground. Better notch characteristics help in effectively filtering out unwanted signals and interference from other communication systems, ensuring cleaner and more reliable signal reception and transmission[10-11]. This architecture furnished a huge bandwidth of 3.1 GHz till 34.5 GHz.

3.1 Reflection Coefficient Characteristics

The reflection coefficient S_{11} remain below -10 dB for the given range as shown in Fig. 1(b).

3.2 Gain and Efficiency Characteristics

Figure 1(c) plots the gain and efficiency graph for the entire frequency range. It is clear that the antenna acquires the highest gain of 7.14 dBi at 32GHz. Efficiency acquired is 96 % although at higher frequencies, the efficiency is reduced and that is to happen due to mismatch losses. It can be seen that gain at 3.1GHz is negative, hence a reduced efficiency of 11 %. FSS structures can enhance radiation characteristics by controlling the propagation of electromagnetic waves, leading to improved antenna performance in terms of signal strength and coverage area[3-4]. The advantage of incorporating FSS is discussed in details through all performance characteristics

3.3 FSS Formation

Unit cell is formed initially. It is printed on the 0.254 mm wide RT Duroid 5880 (Lossy) that has a permittivity of 2.2, and loss tangent of 0.0009.

The step-by-step making of a unit cell is shown in Fig. 2(a). The unit cell (L) dimension of FSS can be calculated approximately from Eqn. (1)[4]

$$L_{fss} = \frac{c}{4f_L\sqrt{(\varepsilon_r + 1)/2}} \quad (1)$$

In Fig. 2a(a), the square patch of side length14mm is constructed and another square with side of 12.3 mm is separated leaving the patch with bordered square of width 1.7

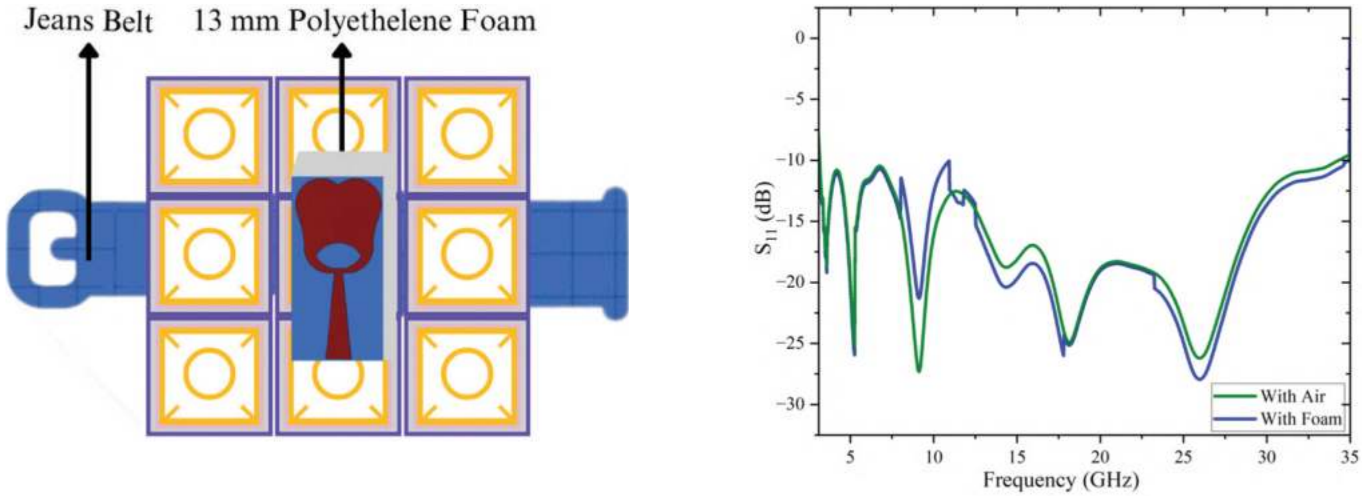

(a) (b)

Figure 3. (a) Complete set-up; and (b) S_{11} Comparison of air and foam filled structure.

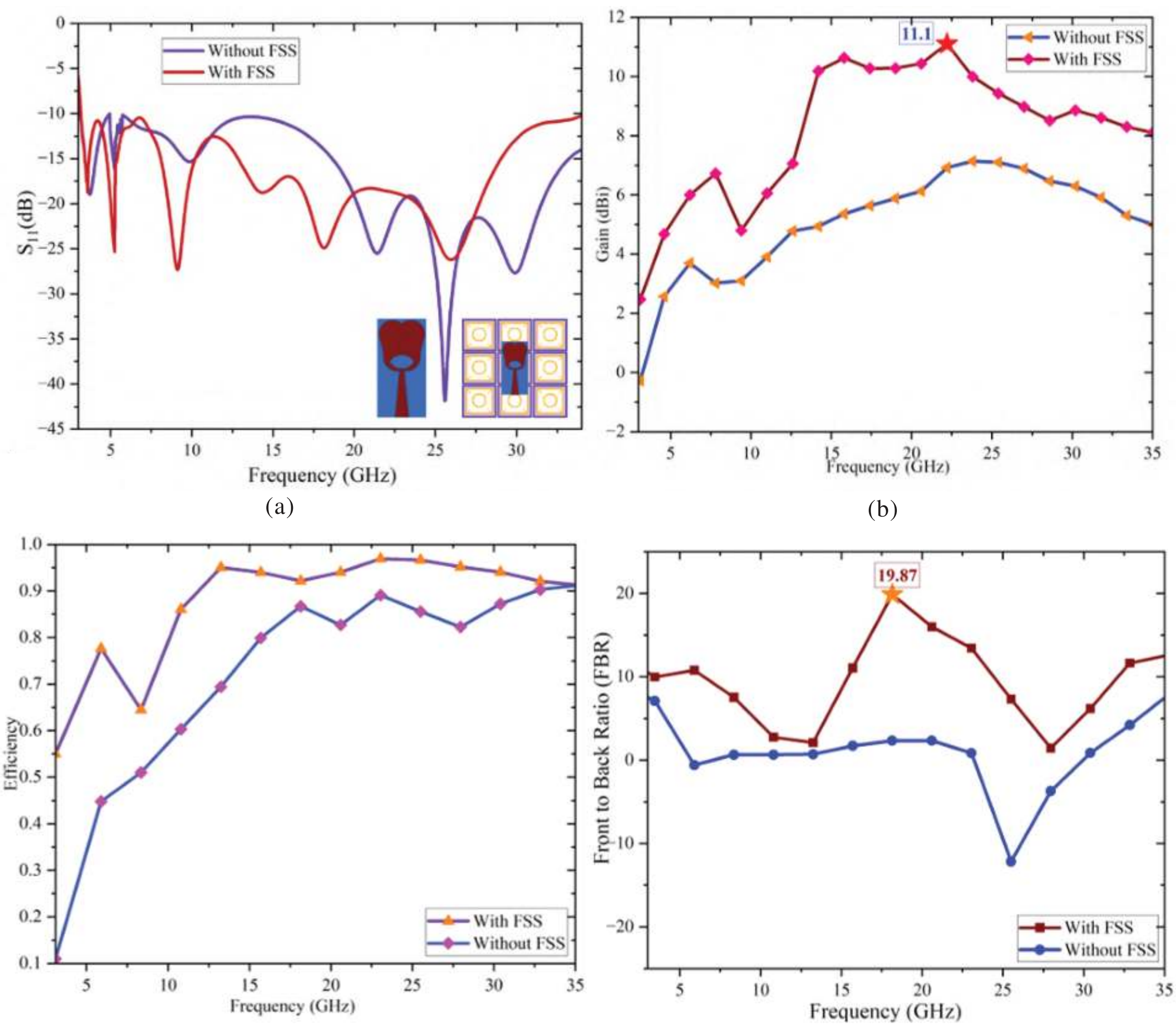

(a) (b)

(c) (d)

Figure 4. (a) S_{11}; (b) Gain; (c) Efficiency v/s Frequency; and (d) Analysis of FBR with and without FSS.

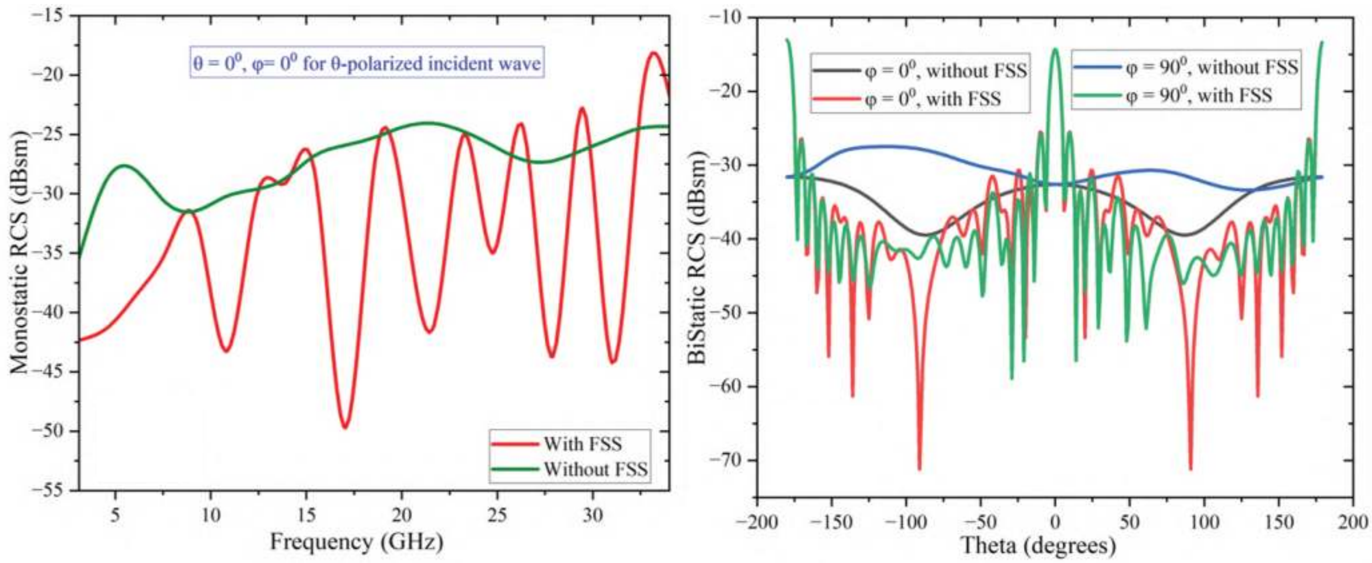

(a) (b)

Figure 5. (a) Monostatic RCS for θ-polarized incident wave; and (b) Bi-Static RCS for complete bandwidth.

mm. This provides the frequency bandwidth from 5.2 till 18.3 GHz. In Fig. 2a(b), a cylinder of outer and inner radius of 4 mm and 3 mm respectively is added to the patch. This results in the improvement in the frequency range from 4.7 till 23 GHz. Finally, in Fig. 2a(c), notches on 4 sides of square patch of 0.5 mm width and 8.5 mm length are added diagonally, due to which the bandwidth comes out from 3.1 till 34 GHz. By suppressing specific frequency bands, notch filters improve the overall signal-to-noise ratio[10-12]. The design parameters of FSS are given in Table 1. Reflection Coefficient characteristics for each of progression is shown in Fig. 2(b).

The FSS is a periodic structure inclusive of numerous unit cells in certain array form[5]. The proposed 9 unit cells are periodically added in 3×3 matrixes and the array is constructed with dimensions 45×45 mm^2 as shown in Fig. 3(a). The designed FSS deliver the required performance in terms of finer frequency resolution, sharper resonance peaks, and more intricate transmission/reflection characteristics.

4. ANTENNA-FSS PLACEMENT

When an antenna radiates electromagnetic waves, these waves propagate outward in all directions. However, when an FSS is placed behind the antenna, a portion of these waves will be reflected towards the antenna due to the presence of the FSS which ultimately enhances gain and that works if the electromagnetic waves radiated by antenna and those by FSS are in phase, hence satisfying following Eqn. (2)[6]

$$\varphi_{fss}-2\beta d=2n\pi;\ n=\cdots -2, -1, 0, 1, 2..$$

where, 'd' is distance between the FSS and antenna. Taking the center frequency 10.34 GHz, where there is zero phase reflection, the optimum distance d=12.85≈13mm (0.14 λ_0) was evaluated.

The antenna is intended to be worn on wrist of a defence personnel, realistically the gap is filled with a polyethylene foam (dielectric constant of 2.26, loss tangent of 0.00031, and density of 2.2lb) [7]. The width of foam is same as the distance. Fig. 3(a) depicts the final look of the set up. As the air is now replaced with foam, it is necessary to see the implications of the replacement in terms of S_{11} as shown in Fig. 3(b). The analysis confirms minimal impact of using polyethylene foam and no disturbance to impedance bandwidth.

5. PERFORMANCE ATTRIBUTES

Performance attributes prove that antenna is capable of doing the assigned duties especially commandeering a distress signal. This section compartmentalises the improvements and implications of FSS implementation to justify the said application to be used as DLB.

5.1 Electromagnetic Characteristics

S_{11} attributes are shown in Fig. 4(a) for antenna without and with FSS. It can be seen that bandwidth of antenna remain unaffected with the involvement of FSS.

5.2 Gain and Efficiency Characteristics

The main intention of FSS implementation is to achieve enhanced gain that is crucial for identifying locations of soldier whenever a distress signal is sent at an accurate level as it can transmit and receive signals over longer distances[8]. Figure 4(b) shows the improved gain over the entire frequency range. The negative gain at the lowest frequency is now improved to a positive value as expected from implementing FSS. The peak gain achieved was enhanced from 7.14 dBi to 11.1 dBi (at 23 GHz). Figure 4(c) shows the efficiency with FSS addition. Antenna has become more efficient now and hence can pick weaker signals and reject interference from other directions, leading to more reliable communication among the soldiers and command center[10-11]

5.3 Front to Back Ratio (FBR)

It refers to the power ratio between the maximum radiation intensity in the front beam direction versus the back direction of the antenna. A higher FBR value indicates the antenna is more directional and focuses more energy towards the front. This improves the signal quality in the intended direction which is an essential need for recognizing the locations of defence personnel. It is calculated using the Eqn. (3)[9]

$$FBR\ (dB) = 10\ \log 10\ (\frac{P_{forward}}{P_{backward}}) \quad (3)$$

Figure 4(d) shows the comparative analysis of FBR with and without FSS. The peak value achieved was from 3.58 to 19.87 dB (at 18 GHz).

6. RCS REDUCTION ANALYSIS

By controlling the scattering of electromagnetic waves, FSS minimises the delectability of antennas to radars, making them valuable components in defence applications where low observability is essential. Radar Cross Section (RCS) is a measure of how detectable an object is by radar. Larger RCS means the object will reflect more radar signals to the radar receiver, making it easier to detect. A smaller RCS means the object is harder to detect. Monostatic RCS is the typical radar configuration used in most military applications - the transmitter and receiver are co-located. FSS can be engineered to absorb or scatter incoming radar waves, thereby reducing the RCS[13]. The monostatic RCS results of the designed antenna with and without FSS is displayed in Fig. 5(a) under θ – polarised incident plane wave with magnitude of 1 V/m. Bi-static RCS over the entire frequency range for incident angle $\varphi=0^0$ and $\varphi=90^0$ is displayed in Fig. 5(b).

The results display excellent reduction in RCS over the entire frequency range. Peak Mono-RCS reduction achieved is from -25 dB till 50 dB around 17 GHz, average reduction of -25dB is seen across. This ensures the stealth capabilities of the proposed antenna. Bi-Static RCS can be seen for two values of φ, and dip of 25 to 30 dB is seen at -100< θ<100.

7. ON-BODY ANALYSIS

The designed wearable antenna system should allow military personnel to maintain continuous communication capabilities while on the move. Whether deployed on foot, in vehicles, or in urban environments, it should ensure that soldiers can maintain reliable connectivity without being encumbered by traditional fixed antennas or bulky communication equipment[14]. It is therefore paramount to understand the behavior of proposed antenna when it is worn on the wrist of the soldier. The antenna designed here ensures that kind of safety as it possess a very low SAR value well under the pre-mentioned standards of 1.6 W/kg for 1 g and 2 W/Kg for 10g of tissue.

It is calculated using Eqn. (4)[15]

$$\mathrm{SAR} = \sigma|\mathrm{E}|^2/\rho \quad (4)$$

The simulation and values are determined using CST 5-layer phantom model as shown in Fig. 6(a). Figure 6(b) displays the correlation of SAR with and without FSS.

(a)

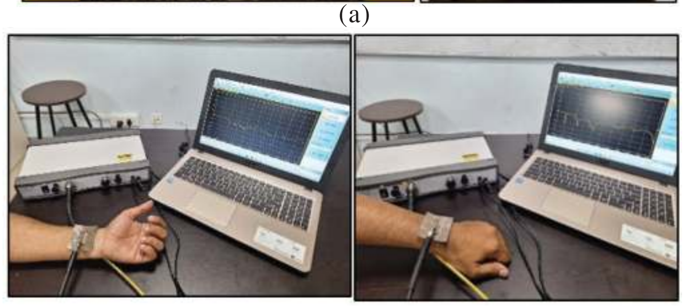

(b)

Figure 7. (a) Complete assembly–fabricated; and (b) Measurement set-up with VNA.

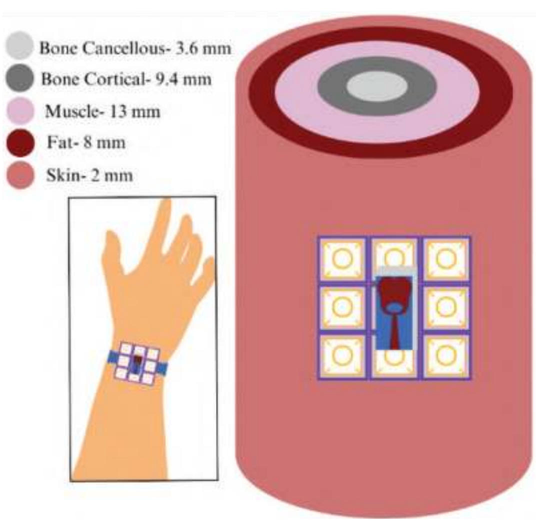

(a)

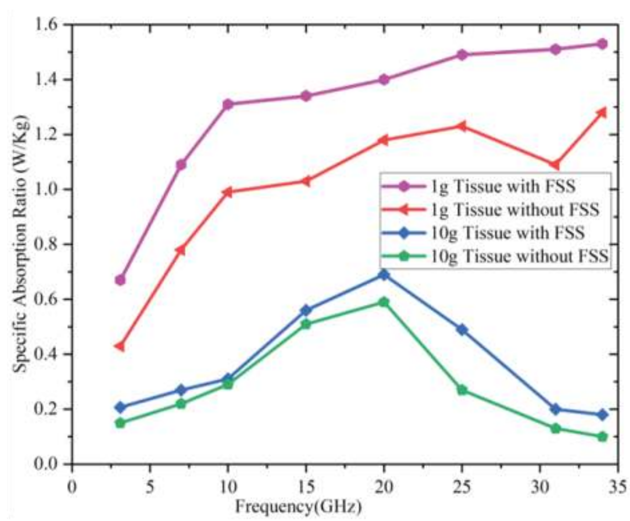

(b)

Figure 6. (a) Phantom model of tissue of wrist with antenna; and (b) SAR v/s Frequency for 1 g and 10 g tissues with and without FSS.

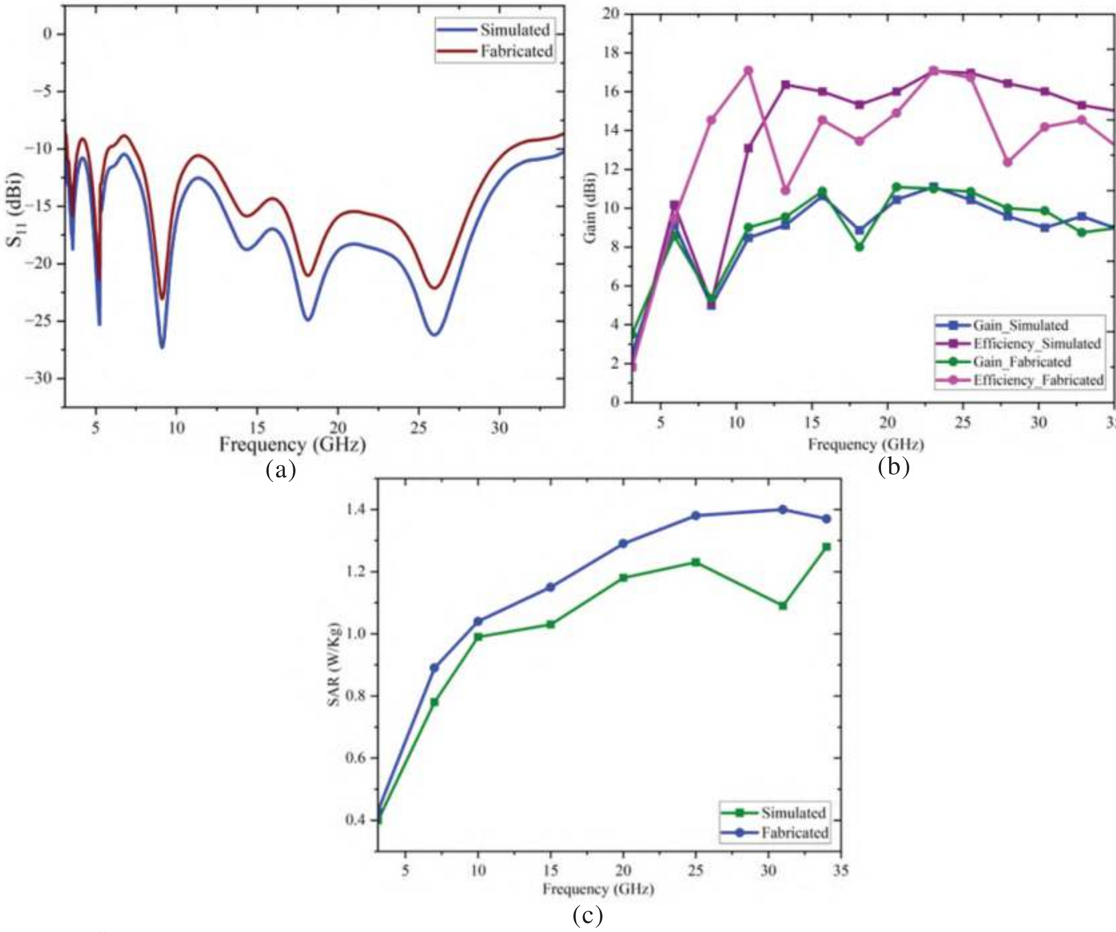

Figure 8. (a) S_{11}; (b) Gain (Left Y) and efficiency (right Y) v/s frequency; (c) SAR for simulated and fabricated values.

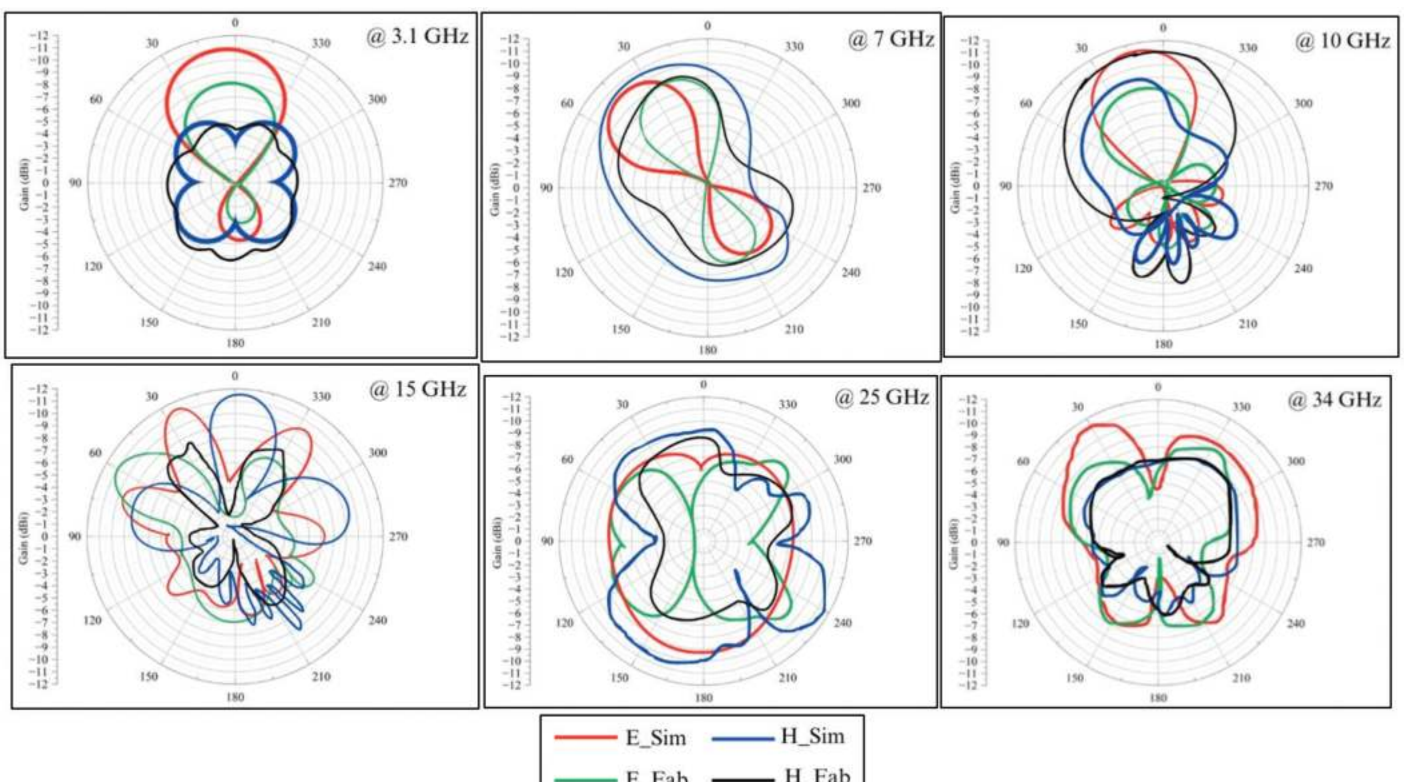

Figure 9. Radiation pattern of simulated and fabricated antenna – for 3.1, 7, 10, 15, 25 and 34 GHz.

It is clear that the antenna itself has a very low value of SAR and implementing FSS reduces it further. The peak SAR was found to be 1.51 W/kg and 1.4 W/kg for 1g tissue and 0.69 W/Kg and 0.59 W/Kg for 10 g tissue without and with implementation of FSS respectively.

8. PROTOTYPE MANUFACTURING

Antenna is fabricated on denim and multifunctional FSS is etched on RT Duroid 5880. Figure 7(a) shows the set up. For user comfort, a denim band of 0.5 mm thickness is attached at the back of FSS to work as a proper wrist band. VNA is connected to the set-up as shown in Fig. 7(a).

8.1 Electromagnetic Characteristics

Simulated and fabricated results of S_{11} can be seen in Fig. 8(a).

8.2 Gain and Efficiency Characteristics

Figure 8(b-Left-Y) shows the comparison of simulated and fabricated antenna gain. It can be seen that the highest gain acquired was 11 dBi at 23.05 GHz. The gain values are in good agreement. Similarly, when the efficiency was calculated as shown in Figure 8(b-Right-Y) along the frequency range and compared with the simulated ones, the values are analogous to each other.

8.3 On-Body Characteristics

The SAR values for the antenna itself were very low and implementation of FSS supported those measurements. The SAR was measured practically as well using Temperature Method with Eqn. (5)[8]

$$SAR=c(\Delta T/\Delta t) \quad (5)$$

where, 'c' is the heat capacity of a human skin and that value is 3391. Figure 8(d) displays the measured and simulated values

(a) (b)

Figure 10. Antenna set up working as transmitter on human wrist and receiver at a distance of 300 cm.

Table 2. Link margin at various frequencies

Frequency(GHz)	**5.5**		**10**		**25**		**34**	
FSS	**Without**	**With**	**Without**	**With**	**Without**	**With**	**Without**	**With**
Transmitter gain	0.947	1.41	4.19	4.64	5.89	6.29	7.04	7.85
Receiver gain	1.79	2.14	4.73	4.95	5.7	5.96	7.26	7.57
Data rate (B_r) (Mbps)	100/200	100/200	100/200	100/200	100/200	100/200	100/200	100/200
LM at 300 cm	**61.8/58.8**	**67.4/64.3**	**57.9/54.9**	**61/59.9**	**57.4/54.1**	**65.1/62.1**	**57.3/54.2**	**59.3/56.3**

Table 3. Related Works in terms of various attributes

Reference	**Dimensions**	**Frequency range**	**Material used**	**Peak gain**	**RCS (dB)**	**Link margin**	**SAR**
[1]	30x35	3.1-15	FR4	7.6	NP	NP	NP
[2]	16x22	3.1-18.6	FR4	9.4	NP	NP	NP
[3]	40x30	2.39-19.94	Rogers 6002	9.5	NP	NP	NP
[4]	30x40	2.27-5.55	FR4	7.3	NP	NP	NP
[5]	29x35	24.5-25.7	FR4	9	NP	NP	NP
[6]	50x50	2.2-12.7	FR4	11.5	NP	NP	NP
[7]	35x30	3.16-15	FR4	10.9	NP	NP	NP
[10]	24x29	2.92-7.36	FR4	8.87	10	NP	NP
[11]	9.4x11.3	4.72-6.19	polydimethylsiloxane	8.54	NP	NP	Yes
[12]	42x43	1.5-6	Flannel	3.35	NP	NP	Yes
Proposed	**10.5x21**	**3.1-34.5**	**Denim**	**11.1**	**Implemented and demonstrated**		

of SAR and it is evident that the antenna prototype is safe for human use.

8.4 Radiation Characteristics

2-D polar plots for simulated and measured radiation patterns of the designed antenna set-up for various frequencies are shown in Fig. 9 for 3.1 GHz, 7 GHz, 10 GHz, 15 GHz, 25 GHz and 34 GHz.

9. LINK MARGIN ANALYSIS

In military operations, real-time sharing of tactical information between different units, such as ground forces, aircraft, and naval vessels, is vital for situational awareness and coordination. Our goal is to ensure the DLB has strong strength of signal to provide the location of the soldier to the command center and back. In high-speed communication, maintaining a reliable link is essential to prevent data loss or interruption. Link budget analysis helps in evaluating link reliability by accounting for factors like fading, multipath propagation, and atmospheric conditions.

To comprehend to the link budget analysis, two identical antennas working as transmitter (T_x) and Receiver (R_x) respectively are placed at the wrist of human and at a distance of 300 cm respectively. The set up and practical approaches are depicted in Fig. 10. An ideal PSK modulation scheme is assumed, with a BER of 10^{-4} at an SNR of 9.64 dB for high data rates of 100Mb/s and 200 Mb/s. Link margin is calculated using following Eqn. (6)

$$LM=Ap(dB)-Rp(dB) \quad (6)$$

The results achieved are displayed in Table 2.

The improvement in communication strength can be seen as the FSS is implemented in Table 2. The LM improved from 61 m to 67 m for 100 Mbps and 59 m to 64 m for 200 Mbps. With the values acquired, it is undisputable to state the fact that the proposed antenna set up is entirely capable to work as a DLB for wide range distance and provide subtle and reliable high-speed communication.

10. CONCLUSION

The designed structure stands out as a cutting-edge solution tailored for Defence Locator Beacon applications. Its impressive gain signifies its ability to amplify signals efficiently and is pivotal for maintaining connectivity and locating defence personnel swiftly and accurately. Moreover, the antenna's exceptional reduction in RCS and FBR enhances stealth capabilities, signal integrity, reducing interference, enabling defence operations to maintain covert profiles. The antenna's compliance with SAR standards underscores its commitment to safety. Furthermore, the antenna's impressive Link margin facilitates high-speed data transfer which is instrumental in transmitting critical information swiftly and accurately. In summation, the multifaceted capabilities of this antenna make it an indispensable asset for defence and military endeavors, offering unparalleled performance in locating and safeguarding defence personnel through the Defence Locator Beacon technology, thereby bolstering national security and operational effectiveness.

REFERENCES

1. Aggarwal, I.; Pandey, S. & Tripathy, M.R.A High gain super wideband metamaterial based antenna. *J. Microwaves, Optoelectron. Electromagn. Appl.*, 2021, **20**(2), 248–273.
doi: 10.1590/2179-10742021v20i21147
2. Mondal, R.; Reddy, P.S.; Sarkar, D.C. & Sarkar, P.P. Compact ultra-wideband antenna: improvement of gain and FBR across the entire bandwidth using FSS. *IET Microw., Antennas & Propag.*, 2020, **14**(1), 66–74.
doi: 10.1049/iet-map.2019.0536
3. Tariq, S.; Hussain, Q.; Alzaidi, M.S.; Ghoniem, R.M.; Alibakhshikenari, M.; Althuwayb, A.A.; Virdee, B. S.;& Aslam, M.. Frequency selective surfaces-based miniaturized wideband high-gain monopole antenna for UWB systems. *AEU – Int. J. Electron. Commun.*, 2023, **170**,154841–154841.
doi: 10.1016/j.aeue.2023.154841
4. Tapas T.; Maity S.; Mukherjee, A.S.; Roy, A. & Bhunia S. FSS integrated high gain broadband antenna. *J. Nano-and Electr. Physics*, 2023,**15**(3), 03015-5.
doi: 10.21272/jnep.15(3).03015
5. Kalaiarasi M. & Dwivedi R.P.. Wideband high gain antenna using a slot loading and FSS for 5G Application. *J. Nano-and Electron. Physics*, 2023, **15**(4), 04013-5.
doi: 10.21272/jnep.15(4).04013
6. Mondal, K.; Sarkar, D.C. & Sarkar, P.P. 5×5 matrix patch type frequency selective surface based miniaturized enhanced gain broadband microstrip antenna For WLAN/ WiMAX/ISM band applications. *Prog. Electromagn. Res. C*, 2019, **89**, 207–219.
doi: 10.2528/pierc18110803
7. Pandhare, R.A.; Abegaonkar, M.P. & Chandresh Dhote. UWB antenna with novel FSS reflector for the enhancement of the gain and bandwidth. *Int J. Microw. Wirel. T.*, 2022, **14**(10), 1353–1368.
doi: 10.1017/s1759078721001781
8. Sagne, D. & Pandhare, R.A. SAR reduction of wearable SWB antenna using FSS for wireless body area network applications. *Sādhanā*, 2024, **49**(1).
doi: 10.1007/s12046-024-02427-w
9. Devarapalli, A.B. & Moyra T.. Design of a metamaterial loaded w-shaped patch antenna with FSS for improved bandwidth and gain. *Silicon*, 2022.
doi: 10.1007/s12633-022-02123-6
10. Mukherjee, S.D.; Roy, A.; Kundu S.; Sarkar, P.P. & Bhunia, S. Notch band characteristics improvement of a printed ultra wideband antenna by embedding frequency selective surface. *AEÜ. Int. J. Electron. Commun.,* 2024, **178**, 155276–155276.
doi: 10.1016/j.aeue.2024.155276
11. Mukherjee, S.D.; Roy, A.; Tewary T.; Dutta, K. & Bhunia S.. Electromagnetic band gap coupled tri-notched miniaturized ultra-wideband antenna loaded with slot and parasitic strip. *Int. J. Commun. Syst.,* 2023.
doi: 10.1002/dac.5565
12. Mukherjee, S.D.; Roy, A.; Tewary, T.; Sarkar, P.P. & Bhunia, S. Design of dual band-notched UWB hexagonal

printed microstrip antenna. *Int. J. Microw. Wirel. T.,* 2022, 1-9.
doi: 10.1017/s1759078722000447

13. Zheng, Y.; Gao, J.; Zhou, Y.; Cao, X.; Xu, L.; Li, S. & Yang, H. Metamaterial-based patch antenna with wideband RCS reduction and gain enhancement using improved loading method. *IET Microwaves, Antennas & Propagation*, 2021, **11**(9), 1183–1189.
doi: 10.1049/iet-map.2016.0746
14. Gao, G.; Meng, H., Geng, W., Zhang, B., Dou, Z., & Hu, B. Design of a wide bandwidth and high gain wearable antenna based on nonuniform metasurface. *J. Microwaves, Optoelectron. Electromagn. Appl.*, 2021, **63**(10), 2606–2613.
doi: 10.1002/mop.32937
15. Amit, S.; Talasila V.; Ramya, T.R. & Shashidhar, R. Frequency Selective surface textile antenna for wearable applications. *Wireless Personal Commun.*, 2023 **132**(2), 965–978.
doi: 10.1007/s11277-023-10644-5

CONTRIBUTORS

Ms Pooja Bhatt is a PhD Scholar at IIIT, Nagpur in Department of Electronics and Communication Engineering. She is working as an Assistant Professor in IPS Academy, Indore in Department of Electrical and Electronics Engineering. Her area of interests are wearable antennas.
In the current study, she has conceptualised and carried out the methodology and manuscript preparation.

Dr Rashmi A. Pandhare is an Assistant Professor at IIIT, Nagpur in Department of Electronics and Communication Engineering since 2019. She was awarded her PhD in Antennas. Her areas of interests are High gain, UWB and reconfigurable antennas. In this work, she has contributed in fabrication and measurement and reviewed/edited the manuscript for betterment.

Mr Saurabh Shukla is a Scientist 'F' at DRDO Delhi. His areas of research include: Design and development of various broadband electronically scanned antenna arrays for electronic warfare jammers.
In this study, he contributed in the search for requirements of wearable antenna in defence applications and helped with gaps and scope for improvement in location identification in defence and military systems.

Defence Science Journal, Vol. 75, No. 1, January 2025, pp. 100-110, DOI : 10.14429/dsj.20284

A Comprehensive Investigation of ESP32 in Enhancing Wi-Fi Range and Traffic Control for Defence Networks

A.K. Kowsalyadevi* and G. Umamaheswari

Department of Electronics and Communication Engineering, PSG College of Technology, Coimbatore - 641 004, India

**E-mail: akkowsalyadevi@gmail.com*

ABSTRACT

The study examines ESP32-based static and dynamic load-balancing algorithms to enhance defence networks' Wi-Fi range and traffic control. This study is essential due to the growing need for dependable and efficient wireless communication in defence operations, where maintaining network stability and performance is necessary. Real-time Wi-Fi scanning assessed the performance of these algorithms, covering response time, throughput, network latency, jitter, and packet loss. The static algorithm demonstrated a 5 % lower average response time and 3 % higher throughput than the dynamic algorithm, leading to significant improvements in jitter (from 1.01 ms to 0.80 ms) and packet loss rate (from 1.50 % to 0.88 %). On the other hand, dynamic load balancing reduced Access Points (APs) overload by 20 % during peak periods, enhancing network stability and resource utilisation, which is crucial for defence operations. These findings underscore the impact of ESP32-based load balancing, presenting a practical solution to optimise defense network performance by improving throughput scalability and Access Point (AP) resource efficiency. The study provides essential insights into managing signal variability, congestion, and disruptions, offering valuable guidance for defence and security professionals in optimising wireless network infrastructure.

Keywords: Wi-Fi coverage extension; Load balancing algorithms; ESP32 microcontroller; Network reliability; Real-time Wi-Fi scanning; Performance comparison

NOMENCLATURE

ACL	: Access control list
$T(x)$	: Throughput scalability
AI	: Artificial Intelligence
$R(x)$	: Response time
AP	: Access Point
$S(i)$, $S(x)$	: Signal strength for each APi, APx
AWS	: Amazon web services
$Q(i)$, $Q(x)$	: Quality for each APi, APx
BSSID	: Basic Service Set Identifier
n	: Number of APs
DHCP	: Dynamic host configuration protocol
SSID	: Service set identifier
DNS	: Domain name system
STA	: Station
DWLC	: Dynamic wireless load controller
IoMT	: Internet of military things
IoT	: Internet of things
IP	: Internet protocol
MQTT	: Message queue telemetry transport
NAT	: Network address translation
QoS	: Quality of service
RSSI	: Received signal strength indicator
SPI	: Serial peripheral interface

Received : 10 June 2024, Revised : 20 August 2024
Accepted : 05 September 2024, Online published : 10 January 2025

1. INTRODUCTION

The rapid expansion of the Internet of Things (IoT) and the Internet of Military Things (IoMT) necessitates a stable and adaptable communication infrastructure for defence and security applications[1-2]. Military operations rely on secure, reliable networks, and recent field exercises demonstrate that Wi-Fi technology can reduce communication failures by up to 30 % owing to its security, reliability, and cost-effectiveness[3]. Wi-Fi's efficiency, flexibility, and compatibility make it a viable alternative to 5G in remote or rapidly changing military environments[4]. Extending Wi-Fi range and ensuring reliable backhaul connectivity are critical, especially in disaster recovery scenarios[5].

However, current Wi-Fi solutions often rely on vulnerable physical infrastructure, leading to communication breakdowns during disasters[6]. Ad-hoc networking approaches lack sufficient range and effectiveness in post-disaster recovery operations, necessitating improved coverage extensions and traffic regulation technologies[7]. This study addresses connectivity challenges in military operations, especially in remote locations, by leveraging the ESP32 microcontroller as a Wi-Fi repeater and load balancer to extend coverage and regulate traffic[8].

The ESP32 microcontroller enhances network resource allocation and minimizes latency by balancing loads across multiple Access Points (APs), optimizing resource utilisation, and reducing congestion.[9]. Dynamic load balancing is crucial in high-demand situations, improving Quality of Service

(QoS) and network reliability by preventing AP overloads and reducing delays[10]. Static and dynamic load distribution mechanisms are compared, with the ESP32's dual-core architecture facilitating effective load balancing and real-time data processing[11].

The study aims to enhance Wi-Fi performance and reliability in critical situations by:

- Improving response time and throughput with ESP32-based load balancing.
- Reducing AP overloads through dynamic load redistribution.
- Optimising resource use by continuously adjusting connections.

Section 2 provides a detailed technical overview of ESP32 operation modes and load-balancing algorithms, highlighting configurations for single-core and dual-core setups tailored to diverse network environments. It covers experimental setups using ESP32 microcontrollers for load balancing, network extension, and performance enhancement through various operational modes and configurations. Section 3 compares static and dynamic load-balancing algorithms, highlighting their impact on performance metrics like response time, throughput, and network stability. The conclusion emphasises the effectiveness of ESP32-based load management and suggests future research directions in advanced algorithms to enhance network efficiency and adaptability, particularly in defence applications.

2. METHODOLOGY

This study uses the ESP32 microcontroller as a concept and a tool. It acts as a load balancer and a range extender. They programmed it to extend Wi-Fi coverage and enhance network performance. Built-in Access Control Lists (ACLs) ensure only authorised devices can access the network, bolstering security. Tools such as Wireshark integrate effectively with the ESP32, enabling detailed traffic analysis and detection of security threats[12]. The ESP32's Wi-Fi scanning capabilities detect nearby networks, enhancing performance and reducing latency. Additionally, it automates Internet Protocol (IP) address assignments using the Dynamic Host Configuration Protocol (DHCP), streamlining network management[13].

The ESP32's versatility is a critical factor in its effectiveness in network management and performance enhancement. Its Serial Peripheral Interface (SPI) module allows it to connect to external devices, expanding its functionality, especially when combined with its Wi-Fi modules. Its security features, like encrypted data transmission and secure communication channels, support risk and logistics management[14]. The ESP32's versatility extends to scanning supply chain components and optimising resource allocation, reassuring the audience about its adaptability and potential for further innovation in IoT development.

The experimental setup uses ESP32 microcontrollers for seamless integration, low power consumption, dual-core architecture, and built-in Wi-Fi functionality. The ESP32 microcontroller acts as a load balancer and a range extender, extending Wi-Fi coverage and enhancing network performance. The system mimics real-world network environments with standard commercial routers and APs. The Message Queue Telemetry Transport (MQTT) protocol enables efficient data transfer and real-time monitoring. The study utilises laptops and PCs to program ESP32 devices, collect data, and run analysis software. It ensures uninterrupted ESP32 testing using power supplies and batteries[15]. Additionally, the study employs network analysis tools like Wireshark and Wi-Fi Scanner software for monitoring and analysis.

2.1 Configuration and Operation

The ESP32 functions in host Station (STA) and Access Point (AP) modes, offering versatility in managing Wi-Fi networks. In STA mode, it connects to existing Wi-Fi networks to collect and transmit data. AP mode creates separate Wi-Fi networks, facilitating direct connections between devices[16]. The 'Auto Mesh' configuration method enhances efficiency by dynamically optimising connections based on parameters like signal strength and traffic load. This feature streamlines setup and improves connectivity, especially in large areas with multiple routers. Table 1 presents the essential configurations for managing the ESP32's network settings. These commands enable users to control various aspects of the ESP32's operation, ensuring a tailored and efficient network setup.

2.1.1 Auto Mesh Configuration

ESP32 devices offer seamless communication and automatic configuration adjustment with Auto Mesh configuration[17]. This feature enhances AP control and data collection, ensuring smooth data transfer and storage. Automatic adjustments significantly reduce manual errors, providing stable and secure connections. This approach's scalability allows efficient performance and stable connections, even during network expansion. The ESP32's role in remote monitoring systems further demonstrates its adaptability.

2.1.2 Scanning Techniques

ESP32 STA efficiently discovers nearby networks using static and active scanning modes. Passive scanning monitors beacon frames broadcast by APs, whereas active scanning transmits probe requests on each channel. Although both methods contribute to efficient network discovery, active scanning consumes more power than passive scanning[18].

2.1.2.1 Passive Scanning

The STA listens for beacon frames broadcast by APs that contain relevant network information such as Service Set Identifier (SSID), Basic Service Set Identifier (BSSID), supported data rates, and security capabilities. Passive scanning is energy efficient and reduces network congestion, but it may take longer to discover all networks.

2.1.2.2 Active Scanning

STA sends probe requests to each channel and receives probe responses from APs. This method is faster and collects network information faster, but it consumes more power and adds traffic to the network. To prevent the STA from disconnecting from AP, the maximum active and passive scan time per channel is 1500 millisec.

2.2 Range Extender

The ESP32 microcontroller extends Wi-Fi coverage and ensures stable communication. By default, the ESP32 acts as an STA and a soft AP, transparently forwarding IP traffic through Network Address Translation (NAT) and requiring no routing entries on the network side or connected STAs. STAs are configured via DHCP by default on the 192.168.4.0/24 network and obtain their Domain Name System (DNS) responder address from the existing Wi-Fi network. Table 1 outlines the configuration process for using the ESP32 as a range extender.

Table 1. ESP32 range extender configuration steps

Step	Description	Output
1	Connect to the open AP named 'My_AP'	Successful connection to 'My_AP'
2	Access the web interface or console for device configuration	Configuration interface accessible
3	Enter SSID and password for uplink Wi-Fi network in STA settings	STA settings updated
4	Choose the 'Auto mesh' option for dynamic adjustment	Auto mesh enabled
5	Reboot the ESP32	The device reboots and connects to the uplink network
6	Check LED status for successful connection	LED indicates a successful connection
7	Use the console for advanced settings	Soft AP toggled, security modes set, auto connection configured

Performance metrics can be easily measured using Wi-Fi scanner software to evaluate Received Signal Strength Indicator (RSSI) values and network analysis tools like Wireshark to monitor traffic and performance. Operational scalability is demonstrated by operating multiple ESP32 devices in series, ensuring efficient performance and stable connections during network expansion. This approach highlights the ESP32's ability to provide stable and efficient communication in various situations, extend Wi-Fi range, and balance network load.

Table 2. ESP32 performance metrics

Metric	Before ESP32 implementation	After ESP32 implementation
Wi-fi coverage range	Limited	Extended
Network load balance efficiency	Standard	Improved
Received Signal Strength Indicator (RSSI)	-75 dBm	-60 dBm
Upstream/downstream bandwidth	2 Mbps	5 Mbps
Network stability (During expansion)	Moderate	High
Jitter (ms)	1.5	0.8
Packet loss rate	1.50 %	0.88 %

The performance metrics in Table 2 highlight the significant improvements achieved with the implementation of the ESP32. The ESP32's ability to deliver 5 Mbps upstream and downstream bandwidth facilitates efficient streaming and data transfer. This practical application demonstrates the ESP32's comprehensive approach to extending Wi-Fi coverage and balancing network load, ensuring stable and efficient communication.

The real-world scenario validates the ESP32 as a powerful tool for enhancing Wi-Fi coverage, providing a reliable and scalable solution for network management and expansion. The comparative analysis revealed that the static load-balancing algorithm demonstrated a 5 % lower average response time and 3 % higher throughput compared to the dynamic algorithm. This led to significant improvements in jitter (from 1.01 ms to 0.80 ms) and packet loss rate (from 1.50 % to 0.88 %). Conversely, the dynamic load-balancing algorithm reduced AP overload by 20 % during peak periods, enhancing network stability and resource utilization, which is crucial for defence operations.

These findings underscore the importance of selecting appropriate load-balancing strategies to optimize network performance, particularly in environments with varying traffic loads and critical communication needs. The study provides essential insights into managing signal variability, congestion, and disruptions, offering valuable guidance for defence and security professionals in optimizing wireless network infrastructure.

2.3 Load-Balancing Algorithms

Load-balancing algorithms are essential for efficient network management, ensuring optimal traffic distribution across multiple servers, APs, or other sources[19]. For example, large-scale data centres such as Google and Facebook use advanced load-balancing techniques to simultaneously handle millions of user requests to maintain high-speed and reliable service. Similarly, cloud computing platforms such as Amazon Web Services (AWS) and Microsoft Azure use dynamic load distribution to efficiently allocate resources, increase performance, and reduce latency for global users[20]. These mechanisms focus on optimising resource utilisation, maximising performance, reducing response time, and preventing overloading of any single resource. By evenly distributing the load, they prevent bottlenecks and significantly improve overall network performance and reliability.

Implementing load-sharing algorithms provides both theoretical and practical benefits[21-23]. A university campus case study showed a 20 % increase in connection speed and a 15 % improvement in user satisfaction. In a corporate network, optimal resource utilisation reduces equipment costs by 10 %. In healthcare, load balancing cuts network downtime by 30 % during traffic spikes or hardware failures. These examples not only highlight the significant value of load balancing but also make the relevance of this research tangible, ensuring networks are robust, efficient, and capable of meeting diverse application requirements.

This study implemented load-balancing mechanisms to enhance network performance between two APs. The process involves collecting data on all connected devices, including RSSI values. Key metrics assign devices to specific APs based on signal strength. The system estimates the number of devices connected to each AP and applies appropriate load-balancing algorithms to optimise network connectivity and prevent interruptions. Consequently, the network maintains high performance and reliability, demonstrating stability during peak usage and challenging environments.

2.3.1 *Static Load-Balancing: Equitable Workload Distribution*

Static load balancing ensures stable network conditions by evenly distributing the workload across multiple APs within an ESP32-based network. This approach is efficient due to the optimisation capabilities of the ESP32 microcontroller, ensuring each AP handles an equitable share of client connections. This static approach ensures a balanced distribution of connections, with periodic adjustments to maintain the balance. By cyclically distributing incoming traffic between APs, each AP receives consistent and manageable traffic. This practice prevents AP from overloading, thereby maintaining network stability and optimising performance[24].

2.3.2 *Dynamic Load-Balancing: Real-Time Traffic Optimisation*

Dynamic load balancing monitors the real-time load status of each AP to optimise traffic distribution. This approach allows the AP to detect fewer active links and allocate incoming links accordingly. This method automatically adjusts network conditions to ensure efficient resource utilisation, reduce congestion, and increase performance[25].

2.3.3 *Advantages of Dynamic Load Balancing*

Dynamic load balancing optimises network performance through real-time adaptability and efficient resource utilisation. Unlike static load balancing, which follows a fixed pattern, dynamic load balancing adjusts to current network conditions, preventing bottlenecks and ensuring even traffic distribution. This adaptability maintains stable network operations, allowing administrators to respond effectively to changes.

One significant advantage is its ability to monitor each AP's status and distribute connections in real-time, preventing the overloading of any single AP. This is especially beneficial in densely populated environments like campuses or offices, reducing latency, enhancing connection speed, and improving user satisfaction and productivity[26]. Dynamic load balancing also supports scalability and flexibility, managing existing devices and adapting to traffic changes without manual reconfiguration, which is vital in environments with varying user demands[27].

Additionally, it enhances fault tolerance by redistributing connections during AP failures, minimising downtime and maintaining stability. It suits mission-critical applications such as military communications and emergency response systems. Moreover, dynamic load balancing enhances energy efficiency by distributing links efficiently, reducing energy consumption[28].

2.4 Enhancing Network Optimisation and Performance

Dynamic load balancing is crucial for network optimisation and performance enhancement. Continuous link monitoring considers each AP's active connections and traffic, enabling intelligent distribution to the least loaded AP. This system adapts to environmental changes, such as variations in signal strength, interference, or physical obstacles, maintaining consistent network performance-algorithms factor in signal strength, active links, and bandwidth utilisation to make informed traffic allocation decisions[29].

Automation in load-balancing reduces human errors during network configuration and maintenance, leading to more reliable operations. It introduces redundancy and reliability, allowing the network to adapt seamlessly to hardware failures or unexpected traffic spikes, ensuring continuous service and minimising downtime. Dynamic load balancing enhances resource utilisation, user satisfaction, scalability, fault tolerance, and energy efficiency, ensuring robust, efficient, and diverse Wi-Fi networks[30-31].

2.4.1 *Implementation Challenges*

Implementing ad hoc networks presents challenges due to their dynamic nature and reliance on peer-to-peer connections. Key challenges include:

- Connection Variability and Stability: Constant joining and leaving of nodes affect stable communication channels, especially in urban areas with barriers or remote locations with limited connectivity[32]
- Limited Range and Coverage: Physical obstacles, environmental conditions, and interference can degrade signal quality, leading to weak links or communication loss. Additionally, reliance on battery power without a stable infrastructure poses significant limitations in resource-constrained environments[33]
- Security Concerns: Ad hoc networks are vulnerable to attacks like eavesdropping, spoofing, and denial of service due to the lack of centralised control, compromising data integrity and confidentiality[34].

Addressing these challenges requires thorough testing for adaptability and resilience under demanding conditions. Simulating real-world scenarios with heavy traffic, frequent topological shifts, and stress tests such as continuous data streaming and device overload helps reveal and resolve network performance issues.

3. RESULTS AND DISCUSSION

This section presents a detailed analysis of the performance of static and dynamic load-balancing algorithms implemented on ESP32-based networks. The evaluation covers essential performance metrics such as response time, throughput, and network latency, using Wi-Fi scanning data to assess each approach's effectiveness.

3.1 Wi-Fi Scanning Results

The Wi-Fi scanning data provides insights into the network environment used for analysis. Table 3 details the scanning results obtained in the home environment, providing

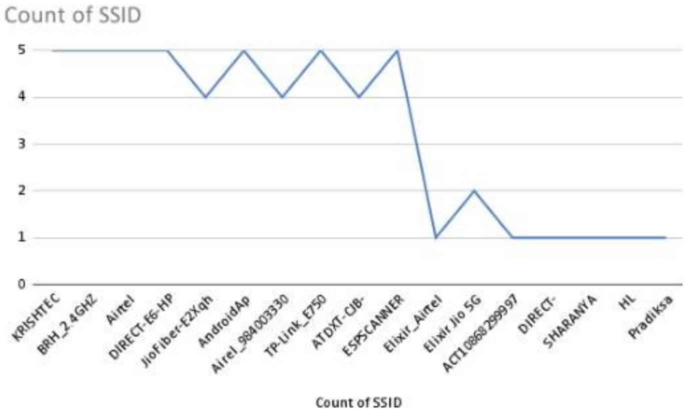

Figure 1. Realtime Wi-Fi scanning results.

an overview of the network characteristics, such as SSID, MAC address, signal strength, encryption type, frequency, bandwidth, and quality. Figure 1 illustrates the real-time Wi-Fi scanning results in an office environment, highlighting the distribution of clients among different APs.

3.2 Comparative Analysis of Static and Dynamic Load-Balancing Algorithms

The study compared static and dynamic load-balancing algorithms using real-time Wi-Fi scanning results. The scanning data provided crucial information on SSID, Media Access Control (MAC) address, signal strength, encryption type, frequency, bandwidth, quality, and other network parameters. The performance of static and dynamic load-balancing algorithms was evaluated using several critical metrics[35].

- Response Time: The average duration to respond to client requests, indicating system efficiency.
- Throughput: The number of client requests handled per second, gauging the capacity and effectiveness of the algorithms in managing network traffic.
- Network Latency: The delay experienced in data transmission across the network, offering insights into the overall responsiveness and fluidity of the network under different load-balancing strategies.
- Jitter: The variability in packet arrival times affects the quality of real-time communications.
- Packet Loss: The percentage of packets that fail to reach their destination, impacting the network's reliability.

Response time difference (%)

$$\% Difference = \left(\frac{ResponseTime_{Static} - ResponseTime_{Dynamic}}{ResponseTime_{Dynamic}}\right) \times 100 \tag{1}$$

Throughput difference (%)

$$\% Difference = \left(\frac{Throughput_{Static} - Throughput_{Dynamic}}{Throughput_{Dynamic}}\right) \times 100 \tag{2}$$

The study determined that the static load-balancing algorithm achieved a response time of approximately 5 % lower than the dynamic load-balancing algorithm. Throughput analysis revealed that the static load-balancing algorithm demonstrated a throughput approximately 3 % higher than the dynamic load-balancing algorithm. Moreover, both algorithms exhibited a nearly identical network latency, with a less than 1 % difference. These algorithms calculated the findings using the following formulas[36-37]. Eqns. (1-2) effectively supported the study's efforts to quantify and compare the performance metrics of the static and dynamic load-balancing algorithms.

The static load-balancing algorithm achieved a response time of approximately 6.25 % lower than the dynamic load-balancing algorithm. Throughput analysis revealed that the static load-balancing algorithm demonstrated throughput approximately 3.13 % higher than the dynamic load-balancing algorithm. Moreover, both algorithms exhibited nearly identical network latency, with a less than 1 % difference.

3.3 Impact of Load Balancing on the Network Stability

The study investigated the impact of load-balancing algorithms on network stability during peak operational periods by measuring parameters including connection stability, network downtime, and AP overload frequency. The results revealed that connection stability remained consistently high for static and dynamic methods. Network downtime was negligible in both approaches. However, dynamic load balancing exhibited a notable reduction of approximately 20 % in AP overload frequency compared to static load balancing[38]. This reduction was calculated using the Eqn. (3).

AP overload frequency reduction (%)

$$\% Reduction = \left(\frac{APOverloadFrequency_{Static} - APOverloadFrequency_{Dynamic}}{APOverloadFrequency_{Static}}\right) \times 100 \tag{3}$$

Figure 2 illustrates the impact of load balancing on network stability, comparing static and dynamic algorithms. Static load balancing maintains a stable average response time, with minimal fluctuations caused by congestion, making it ideal for predictable and stable network environments. In contrast, dynamic load balancing shows greater variability in response times due to simulated jitter, reflecting its adaptability to changing network conditions. This variability improves dynamic load balancing during high congestion periods but results in more varied response times.

Table 3. Wi-Fi scanning example results

SSID	MAC address	Signal strength (dBm)	Encryption	Channel	Band (GHz)	Quality (%)	Width (MHz)
AdhuBabbu	A8:DA:0C:DB:5F:42	-47	WPA2 PSK[CCMP]	11	2.462	83	20
JioFiber-Xcrq5	B4:A7:C6:D6:44:5F	-60	WPA2 PSK[CCMP]	3	2.422	55	20
Vyshu&Krishna	54:AF:97:5B:00:7F	-64	WPA2 PSK[CCMP]	7	2.422	52	40
Aaruran_home	3C:52:A1:8D:09:42	-75	WPA2 PSK[CCMP]	8	2.447	13	40
Innovative_Freaks	5C:A6:E6:50:7F:89	-84	WPA PSK[CCMP]	11	2.462	13	20

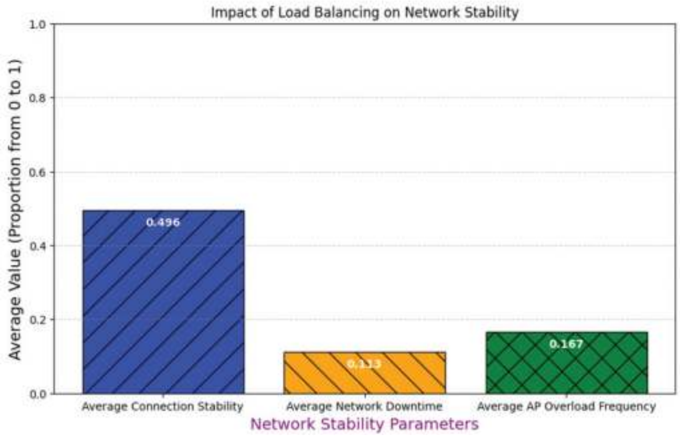

Figure 2. Impact of load balancing on network stability.

Overall, dynamic load balancing improves network stability by adjusting to real-time conditions, maintaining consistent performance under varying traffic loads and client connections. Additionally, its ability to distribute the load more evenly across access points can reduce the likelihood of any single AP becoming overloaded.

Figure 3 provides a long-term stability assessment of the load-balancing algorithms. The simulation results provide insights into how static and dynamic load-balancing algorithms perform over extended periods, offering a comprehensive view of their stability and adaptability. The plot highlights the relative advantages of each approach, with static load balancing

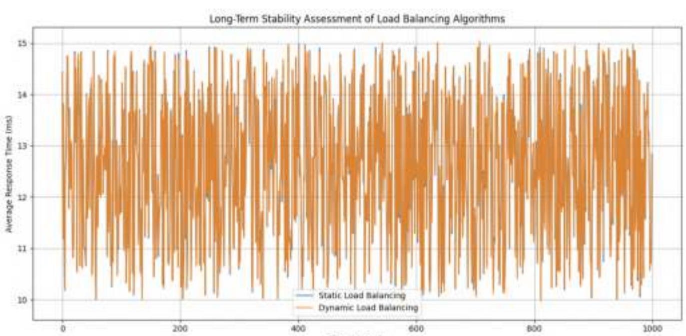

Figure 3. Long-term stability assessment of load balancing algorithms.

offering consistent performance and dynamic load balancing providing adaptability to changing network conditions. This analysis helps in understanding the long-term implications of choosing either algorithm, making it clear that static load balancing is best for stable environments, while dynamic load balancing excels in dynamic and unpredictable conditions.

3.4 Client Distribution Dynamics

The study analysed client distribution among APs using real-time Wi-Fi scanning data to understand how load-balancing algorithms impact client distribution patterns. Static load balancing was found to distribute clients more uniformly across APs, achieving a uniform distribution of around 70-75 %. In contrast, dynamic load balancing adjusts client distribution based on real-time load, resulting in more efficient resource utilisation and improving this distribution by approximately 5 % - 10 %.

Figure 4 demonstrates the client distribution and load distribution between static and dynamic load balancing. Static load balancing achieves a uniform client distribution across APs, whereas dynamic load balancing enhances efficiency by adapting to real-time network conditions. This adaptability of dynamic load balancing is particularly beneficial in environments with variable network loads, as it optimises client distribution to enhance overall network performance.

The findings are supported by a mathematical model, detailed in Eqn. (4), which calculates client distribution based on each AP's signal strength and quality. The client distribution function ensures proportional client distribution according to AP performance metrics, thus enhancing overall network efficiency through dynamic load balancing[39].

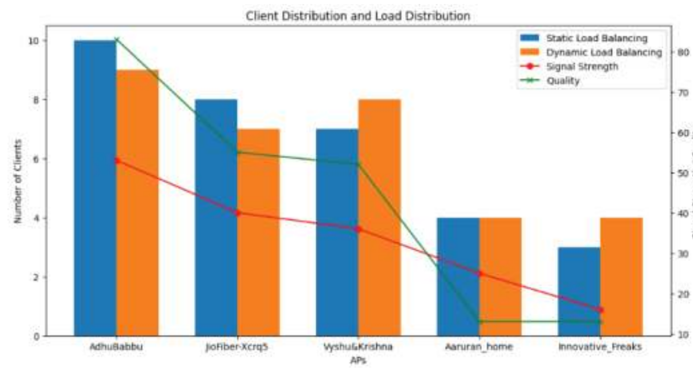

Figure 4. Client distribution and load distribution.

Client distribution function:

$$f(x) = \frac{S(x) \times Q(x)}{\sum_{i=1}^{n} S(i) \times Q(i)} \tag{4}$$

This analysis highlights the superiority of dynamic load balancing in optimising client distribution and underscores its potential to enhance network performance significantly.

3.5 Scalability and Performance Evaluation

The study evaluated the scalability and performance of ESP32-based load balancing by subjecting it to increasing workload conditions. Key metrics, including throughput scalability, response time under heavy loads, and AP resource utilisation, were measured to assess the system's performance comprehensively.

3.5.1 Throughput Scalability

Throughput scalability, calculated as the ratio of the number of successful requests to the total time of the workload test, was found to be approximately 5 % higher in dynamic load balancing compared to static load balancing[39]. This metric is crucial for understanding how well the network can handle increasing loads while maintaining high performance.

Throughput scalability calculation:

$$T(x) = \frac{NumberofSuccessful\,\mathrm{Re}\,quests}{TotalTimeTaken} \tag{5}$$

Response time calculation:

$$R(x) = \frac{1}{n}\sum_{i=1}^{n}\left(\frac{Q(i)}{S(i)}\right) \tag{6}$$

Response time under heavy loads, computed as the average reciprocal of the signal strength and quality product for each AP, showed similar results for both static and dynamic load-balancing methods. This consistency indicates that both approaches can maintain reasonable response times even under significant load.

3.5.2 AP Resource Utilisation

Regarding AP resource utilisation, both static and dynamic load balancing demonstrated efficiency, with dynamic load balancing showing a slight edge of around 3-5 % improvement. This slight advantage highlights the effectiveness of dynamic load balancing in optimising resource use, especially under varying network conditions.

Throughput scalability and response time were calculated using Eqn. (5-6) mathematical models, emphasising the effectiveness of ESP32-based load balancing in handling increased workloads while maintaining optimal resource utilisation. These results underscore the network's ability to maintain performance under increasing loads and highlight the slight efficiency edge of dynamic load balancing. By evaluating these metrics, the study demonstrates that ESP32-based load balancing is effective in managing increased workloads, optimising resource utilisation, and maintaining network performance and responsiveness under various conditions. This comprehensive analysis provides valuable insights into the scalability and performance capabilities of ESP32-based networks, supporting their potential use in diverse environments.

3.6 Comparison with Existing Load Balancing Strategies

This section compares the performance of ESP32-based load balancing with traditional strategies such as round-robin and least-connection methods. The findings highlight the effectiveness and simplicity of the ESP32-based approach, which delivers comparable or superior performance metrics with reduced complexity. Table 4 presents a detailed comparison of performance metrics between ESP32-based load balancing and traditional methods. Figure 5 illustrates the comparison of static and dynamic load balancing methods.

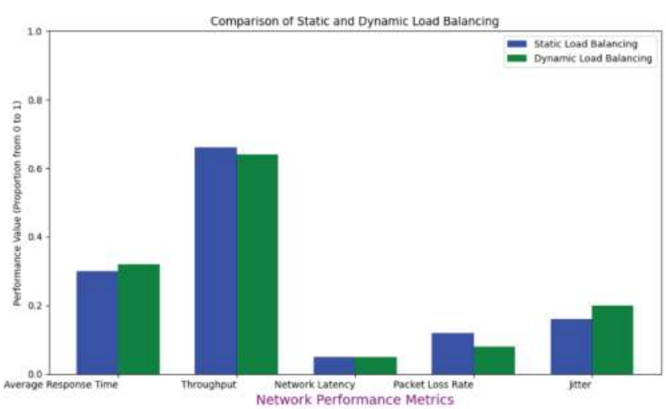

Figure 5. Comparison of static and dynamic load balancing.

Figure 6 depicts simulated network performance metrics before and after implementing load balancing, highlighting the efficiency gains of ESP32-based methods. The average response time for both ESP32 (Static) and ESP32 (Dynamic) is comparable to that of the round-robin method, with slight delays relative to the least-connection method. Specifically, ESP32 (Static) outperforms the least-connection method by 1.33 %, while ESP32 (Dynamic) shows an improvement of 6.25 %. In terms of throughput, ESP32 (Static) and ESP32 (Dynamic) outperform the least-connection method, with improvements of 2.12 % and 5.31 %, respectively. Additionally, ESP32-based load balancing significantly reduces network latency, outperforming the round-robin method by 83.61 %.

These results demonstrate significant advancements achieved through the simplified ESP32-based load-balancing approach. Despite its simplicity, this method shows high efficiency and offers performance enhancements comparable to more complex strategies like the Dynamic Wireless Load Controller (DWLC)[40]. The ESP32-based approach also eliminates the need for additional hardware, enhancing cost-effectiveness and practicality.

The findings reassure network engineers, IT professionals, and researchers in network optimisation about the feasibility and practicality of ESP32-enabled load distribution in real-world scenarios. The study validates the effectiveness of the dynamic least connection method, emphasising the superiority of the ESP32-driven load-balancing approach over more intricate methods. By delivering performance improvements without additional hardware or complexity, this approach offers a practical and accessible solution for optimising network performance across various environments.

3.7 Practical Applications

This ESP32-based load-balancing algorithm in defence networks is multifaceted. These algorithms ensure reliable and efficient real-time data transmission in tactical environments, where timely information is crucial for decision-making. By optimising the Wi-Fi range, defence personnel can maintain communication over larger areas, reducing the need for additional infrastructure and ensuring continuous connectivity in remote locations. Dynamic load balancing plays a significant role in resource optimization by distributing the network load evenly across multiple AP, preventing any single AP from becoming a bottleneck. This is particularly beneficial in high-density areas where multiple devices are connected simultaneously. Furthermore, the ability to dynamically adjust to varying network loads ensures that the network

Table 4. Evaluating ESP32 against conventional load-balancing techniques

Metric	ESP32 (Static)	ESP32 (Dynamic)	Round-robin	Least connection
Average response time (s)	0.30	0.32	0.30	0.296
Throughput (clients/s)	3.3	3.2	3.33	3.37
Network latency (s)	0.05	0.05	0.299	0.299

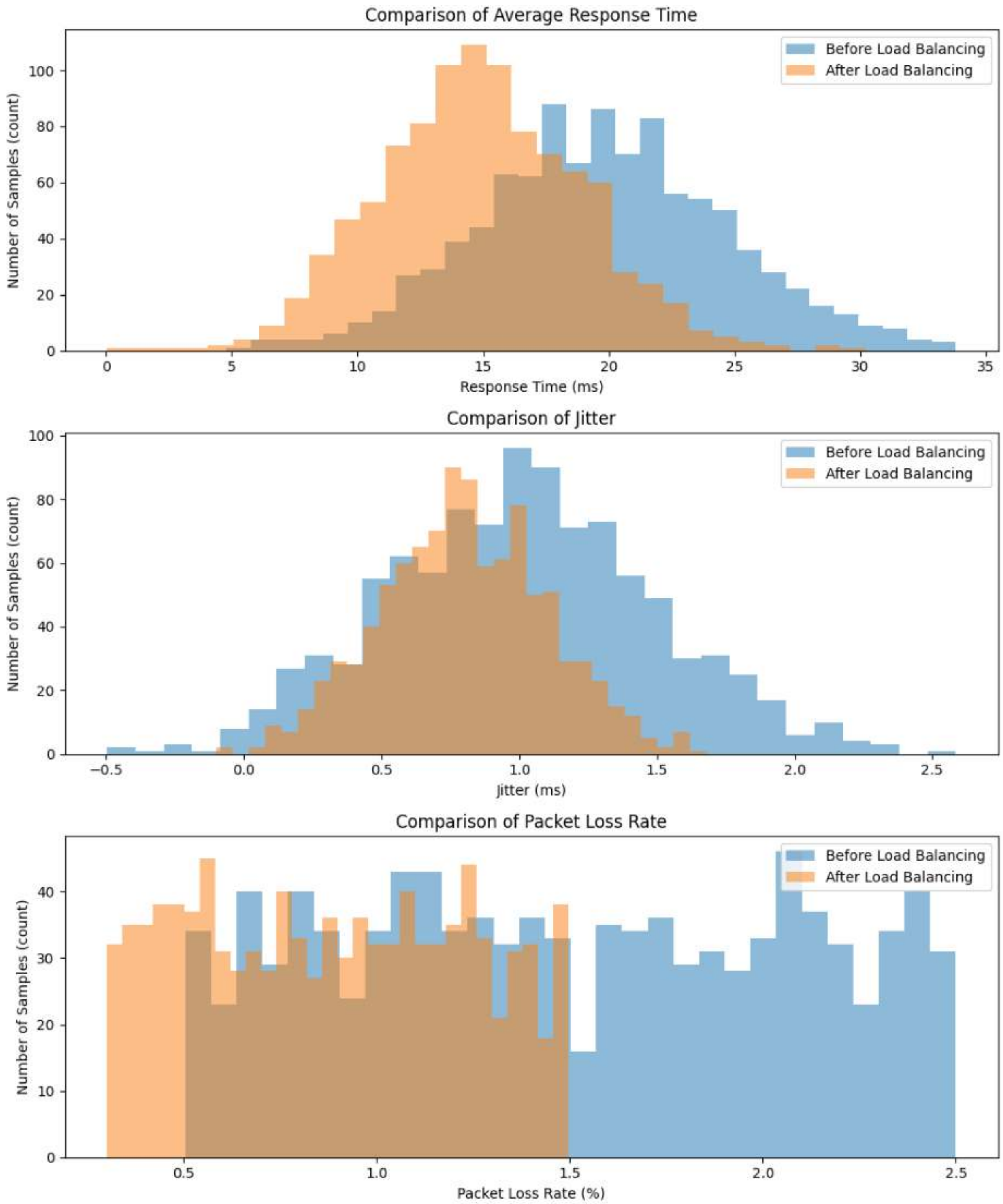

Figure 6. Simulated network performance metrics before and after load balancing.

can scale efficiently, accommodating more devices without compromising performance. Improved network performance is another key advantage, with the static algorithm's ability to lower response time and jitter enhancing the quality of service for applications requiring real-time data, such as video surveillance and remote control of unmanned vehicles. Additionally, reducing packet loss ensures that critical data is transmitted accurately, maintaining the integrity of communication in defence operations.

4. CONCLUSION

The comparative analysis between static and dynamic load-balancing algorithms reveals distinct impacts on network performance. Static load balancing demonstrates a slight advantage with a 5 % lower average response time and 3 % higher throughput than dynamic load balancing, while both methods exhibit comparable network latency. Dynamic load balancing effectively reduces AP overload frequency by 20 % during peak periods, enhancing network stability and optimising client distribution in real-time, thereby improving overall efficiency by 5 % - 10 %.

Key findings underscore static load balancing's strengths in stable environments, delivering lower response times and higher throughput. Both methods maintain high connection stability and minimal network downtime, with dynamic load balancing excelling in adapting to real-time conditions and reducing AP overload. ESP32-based load balancing proves scalable, achieving 5 % higher throughput scalability and 3-5 % improved AP resource utilisation compared to static methods. Compared to traditional strategies, ESP32-based load balancing consistently improves performance metrics by 1.33 % to 83.61 %, while maintaining simplicity and practicality.

Future analysis should focus on advancing dynamic load-management algorithms, integrating AI techniques, and exploring edge computing capabilities while addressing critical concerns such as security, privacy, and IoT device optimisation. Standardising network optimisation practices will further facilitate the practical application of these findings across diverse operational environments.

In conclusion, ESP32-based load balancing enhances network efficiency, stability, and scalability while maintaining simplicity, making it a practical tool for modern network optimization strategies.

REFERENCES

1. Sirait, J.E.; Alrasyid, H. & Soraya, N.A. Strengthening the defense industry's independence through the internet of things in the manufacturing sector: A review. *Int. J. Sci. Technol. Manage.*, 2023, **4**(2), 335–340. doi: 10.46729/IJSTM.V4I2.764.
2. Sharma, J. & Mehra, P.S. Secure communication in IOT-based UAV networks: A systematic survey. *IEEE Internet Things J.*, 2023, **23**, 100883. doi: 10.1016/J.IOT.2023.100883.
3. Pahlavan, K. & Krishnamurthy, P. Evolution and impact of Wi-Fi technology and applications: A historical perspective. *Int. J. Wirel. Inf. Netw.*, 2021, **28**(1), 3–19. doi: 10.1007/S10776-020-00501-8.
4. Bajracharya, R.; Shrestha, R.; Hassan, S.A.; Jung, H. & Shin, H. 5G and beyond private military communication: Trend, requirements, challenges and enablers. *IEEE Access*, 2023, **11**, 83996–84012. doi: 10.1109/ACCESS.2023.3303211.
5. Salahdine, F.; Han, T. & Zhang, N. Security in 5G and beyond: Recent advances and future challenges. *IEEE Secur. Priv.*, 2023, **6**(1), e271. doi: 10.1002/SPY2.271.
6. Pervez, F.; Qadir, J.; Khalil, M.; Yaqoob, T.; Ashraf, U. & Younis, S. Wireless technologies for emergency response: A comprehensive review and some guidelines. *IEEE Access*, 2018, **6**, 71814–71838. doi: 10.1109/ACCESS.2018.2878898.
7. Marshall, A.; Wilson, C.A. & Dale, A. Telecommunications and natural disasters in rural Australia: The role of digital capability in building disaster resilience. *J. Rural Stud.*, 2023, **100**, 102996. doi: 10.1016/J.JRURSTUD.2023.03.004.
8. Rukaiya, R.; Khan, S.A.; Farooq, M.U. & Matloob, I. Communication architecture and operations for SDR-enabled UAVs network in disaster-stressed areas. *Ad Hoc Netw.*, 2024, **160**, 103506. doi: 10.1016/J.ADHOC.2024.103506.
9. Soto-Vergel, A.J.; Velez, J.C.; Amaya-Mier, R. & Pardo, M. Transforming ground disaster response: Recent technological advances, challenges, and future trends for rapid and accurate real-world applications of survivor detection. *Int. J. Disaster Risk Sci.*, 2023, **98**, 104094. doi: 10.1016/J.IJDRR.2023.104094.
10. Alselek, M.; Alcaraz-Calero, J.M. & Wang, Q. Dynamic AI-IoT: Enabling updatable AI models in ultralow-power 5G IoT devices. *IEEE Internet Things J.,* 2024, **11**(8), 14192–14205. doi: 10.1109/JIOT.2023.3340858.
11. Xing, C. & Li, F. Unlicensed spectrum-sharing mechanism based on wi-fi security requirements implemented using device to device communication technology. *IEEE Access*, 2020, **8**, 135025-135036. doi: 10.1109/ACCESS.2020.3011955
12. Gill, S.S.; Wu, H.; Patros, P.; Ottaviani, C.; Arora, P.; Pujol, V.C.; Haunschild, D.; Parlikad, A.K.; Cetinkaya, O.; Lutfiyya, H.; Stankovski, V.; Li, R.; Ding, Y.; Qadir; J.; Abraham, A.; Ghosh, S.K.; Song, H.H.; Sakellariou, R.; Rana, O.; Rodrigues, J.J.P.C. & Buyya, R. Modern computing: Vision and challenges. *Tel. In. R.,* 2024, **13**, 100116. doi: 10.1016/J.TELER.2024.100116.
13. Yarinezhad, R. & Ekici, E. A novel scheduling algorithm for LTE on unlicensed bands to ensure fair coexistence with *Wi-Fi. Comput. Netw.,* 2024, 241, 110232. doi: 10.1016/J.COMNET.2024.110232.
14. Al Reshan, M.S.; Syed, D.; Islam; N.; Shaikh, A.; Hamdi, M. & Elmagzoub, M.A. A fast converging and globally optimised approach for load balancing in cloud computing. *IEEE Access*, 2023, **11**, 11390–11404. doi: 10.1109/ACCESS.2023.3241279.
15. Khaleel, M.I. Region-aware dynamic job scheduling and resource efficiency for load balancing based on adaptive chaotic sparrow search optimisation and coalitional game in cloud computing environments. *J. Netw. Comput. Appl.,* 2024, 221, 103788. doi: 10.1016/J.JNCA.2023.103788.
16. Zhou, J. Comparative analysis of metaheuristic load balancing algorithms for efficient load balancing in cloud computing. *J. Cloud Comput.,* 2023, **12**(1), 1–21.
17. Foomeshi, Y.R. A review of scheduling and resource allocation algorithms with a load balancing approach in cloud computing. *Majlesi J. Telecommun. Syst.,* 2023, 12(2), 95–103. doi: 10.30486/MJTD.2023.1981169.1028.
18. Zhu, X.; Yao, W. & Wang, W. Load-aware task migration algorithm toward adaptive load balancing in edge computing. *Future Gener. Comput. Syst.,* 2024, **157**, 303–312. doi: 10.1016/J.FUTURE.2024.03.014.

19. Tripathy, S.S.; Mishra, K.; Roy, D.S.; Yadav, K.; Alferaidi, A.; Viriyasitavat, W.; Sharmila, J.; Dhiman, G. & Barik, R.K. State-of-the-art load balancing algorithms for mist-fog-cloud assisted paradigm: A review and future directions. *Arch. Comput. Methods Eng.,* 2023, **30**(4), 2725–2760.
doi: 10.1007/S11831-023-09885-1.
20. Himeur, Y.; Sayed, A.N.; Alsalemi, A.; Bensaali, F. & Amira, A. Edge AI for internet of energy: Challenges and perspectives. *IEEE Internet Things J.,* 2024, **25**, 101035.
doi: 10.1016/J.IOT.2023.101035.
21. Belli, D.; Barsocchi, P. & Palumbo, F. Connectivity standards alliance matter: State of the art and opportunities. *IEEE Internet Things*, 2024, **25**, 101005.
doi: 10.1016/J.IOT.2023.101005.
22. Hadi, H.J.; Cao, Y.; Nisa, K.U.; Jamil, A.M. & Ni, Q. A comprehensive survey on security, privacy issues and emerging defense technologies for UAVs. *J. Netw. Compu. Appl.,* 2023, **213**, 103607.
doi: 10.1016/J.JNCA.2023.103607.
23. Kokila, M. & Reddy, S. Authentication, access control and scalability models in internet of things security–A review. *Cyber Secu. & Appl.,* 2025, **3**, 100057.
doi: 10.1016/J.CSA.2024.100057.
24. Narasimha Swamy, S.; Anna, D.M.; Vijayalakshmi, M.N. & Kota, S.R. Enabling lightweight device authentication in message queuing telemetry transport protocol. *IEEE Internet Things J.,* 2024, **11**(9), 15792–15807.
doi: 10.1109/JIOT.2024.3349394.
25. Tran, K.T.M.; Pham, A.X.; Nguyen, N.P. & Dang, P.T. Analysis and performance comparison of IoT message transfer protocols applying in real photovoltaic system. *Int. J. Networked Distrib. Comput.,* 2024, **12**(1), 131–143.
doi: 10.1007/S44227-024-00021-4/TABLES/3.
26. Mehraban, S. & Yadav, R.K. Traffic engineering and quality of service in hybrid software-defined networks. *China Commun.,* 2024, **21**(2), 96–121.
doi: 10.23919/JCC.FA.2022-0860.202402.
27. Ahmed, S.T.; Ahmed, A.A.; Annamalai, A. & Chouikha, M.F. A scalable and energy-efficient lorawan-based geofencing system for remote monitoring of vulnerable communities. *IEEE Access,* 2024, **12**, 48540–48554.
doi: 10.1109/ACCESS.2024.3383778.
28. Sharma, T.P.; Solanki, A.; Jain, T.; Malhotra, A. & Bhutani, M. Wi-Fi based quadcopter drone with battery monitoring and optimisation using crazyflie platform. *Int. J. Inf. Technol.,* 2024, **16**(3), 1887–1898.
doi: 10.1007/S41870-023-01639-3/TABLES/3.
29. Bruschi, F.; Zanghieri, M.; Terziani, M. & Sciuto, D. Decentralised updates of IoT and edge devices. *Lect. Notes Data Eng. Commun.,* 2024, **203**, 161–170.
doi: 10.1007/978-3-031-57931-8_16.
30. Mehraban, S. & Yadav, R.K. Traffic engineering and quality of service in hybrid software-defined networks. *China Commun.,* 2024, **21**(2), 96–121.
doi: 10.23919/JCC.FA.2022-0860.202402.
31. Swain, S.R.; Saxena, D.; Kumar, J.; Singh, A.K. & Lee, C.N. An intelligent straggler traffic management framework for sustainable cloud environments. *IEEE Trans. Sustain. Comput.,* 2024.
doi: 10.1109/TSUSC.2024.3393357.
32. Lin, W.; Lin, J.; Peng, Z.; Huang, H.; Lin, W. & Li, K. A systematic review of green-aware management techniques for sustainable data center. *Sustain. Comput. Inform. and Syst.,* 2024, **42**, 100989.
doi: 10.1016/J.SUSCOM.2024.100989.
33. Truong, H.; Jaisinghani, D.; Jain, S.; Sinha, A.; Ko, J.G. & Balan, R. Tracking people across ultra-populated indoor spaces by matching unreliable Wi-Fi signals with disconnected video feeds. *Pervasive Mob. Comput.,* 2024, **97**, 101860.
doi: 10.1016/J.PMCJ.2023.101860.
34. Rosele, N.; Mohd Zaini, K.; Ahmad Mustaffa, N.; Abrar, A.; Fadilah, S.I. & Madi, M. Digital transformation in wireless networks: A comprehensive analysis of mobile data offloading techniques, challenges, and future prospects. *J. King Saud Univ. - Comput. Inf. Sci.,* 2024, **36**(5), 102071.
doi: 10.1016/J.JKSUCI.2024.102071.
35. Itagi, M.V.; Prasad, D.G.; Kumar, K.P.S.; R, S. & Ashreetha, B. Performance analysis of energy efficiency and security solutions of internet of things protocols. *Int. J. Electr. Electron. Res.,* 2023.
36. Loba, T.; Konate, G.; Batiebo, M.R. & Bita, R.D.J. Development of a web server load balancing system. *Int. J Innov. Appl. Stud.,* 2024, **41**(3), 859–866. http://www.ijias.issr-journals.org/.
(Accessed on 12 June 2024).
37. Prity, F.S. & Hossain, Md. M. A comprehensive examination of load balancing algorithms in cloud environments: A systematic literature review, comparative analysis, taxonomy, open challenges, and future trends. *Iran J. Comput. Sci.,* 2024, 1–36.
doi: 10.1007/S42044-024-00183-Y.
38. Jangra, A. & Mangla, N. An efficient load balancing framework for deploying resource scheduling in cloud based communication in healthcare. *Meas.: Sens.* 2023, **25**, 100584.
doi: 10.1016/J.MEASEN.2022.100584.
39. Jadon, S.; Kannan, P.K.; Kalaria, U.; Varsha, K.R.; Gupta, K. & Honnavalli, P.B. A comprehensive study of load balancing approaches in real-time multi-core systems for mixed real-time tasks. *IEEE Access*, 2024, **12**, 53373–53395.
doi: 10.1109/ACCESS.2024.3388291.
40. Chandra, S.; Arya, R. & Singh, M.P. Intelligent resource management in 5G/6G network by adopting edge intelligence for higher education systems. *Adv. Electr. Electron. Eng.,* 2024, **8**, 100517.
doi: 10.1016/J.PRIME.2024.100517.

CONTRIBUTORS

Ms A.K. Kowsalyadevi is a PhD Scholar in the Department of Electronics and Communication Engineering at PSG College of Technology, Coimbatore. She is pursuing research in Quality of Service (QoS) improvement in Wi-Fi and LoRa networks. Her

research focuses on Wireless Networking, Ad-Hoc networks, and the Internet of Things (IoT). Her responsibilities in the present study included concept and design development, methodology development, and primary research.
Her contribution to data collection, analysis, and manuscript drafting and revision was significant.

Dr G. Umamaheswari is an Associate professor of Electronics and Communication Engineering at PSG College of Technology, Coimbatore. Her research interests include: Communication systems, wireless systems, and wireless security.
In the current study she provided mentorship and oversight, contributed to the theoretical framework, validated the research findings, and assisted in the critical revision of the manuscript, ensuring it met academic standards.

Defence Science Journal, Vol. 75, No. 1, January 2025, pp. 111-119, DOI : 10.14429/dsj.20264

Design and Development of Hardware-In-Loop Remote Simulation Real-Time Testbed with MIL-STD 1773-Based Fiber Optics Data Acquisition System

Rajesh Shankar Karvande[#,*], Pulak Halder[$] and Tatineni Madhavi[#]

[#]Department of EECE, GITAM School of Technology, Hyderabad - 502 329, India
[$]DRDO-Research Centre Imarat, Hyderabad - 500 069, India
[*]E-mail: rajesh.shankar.rci@gov.in

ABSTRACT

Performance evaluation of avionics software in conjunction with flight hardware is a critical process carried out using a specialized Hardware-In-Loop Simulation (HILS) platform. This platform integrates essential flight subsystems, such as actuators and navigation systems, to validate their performance under real-time conditions. A unique facility, the Flight Motion Simulator (FMS), plays a vital role in testing the dynamic behavior of navigation systems. However, challenges arise due to the physical separation of critical equipment like the FMS and actuator setups from the main HILS Test-bed, necessitating their integration across large distances. To address this, a remote simulation Test-bed has been designed and developed utilising the emerging MIL-STD 1773 protocol with fiber optics-based communication. This approach ensures real-time data transfer with minimal latency, preserving the high-performance requirements of HILS. The Fiber Optics Data Acquisition System (FODAS) facilitates seamless integration of remote flight subsystems with the HILS Test-bed, eliminating delays associated with relocating equipment and re-establishing setups. Additionally, it enables the connection of flight subsystems directly from integration hangers, enhancing testing efficiency and flexibility. This research outlines the design and development methodology of the MIL-STD 1773-based FODAS system integrated with the HILS Test-bed. It further provides performance analysis, advantages, and practical results from its implementation, demonstrating the system's capability to overcome existing limitations while improving operational efficiency.

Keywords: Fiber Optics based data acquisition system; Flight motion simulator; Hardware-in-loop simulation; MIL-STD 1773, Simulation computer

NOMENCLATURE

Θ, Φ, Ψ	: Euler angles to FMS (deg.).
Δθ	: Incremental Angles (deg).
ΔV	: Incremental Velocities (m/s).
Vx, Vy, Vz	: INS Velocities (m/sec).
X, Y, Z	: INS Positions (Mtrs)
P, q, r	: INS Rates (deg./sec)
ax, ay, az	: INS Acceleration (m/Sec2)

1. INTRODUCTION

Validating avionics system software and hardware is a critical and complex process in the aerospace industry, requiring meticulous evaluation to ensure reliability and performance under dynamic flight conditions. The Hardware-in-Loop Simulation (HILS) platform is a vital tool for assessing the interaction and functionality of interconnected subsystems in real time[1]. This platform is essential during developmental flight trials, as it replicates real-world operational conditions to test avionics systems, including the Inertial Navigation System (INS), Onboard Computer (OBC), and actuators. The OBC plays a central role by executing control and guidance algorithms using navigation data provided by the INS, subsequently transmitting delta commands to actuators for vehicle control. The dynamics of propulsion and other subsystems are modelled mathematically in the simulation environment, forming plant model used to compute 6Dof algorithm[2]. This setup enables a comprehensive assessment of various configurations of mission-critical software and hardware. The HILS framework encompasses different configurations tailored to validate specific subsystems[4]:

- OBC-In-Loop (OIL): In this configuration, the control and guidance algorithms reside solely within the OBC, while other subsystems such as actuators and INS are represented as mathematical models within the simulation computer. This setup focuses on validating the algorithms without requiring real hardware.
- Actuator-In-Loop (AIL)*:* Real actuators are integrated into the HILS platform, allowing the performance of physical actuators to be validated under simulated conditions[9].
- Sensor-In-Loop (SIL): The INS undergoes validation in this configuration. The Flight Motion Simulator (FMS), driven by trajectory dynamics, rotates in three axes, generating inputs that simulate flight conditions[2]. The INS processes these inputs to produce navigation data, which is then sent to the OBC for further computation of control and guidance algorithm.
- Sensor-Actuator-In-Loop (SAIL): This is the final and

Received : 10 June 2024, Revised : 20 August 2024
Accepted : 13 September 2024, Online published : 10 January 2025

most comprehensive configuration, integrating the OBC, actuators, and INS in real-time for a complete end-to-end validation of the avionics system clearing the software.

These configurations rely on diverse communication protocols, such as RS-422, Ethernet, and MIL-STD 1553, alongside signal conversion interfaces like ADC and DAC. MIL-STD 1553 is preferred in avionics due to its redundancy and simple architecture, which ensures robust data exchange between subsystems[3].

Despite the advancements, two significant challenges persist:

1.1 Flight Motion Simulator (FMS) Accessibility

The FMS is a critical piece of equipment used for INS validation, capable of simulating high-dynamic rotational movements based on trajectory dynamics. Due to its complexity and operational requirements, the FMS is typically housed in a controlled and secure environment, often located far from the HILS laboratory[5]. Relocating HILS setups to the FMS site or establishing parallel setups introduces delays, operational inefficiencies, and potential safety risks due to proximity work conditions. Additionally, simultaneous usage of the FMS by multiple aerospace projects further complicates the scheduling and testing process.

1.2 Actuator Integration

Actuators, which are often installed in flight subsystems or undergoing testing in integration hangars, present logistical challenges for transportation and re-installation in the HILS laboratory. Their remote integration is critical to optimizing the testing process while maintaining real-time communication and feedback.

To address these challenges, this research proposes a novel Fiber Optics Data Acquisition System (FODAS) based on the MIL-STD 1773 communication protocol. This system enables real-time, low-latency data transfer over long distances using fiber-optic communication, ensuring seamless integration of critical subsystems with the HILS platform[6-7]. The proposed FODAS system is designed to encode and transmit both discrete and continuous signals over fiber-optic links, supporting a wide range of communication standards, including MIL-STD 1553 and RS-422[8].

Key benefits of the FODAS system include:

- Remote operation of the FMS for INS validation without requiring physical relocation of the HILS setup, thereby optimizing resource utilisation and eliminating setup re-establishment delays.
- Seamless integration of actuators located in distant integration hangars, enabling real-time testing with digital or analog feedback transmitted back to the HILS simulation computer.

This research outlines the design methodology and development of the FODAS system, considering the stringent requirements of aerospace safety standards such as AS9100. The proposed solution not only enhances the efficiency and flexibility of HILS testing but also ensures compliance with operational safety guidelines. By addressing the challenges of remote integration and communication, this approach facilitates faster project completion, reduces logistical complexities, and significantly improves the accuracy and reliability of avionics system validation. Detailed analysis, results, and conclusions from the implementation of the FODAS system are discussed in subsequent sections.

2. LITERATURE REVIEW

An extensive literature survey has been carried out about the remote simulation feasibility in the HILS area. A paper is studied on SCRAMNET Technology which is popularly used in the avionics field[7]. It is based on a shared memory interface card. The disadvantage of this network is that it is not an integrated solution with the other data communication interfaces like ADC, DAC, and RS-422 commonly used in the avionics field. It is only an I/O card integrated into the system. A research paper titled “Investigation into Network Architecture and modulation scheme for MIL-STD-1773 Optical Fiber Data Buses” focuses on the concept of the MIL-STD 1773 communication protocol[6]. Similarly, a paper titled “cPCI-based Hardware In Loop Simulation” explained about the I/O interfaces of the HILS system[3]. This is a detailed explanation of the system development for the HILS. These papers do not cover any development of MIL-STD 1773-related information for HILS application. So, the unique concept of a Fiber optics Data Acquisition System development based on MIL-STD 1773 for HILS remote simulation has been designed, developed, and deployed for the HILS application.

3. PROBLEM DEFINITION

3.1 Existing HILS Setup

The current Hardware-In-Loop Simulation (HILS) infrastructure has been extensively tested with various avionics-based configurations, ensuring robust performance under simulated flight conditions[9-10]. As illustrated in Fig. 1, different HILS setups are designated to specific locations and operate independently to validate various avionics subsystems[10].

During the Sensor-In-Loop (SIL) configuration, real hardware such as the Inertial Navigation System (INS) must be validated against simulated flight dynamics. To achieve this, the HILS setup often needs to be relocated temporarily to the Flight Motion Simulator (FMS) facility. The FMS, a critical piece of equipment used for simulating high-dynamic flight trajectories, is typically housed in a controlled and secure environment. Relocating the HILS test-bed close to the FMS for each project introduces significant challenges, including:

- Schedule Disruptions: Re-establishing the HILS setup for every project delays the testing timeline, affecting the overall project schedule.
- Operational Risks: Working in proximity to the FMS and other critical equipment can lead to unsafe conditions due to the complexity and scale of the machinery.
- Logistical Constraints: Frequent relocation of the HILS setup is labor-intensive and prone to errors, potentially leading to inefficiencies.

Similarly, actuators, which must be tested before launch, face logistical challenges. Once integrated into the flight

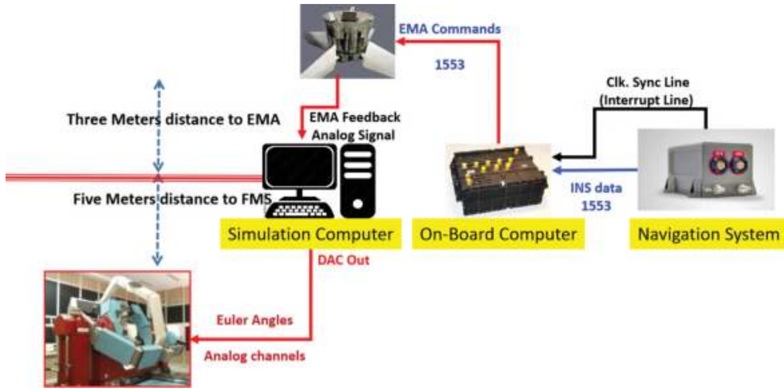

Figure 1. Existing HILS test-bed in proximity of FMS and Actuator.

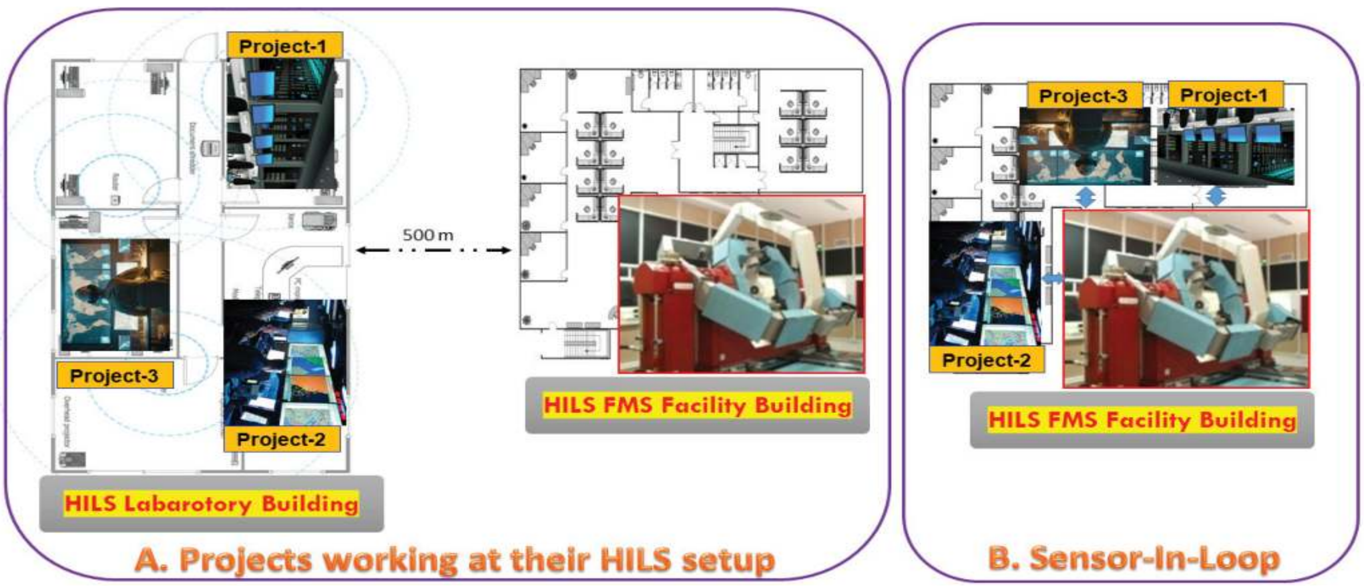

Figure 2. HILS testing of various avionics configuration, A. HILS Lab. B. Near FMS location.

vehicle's sub-system, transporting them to the HILS facility for validation becomes difficult. This process not only risks minor damages during transit but also requires extensive reassembly efforts, further delaying the testing schedule.

3.2 Proposed HILS Remote Simulation

To overcome these limitations, this research proposes a remote simulation methodology that leverages advanced communication and automation technologies to enable the remote operation of critical flight subsystems without compromising real-time performance[11]. Key features of the proposed solution include:

3.2.1 Remote Operation

Flight subsystems, such as actuators and the INS, can remain in their original locations while being integrated with the HILS test-bed. This eliminates the need for physical relocation, thereby reducing risks and delays.

3.2.2 Versatile Data Acquisition System

The system must support both analog and digital communication interfaces to seamlessly acquire data from a variety of avionics components. This ensures compatibility with existing systems while enabling future scalability.

3.3.3 All-in-One Communication Solution

An integrated, unified data communication system will be developed to handle multiple protocols, including analog, digital, and high-speed fiber-optic communication.

The implementation of this proposed remote simulation framework is expected to:

Significantly optimise the HILS testing schedule by reducing the time required for setup re-establishment.

Improve the safety and reliability of operations by minimizing handling and transportation risks associated with sensitive equipment.

Enhance flexibility and scalability, allowing for simultaneous testing of multiple projects without interference.

By addressing these challenges, the HILS remote simulation methodology represents a significant step toward a more efficient and robust testing framework for modern avionics systems. This development will ensure timely project delivery and maintain compliance with stringent quality standards in the aerospace industry[11-12].

4. METHODOLOGY

The architecture of the FODAS-based system is based on the processor and the interfaces. The software modifications have been done in the simulation computer to send and receive the data from FODAS systems. Design and development of hardware and software for remote simulation has been done in a phase-wise manner. Both the FODAS systems are the same in the hardware architecture. Only the difference is the BC and RT configuration that is done through the software[12]. The component of the full setup is explained point wise and then the integration and communication have been discussed in this section.

4.1 Brief Technical details of MIL-STD 1773

The foundation of the 1773 protocol is based on the MIL-STD 1553. It is a serial bus with redundancy and duplex communication architecture popularly used in avionics buses with Bus-Controller (BC) and Remote Terminal (RT) architecture. BC is responsible for scheduling the data messages to RT.

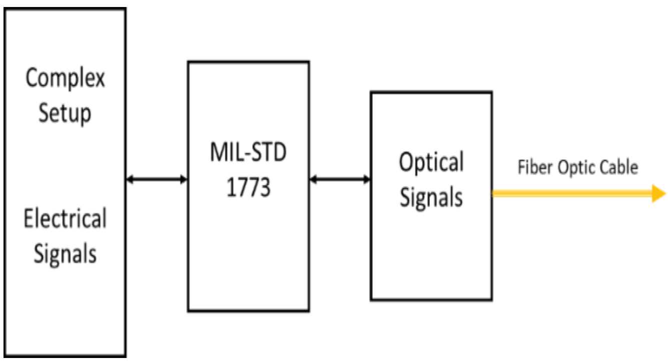

Figure 3. Basic diagram of MIL-STD 1773.

MIL-STD 1773 is a bus architecture with Fiber as a medium of transmission as shown in Fig. 3. The protocol wise it is the same as MIL_STD 1553. One side MIL-STD 1773 is the electrical bus of MIL-STD 1553 and the other side is the optical signals that are transmitted through optical Fiber cable. Optical Fiber is used to travel the distance at longer distances, immune to noise and electrical interference. The data rate is the same as MIL-STD 1553 which is 1 Mbps. MIL-STD 1773 protocol is used in the case of remote control, configuration, and operation. Mainly in the case of the avionics field, it is used to send signals at remote locations. This signal has been transmitted via Fiber optical cable.

4.2 Fiber Optics Communication

The Optical Fiber communication process transmits a signal in the form of light which is first converted into the light from electrical signals and transmitted, and then vice versa happens on the receiving side.

Fiber optic cable generally consists of a glass material covered by the cable.

4.3 MIL-STD 1553 to/from MIL-STD 1773

FODAS is a Fiber Optic Data Acquisition System as shown in Fig. 4. This is used to configure specific application requirements for remote operation by using the micro-controller-based software that resides in the ROM memory. This system will convert the 1553B Electrical data to Fiber optic 1773 and Analog IO, Digital IO, Muxing, and framing, converting into Fiber optic and vice versa. Separate two channels of RS-422 are configured for interrupt signal[8]. This unit finds applications requiring long-distance data transfer through MIL-STD-1553B protocol involving bus lengths of the order of 1-3 km. The unit also can be used for 1773 to MIL-STD 1553B conversions facilitating the testing of optical systems with existing MIL-STD-1553B test equipment. The unit also can be used for wire to/from Fiber Conversion applications. The unit facilitates the MIX and Match of MIL-STD-1553B/1773 Buses. The main Specifications are as follows:

- Processor: MC68LK332 (3.3V)
- 512 MB SRAM with 1 MB FLASH
- Digital Inputs/Outputs: 16 Channels, 28V
- Analog Inputs: 16 Channels, +/- 10V, 16 bit
- Analog Output: 16 Channels, +/- 10V, 16 bit
- RS-422 Channels: up to 115. Kbps
- 1553 Receiver: 01 Node, Redundant.
- 1553 Transmitter: 01 Node, Redundant.
- Fiber Optic Channels: 5 Nos, FC/ST/SC
- Easy interface connectivity to an external

MC68LK332 is a modular 32-bit micro-controller operating at 16.78 MHZ. It incorporates a central processing unit (CPU32), a system integration module (SIM), a queued serial module (QSM), a time processor unit (TPU), and a static 2K-byte static RAM module with TPU emulation capability. This is the main unit of FODAS and interfaces built with this micro-controller.

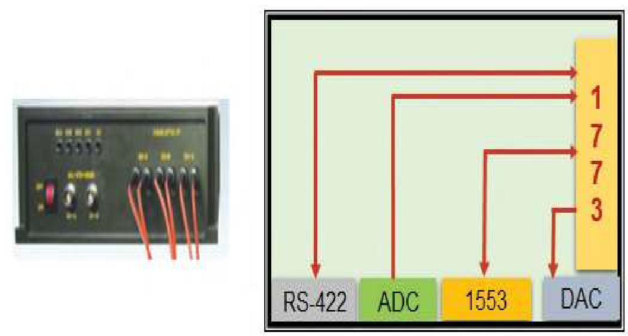

Figure 4. FODAS internal architecture.

Two FODAS systems have been developed that work in the Master and slave configuration. The software is developed according to the configuration. In the master configuration 1553 interface on FODAS is configured as BC and on the other side FODAS-2 is programmed to work as RT. The communication between FODAS-1 to FODAS-2 is via optical Fiber media and this does not affect the external interfaces and subsystems connected with this. The system is configured and integrated according to the vehicle configuration details. The number of channels for DAC, ADC, RS-422, and MIL-STD 1553 interface is explained below. All the required interfaces for the avionics integration is available with the FODAS. The resolution is 16 bit that offers the good sensitivity that is sensed by the FMS and the simulation is carried out with integration of the HILS test setup . This is cost effective solution for the data acquisition system integrated with the distance simulation and all the subsystems has been integrated and simulated with

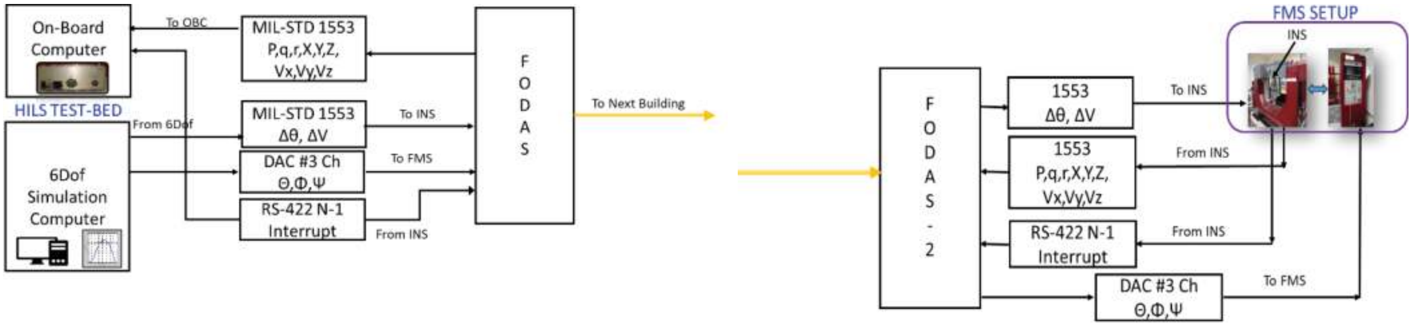

Figure 5. HILS test-bed interfaces to FODAS.

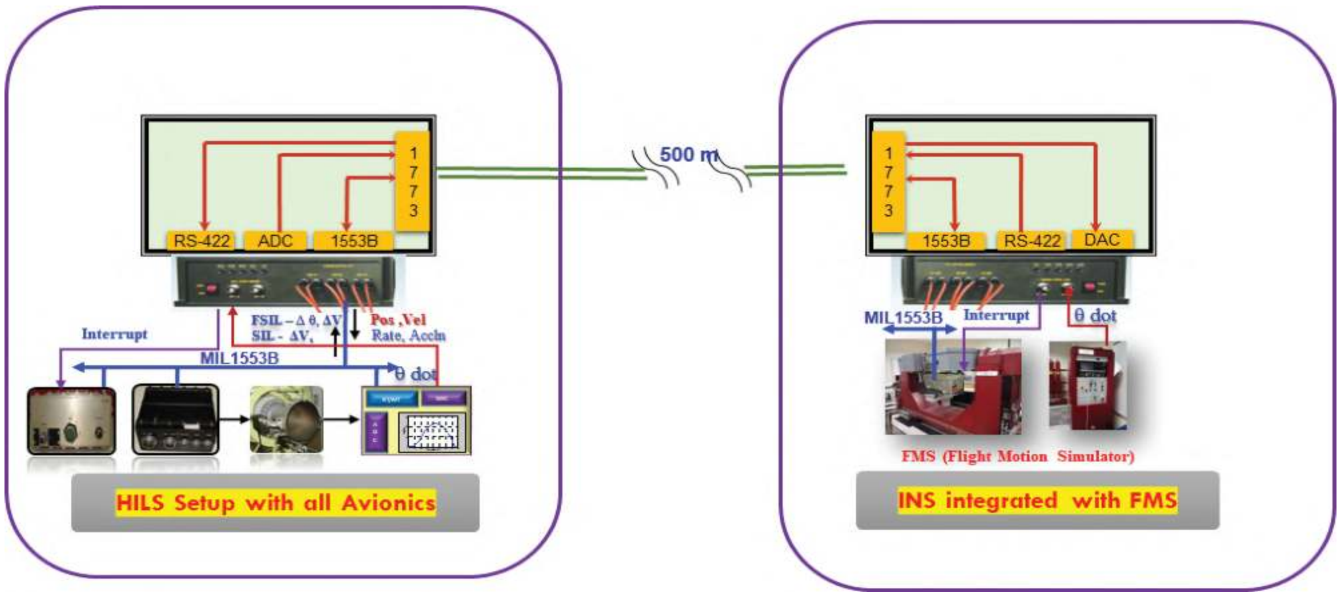

Figure 6. Remote Simulation Integrated Setup with FODAS system deployed at both sites.

the remote simulation. The following section explains the integration of hardware and software.

4.4 Test-bed Integration and Methodology

4.4.1 FODAS-1 (at HILS Testbed side)

The data communication from the HILS Testbed is interfaced with FODAS-1 to send incremental angles and velocities to INS, Euler angles to drive FMS, and RS-422 to receive clock sync to OBC. Both sides' configuration is shown in Fig. 5.

- Analog to Digital Channels: The Euler angle information is sent via DAC of the simulation computer and input as ADC to FODAS-1. 3 Channels are configured.
- MIL-STD 1553 Node-1: The incremental angle and velocities information is sent to INS via node-1. The INS information is received by the MIL-STD 1553 interface to OBC. OBC schedules the messages according to the algorithm on the mission node.
- RS-422 Interface: The clock synchronization of INS as a master to OBC is done by the RS-422 interface. At HILS side RS-422 receives the interrupt signal @2.5 ms and is connected with OBC via Digital Input.

4.4.2 FODAS-2 (at FMS side)

The processed information is sent back to the HILS Testbed by FODAS-2. The INS processed data that is position, and velocities have been sent. The Euler angles have received and interfaced with FMS as well as interrupt generated by the INS is sent for synchronization with OBC through the RS-422 interface.

- Analog to Digital Channels: The Euler angle information is sent via DAC of the simulation computer and input as ADC to FODAS-1.
- MIL-STD 1553 Node-1: The incremental angle and velocities information is sent to INS via node-1. The INS information is received by the MIL-STD 1553 interface to OBC.
- RS-422 Interface: The clock synchronisation of INS as a master to OBC is done by the RS-422 interface. At HILS side RS-422 receives the interrupt signal @2.5 ms and is connected with OBC via digital input.

There is no change in the avionics software as well as mission software. Plant Simulation Software Undergo the change in the software. In the broader view of the HILS process, for avionics subsystems, both the methodologies that are set up in the proximity of FMS and FODAS-based remote HILS simulation should show exact simulation performance. The newly developed methodology has been tested with several test cases with FSIL and SIL configurations.

The integrated remote simulation setup is shown in Fig. 6. The HILS setup is connected with FODAS with the

FMS simulation facility. The HILS Test-bed is located at about 500 mtr distance from the FMS and the FMS is operated in real time with the minimum latency that simulate the trajectory dynamics with high sampling rate.

5. METHODOLOGY

Interfacing software for the simulation computer is modified according to the new methodology of FODAS and the software is developed to test INS fully with different configurations. Two main configurations have been explained below.

5.1 Full Stimulation-In-Loop (FSIL) Mode

In this configuration, only the navigation algorithm is validated. The raw data as measured by INS are incremental angles and velocities that have been sent (stimulated) by the simulation computer[10] to the navigation algorithm. So, the INS does not experience any dynamic movement or rotation but only the navigation algorithm is validated by using the simulation computer's information bypassing the real sensors. With the remote simulation setup, only the MIL-STD 1553 and interrupt on RS-422 in real-time are evaluated. The main focus is to establish the communication and evaluate the that real-time exchange of the data packets is being communicated properly without any delay and dropping of packets to and from FODAS systems.

In Fig. 7, the software interaction with FODAS is shown. When the run configuration flag is set to FSIL and SIL as 2/3 then the code is executed to compute the incremental angles and velocities.

Rate_Body_Flight[] is converted to *Gyro_Samples[]* by using the *update_inc_vel_vector()* function. Similarly, the accelerometer samples are computed based on the acceleration computation.

A number of test cases have been executed with FSIL mode to monitor the data consistency and latency. Data shows the exact match of the parameters throughout the trajectory[11]. The Jitter and latency values are within the limit that is observed maximum to be a maximum of 10 microseconds due to the Fiber optics communication that has not affected the real-time simulation run. This proves that the real-time communication performance is as per the trajectory scheduling and the delays are in the tolerance limit.

```
Source2.cpp*  TextFile1.txt*
(Unknown Scope)

void GetRateAcc(double *dphidot, double *dthetadot,double *dsyidot, double *dphi,double *dtheta,double *dsyi)
{
    /* Conversion of Rate to Euler angles */
thetadot=(Rate_Body_Flight[1]*cos(phin)*(1.0/cos(syin))) - Rate_Body_Flight[2]*(sin(phin)*(1.0/cos(syin)));
syidot=(Rate_Body_Flight[2]*cos(phin)+Rate_Body_Flight[1]*sin(phin));
phidot=Rate_Body_Flight[0]-Rate_Body_Flight[1]*(cos(phin)*(sin(syin)/cos(syin)))+Rate_Body_Flight[2]*(sin(phin)*(sin(syin)/cos(syin)));

}

write_to_dac(fd_adlink,phidot*RAD_TO_DEG,-thetadot*RAD_TO_DEG,-syidot*RAD_TO_DEG);
```

```
Source1.cpp*  TextFile1.txt*
(Unknown Scope)
double Accl_Body_Flight[3],Rate_Body_Flight[3];

 if(config.sensor == 2 || config.sensor == 3) /* 2= FSIL and 3=SIL */
 {
     /* Update Incremental angles and velocities from rates and accelerations */
   update_inc_vel_vector(accelarometer_samples,Accl_Body_Flight);
   update_inc_angle_vector(Gyro_samples,Rate_Body_Flight);

   /*send the Incremental angles and velocities */
   send_Inc_Angles(Dev53_1,Gyro_samples); /* Send Gyros on 1553 subaddress as per ICD of INS */
   send_Inc_Velocities(Dev53_1,accelarometer_samples);/* Send Acclerometers on 1553 subaddress as per ICD of INS */

 }
```

This information was then sent to 1553 devices by using:

Send_inc_Velocities(Dev53_1,accelerometer_samples);
Send_inc_Velocities(Dev53_1,Gyro_samples);
Where Dev53_1 is the driver ID of 1553 node-1.

Figure 7. Simulation computer's software flow.

5.2 Sensor-In-Loop Mode

The dynamic movement according to the trajectory[5] is simulated in this configuration and this is experienced by the sensors of the INS system. All the interfaces, 1553, ADC, DAC, and RS-422 have been utilized for SIL. The INS mounted on the FMS is driven by the simulation computer's Euler angles. In this case, the FMS is in a closed loop and the DAC output of the FODAS-2 is integrated with FMS. The sensed gyros rotations in three directions are being given to the INS algorithm and the navigation output is sent in the form of a 1553 message as FODAS-2 input. That information is decoded by FODAS-1 and given to OBC as shown in Fig. 7. In the SIL configuration, the additional software part is DAC and ADC interfaces. As shown in Fig. 8, thetadot, syidot, and phidot are computed and sent to DAC channel driver ID fd_adlink. This further sends the voltage to DAC channels. The voltage sensitivity is based on the dynamic range required by the simulation. In this case voltage range of DAC channels is +/- 10V for a +/- 57.3 deg/sec rate. So, for 1V FMS is commanded to 5.7 deg./sec rotation. The simulation in real time @2.5 ms.

The real-time sampling rate for rates output to DAC channels @2.5 ms and incremental rates and acceleration to 1553 is @2.5 ms remains unchanged. The interrupt of INS to OBC is synchronized @2.5 ms. So, the real-time data communication from HILS Setup to FODAS and Fiber optic communication should be minimal with latency and jitter values in tolerance limit that should not affect the real-time performance of close loop HILS testing.

6. TESTING AND VALIDATION

Before the deployment of the new methodology rigorous testing has been carried out with a number of test cases to create disturbance within the boundary limits of the dynamics[12]. The remote simulation test bed is established with the two buildings connecting with fiber optics interface. The real time data is sent and received with the HILS test setup. Following are the observations during the HILS simulation:

Table 1. HILS test-case matrix

Test cases	Trajectory-1	Trajectory-2	Trajectory-3
Full stimulation in loop			
FSIL Case-1	Pass	Pass	Pass
FSIL Case-2	Pass	Pass	Pass
FSIL Case-3	Pass	Pass	Pass
FSIL Case-4	Pass	Pass	Pass
FSIL Case-5	Pass	Pass	Pass
Actuator In Loop Simulation (AIL)			
AIL Case-1	Pass	Pass	Pass
AIL Case-2	Pass	Pass	Pass
AIL Case-3	Pass	Pass	Pass
AIL Case-4	Pass	Pass	Pass
AIL Case-5	Pass	Pass	Pass

6.1 Observations during HILS Runs

6.1.1 Grounding of the Test Setup

Noise affects the analog signal and the remote simulation is also affected because of the noise entered into the signal dominating the amplitude of the signal as the FODAS communication is mixed signal-based for simulation. The real-time performance is affected by the noise interference. Low-Pass-Filter (LPF) at the FODAS-2 Output side i.e. at the FMS side is designed to eliminate the noise at 50 Hz frequency. The values of the R= 1000 ohms and C=3.15 uF for the elimination of 50 Hz noise. After this additional circuit in the FMS input path, the analog signal noise was eliminated and the real-time performance of HILS runs has been assured with the same as close proximity run.

6.1.2 RS-422 Interface for Interrupt

The INS and OBC are synchronized by the clock signal of the INS. So, this signal has to be connected to the HILS test bed. In the initial development, the RS-422 interface for interrupt was not available with FODAS. The RS-422 interface is integrated as per the requirement of this application. It is tested and integrated.

6.2 Jitter and Latency in Real-Time

The latency observed is 10 us for the 1553 and 1773 channels and for the ADC and DAC channels, it is 12 us which is well within the limits of the execution cycle of the algorithm. This does not affect the performance of the HILS simulation in real-time. The delays of the fiber optics communication are negligible and the execution of the simulation algorithm data @2.5 ms

7. RESULTS ANALYSIS

Various parameters of the trajectory are analysed for the delay in communication, latency and drop in the packets. Before deployment of this new methodology, the old HILS run data (HILS set up in proximity to FMS) is compared with this new methodology. The simulation conditions are the same with the trajectory profile maintained the same. As shown in Fig. 8, the data is plotted in blue color representing the trajectory parameters for the new methodology, and in red color for the old data. The result analysis shows that both simulations are exactly matching. With remote simulation, the exact behaviour throughout the trajectory is observed even with the analog signal communicated with the MIL-STD 1773-based FODAS system. There are no effects of latency and noise on the performance and the methodology is accepted for the ongoing and future HILS setup to validate the avionics system.

8. CONCLUSION AND SUGGESTIONS

The FODAS scheme was conceptualized, designed, developed, and deployed indigenous. The results from real-time simulation runs demonstrate the system's reliable performance, with no jitters and minimal latency. This product uses a single-node MIL-STD 1553 bus, which meets the requirements of various avionics test-beds. However, for broader use in avionics projects, configurations requiring a dual-node MIL-STD 1553 bus can be implemented. The remote integration of the subsystems are now possible with the FODAS based Test setup. Many of the test-cases have been tested and the performance of this setup is matching the legacy simulation. That prove that with the adoption of the new

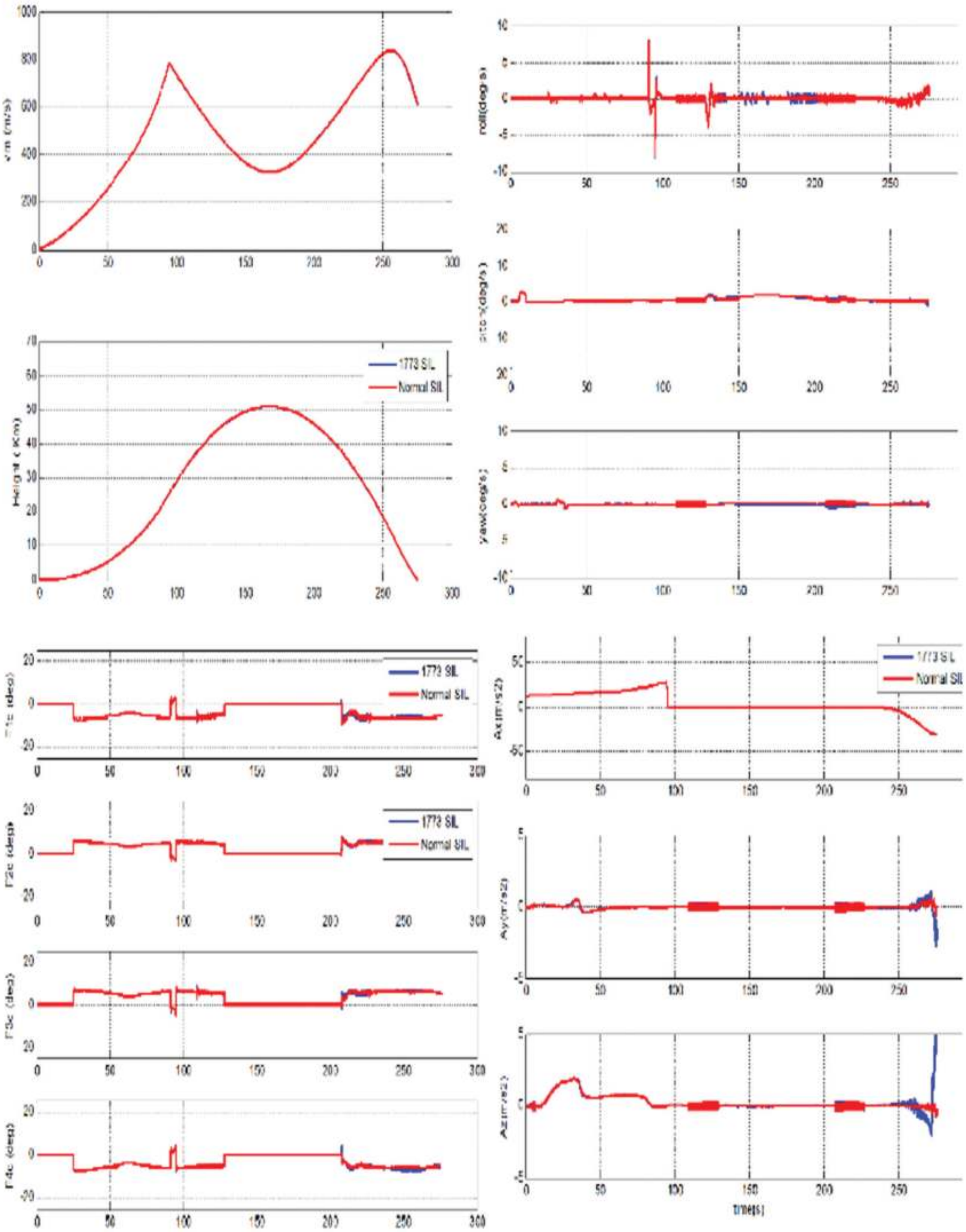

Figure 8. Result analysis with HILS simulation.

methodology has enhanced the performance of the simulation with the significant improvement in HILS technology.

Furthermore, the adaptation of newer interfaces to the FODAS hardware data acquisition architecture can be made to increase processing speed, aligning with the execution speed of weapon systems. This enhancement would make the FODAS system more agile and flexible, enabling its adoption for a wider range of applications.

REFERENCES

1. Xu, H.; Zhang, X. & Liang, Y. A General platform of hardware-in-loop simulation for integrated design. *In* Proceeding of 40th Chinese Control Conference 2021, pp. 6766-6771.
doi: 10.23919/CCC52363.2021.9549542.
2. Rajesh, K. & Ramesh, K.B. Development of hardware-in-loop simulation test-bed for testing of navigation system-INS. *In* Proceeding of International Conference on Machine Intelligence Research and Advancement 2013, pp. 536-539.
doi: 10.1109/ICMIRA.2013.112.
3. Randhawa, R.H. & Imran, M.A. Low-cost design of

MIL-STD 1553 devices. *In* IEEE First AESS European Conference on Satellite Telecommunications (ESTEL) Rome 2012, pp.1-4.
doi: 10.1109/ESTEL.2012.6400062.

4. Rajesh, K. cPCI based hardware-in-loop simulation system development under real time operating system. *In* Proceeding of International Conference on Advances in Computing, Communications and Informatics 2014, pp. 736-739.
doi: 10.1109/ICACCI.2014.6968563.
5. Weiss E.; Guillaume S.; Geiger A.; Hohensinn R. & Wipf H. Optimisation of safety critical IFR helicopter trajectories in alpine areas using MILP. *IEEE Trans. Aerosp. Electron. Syst. J.*, 2023, **59(2)**, 1127-1138.
doi: 10.1109/TAES.2022.3197563.
6. Zhang, J.; Sharma, A.B.; Ni, Y. & Li, Z. Investigation into network architecture and modulation scheme for MIL-STD-1773 optical fiber data buses. *Aircr. Engg. J.*, 2000, **72(2)**, 126-137.
doi: 10.1108/00022660010325229.
7. Ni Yu-De; Li Zheng & Zhang Jian-Guo A high-performance fiber optic data bus based on MIL-STD-1773, *In* Proceedings IEEE/AIAA 11th Digital Avionics Systems Conference 1992, p. 400-406.
doi: 10.1109/DASC.1992.282126.
8. Karvande, R.S.; Sobhan, K.L. & Raman, M. Multi-node MIL-STD-1553 Avionics bus-monitor development under linux platform. *In* Advances in Decision Sciences, Image Processing, Security and Computer Vision ICETE 2019, **3**, pp. 245-249.
doi:10.1007/978-3-030-24322-7_32.
9. Rajesh K. & Tatineni, M. Optimised digital simulation methodology for system validation using real-time hardware-in-loop simulation platform. *IEEE Aero. El. Sys. Mag.*, 2024, **39**(8), 18-27.
doi: 10.1109/MAES.2024.3412034.
10. Qian, X.; Xiaodong, L.; Wenjing, Z.; Ya, B.; Le, M. & Penghzen, H. A servo simulation test calibration and compensation method for hardware-in-loop simulation of aerocraft control system. *In* Proceeding of 34th Chinese Control and Decision Conference (CCDC) 2022.
doi: 10.1109/CCDC55256.2022.10033579
11. Zhou Y.; K.V. Ling, F. Ding & Y. Hu, Online network-based identification and its application in satellite attitude control systems. *IEEE Trans. Aerosp. Electron. Syst.*, 2023. **59**(3), 2530-2543.
doi: 10.1109/TAES.2022.3215946
12. Roy, R. & Kailath, T. ESPRIT-estimation of signal parameters via rotational invariance techniques. *IEEE Trans. Acoust., Speech, Signal Process*, 1989, **37**(7), 984-995.
doi: 10.1109/29.32276.
13. Karvande, R. & Madhavi, T. High-performance optimized and unified bus monitor for distributed avionics architecture validation under hardware-in-loop simulation framework. *In* International Conference on Current Trends in Advanced Computing 2024, pp. 80-84.
doi: 10.1109/ICCTAC61556.2024.10581142.

CONTRIBUTORS

Mr Rajesh Shankar Karvande obtained MTech (Software Systems) from BITS, Pilani, India. He is pursuing PhD from GITAM Deemed to be a university, Hyderabad, India. He is working as a Scientist in DRDO-RCI. His areas of interest are modeling & simulation, real-time operating systems, and embedded software development and validation.
In the current study, he has conceptualised, designed, and developed the hardware and software. Testing and HILS runs have been carried out by him.

Mr Pulak Halder obtained M.E. from the Department of Electrical Engineering, Jadavpur University, India. He is working as a Scientist-G at DRDO-RCI, India. His research interests include: Fault detection and isolation and hardware-in-loop simulation.
In this research, he is involved in the design and development of the FODAS system, simulation, and defining the goals and validation of results.

Dr Tatineni Madhavi obtained PhD from Andhra University, India. She is working as a professor at GITAM Deemed to be the University, Hyderabad, India. Her main research interest include: Modelling and performance analysis of wireless communication systems and wireless sensor networks.
In the present work, She has reviewed the design and the research paper. She has given many guidelines and suggestions to resolve the problems during testing.

Defence Science Journal, Vol. 75, No. 1, January 2025, pp. 120-128, DOI : 10.14429/dsj.19326

The Degradation in Load Carrying Capability of Delaminated Specimens

Narendra Kumar Shrivastava[#,*], V. Suresh Babu[$], Manoj Kumar Buragohain[#] and Pushpam Dayal[#]

[#]DRDO-Advanced Systems Laboratory, Kanchanbagh, Hyderabad - 500 058, India
[$]National Institute of Technology, Warangal - 506 004, India
[*]E-mail: narendrashrivastava2010@gmail.com

ABSTRACT

Polymeric composites find extensive usage in aerospace applications, and their performance is influenced by environmental conditions throughout their life cycle. This study focuses on assessing the performance of composite laminates under different environmental conditions to evaluate the load carrying capacity (LCC) due to delamination. The laminates were specifically designed to withstand high pressure and temperature, ensuring satisfactory performance throughout their service life. The specimens, prepared according to ASTM standards with a thickness of 3 mm, featured different fibre orientations between the upper and lower laminates, including 0/0°, 0/30°, 0/45°, and 0/60°. The change in the delamination growth behavior for specimens subjected to different initial delamination lengths (a0) was studied using pre and post-radiographic tests (RT). The investigation encompassed a range of initial delamination lengths, from 70 mm to 110 mm, incremented by 10 mm. Notably, failure was observed in specimens with a 0/30º angle when the initial crack length (a0) reached 110 mm, while specimens with a 0/60º angle failed at an initial crack length of 80 mm. Additionally, it was noted that the maximum force required for the 0/30º angle laminate was observed when the initial crack length was 70 mm.

Keywords: Delamination; Double cantilever beam (DCB) specimen; Laminate; Mode-I; Load carrying capacity; VCCT

NOMENCLATURE

LCC	: Load carrying capacity
ASTM	: American society for testing and materials
RT	: Radiographic tests
a0	: Initial delamination lengths
DCB	: Double cantilever beam
MERS	: Modified epoxy resin system
VCCT	: Virtual crack closure technique
LEFM	: Linear elastic fracture mechanics
SERR	: Strain energy release rate
UT	: Ultrasonic testing
FEM	: Finite element method
CRMC	: Composite rocket motor casing
UD	: Unidirectional
UTM	: Universal testing machine
dB	: Decibel
SFD	: Source-to-film distance

1. INTRODUCTION

The use of metal is as old as civilization started. With the development of technology, we have shifted from metal to composites and used in various aerospace applications. The utilisation of composite materials has expanded from small-scale applications such as toys to more intricate components like aircraft, prosthetics for the human body, rockets, and other systems due to their lightweight nature and comparable mechanical properties to metals[1]. Consequently, scientists and engineers are keen on selecting an optimal blend of reinforcement and matrix materials to attain properties that precisely meet the specific structural requirements for a given purpose. The anticipated environmental conditions throughout various stages of the composite's life cycle greatly impact its performance. The failure of composite materials significantly diminishes their LCC. Failures can arise from different types of intralaminar fractures, including fibre breakage, microcrack development in the matrix, bonding issues between fibres and matrix, and delamination. Delamination, in particular, is a critical factor affecting the performance of composite materials[2]. During the manufacturing process, delamination occurs as voids between layers. These delamination defects, along with other manufacturing flaws, become embedded and can damage the composite structures during their service life. Delamination typically occurs at relatively low load levels, well before the full load capacity of the fibres is reached. As the presence and growth of such defects can adversely affect safety and durability, comprehending the impact of environmental conditions on the structural performance of composites is of utmost importance. This study focuses on identifying the reduction in LCC in laminates composed of T700 fibres with a Modified Epoxy Resin System (MERS) (LY556 & HY5200) (V_f=60 %). While a delaminated composite sample may experience a certain "mode" of failure initiation, the propagation and final failure modes can vary[3-5.] Three fundamental modes of interlaminar fracture are illustrated in Fig. 1.

Received : 31 July 2023, Revised : 28 April 2024
Accepted : 15 May 2024, Online published : 10 January 2025

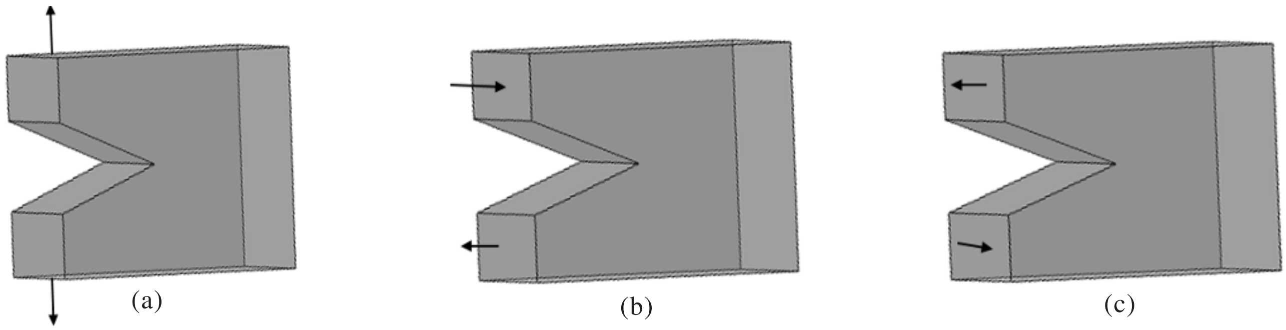

Figure 1. Basic diagram of (a) Mode I; (b) Mode II; and (c) Mode III.

Mode 1- The opening mode or peel mode
Mode II- The in-plane shear mode or sliding shear mode
Mode III -The out-of-plane shear mode or twisting shear mode

Delamination under tensile modes was investigated for T700 carbon fibre/ modified epoxy laminates under three-point bending using the virtual crack closure technique (VCCT) to measure the strain energy release rate (SERR)[6]. It is based on Linear Elastic Fracture Mechanics (LEFM). The energy released by a crack to grow its length from a to a+ Δa, must be the same to close the crack of length a + Δa to a. Experiments were conducted to find out the Mode I critical energy release rate (G_1C) at the interface of two laminate layups[7].

2. LITERATURE REVIEW

However, composite structures are susceptible to the accumulation of damage. To ensure reliability, timely and accurate damage detection throughout the life cycle of a structure is critical. In this context, a comprehensive approach to laminate delamination detection using Ultrasonic Testing (UT) and transmission RT was developed. Although there have been many publications on the design, development, and qualification of composite materials over the past decade, there is a lack of comprehensive work on structural integrity assessment using the above-mentioned techniques. The purpose of this paper is to gain an in-depth understanding of delamination issues arising from process parameter variations during manufacturing and to conduct transmission detection using UT and RT. However, there are some challenges due to the lack of foolproof methods and reference standards in the open-source literature. To address this issue, custom reference laminates were fabricated to simulate defects such as delamination, different thicknesses, and layer sequence angles, and their ultrasonic response was characterised. The ultrasonic response of full-scale composites is also studied, and an overview for assessing the structural integrity of the samples is provided. Most studies focus on Finite Element Method (FEM) analysis or individual experimental evaluations. However, in this study, finite element analysis was first performed to experimentally verify the results[8]. The main goal is to achieve a close match between the finite element method and the analytical design so that the two sets of data verify each other and ensure that the design is safe and free of laminate failures. Therefore, this study was conducted at the subsystem level to simulate actual hardware configurations and experimentally evaluate the overall impact of delamination on MERS laminate performance in a comprehensive manner.

3. MATERIAL SELECTION

The manufacturing processes and materials used to make the laminates are similar to those used to make Composite Rocket Motor Casings (CRMCs). Carbon-epoxy and glass-epoxy composites are suitable candidates for filament-wound CRMC[9]. In this study, carbon fibre T-700 samples with MERS (LY556 and HY5200) (Vf = 60 %) were prepared by filament development and subsequent curing in the same way as CRMC, aiming to track and test various physical and Mechanical behaviour. Characterisation in the context of raw material properties and validation of design properties[10]. The coupons were fabricated using a wet filament winding process and tested on unidirectional (UD) laminates, as shown in Fig. 2 and Fig. 3, respectively. The cured samples were examined for resin content and density according to ASTM D3171 and ASTM D792, respectively. All mechanical testing was performed using a universal testing machine. (Instron UTM 4505). All test samples were dried in a dehumidification chamber and the moisture content was calculated. The first sample is weighed at ambient temperature, then dried and weighed again. Moisture content $\leq$0.1 % was observed. Tensile tests were performed on longitudinal specimens (Fig. 3) to determine the longitudinal tensile strength, modulus, and principal Poisson's ratio. Sample preparation and testing were performed in accordance with ASTM D3039 standards. To evaluate transverse tensile strength and transverse tensile modulus, tensile tests were performed on flat (90°) transverse directions specimens. The tensile modulus was determined by performing tensile testing on samples with 45° fibre orientation to determine the shear modulus (G12). The evaluated properties of Carbon T700/ Modified Epoxy composite are given in Table 1.

Figure 2. Winding of laminate.

Table 1. Properties evaluated for carbon T700/modified epoxy composite (V_f =60 %) from experimental result

Property	T 700 / Modified Epoxy resin composite
Longitudinal tensile strength, MPa	2000
Longitudinal tensile modulus. GPa	128
Poisson's ratio	0.29
Transverse tensile strength, MPa	14
Transverse tensile modulus, GPa	9.0
Longitudinal compressive strength, MPa	800
Transverse compressive strength, MPa	60

Table 2. Physical properties of cured composite – carbon fibre T-700 (LY556 & HY5200) (V_f=60 %)

Properties	ASTM Std. No.	Tested value
Tex, g/km	D 3800	804
Density, g/cc	D 3800	1.785
Filament diameter, micron	-	6.98
Tensile strength of Fibre, MPa	D 4018	4800
Tensile Modulus of Fibre, GPa	D 4018	225

(a)

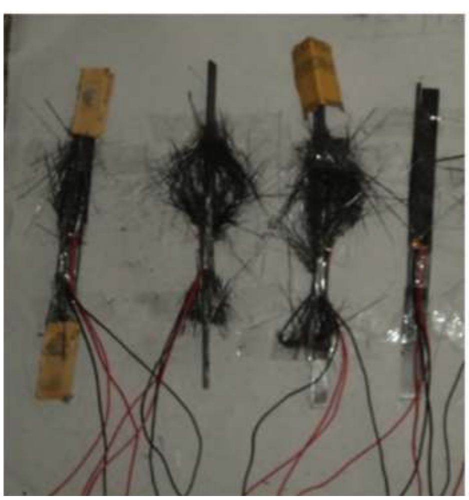

(b)

Figure 3. (a) Laminate with strain gauge; and (b) Failure modes of test results of composite (Vf = 60 %).

4. ANALYSIS ON MODE-1 DOUBLE CANTILEVER BEAM (DCB) SPECIMENS

FEM analysis was carried out to evaluate the damage tolerance capabilities, due to the different delamination topology. The crack was embedded inside the laminates and consequently, the crack area started to grow sy mmetrically with respect to the orthogonal axes, the length of the crack front increased accordingly. The following parameter can be changed in the macro element model to evaluate the effect of delamination:

- Delamination size[11]
- Ply sequence angle

4.1 FEM Flowchart

Tree diagram for FEM analysis is shown in Fig. 4. The laminate has a thickness of 1.5 mm, and delamination occurs between the 4th and 5th layers. To investigate the performance due to degradation of the laminate caused by delamination, 16 different pre-damaged (delaminated) models were created. These models specifically have delamination between the 4th and 5th layers. Initially, the ply sequence angle between the laminates was set at 0/0°, and the stress values were analysed by varying the initial delamination length. The initial delamination length starts at 70 mm and increases in increments of 10 mm until failure occurs. Furthermore, to analyse the impact of different ply sequence angles, four ply sequences were chosen: 0/0°, 0/30°, 0/45°, and 0/60°. The same methodology was repeated as 0/0° sequence[1.] For our study, we employed explicit finite element simulation using the APDL software. Initially, a 3D solid brick element with eight nodes (SOLID185) was selected, with the same properties as the T-700 with MERS carbon fibre, which were evaluated through an experiment (refer to Table 1 and Table 2). The software's INTER205 element was utilised to simulate the interface between two surfaces and the subsequent delamination process. Within the interface element, separation was depicted by a progressive

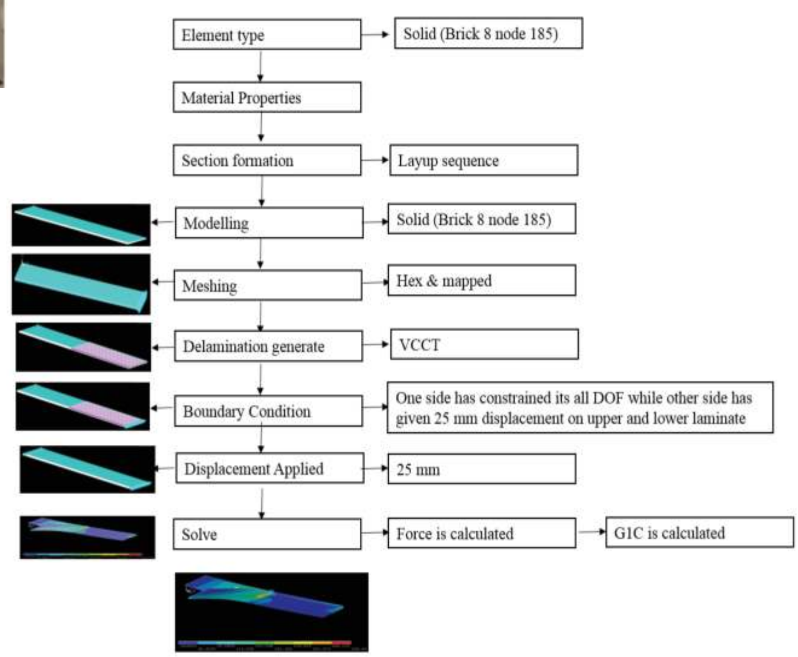

Figure 4. Algorithm of Mode I specimen for FEM.

displacement between nodes. All the relevant mechanical properties obtained from Table 1 were extensively used for the FEA. Cohesive elements were employed to describe delamination initiation and growth, aiding in capturing the intralaminar material behaviour of the composite. The VCCT approach was utilised for the delamination analysis. The FEM analysis model is depicted in Fig. 5.

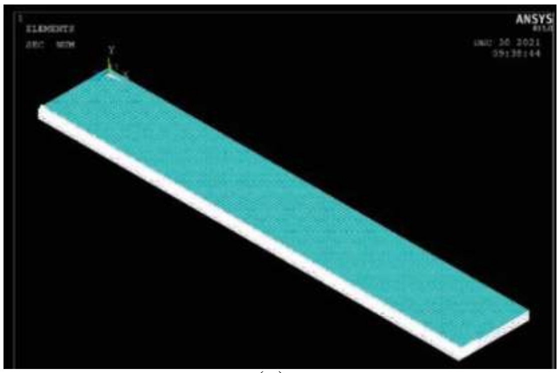

(a)

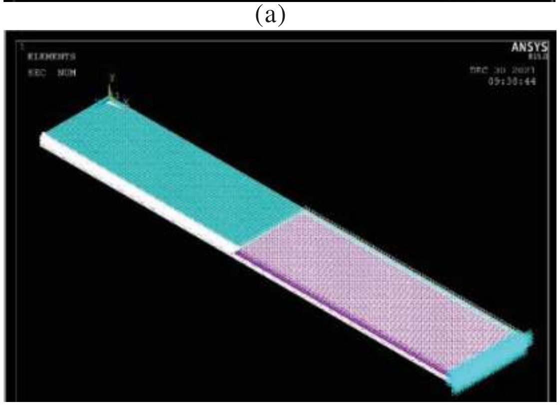

(b)

Figure 5. (a) Model with meshing; and (b) Model with various initial delamination length.

4.2 Modelling Setup

Sixteen different types of pre-damage models were created. To study the extended growth effect of the sample, initial cracks with different initial delamination lengths were found on the left, which occurred between layers 4 and layer 5, forming a cohesive zone. After the model is completed, meshing needs to be performed. Select "Hex" and "Mapping" as the meshing type.

4.3 Boundary Conditions

The analysis involves the use of a cantilever configuration for the composite panels, where one end is fixed and dynamic displacement constraints are applied to the other end. This configuration is shown in Fig. 6. The boundary conditions are:

- One side is fixed (all degrees of freedom are fixed)
- On the other hand, displacements were applied to the bottom and top laminates (initial displacement limited to 25 mm).

Figure 6. Boundary conditions and displacement at left end side.

4.4 Analysis Results

Load v/s displacement diagrams were recorded for 3 mm thick hybrid laminates at different layer sequences and different initial crack lengths in mode I, as shown in Fig. 7.

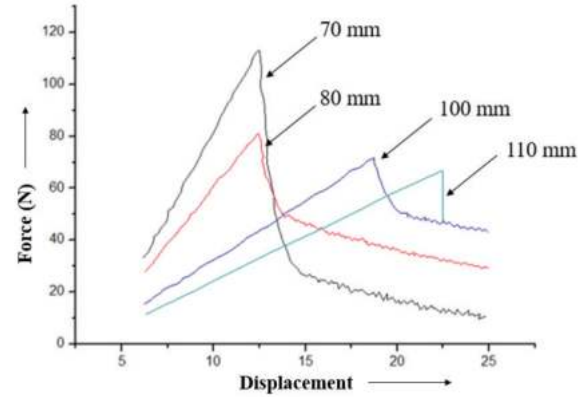

(a)

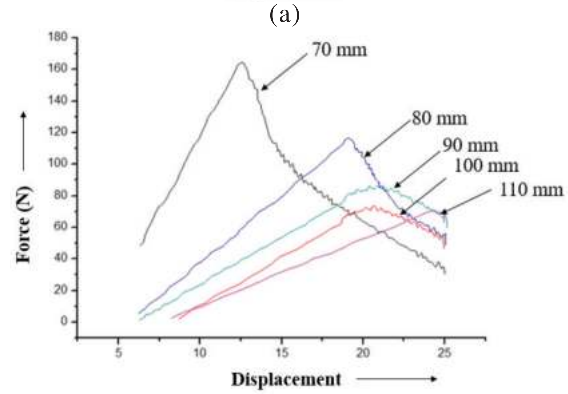

(b)

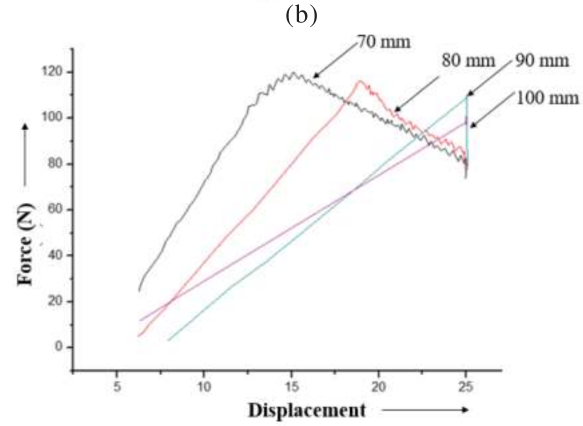

(c)

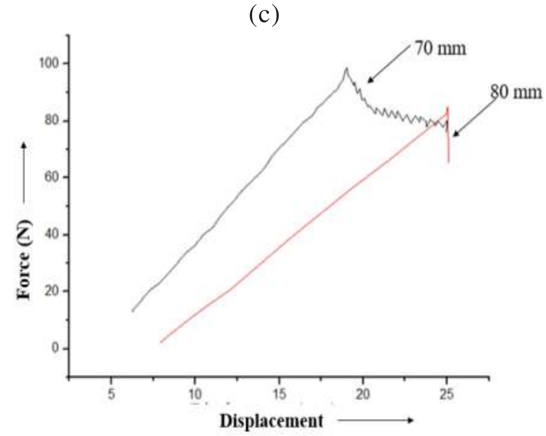

(d)

Figure 7. Force v/s displacement curve (a) 0/0°; (b) 0/30°; (c) 0/45°; and (d) 0/60° between upper and lower laminate.

Table 3. Theory used for evaluation of G1C

Theory	Formula	Parameter
Beam theory	$GIC = \frac{3Pc\delta}{2ba}$	
Modified beam theory	$GIC = \frac{3Pc\delta}{2b(a+\Delta)}$	Where, Δ = x-intercept of $C^{1/3}$ vs a compliance
Calibration method	$GIC = \frac{nPc\delta}{2ba}$	Where, n= slope of log(C) vs log(a)
Modified compliance calibration method	$GIC = \frac{3Pc^2\delta^{\frac{2}{3}}}{2A_1bh}$	Where, A_1 = slope of a/2h vs $C^{1/3}$; h = specimen thickness (mm)

The specimens exhibit a steep linear increase in the curves until a certain point, at which they abruptly fail, leading to a nonlinear decrease in the applied force. Figure 7 illustrates that the failure behaviour of the laminate varies in each case. As the angle between laminates increases, the peak values of force required for failure decrease, and this reduction occurs at a shorter initial crack length, which was crucial for calculating G1C. For instance, in the case of a 0/30º angle, the laminate fails after an initial crack length (a0) of 120 mm, while for a 0/60º angle, the failure occurs at just 80 mm of initial crack length. Similarly, increasing the initial crack length results in decreased force required for failure, but it also leads to greater displacement for a valid G1C determination. The FEM results are depicted in Fig. 8. In our study, various theories were employed to evaluate G1C, as outlined in Table 3. The evaluated values of G1C through FEM analysis are presented in Table 4.

Table 4. G1C evaluated value through FEM

Angle	a_o (mm)	P_c (N) (Max)	G1C value using Beam Theory (J/m²) (Avg)	G1C value using Modified Beam theory (J/m²) (Avg)	G1C value using Compliance calibration method (J/m²) (Avg)	G1C value using modified compliance calibration method (J/m²) (Avg)
0/0°	70	113.85	1219.82	1222.23	1220.32	1221.56
	80	81.168	760.95	763.42	758.32	765.37
	90	75.26	928.20	935.67	933.42	934.24
	100	71.22	799.3147	805.24	807.51	807.68
	110	61.48	753.521	742.35	743.12	748.32
0/30°	70	163.012	1746.01	1751.69	1748.96	1750.61
	80	116	1660.09	1666.34	1658.48	1664.18
	90	86.54	1198.291	1195.04	1199.64	1124.86
	100	73.67	914.69	919.84	910.25	912.54
	110	70.53	928.69	925.63	928.68	927.95
0/45°	70	120.966	1564.714	1574.35	1570.19	1572.43
	80	111.735	1647.197	1651.35	1654.73	1657.28
	90	110.397	1839.95	1836.21	1841.55	1843.61
	100	100.731	1510.965	1517.89	1521	1526.44
0/60°	70	98.82	1613.813	1612.52	1615.78	1614.2
	80	85.616	1642.814	1638.75	1640.85	1638.85

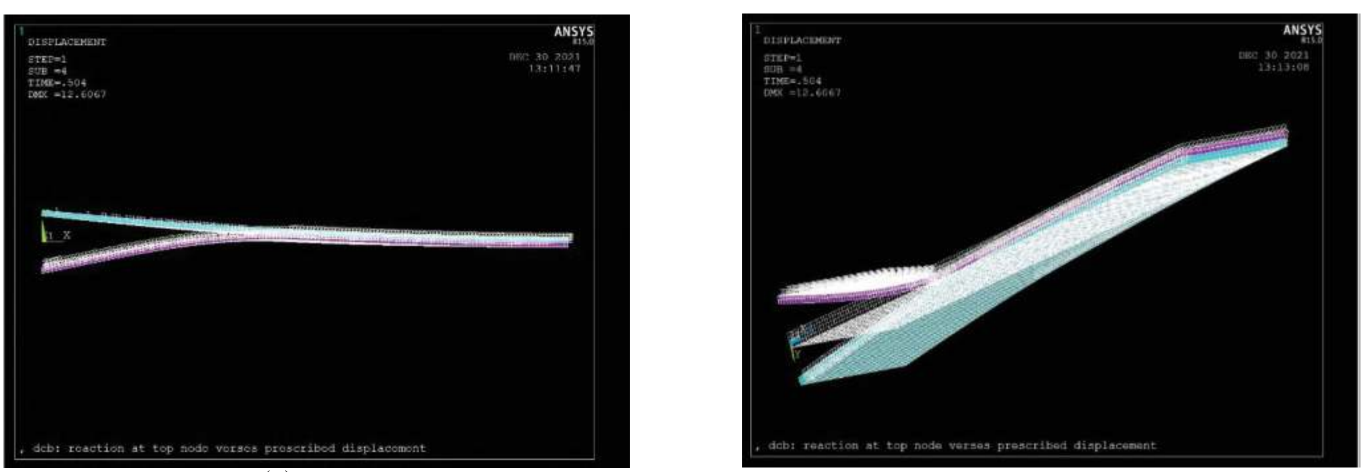

(a) (b)

Figure 8. For a0= 80 mm (a) Deformed shape; and (b) Deformed shape with un-deformed shape.

5. EXPERIMENTAL EVALUATION

5.1 Test Setup & Methodology

In this study, we fabricated test laminates with the same orientation and initial crack length used in the FEM analysis. The dimensions of each test sample are 200 mm long, 25 mm wide and 3 mm thick. The fibre orientations selected for the test samples matched those of the FEM analysis, which included 0/0°, 0/30°, 0/45°, and 0/60° angles. For experimental purposes, a pre-crack was introduced at the tip between the bottom laminate and the top laminate. Additionally, an additional 50 mm pre-crack was fabricated to accommodate the 50 mm long bracket, allowing the UTM to exert forces similar to the FEM analysis setup. The midplane of each sample contained polytetrafluoroethylene inserts of varying lengths that acted as delamination initiators. The flat test specimen is produced using a filament winding process, as shown in Fig. 9. The process involves wrapping the UD matrix around a large mandrel, cutting and removing the wrapped material from the mandrel, then laying the material flat, setting and curing in an autoclave. The carbon fibres are impregnated using filament winding technology by heating the resin system to 45 °C. After the filaments are developed, the laminate undergoes a curing process in an oven with precisely controlled temperatures. The flat mandrel is placed in the oven and supported by a metal stand. Table 5 provides details of the cure cycle.

(a)

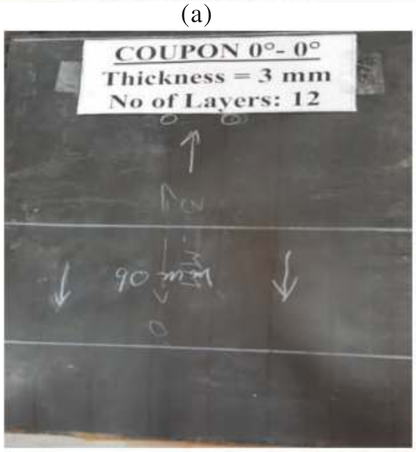

(b)

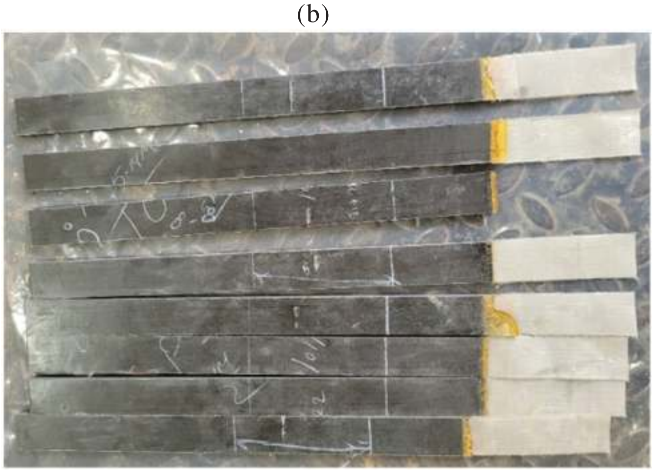

(c)

Figure 9. (a) During filament winding; (b) Coupon prepared; and (c) Coupon with teflon sheet coupons.

Table 5. Cure cycle

Initial temperature (°C)	Final temperature (°C)	Time (min.)	Remarks (heating rate per minute)
Room temperature	120	30	2 to 4°C
Hold at 120° C		180	
120	160	30	2 to 4°C
Hold at 160° C		180	
Switch off the oven and allow the component to cool naturally.			
Open the door and remove mandrel when it is below 40°C.			

Delamination is detected and confirmed using Non-Destructive evaluation techniques such as radiographic imaging. RT was carried out for each specimen and found to be as predicted. Radiographic image for 0/30° having 70 mm initial crack length as shown in Fig. 10. To precisely identify the type of discontinuity present, we correlated areas of high decibel (dB) loss with tangential X-ray radiography images. The X-ray radiography was conducted in regions exhibiting significant dB loss using a 4MeV LINAC machine.

(a)

(b)

Figure 10. Delamination (a) Before the experiment; and (b) After the experiment.

We opted for a source-to-film distance (SFD) of four meters and an exposure time ranging from one to two minutes for the examination. In Fig. 10, we depict radiographic images capturing the high dB loss zones. Zones exhibiting a dB loss greater than 12 have been determined to indicate delamination. In essence, we characterized and analysed the high dB zones, identifying their nature and extent relative to the overall inspected area, shedding light on potential structural issues such as delamination.

Use a band saw to cut the laminate in different directions. Assemble the load application system and place the plate in the machine's handle and secure by adjusting first the lower hinge and then the upper hinge to fully level. The samples were loaded with UTM in displacement-controlled mode at a loading rate of 0.5 mm/min following ASTM standard D 6671/D 6671M-06. The experimental test setup and camera setup are shown in Fig. 12 and Fig. 13 respectively. A custom-made loading system was used to accurately measure the load applied during the experiment as well as the extent and propagation of the crack front. These measurements were recorded numerically and visually as shown in Fig. 13. Displacements were measured throughout the experiment and by crosshead movement of the UTM.

Figure 11. Test setup.

Figure 12. Camera setup.

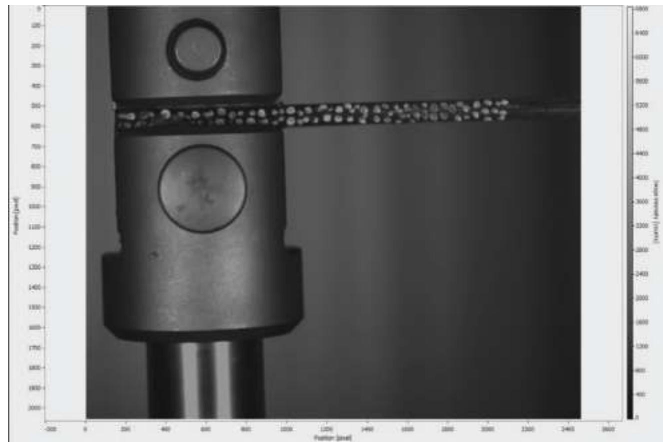

(a)

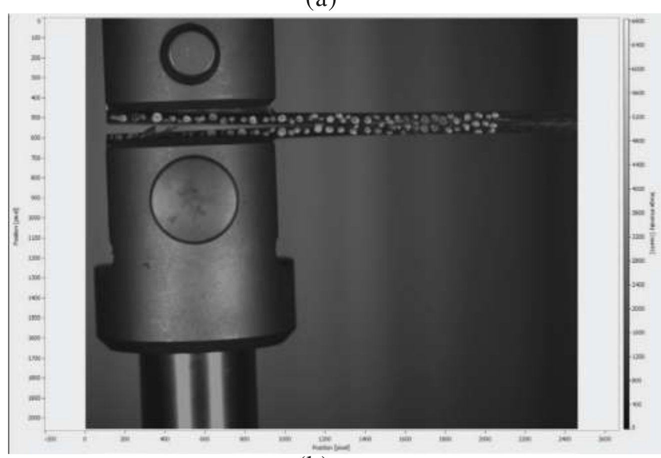

(b)

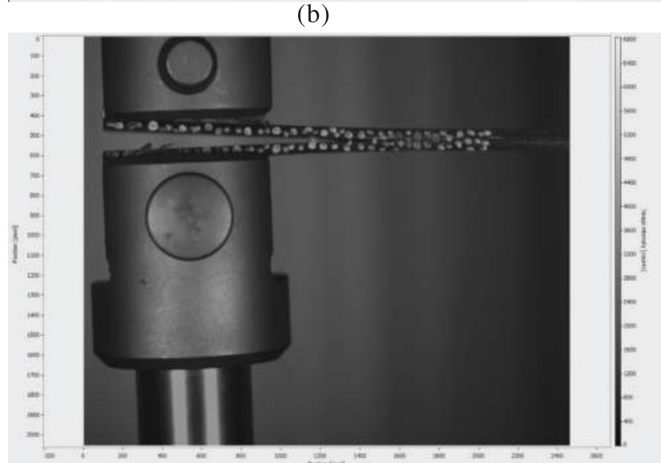

(c)

Figure 13. Experiment during (a) Initial stage; (b) Somewhere in the middle; and (c) At the end.

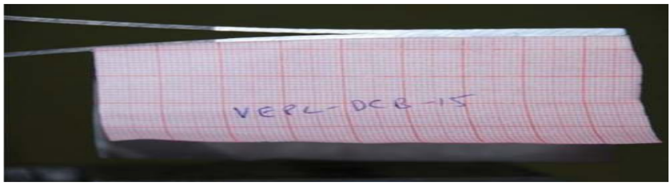

Figure 14. Experimental value was evaluated.

Laminate after carried out test for 0/30° having 70 mm initial crack length was shown in Fig. 14.

5.2 Test Results And Discussion

Table 6 gives the experimentally determined G1C values. As shown in Table 6, we found that the first Pc value obtained during the experiment continued to increase as the layer following angle increased, reaching a maximum value at 0/45°, and then began to decrease, as analyzed by FEM as predicted. However, the G1C value decreases with increasing initial crack length and reaches the maximum value when a0 is 70 mm.

The difference between G1C based on numerical simulations and experimental simulations is less than 10%. Theoretical laminates for comparison with the proposed G1C were calculated under the same initial conditions as the experiments. Gain insights into laminate G1C values based on physical modeling results.

6. CONCLUSIONS

In this study, the delamination effect of LCC was investigated using a combination of experimental results and finite element models. Stratified FEM analysis was performed on 16 bidirectional samples. All samples were prepared following the same orientation as for FEM analysis. For different layer sequences and initial crack lengths, changes in load and displacement are observed and further G1C values are calculated. The force required to fracture the sample was found to depend on the initial crack length and layer orientation. Testing was conducted in accordance with ASTM standard D6671/D6671M-06.

Based on the above study, the following points were noted: -

- Finite element analysis showed that the sample exhibited a steep linear increase in the applied force-displacement curve until a certain threshold was reached, beyond which sudden failure occurred, resulting in a nonlinear decrease in the applied force.
- Different failure modes of laminates under different conditions are analyzed. The study found that as the angle between the laminates increases, the peak force value required to fail increases to 30° (i.e., the angle between the laminates is 30°) and then decreases, and this decrease occurs in shorter The length of the initial crack is important for the calculation of G1C.
- Likewise, increasing the initial crack length will result in less force required to failure, but will also result in larger displacements, thus affecting the determination of the effective G1C value.
- Further improvement in FEM results may be obtained by considering factors such as fibre bridging, delayed failure due to off-axis plies, inaccurate crack length measurement, etc.

REFERENCE

1. Abramovich, H. Introduction to composite materials. Stability and vibrations of thin walled composite structures, Woodhead Publishing, 2017, pp. 1-47.

Table 6. Experimental evaluated value of G1C

Angle	a_o (mm)	Pc (N) (Max)	G1C using beam theory (J/m²) (Avg)	G1C using modified beam theory (J/m²) (Avg)	G1C using compliance calibration method (J/m²) (Avg)	G1C using modified compliance calibration method (J/m²) (Avg)
0/0	70	112.616	1320.45	1340.20	1334.44	1327.27
	80	81.966	830.38	838.75	830.967	836.83
	90	76.53	1022.18	1016.36	1017.10	1022.99
	100	72.24	878.09	871.38	881.10	881.30
	110	63.69	821.03	810.01	805.89	808.11
0/30	70	167.96	1915.78	1914.99	1899.72	1888.73
	80	118.52	1808.37	1812.19	1793.09	1840.41
	90	83.17	1323.60	1321.02	1312.80	1227.75
	100	73.21	996.55	994.43	999.90	988.75
	110	72.14	1018.08	1000.73	1009.93	1014.722
0/45	70	117.43	1721.85	1702.06	1681.30	1707.97
	80	114.51	1789.25	1810.90	1790.07	1800.27
	90	113.95	2012.03	2021.94	2015.70	2020.04
	100	99.54	1656.77	1643.08	1679.94	1669.17
0/60	70	100.25	1744.69	1767.64	1770.41	1768.67
	80	87.37	1804.79	1794.10	1782.91	1780.61

doi: 10.5772/intechopen.91285

2. Khayal, O.M.E.S. A review study of delamination in composite laminated plates, 2019. doi: 10.13140/RG.2.2.12740.07041
3. Jia, R.; Zhao, L.; Curti, R. & Gong, X. Determination of pure mode-I fracture toughness of multidirectional composite DCB specimens. *Engin. Fracture Mech.*, 2021, **252**, 107776.
4. Liu, C.; Bai, R.; Lei, Z.; Di, J.; Dong, D.; Gao, T. & Yan, C. Study on mode-I fracture toughness of composite laminates with curved plies applied by automated fibre placement. *Materials & Design*, 2020, **195**, 108963. doi: 10.1016/j.matdes.2020.108963
5. Gong, Y.; Hou, Y.; Zhao, L.; Li, W.; Zhang, J. & Hu, N. A modified mode I cohesive zone model for the delamination growth in DCB laminates with the effect of fibre bridging. *Int. J. Mech. Sci.*, 2020, **176**, 105514.
6. Teimouri, F.; Heidari-Rarani, M. & Aboutalebi, F.H. An XFEM-VCCT coupled approach for modeling mode I fatigue delamination in composite laminates under high cycle loading. *Engin. Fracture Mech.*, 2021, **249**, 107760.
7. Sebaey, T.A.; Blanco, N.; Costa, J. & Lopes, C.S. Characterisation of crack propagation in mode I delamination of multidirectional CFRP laminates. *Composites Scie. Technol.*, 2012, **72**(11), 1251-1256.
8. Yu, J.; Zhou, C. & Li, S. Experimental and numerical research on the mode I delamination of looped fabric reinforced laminate. *Composites Part B: Engin.*, 2020, **182**, 107566.
9. Tang, Z.; Zhang, H.; Sun, M. & Zhao, X. Advanced composite materials manufacturing technology. *Materials Scie., Adv. Composite Material.*, 2017. *doi: 10.18063/msacm.v1i1.498*
10. Cross, J.O.; Opila, R.L.; Boyd, I.W. & Kaufmann, E.N. Materials characterization and the evolution of materials. *MRS Bulletin*, 2015, **40**(12), 1019-1034. doi: 10.1557/mrs.2015.271
11. Ipek, G.; Arman, Y. & Celik, A. The effect of delamination size and location to buckling behavior of composite materials. *Composites Part B: Engin.*, 2018, **155**, 69-76. doi: 10.1016/j.compositesb.2018.08.009

CONTRIBUTORS

Mr Narendra Kumar Shrivastava completed his BE (Mechanical Engineering) from GEC (NIT) Raipur. He is presently working as a Scientist in DRDO-ASL, Hyderabad. His areas of interest include: Polymeric composite materials and processes, solid propulsion, and projects.
His contribution to the current study includes conceptualisation, planning of experiments, carrying out experiments, test results, analysis and conclusion.

Dr V. Suresh Babu is presently working as a professor & H.O.D. at MED, NIT Warangal. His research interests include: Machine design and strength of material.
In this current study he has given valuable suggestions. supervision, guidance for writing this manuscript, and finalizing the methodology.

Dr Manoj Kumar Buragohain obtained PhD from IIT, Chennai. He is presently working as a Scientist 'G' in DRDO-ASL, Hyderabad. His areas of research include: Design, development, and production of composite products & technology. His main contribution in developing large composite pressure vessels.
In the current study he has given valuable suggestions in conducting the experiments, and supervision. guidance for writing this manuscript and basic

Mr Pushpam Dayal obtained his BE degree in Mechanical engineering from Panjab University, Chandigarh. He is presently working in DRDO-ASL, Hyderabad. His research interests include: Composite materials, aerospace mechanisms, propulsion, systems engineering, and project management.
In the current study he conceptualised, FEM analysis, and carried out experiments, evaluating test results and analysis, and writing the manuscript.

Defence Science Journal, Vol. 75, No. 1, January 2025, pp. 129-138, DOI : 10.14429/dsj.20287

Navigating the Future: A Comprehensive Review of Vessel Trajectory Prediction Techniques

Nitish Raj[#,*] and Prabhat Kumar[!]

[#]Weapons and Electronics System Engineering Establishment, Delhi - 110 066, India
[!]National Institute of Technology, Patna - 801 503, India
[*]E-mail: raj.nitp@gmail.com

ABSTRACT

Autonomous ships will be an inevitable part of the maritime transportation industry. The maritime industry is working to ensure a safe and secure transition towards autonomous and effective vessel navigation. This paper presents a brief review of the Automatic Identification System (AIS) based Artificial Intelligence studies done in the domain of vessel trajectory prediction. Vessel trajectory prediction has significance in ensuring maritime safety, collision avoidance, and efficient trajectory selection. This paper thoroughly reviews various trajectory prediction methodologies used for training the models, the performance of models, and an in-depth discussion about the comparison of models using evaluation metrics. The study includes categorical analytics for the prediction techniques. The findings of this paper summarize various vessel trajectory prediction methodologies.

Keywords: Machine learning; Ship trajectory prediction; Neural network; Automatic identification system

NOMENCLATURE

AIS : Automatic Identification System
ANN : Artificial Neural Network
Bi-LSTM : Bidirectional Long Short-Term Memory
BPNN : Back Propagation Neural Network
CNN : Convolutional Neural Network
COG : Course Over Ground
DCNN : Deep Convolutional Neural Network
DNN : Deep Neural Network
ELM : Extreme Learning Machine
EM : Expectation-Maximization
FCNN : Fully Connected Neural Network
FDE : Final Displacement Error
GA-BP : Genetic Algorithm - Back Propagation
GAN : Generative Adversarial Network
GAT : Graph Attention Network
GMM : Gaussian Mixture Model
GRU : Gated Recurrent Unit
HMM : Hidden Markov Model
KNN : K-Nearest Neighbours
LM-ANN : Levenberg-Marquardt Artificial Neural Network
LSTM : Long Short-Term Memory
MAE : Mean Absolute Error
MDPI : Multidisciplinary Digital Publishing Institute
MSE : Mean Square Error
MLNN : Multilayer Neural Network
MMSI : Maritime Mobile Service Identity
NPC : Non-Parametric clustering
PF : Particle-Filter
PSO : Particle Swarm Optimization
RGRU : Residual GRU
RMSE : Root Mean Square Error
SOG : Speed over Ground
SPNS : Single Point Neighbour Search
SSL : Semi-Supervised Learning
SVM : Support Vector Machine
T-GCN : Temporal Graph Convolutional Network
T-LSTM : Time Aware LSTM
TCN : Temporal Convolutional Network
VTC : Vessel Trajectory Classification
UTC : Coordinated Universal Time

Received : 26 June 2024, Revised : 09 August 2024
Accepted : 28 August 2024, Online published : 10 January 2025

1. INTRODUCTION

The Majority of global trade is supported by the maritime transportation system. Compromised vessel safety can result in significant loss of property, goods, and human lives and can further damage the marine environment. Given this, the safety and security of vessels are becoming increasingly important. Thus, an efficient vessel trajectory prediction model that ensures safe and secure navigation is required to achieve autonomy.

Vessel movement prediction provides useful information for other applications such as traffic management[1], port operations[2], planning of routes[3], detection of anomalies in maritime traffic[4], etc.

A transponder system called AIS is used to transmit data between ship to ship as well as between AIS-equipped shore stations and ships. AIS improves marine environment protection, vessel navigation, safety, and life at sea. The goals of AIS are to facilitate information sharing, aid in tracking targets, aid in vessel identification, and increase situation awareness by supplying extra data.

The AIS transponder sends data to shore stations and other ships within its range. There are three different categories for the AIS data that ships transmit. Information that is either fixed or static, dynamic, or voyage-related. Examples of fixed or static data are information like the MMSI number, call sign, name of ship, IMO number, ship type, and antenna placement. During installation, this data is input into the AIS. The term "dynamic information" refers to the following: direction, geographical coordinates, navigational status, rate of Turn, COG, accuracy indication, SOG, and integrity state of the vessel and timestamp (UTC). This data is automatically updated by the onboard fitted AIS sensor, in addition to navigational status information. Predicting ship trajectories involves examining past AIS data, combined with environmental and other relevant factors, to anticipate future ship movements. This field is vital for enhancing both the efficiency and safety of maritime transport. Various methods exist for trajectory prediction, with statistical models being particularly prominent. These techniques leverage historical data to develop probability or regression models for forecasting future paths of ships. Prominent statistical models used in this context include linear regression, the Kalman filter, and ARIMA (autoregressive integrated moving average), which help in analyzing metrics such as the mean, variance, and distribution of trajectory data.

The AIS is one of the main components of contemporary marine safety and navigation. The use of AIS has ushered in a new era of maritime efficiency and safety, which is noteworthy in several crucial areas. However, relying solely on AIS data for vessel trajectory prediction may not fully capture the complexities of maritime navigation. While AIS data provides valuable information about a vessel's position, speed, and course, it often lacks detailed insights into operational factors that influence trajectory, such as rudder movements or engine performance. Integrating Voyage Data Recorder (VDR) information could significantly enhance trajectory prediction accuracy. VDRs record comprehensive data, including detailed navigational inputs, engine parameters, and crew actions, which offer a richer context for understanding a vessel's behavior.

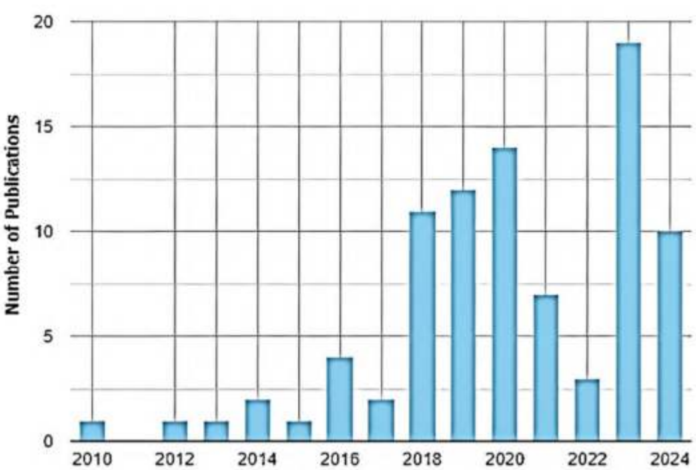

Figure 1. Counts of publications between 2010 and 2024. A notable upsurge is observed approximately around 2023.

By incorporating VDR data, predictive models could account for these additional variables, leading to more precise and reliable forecasts of vessel movements and a better understanding of the factors affecting trajectory. Therefore, emphasizing the role of VDR data in trajectory prediction would provide a more complete and nuanced approach to maritime navigation.

2. LITERATURE REVIEW

The examined research publications were produced to predict the trajectory of vessels. As you can see in Fig. 1. Numerous articles have been published since 2010, but since 2018 a sharp rise can be seen in the count of articles published for vessel trajectory prediction using various statistical, machine learning, deep learning, and mixed method model approaches.

Figure 2. Improved domains in the maritime shipping industry by using various predictions.

However, the prediction of vessel trajectory impacts several other domains such as resource utilization, improvement in navigation, maritime safety operations, collision prediction, route planning, and achieving autonomy of vessel navigation as depicted in Fig. 2.

The studies conducted on the prediction of vessel trajectory from 2019 to 2024 were included in this review analysis. Figure 3 shows that the review included around 408 research articles published in journals such as Research Gate, IEEE Explore, Science Direct, Google Scholar, Defence Science Journal, Sensors, and Journal of Ocean Engineering & Science. From the journal above's articles, a total of 251 articles were shortlisted based on keywords such as AIS, Trajectory, Vessel Trajectory, Ship Trajectory, and Machine Learning. Furthermore, out of 108 high-quality research articles filtered were high-quality published research papers, and 70 articles were selected for review.

A notable evolution in the methodologies employed for vessel trajectory prediction is shown in Fig. 4. Specifically, deep learning models have emerged as the predominant approach since 2019. In contrast, the utilization of machine learning models peaked between 2017 and 2020, subsequently experiencing a decline. The adoption of mixed method models is observed to have commenced in 2017, while the prevalence of statistical methods has diminished since 2019.

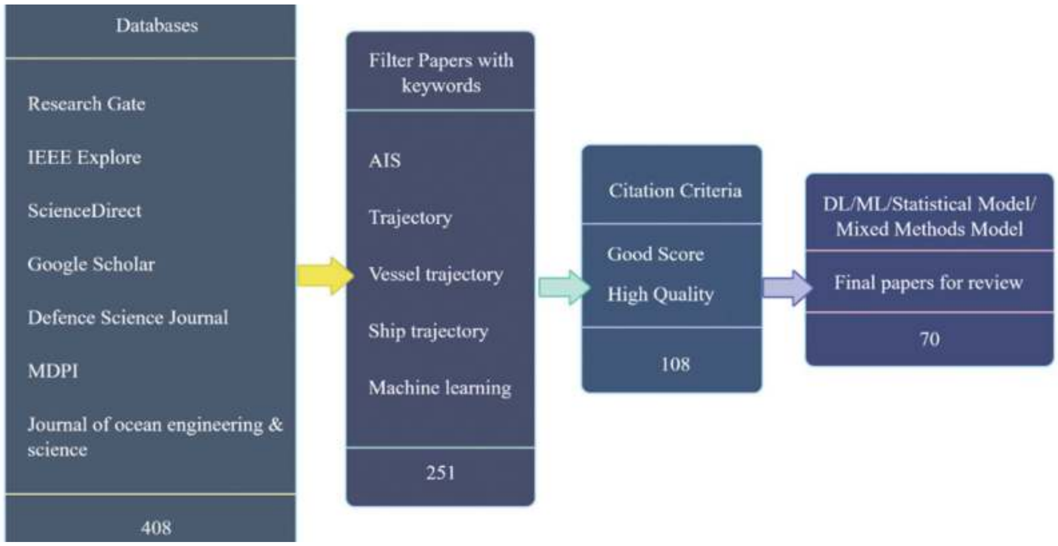

Figure 3. Summary of the filtering standards for the examined articles based on vessel trajectories.

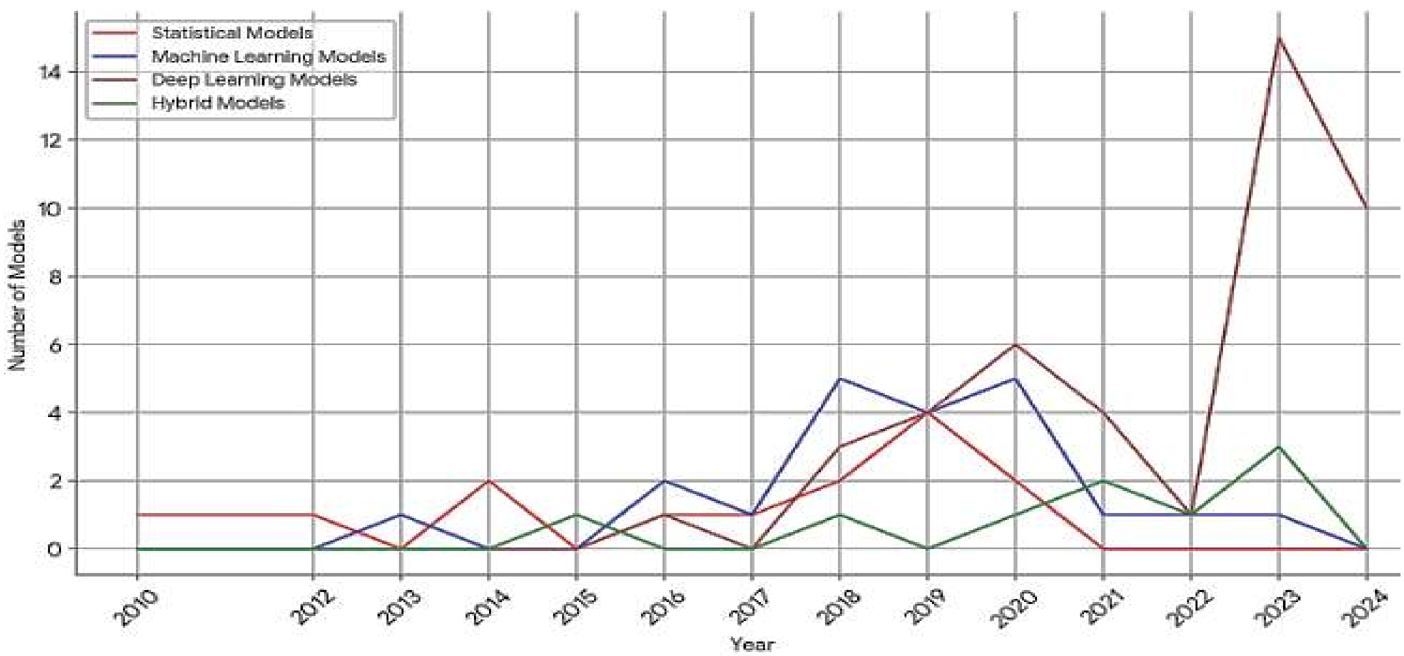

Figure 4. Vessel trajectory prediction models publication trend.

Table 1. Model-wise and year-wise count of vessel trajectory prediction research articles reviewed

Year	Statistical models	Machine learning models	Deep learning models	Mixed models
2019	4	4	4	-
2020	2	5	6	1
2021	-	1	4	2
2022	-	1	1	1
2023	-	-	15	3
2024	-	-	10	-

3. PREDICTION MODEL(S)

Table 1, which presents a breakdown of research articles by year and adopted model, reveals several significant trends in vessel trajectory prediction methodologies. Statistical models, while initially prevalent, have seen a decline in usage since 2019. Machine learning models experienced a surge in popularity from 2019 to 2020 but have since plateaued. Notably, deep learning models have emerged as the dominant approach, with a marked increase in adoption since 2019. The use of hybrid models, while less frequent. These trends underscore the evolving landscape of vessel trajectory prediction research, with a clear shift towards more sophisticated, data-driven approaches.

3.1 STATISTICAL METHOD MODELS

Statistical methods have been a cornerstone in vessel trajectory prediction, offering a robust framework to model the inherent uncertainty and randomness of vessel movements. These methods, grounded in mathematical and statistical principles, analyse historical data to uncover patterns and extrapolate future trajectories based on probabilistic models.

3.1.1 Methods Using Neighbourhood

To find the identical trajectories from AIS data and combine them to create a probability density field, Alizadeh[2,5], *et al.* explored point-level and trajectory-level similarity measures, using criteria like spatial, speed, and course similarity, as well as Dynamic Time Warping, to predict vessel locations.

3.1.2 Methods Using Stochastic Process

Uney[3], *et al.* employed the OU process-based hierarchical generative model to capture non-manoeuvring motion characteristics and forecast vessel trajectories, demonstrating its suitability for long-term prediction.

3.1.3 Markov Chain-Based Methods

Liu[6], *et al.* proposed a model for predicting vessel trajectory having long duration, incorporating position, heading course, and speed information which is further used in building a state transition matrix within a structure that is grid-based. Zhang[7], *et al.* applied wavelet transforms to convert trajectory sequences into input vectors for an HMM, showcasing its effectiveness in predicting trajectories of large vessels.

3.1.4 Filtering-Based Methods

Lian[8], *et al.* demonstrated predicting AIS trajectories using PF, aiming to address the issue of latency in information which further causes blind spots.

3.1.5 Probabilistic Model Checking

Gao[9], *et al.* applied probabilistic model-based checking to address the planning of paths in intelligent transportation systems, leveraging movable trajectories and data from statistical models for informed decision-making.

These statistical methods collectively demonstrate a wide array of approaches to tackle the complexities of vessel trajectory prediction. However, challenges such as data quality, model assumptions, and computational efficiency need to be addressed to enhance their effectiveness and reliability in real-world maritime applications.

3.2 MACHINE LEARNING MODELS

In the field of vessel trajectory prediction, machine learning (ML) techniques have become a potent tool thanks to their data-driven methodologies that can recognize intricate patterns in past data and extrapolate them to new and unknown scenarios.

3.2.1 Clustering

Clustering techniques group similar trajectories or data points, aiding in identifying patterns and reducing complexity.

Chen[10], *et al.* explored NPC clustering as an unsupervised method for vessel movement trajectory prediction, showcasing its ability to group similar trajectories based on proximity to prototype points. Murray and Perera[11] used Gaussian Mixture & Principal Component Analysis model clustering for trajectory analysis in their multiple predictions of trajectories for avoiding collision. By finding trajectory patterns in AIS data, Li[12], *et al.* used DBSCAN clustering to model long-term vessel movements, demonstrating its effectiveness in handling huge and noisy datasets.

3.2.2 Support Vector Machines

SVMs excel at classification and regression tasks, making them well-suited for vessel trajectory prediction.

Liu[13], *et al.* integrated SVM with ACDE to optimize hyperparameters and enhance prediction accuracy in their AIS-based trajectory prediction model. Liu[14], *et al.* utilized LS-SVM for online multiple-output trajectory prediction, highlighting the method's suitability for real-time processing of AIS data streams. Further Liu[15], *et al.* combined LS-SVM with PSO for parameter optimization, demonstrating the potential for improving prediction accuracy through intelligent parameter tuning.

3.2.3 Artificial Neural Networks and Variants

ANNs offer flexibility and adaptability for modelling complex relationships in vessel trajectory data.

Zhou[16], *et al.* and Zhang[17], *et al.* employed BPNN for ship trajectory prediction, highlighting its capability to learn nonlinear relationships between input features and output trajectories. Volkova[18], *et al.* used LM-ANN for predicting ship trajectories based on AIS data, leveraging the LM algorithm for efficient training and optimization.

These machine-learning methods have contributed significantly to the advancement of vessel trajectory prediction.

3.3 DEEP LEARNING MODELS

Deep learning, a machine learning branch, has emerged as a dominant force in vessel trajectory prediction due to its capacity to discern intricate patterns and representations from massive datasets. The trends in using Deep learning can be seen in recent years as compared to other categories of models.

3.3.1 Recurrent Neural Networks (RNNs)

As long-term dependencies in sequential data can be captured by LSTMs, many studies have successfully used them for vessel trajectory prediction[19-22]. Their capacity to retain information over extended periods makes them particularly well-suited for modelling the temporal aspects of vessel movements. Recent research has seen the development of LSTM variants such as Difference LSTM by Tian and Suo[23], which focuses on changes in consecutive positions to improve prediction accuracy.

Tang[20], *et al.* also highlighted the effectiveness of LSTM in modelling vessel trajectories using AIS data, where the model was stacked with two layers and used a 10-minute observation window as input. GRUs, a streamlined variant of LSTMs, have also proven effective in trajectory prediction[24-25]. Their reduced number of parameters often leads to faster training times without compromising performance. Hybrid models integrating LSTMs, GRUs, and Transformers have also been explored to create hierarchical approaches, such as the G-Trans model proposed by Xue[26], *et al.*, for predicting vessel trajectories. An optimized Seq-to-Seq model with spatiotemporal features employing GRU blocks was presented by You[24], *et al.* and showed noticeable improvement in predicting short-term trajectory tasks compared to GRU architectures and vanilla LSTM. Bi-LSTMs have been employed in several studies for improved prediction accuracy[27-30]. Hu and Shi[28] explored Bi-LSTM for ship trajectory prediction and demonstrated its potential in this domain. Zhou[30], *et al.* introduced an Optuna-BiLSTM model, incorporating hyperparameter optimization to enhance prediction performance in maritime applications. Ding[31], *et al.* introduced variational LSTMs, incorporating variational inference to model uncertainty in vessel trajectory prediction. Attention[22,27,32-35] mechanisms have been particularly effective in models such as the ACoAtt-LSTM proposed by Li[22], *et al.* for enhancing maritime navigational safety. Wang and Fu[33] also investigated the use of attention mechanisms in Bi-LSTM for ship trajectory prediction.

3.3.2 Encoder-Decoder Architectures

Forti[36], *et al.* further validated the superiority of LSTM encoder-decoder models over traditional methods like the Ornstein-Uhlenbeck process. The adaptability of this architecture was highlighted in a recent study by Düz and van Iperen[37] that investigated encoder-decoder-based deep learning models for ship trajectory prediction. A generative transformer model for AIS trajectory prediction called TrAISformer was proposed by Nguyen and Fablet[38], and an enhanced model based on TrAISformer was introduced by Cheng[39], *et al.* Furthermore, TATBformer, a divide-and-conquer strategy employing Transformers for ship trajectory prediction, was created by Xia[40], *et al*.

3.3.3 Convolutional Neural Networks Architectures

Liu[41], *et al.* proposed a model integrating Bi-LSTM with attention mechanisms and a CNN for vessel trajectory prediction, and Liu[35], *et al.* introduced a CNN-RGRU-Attention fusion model for ship trajectory prediction. Wu[42], *et al.* proposed a ConvLSTM-based sequence-to-sequence model.

3.3.4 Other Deep Learning Models

Chen[43], *et al.* utilized DNNs for ship trajectory reconstruction to model complex relationships in high-dimensional data. CNNs' potential in this field was further highlighted by Yuan[44], *et al.* who presented a DCNN-based sequence-to-sequence model. Zhang[45], *et al.* combined GANs with T-LSTM to research ship trajectory prediction. Duan[46], *et al.* proposed an SSL approach for VTC, demonstrating the potential of utilizing both labelled and unlabelled AIS data.

Cui[47], *et al.* employed CNN to capture spatial features effectively. Zhao[48], *et al.* combined Temporal Graph Convolutional Networks with Gated Recurrent Units for temporal and spatial data fusion, while Li[49], *et al.* utilized LSTM networks with Encoder-Decoder structures to handle sequential data. Additionally, Zhao[50], *et al.* and Zhang[51], *et al.* applied Temporal Convolutional Networks for sequence modelling, and Wu[52], *et al.* integrated CNN with GRU for enhanced feature extraction. Dijt and Mettes[53] combined LSTM ED with CNN, and Murray and Perera[54] used autoencoders for dimensionality reduction and feature learning. Wang[55], *et al.* and Zhao[56], *et al.* both incorporated Graph Attention Networks with LSTM, demonstrating the effectiveness of graph-based models in capturing complex relationships.

Gao[57], *et al.* introduced SocialVAE, leveraging Variational Autoencoders for learning social interactions, while Hao[58], *et al.* used Bi-directional GRU with GAT. Zhang[59], *et al.* proposed a Gated Spatio-Temporal Graph Aggregation Network, and Wang[60], *et al.* corrected LSTM predictions using a Genetic Algorithm-Backpropagation approach. Liu[61], *et al.* combined MVS-TGP with VAE for multimodal data integration, and Li[62], *et al.* applied Bi-directional LSTM for robust sequence modelling.

3.4 MIXED METHOD MODELS

Various mixed-method models were reviewed, which have been used for the prediction of vessel trajectory. A model is called a mixed method model when there is a combination of statistical and machine learning method models to create one model for performing prediction of vessel trajectory.

A mixed framework[63] was introduced to predict vessel trajectory, which consisted of three phases. Grouping of similar trajectories is done by using GMM clustering. Then kNN is used in the classification of selected trajectories to form a cluster. Then a cluster is fed to a dual linear autoencoder.

Gao[64], *et al.* demonstrated a mixed method model called a multi-step prediction model which uses statistical and deep learning models. A deep learning model is used for predicting support points. Assuming that two trajectories satisfy many conditions, historical data is filtered for destination prediction. Using the cubic spline-interpolation technique, the trajectory is simulated from the support point and destination.

A mixed model using unsupervised clustering and deep learning method was devised by Suo[65], *et al.*, where the vessel trajectory zone is predicted by applying the DBSCAN algorithm to the AIS data and then the GRU model is trained. The author[66] proposed a mixed-method model framework for predicting vessel trajectory in the Singapore Strait. Initially, COG and SOG are predicted by using a Neural Network with multiple layers. Then the vessel's geographical coordinates are obtained by using motion modelling. To correct the COG sequence PF method is applied. In study[67], COG and SOG are computed by using Expectation Maximization clustering and trajectory matching methods. Then, the future trajectory is predicted by using the motion model.

The authors[4] introduced a mixed-method model framework by applying bootstrapping in the encoded-decoded form of the LSTM network. Wherein, geographical position distributions were obtained by constructing a wild bootstrapping technique from LSTM encoder-decoder.

Murray[68], *et al.*'s mixed-method model. The clustering phase, the classification phase, and the local behaviour phase are the three stages of implementation. Initially, latent representations of each trajectory are extracted using a variational encoder-decoder structure. The HDBSCAN clustering method is applied to these latent representations.

Next, the classification module's training Bi-GRU model assigns several clusters to the new trajectory. Bi-GRU-based local models are trained differently for each cluster in the local behaviour module. Cluster-wise predictions are then performed from clusters from the classification module.

4. DISCUSSION & FUTURE SCOPE

In the review of vessel trajectory prediction studies, the performance of prediction models has been evaluated through both qualitative and quantitative methods. The qualitative analysis involved subjective assessments, often using visualizations or case studies, while the majority of studies employed quantitative techniques.

Quantitative evaluations primarily used regression metrics, with many studies measuring error through geographical distance formulas such as Haversine distance. Other methods like Vincenty and Equirectangular distances were also explored. Non-geographical metrics, including Root Mean Square Error (RMSE), Mean Absolute Error (MAE), and Mean Square Error (MSE), were applied in studies that used Cartesian or Spherical Coordinate Systems.

4.1 PERFORMANCE ANALYSIS

Table 2. below summarizes key advancements in vessel trajectory prediction models, highlighting the strengths of various approaches and methodologies. Notably, Deep Learning Models, such as Long Short-Term Memory (LSTM) networks, frequently outperform traditional methods. Context-specific models and enhanced Recurrent Neural Network (RNN) architectures contribute to improved prediction accuracy by incorporating contextual information and advanced structural improvements. Hyperparameter optimization techniques, data pre-processing methods, and state-of-the-art models like Transformers and Generative Adversarial Networks (GANs) also play significant roles in enhancing prediction capabilities. Additionally, the impact of training data on model accuracy, the benefits of ensemble learning, and the superiority of statistical methods for curved trajectories are critical factors in advancing prediction performance.

According to authors[12], LSTM outperformed BPNN and Kalman-Filter. When it comes to curved trajectory prediction MTEM and SPNS perform better than the Constant Velocity Model.

Learning of models using historical vessel trajectory dataset seems to have improved by using variation reparameterization technique[31], by using attention mechanism[27,32-33] in RNN and demonstrated using bidirectional structure[25].

Liu[13]*, et al.* proposed that vessel trajectory prediction precision can be improved by using a certain data pre-processing technique on the dataset for de-noising signals. The Ensemble Extreme Learning Model devised can reduce errors while predicting vessel trajectory by more than one-half compared to the Extreme Learning Model as evaluated by authors[1]. The authors[38,69] have stated that models like Generative Adversarial Networks and transformers have been capable of achieving a significant reduction of prediction errors.

Both Mehri[70]*, et al.* and Murray[46]*, et al.* have demonstrated that models having parameters like geographical zone, the behaviour of vessel, type of vessel, etc performed better than models that were trained on a dataset having all data. Liu[6]*, et al.* concluded that when the training dataset increases, the errors encountered while predicting trajectory reduce when using the Markov-chain model.

These insights reflect the advancements and ongoing improvements in vessel trajectory prediction, emphasizing the importance of adopting advanced techniques and context-specific models for better accuracy and reliability in maritime navigation.

4.2 RESEARCH GAP(s)

The future of maritime trajectory prediction holds significant potential for advancement through the integration of emerging techniques, multi-modal data sources, and enhanced privacy protection. Deep learning approaches, such as Temporal Convolutional Network (TCN), Reinforcement Learning (RL),

Table 2. Summary of advances in vessel trajectory prediction models

Aspect	Description
Deep learning models	Long Short-Term Memory (LSTM) networks often outperform traditional machine learning methods like Backpropagation Neural Networks (BPNN) and Kalman Filters (KF).
Context-specific models	Local models that account for specific contexts, such as geographical regions or ship types, generally provide better performance than global models trained on broad datasets.
Enhanced RNN architectures	Improvements in Recurrent Neural Network (RNN) architectures, such as attention mechanisms, bidirectional structures, and variational schemes, enhance prediction capabilities.
Hyperparameter optimization	Techniques like Adaptive Coordinate Descent Optimization (ACDE), Differential Evolution (DE), and Genetic Algorithms (GA) improve model accuracy, with ACDE showing the best performance.
Data pre-processing	Techniques such as signal de-noising significantly improve prediction accuracy by enhancing data quality.
State-of-the-art models	Advanced models like Transformers and Generative Adversarial Networks (GANs) have shown substantial improvements in prediction accuracy compared to earlier models.
Impact of training data	The accuracy of Markov chain models improves with more training data, significantly reducing prediction errors as the dataset size increases.
Ensemble learning	Combining multiple models through ensemble methods can enhance forecasting accuracy, with models like ensemble Extreme Learning Machines (ELM) reducing prediction errors more effectively.
Statistical methods for curved trajectories	Mixed Trajectory Estimation Methods (MTEM) outperform traditional methods like State Positioning Navigation System (SPNS) and Conventional Velocity Models (CVM), achieving better accuracy in curved trajectory predictions.

and Graph Neural Network (GNN), offer promising avenues for improving prediction accuracy. TCN, with its dilated causal convolutions, excels in capturing spatio-temporal dependencies, while RL and GNN enhance decision-making and feature extraction capabilities. Additionally, incorporating multi-modal data sources like satellite images, radar, LiDAR, and CCTV, beyond the traditional reliance on AIS data, could further refine prediction outcomes. As trajectory predictions become more precise, the risk of privacy leakage, particularly in long-term predictions, grows. Addressing this challenge, future research should focus on integrating privacy protection mechanisms, such as Federated Learning (FL), to safeguard sensitive information while advancing maritime trajectory prediction capabilities.

Despite the extensive review of current literature and methods for ship trajectory prediction, none of the examined approaches have accounted for voyage-related data such as rudder movement. This oversight highlights a significant gap in the existing research, as incorporating such data could greatly enhance the precision of trajectory forecasts. Future work should focus on integrating rudder movement and other voyage-related factors into predictive models to capture more nuanced navigational adjustments and improve the accuracy of trajectory predictions. Addressing this gap could offer new insights and advancements in maritime navigation, leading to more robust and reliable prediction systems. In addition to addressing the gaps related to voyage-related data, future research could benefit from exploring advanced predictive modeling techniques to enhance the accuracy of vessel speed predictions. Specifically, integrating Multiple Linear Regression (MLR) and Random Forest (RF) models presents a promising approach. MLR can offer insights into the linear relationships between vessel speed and influencing factors, while RF can capture complex, non-linear interactions and handle diverse datasets effectively. Combining these methods could provide a more comprehensive understanding of vessel speed dynamics, improving the overall prediction accuracy and robustness of maritime trajectory forecasting systems.

5. CONCLUSION

The maritime transport industry places great importance on the prediction of vessel trajectory. Achieving the desired prediction model which maintains reliability and accuracy in predicting trajectory is challenging. This paper brings advancements in the domain of vessel trajectory prediction with a comprehensive review of prediction methodologies, their strength, limitations, and challenges in achieving complete autonomy. Reviewed research papers demonstrate the growing usage of statistical and machine learning methods to achieve autonomy for vessel trajectory prediction using historical AIS Datasets. Promising outcomes have been achieved by using machine learning methods for predicting trajectories.

It has been noted prediction with accuracy for longer ranges has not been explored so far. Additional investigation is necessary to incorporate data from various sources, including radar and satellite data, and to fuse data from other data sources. The future scope also involves enhancing the capability of algorithms to accommodate the trajectory of a longer time/ range.

REFERENCES

1. Tu, E.; Zhang, G.; Mao, S.; Rachmawati, L. & Huang, G.B. Modeling historical AIS data for vessel path prediction: A comprehensive treatment. arXiv preprint arXiv:2001.01592, 2020. doi:10.48550/arXiv.2001.01592.
2. Alizadeh, D.; Alesheikh, A.A. & Sharif, M. Prediction of vessels locations and maritime traffic using similarity measurement of trajectory. *Annals of GIS*, 2021, **27**(2), 151-62.
3. Üney, M.; Millefiori, L.M. & Braca, P. Data driven vessel trajectory forecasting using stochastic generative models. *In* ICASSP 2019-2019 IEEE International Conference on Acoustics, Speech and Signal Processing (ICASSP), 2019. doi:10.1109/ICASSP.2019.8683444.
4. Venskus, J.; Treigys, P. & Markevičiūtė, J. Unsupervised marine vessel trajectory prediction using LSTM network and wild bootstrapping techniques. *Nonlinear Analysis: Model. Control*, 2021, **26**(4), 718-37. doi:10.15388/namc.2021.26.23056.
5. Alizadeh, D.; Alesheikh, A.A. & Sharif, M. Vessel trajectory prediction using historical automatic identification system data. *The J. Navigation*, 2021, **74**(1), 156-74. doi:10.1017/S0373463320000442.
6. Liu, C.; Guo, S.; Feng, Y.; Hong, F.; Huang, H. & Guo, Z. L-VTP: Long-term vessel trajectory prediction based on multi-source data analysis. *Sens,* 2019, **19**(20). doi:10.3390/s19204365.
7. Zhang, X.; Liu, G.; Hu, C. & Ma, X. Wavelet analysis based hidden Markov model for large ship trajectory prediction. *In* 2019 Chinese Control Conference (CCC), 2019. doi:10.23919/ChiCC.2019.8866006.
8. Lian, Y.; Yang, L.; Lu, L.; Sun, J. & Lu, Y. Research on ship AIS trajectory estimation based on particle filter algorithm. *In* 2019 11th International conference on intelligent human-machine systems and cybernetics (IHMSC), 2019. doi:10.1109/IHMSC.2019.00077.
9. Gao, H.; Huang, W. & Yang, X. Applying probabilistic model checking to path planning in an intelligent transportation system using mobility trajectories and their statistical data. *Int. Autom. Soft Comput.*, 2019, **25**(3). doi:10.31209/2019.100000110.
10. Chen, C.W.; Harrison, C. & Huang, H.H. The unsupervised method of vessel movement trajectory prediction. arXiv preprint arXiv:2007.13712, 2020. doi:10.48550/arXiv.2007.13712.
11. Murray, B. & Perera, L.P. An AIS-based multiple trajectory prediction approach for collision avoidance in future vessels. *In* International Conference on Offshore Mechanics and Arctic Engineering, 2019. doi:10.1115/OMAE2019-95963.
12. Li, W.; Zhang, C.; Ma, J. & Jia, C. Long-term vessel motion prediction by modeling trajectory patterns with AIS data. *In* 2019 5th International Conference on Transportation Information and Safety (ICTIS), 2019. doi:10.1016/j.tre.2023.103152.
13. Liu, J.; Shi, G. & Zhu, K. Vessel trajectory prediction

model based on AIS sensor data and adaptive chaos differential evolution support vector regression (ACDE-SVR). *Appl. Sci.*, 2019, **9**(15).
doi:10.3390/app9152983.
14. Liu, J.; Shi, G. & Zhu, K. Online multiple outputs least-squares support vector regression model of ship trajectory prediction based on automatic information system data and selection mechanism. *IEEE Access*, 2020, **8**, 154727-45.
doi:10.1109/ACCESS.2020.3018749.
15. Liu, X.; He, W.; Xie, J. & Chu, X. Predicting the trajectories of vessels using machine learning. *In* 2020 5th International conference on control, robotics and cybernetics (CRC), Oct 2020. 66-70.
16. Zhou, H.; Chen, Y. & Zhang, S. Ship trajectory prediction based on BP neural network. *J. Artif. Intell.*, 2019, **1**(1).
doi:10.32604/jai.2019.05939.
17. Zhang, Z.; Ni, G. & Xu, Y. Trajectory prediction based on AIS and BP neural network. *In* 2020 IEEE 9th Joint International Information Technology and Artificial Intelligence Conference (ITAIC), 2020, pp. 601-605.
18. Volkova, T.A.; Balykina, Y.E. & Bespalov, A. Predicting ship trajectory based on neural networks using AIS data. *J. Mar. Sci. Eng.,* 2021, **9**(3).
doi:10.3390/jmse9030254.
19. Zhu, F. Ship short-term trajectory prediction based on RNN. *In* Journal of Physics: Conference Series, 2021, **2025**(1). 012023
doi:10.1088/1742-6596/2025/1/012023.
20. Tang, H.; Yin, Y. & Shen, H. A model for vessel trajectory prediction based on long short-term memory neural network. *J. Mar. Eng. Technol.*, 2022, **21**(3), 136-45.
doi:10.1080/20464177.2019.1665258.
21. Xi, D.; Feng, Y.; Jiang, W.; Yang, N.; Hu, X. & Wang, C. Construction of a real-time ship trajectory prediction model based on ship automatic identification system data. *ISPRS Int. J. Geo-Inf.*, 2023, **12**(12), 502.
doi:10.3390/ijgi12120502.
22. Li, M.; Li, B.; Qi, Z.; Li, J. & Wu, J. Enhancing maritime navigational safety: ship trajectory prediction using ACoAtt–LSTM and AIS data. *ISPRS Int. J. Geo-Inf.*, 2024, **13**(3), 85.
doi:10.3390/ijgi13030085.
23. Tian, X. & Suo, Y. Research on ship trajectory prediction method based on difference long short-term memory. *J. Mar. Sci. Eng.*, 2023, **11**(9), 1731.
doi:10.3390/jmse11091731.
24. You, L.; Xiao, S.; Peng, Q.; Claramunt, C.; Han, X.; Guan, Z. & Zhang, J. St-seq2seq: A spatio-temporal feature-optimized seq2seq model for short-term vessel trajectory prediction. *IEEE Access*, 2020, **8**, 218565-74.
doi:10.1109/ACCESS.2020.3041762.
25. Wang, C.; Ren, H. & Li, H. Vessel trajectory prediction based on AIS data and bidirectional GRU. *In* 2020 International conference on computer vision, image and deep learning (CVIDL), 2020.
doi:10.1109/CVIDL51233.2020.00-89.
26. Xue, H.; Wang, S.; Xia, M. & Guo, S. G-Trans: A hierarchical approach to vessel trajectory prediction with GRU-based transformer. *Ocean Eng.*, 2024, **300**,117431.
doi:10.1016/j.oceaneng.2024.117431.
27. Zhang, S.; Wang, L.; Zhu, M.; Chen, S.; Zhang, H. & Zeng, Z. A bi-directional LSTM ship trajectory prediction method based on attention mechanism. *In* 2021 IEEE 5th Advanced Information Technology, Electronic and Automation Control Conference (IAEAC), 2021.
doi:10.1109/IAEAC50856.2021.9391059.
28. Hu, Y. & Shi, G. Ship trajectory prediction based on bidirectional long short-term memory. *In* 2023 3rd International Conference on Electronic Information Engineering and Computer Science (EIECS), 2023.
doi:10.1109/EIECS59936.2023.10435594.
29. Li, H.; Xing, W.; Jiao, H.; Yang, Z. & Li, Y. Deep bi-directional information-empowered ship trajectory prediction for maritime autonomous surface ships. *Transp. Res. Part E: Logist. Transp. Rev.*, 2024, **181**, 103367.
doi:10.1016/j.tre.2023.103367.
30. Zhou, Y.; Dong, Z. & Bao, X. A ship trajectory prediction method based on an optuna–BILSTM model. *Appl. Sci.*, 2024, **14**(9), 3719.
doi:10.3390/app14093719.
31. Ding, M.; Su, W.; Liu, Y.; Zhang, J.; Li, J. & Wu, J. A novel approach on vessel trajectory prediction based on variational LSTM. *In* 2020 IEEE International Conference on Artificial Intelligence and Computer Applications (ICAICA), 2020.
doi:10.1109/ICAICA50127.2020.9182537.
32. Sekhon, J. & Fleming, C. A spatially and temporally attentive joint trajectory prediction framework for modeling vessel intent. *In* Learning for Dynamics and Control, 2020.
doi:10.48550/arXiv.1912.09429.
33. Wang, C. & Fu, Y. Ship trajectory prediction based on attention in bidirectional recurrent neural networks. *In* 5th International Conference on Information Science, Computer Technology and Transportation (ISCTT), 2020.
doi:10.1109/ISCTT51595.2020.00100.
34. Zhao, L.; Zuo, Y. & Li, T. Chen C.P. Application of an encoder–decoder model with attention mechanism for trajectory prediction based on AIS data: case studies from the Yangtze river of China and the eastern coast of the US. *J. Mar. Sci. Eng.*, 2023, **11**(8), 1530.
doi:10.3390/jmse11081530.
35. Liu, W.; Cao, Y.; Guan, M. & Liu, L. research on ship trajectory prediction method based on CNN-RGRU-attention fusion model. *IEEE Access*, 2024.
doi:10.1109/ACCESS.2024.3396475.
36. Forti, N.; Millefiori, L.M.; Braca, P. & Willett, P. Prediction of vessel trajectories from AIS data via sequence-to-sequence recurrent neural networks. *In* ICASSP 2020-2020 IEEE International Conference on Acoustics, Speech and Signal Processing (ICASSP), 2020.
doi:10.1109/ICASSP40776.2020.9054421.
37. Düz, B. & Van Iperen, E. Ship trajectory prediction using encoder–decoder-based deep learning models. *J. Locat. Based Serv.*, 2024, 1-21.
doi:10.1080/17489725.2024.2306339.
38. Nguyen, D. & Fablet, R. TrAISformer--A transformer network with sparse augmented data representation and cross entropy loss for ais-based vessel trajectory

prediction. *arXiv preprint arXiv:2109.03958*, 2021.
doi:10.1109/ACCESS.2024.3349957.

39. Cheng, J.; Wang, J.; Zhang, Z.; Yuan, J. & Shao, W. An improved AIS trajectory prediction model based on TrAISformer. *In* Seventh International Conference on Traffic Engineering and Transportation System (ICTETS 2023), 2024.
doi:10.1117/12.3015737.
40. Xia, C.; Qu, D. & Zheng, Y. TATBformer: A divide-and-conquer approach to ship trajectory prediction modeling. *In* 2023 IEEE 11th Joint International Information Technology and Artificial Intelligence Conference (ITAIC), 2023.
doi:10.1109/ITAIC58329.2023.10409018.
41. Liu, C.; Li, Y.; Jiang, R.; Du, Y.; Lu, Q. & Guo, Z. TPR-DTVN: a routing algorithm in delay tolerant vessel network based on long-term trajectory prediction. *Wireless Commun. Mobile Comput.*, 2021, **2021**(1), 1-5.
doi:10.1155/2021/6630265.
42. Wu, W.; Chen, P.; Chen, L. & Mou, J. Ship Trajectory Prediction: An Integrated Approach Using ConvLSTM-Based Sequence-to-Sequence Model. *J. Mar. Sci. Eng.*, 2023, **11**(8), 1484.
doi:10.3390/jmse11081484.
43. Chen, X.; Ling, J.L.; Yang, Y.; Zheng, H.; Xiong, P.; Postolache, O. & Xiong, Y. Ship trajectory reconstruction from AIS sensory data via data quality control and prediction. *Math. Probl. Eng.*, 2020, **2020**(1), 1-9.
doi:10.1155/2020/7191296.
44. Yuan, J.; Fang, W.; Zhang, J.; Yin, Y.; Wan, J. & Wang, Y. Improved sequence-to-sequence ship trajectory prediction based on AIS.
doi:10.21203/rs.3.rs-3821423/v1
45. Zhang, J.; Wang, H.; Cui, F.; Liu, Y.; Liu, Z. & Dong, J. Research into ship trajectory prediction based on an improved LSTM network. *J. Mar. Sci. Eng.*, 2023, **11**(7), 1268.
doi:10.3390/jmse11071268
46. Duan, H.; Ma, F.; Miao, L. & Zhang, C. A semi-supervised deep learning approach for vessel trajectory classification based on AIS data. *Ocean & Coastal Manage.*, 2022, **218**, 106015.
doi:10.1016/j.ocecoaman.2021.106015
47. Cui, H.; Radosavljevic, V.; Chou, F.C.; Lin, T.H.; Nguyen, T.; Huang, T.K.; Schneider, J. & Djuric, N. Multimodal trajectory predictions for autonomous driving using deep convolutional networks. *In* 2019 international conference on robotics and automation (ICRA), May 2019.pp. 2090-2096.
48. Zhao, L.; Song, Y.; Zhang, C.; Liu, Y.; Wang, P.; Lin, T.; Deng, M. & Li, H. T-gcn: A temporal graph convolutional network for traffic prediction. *IEEE Trans. Intel. Trans. syst*., 2019, **21**(9), 3848-58.
doi:10.48550/arXiv.1811.05320.
49. Li, X.; Ying, X. & Chuah, M.C. Grip: Graph-based interaction-aware trajectory prediction. *In* 2019 IEEE Intelligent Transportation Systems Conference (ITSC), 2019.
doi:10.13140/RG.2.2.16886.63044.
50. Zhao, W.; Gao, Y.; Ji, T.; Wan, X.; Ye, F. & Bai, G. Deep temporal convolutional networks for short-term traffic flow forecasting. *IEEE Access*, 2019**, 7**, 114496-507.
doi:10.1109/ACCESS.2019.2935504.
51. Zhang, K.; Liu, Z. & Zheng, L. Short-term prediction of passenger demand in multi-zone level: Temporal convolutional neural network with multi-task learning. *IEEE Trans. Intell. Trans. Syst.*, 2019, **21**(4), 1480-90.
doi:10.1109/TITS.2019.2909571.
52. Wu, L.; Kong, C.; Hao, X. & Chen, W. A short-term load forecasting method based on GRU-CNN hybrid neural network model. *Math. problems Eng.*, 2020, **2020**(1), p.1428104
doi:10.1155/2020/1428104.
53. Dijt, P. & Mettes, P. Trajectory prediction network for future anticipation of ships. *In* Proceedings of the 2020 International Conference on Multimedia Retrieval, 2020.
doi:10.1145/3372278.3390676.
54. Murray, B. & Perera, L.P. A dual linear autoencoder approach for vessel trajectory prediction using historical AIS data. *Ocean Eng.*, 2020, **209**, 107478.
doi:10.1016/j.oceaneng.2020.107478.
55. Wang, S.; Li, Y. & Xing, H. A novel method for ship trajectory prediction in complex scenarios based on spatio-temporal features extraction of AIS data. *Ocean Eng.*, 2023, **281**, 114846.
doi:10.1016/j.oceaneng.2023.114846.
56. Zhao, J.; Yan, Z.; Zhou, Z.; Chen, X.; Wu, B. & Wang, S. A ship trajectory prediction method based on GAT and LSTM. *Ocean Eng.*, 2023, **289**, 116159.
doi:10.1016/j.oceaneng.2023.116159.
57. Gao, W.; Liu, J.; Zhi, J. & Wang, J. Improved socialVAE: a socially-aware ship trajectory prediction method for port operations. *In* 2023 2nd International Conference on Machine Learning, Cloud Computing and Intelligent Mining (MLCCIM), 2023.
doi:10.1109/MLCCIM60412.2023.00067.
58. Hao, S.; Liu, J.; Zhang, X.; Shi, Q.; Zhi, J. & Jiang X. Multi-ship trajectory prediction framework for high-density maritime traffic areas based on BI-GRU and GAT. *In* 2023 11th International Conference on Information Systems and Computing Technology (ISCTech), 2023.
doi:10.1109/ISCTech60480.2023.00067.
59. Zhang, X.; Liu, J.; Gong, P.; Chen, C.; Han, B. & Wu, Z. Trajectory prediction of seagoing ships in dynamic traffic scenes via a gated spatio-temporal graph aggregation network. *Ocean Eng.*, 2023, **287**, 115886.
doi:10.1016/j.oceaneng.2023.115886.
60. Wang, X.; Zhao, W.; Wang, S. & Liu, J. Multidimensional non-linear ship trajectory prediction based on lstm network corrected by GA-BP. *In* Chinese Intelligent Systems Conference, 2023.
doi:10.1007/978-981-99-6847-3_5.
61. Liu, Z.; Qi, W.; Zhou, S.; Zhang, W.; Jiang, C.; Jie, Y.; Chenyang, L.; Guo, Y. & Guo, J. hybrid deep learning models for ship trajectory prediction in complex scenarios based on AIS data. *Available at SSRN 4650287*.
doi:10.2139/ssrn.4650287.
62. Li, W.; Lian, Y.; Liu, Y. & Shi, G. Ship Trajectory Prediction Model Based on Improved Bi-LSTM. *ASCE-*

ASME J. Risk and Uncert. Engin. Syst., Part A: Civil Engin., 2024, **10**(3), 04024033.
doi:10.1109/ACCESS.2022.3154812.

63. Murray, B. & Perera, L.P. A dual linear autoencoder approach for vessel trajectory prediction using historical AIS data. *Ocean Eng.*, 2020, **209**, 107478.
doi:10.1016/j.oceaneng.2020.107478.
64. Gao, D.W.; Zhu, Y.S.; Zhang, J.F.; He, Y.K.; Yan, K. & Yan, B.R. A novel MP-LSTM method for ship trajectory prediction based on AIS data. *Ocean Eng.*, 2021, **228**, 108956.
doi:10.1016/j.oceaneng.2021.108956.
65. Suo, Y.; Chen, W.; Claramunt, C. & Yang, S. A ship trajectory prediction framework based on a recurrent neural network. *Sensors*, 2020, **20**(18), 5133.
doi:10.3390/s20185133.
66. Xiao, Z.; Fu, X.; Zhang, L.; Zhang, W.; Liu, R.W.; Liu, Z & Goh, R.S. Big data driven vessel trajectory and navigating state prediction with adaptive learning, motion modeling and particle filtering techniques. *IEEE Transact. Intell. Trans. Syst.*, 2020, **23**(4), 3696-709.
doi:10.1109/TITS.2020.3040268.
67. Last, P.; Hering-Bertram, M. & Linsen, L. Interactive history-based vessel movement prediction. *IEEE Intell. Syst.*, 2019, **34**(6), 3-13.
doi:10.1109/MIS.2019.2954509.
68. Murray, B. & Perera, L.P. An AIS-based deep learning framework for regional ship behavior prediction. *Reliability Engin. & Syst. Safety*, 2021, **215**, 107819.
doi:10.1016/j.ress.2021.107819.
69. Wang, S. & He, Z. A prediction model of vessel trajectory based on generative adversarial network. *The J. Navigation*, 2021, **74**(5), 1161-71.
doi:10.1017/S0373463321000382.
70. Mehri, S.; Alesheikh, A.A. & Basiri, A. A contextual hybrid model for vessel movement prediction. *IEEE Access*, 2021, **9**, 45600-13.
doi:10.1109/ACCESS.2021.3066463.

CONTRIBUTORS

Mr Nitish Raj obtained his M.Tech (CSE) from IIT Delhi and working as a Scientist at DRDO, posted at the Weapons and Electronics Systems Engineering Establishment, Ministry of Defence in New Delhi.
He contributed to the current work by coming up with the idea and designing the experiment, optimising the deep learning techniques used in the experiment, creating the programme, analysing the data, and finalising the manuscript.

Mr Prabhat Kumar is a Professor in the Computer Science and Engineering Department at NIT Patna, India. Formerly, he was the HOD of the CSE Department and the State Student Coordinator of Bihar for the Computer Society of India.
He made contributions to the current study by assisting in the conceptualisation of the review, helping in the identification and contributing to the analysis and synthesis of findings.

(ii) Book/Monograph

Hitchins, Derek K. System engineering: A 21st century systems methodology. John Wiley, London, 2007. 502p.

DeMers, M.N. Fundamentals of geographic information systems. Ed. 3. John Wiley, New York, 2005.

(iii) Chapter from a Book

Bodony, D.J. & Lele, S.K. Applications and results for large-eddy simulations for acoustics: Far-field jet acoustics. *In* LES for eddy acoustics, edited by C. Wagner, T. Huttl & P. Sagaut. Cambridge University Press, Cambridge, UK, 2005. pp. 289-310. doi: 10.1017/CBO9780511546143.008

Lokesha, B.N. Advanced avionics and electronic warfare system for fighter aircraft. *In* DRDO Technology Spectrum. Defence Research and Development Organisation, New Delhi, 2008. pp. 10-26.

(iv) Conference Paper

Puszynski, J.A. Recent advances and initiatives in the field of nanotechnology. Paper presented at 31st International Pyrotechnic Seminar, Fort Collins, Colorado, USA, July 2004. pp. 233-40.

Ekstein, J.; Freitag, E.; Hirsch, C. & Sattelmayer, T. Experimental study on the role of entropy diffusion waves in low-frequency oscillations for a diffusion burner. *In* Proceedings of the ASME Turbo Expo 2004: Power for Land, Sea, and Air. edited by R.S. Harris. ASME, Fairfield, NJ, 2004. doi:10.1115/GT2004-54163

(v) Report

Savage, S.J. Defence applications of nanocomposite materials. FOI-Swedesh Defence Research Agency, User Report No. FOI-R-1524-SE. December 2004.

(vi) Patent

Man, T.Y.; Leung, C.Y.; Leung, K.N.; Mok, P.K.T. & Chan, M. Single-transister-control low-dropout regulator. US Patent No. 7285952, 23 October 2007.

(vii) Standard

International Organisation for Standardisation. Document Management–Electronic document file format for long-term preservation–Part1: Use of PDF 1.4 (PDF/A-I). ISO 19005-1:2005, ISO, Geneva, Switzerland, 2005.

(viii) Thesis/Dissertation

De Roek, W. Hybrid methodologies for the computational aeroacoustic analysis of confined, subsonic flows. Katholieke University, Leuven, Belgium, 2007. PhD Thesis.

(ix) Personal Communication

Personal communications shall not be listed under references but included in the text itself. The references shall be given as shown below:

The number of registered publications under Copyright Clearance Centre (CCC), Salem, USA, now totals approx. 6000,000 titles used by 3,600 publishers (personal communication with CCC), whereas in 1986 there were only 58,000 publications registered from 1,100 publishers.

Apart from the above guidelines, the form in which the cited document is published, for example, microfiche, CD-ROM or other electronic medium; and the language of publication if other than English should be indicated in parentheses at the end of the reference. If the cited document is unpublished, it should be indicated in parentheses at the end of the reference as 'in press' with DOI No.

(g) Tables

Tables should supplement and not duplicate the information contained in the text. They should be explicitly referred to in the text in numerical order with brief titles. Column headings should be brief, bold and the units of measurement should be placed below the headings in parentheses.

Maximum Five (5) tables are allowed in a manuscript.

(h) Illustrations

All figures (charts, diagrams, line drawings, and photographic images) should be of good quality and submitted both electronic and hard copy originals. Illustrations should be numbered in order of their occurrences in the text with Indo-Arabic numerals and with short descriptive captions. Lettering should be in capital only and remain legible after a reduction of 50-60 per cent. Scanned/photocopied images reproduced poorly should be avoided. Illustrations taken from other publications must be acknowledged. It is the author's responsibility to obtain permission for reprinting such illustrations in *Defence Science Journal*. The preferred format is encapsulated postscript (.eps) for line figures and .tif for halftone figures with minimum resolution of 300 dpi (dots per inch). Colour should be used only where absolutely necessary for understanding of the figure. Colour should not be used for distinguishing data in line diagrams.

Maximum Six (6) figures are allowed in a manuscript.

(i) Symbols/Units

Non-standard abbreviations should be shown in brackets when first mentioned, and should be used whenever the same terms appear again in the text and not in the title and abstract. Usage of metric units is preferred.

(j) Nomenclature

The nomenclature of mathematical symbols and signs used in the text should be given immediately after the keywords. Authors can follow any of the standard units and symbols developed by international agencies in their fields for this purpose.

(k) Special Items

When chemical/mathematical equations are used in papers, these should be legible. The symbols, not covered in nomenclature (or when nomenclature is not given), should be explained immediately after their first usage in the text. Equations should be consecutively numbered in whole numbers in parentheses (for example, (2), (15), (19), etc.) at the right margin. Reference to the equations in the text should be abbreviated as Eqn (1), Eqns (5-7), etc. Complex structural formulae of chemical compounds should be prepared as illustrations. Capital, lower case and Greek letters should be distinguished clearly. Letters which are sometimes confused for one another (for example, O & 0; l & 1; V, v & n; r & p; X, x & ^{c}; K, k & k; E & e; etc.) should be clearly distinguished. A Greek letter should be spelt out in margin where it is first used.

(l) Proofs and Complimentary Journal

The final proof of the paper will be sent for correction in three working days to the author for clearance before printing. All the author(s) will be supplied with a softcopy of issue, free of charge. Author will receive one printed copy of the issue as complimentary.

Printed and published by the Defence Scientific Information and Documentation Centre, Metcalfe House, Delhi-110 054.

PDSL/01.01.2025/250

INSTRUCTIONS FOR CONTRIBUTORS

Objective

Defence Science Journal, a bi-monthly Journal of the Defence Research & Development Organisation (DRDO), publishes original research papers having a direct bearing on Military/Defence applications. It covers natural science, technology, and engineering.

(a) Typescript Requirements

Research papers (max length: 3000 words or 10 typed pages of A4 size including figures) containing original research findings in a clear and concise manner. Papers reporting theoretical, laboratory and field test results are also accepted.

Review articles (max length: 5000 words or 20 typed pages of A4 size including figures) are expected to cover survey, integrate, and critically examine new information accumulated in recent years in a particular subject field. Review articles from subject experts are also commissioned by the Editor.

Short communications/research notes/scientific correspondence (Max length: 2000 words or 8 typed pages including figures) are normally brief reports or technical notes on the progress of ongoing research and/or an application.

(b) Refereeing Process

Papers received for publication are to be peer reviewed by a panel or research experts.

(c) Submission of Typescripts

Typescript should be neatly typed in single space on one side of the A4 size (210 mm x 297 mm) paper, with a margin not less than 40 mm on the left side. It should include: (i) title page with a running (short) title, (ii) abstract, (iii) keywords, (iv) nomenclature of symbols used, (v) tables/figures/illustrations typed/drawn on separate sheets along with their captions in serial order as these appear in text, and (vi) a separate list of figure captions. The reporting in the paper should be in third person.

Manuscripts should be submited online at: **https://publications.drdo.gov.in/ojs/index.php/dsj** in MS Word format. In case of problems in uploading, a copy can be sent at **dsj.desidoc@gov.in**

Authors may furnish the following certificate at the time of submission of manuscript along with covering letter.

[This is to certify that the reported work in the paper entitled "………" submitted for publication in the Defence Science Journal is an original one and has not been submitted for publication elsewhere. I/we certify that citations to the previously reported works have been given and no data/tables/figures have been quoted verbatim from the other publications without giving due acknowledgement and without permission of the author(s). The consent of all the authors of this paper has been obtained before submitting.

[Signatures and names of all the authors]

(d) Title Page

The title page should include: title of the article, name(s) of author(s) and affiliation(s); complete address (including telephone/fax numbers, e-mail address) of the author (in case of a single author paper) or the contact person (in the case of a Co-authored paper) to whom communications should be sent. It should also include a short title not more than 50 characters to be used as running title. The titles should be brief, clear and provide a broad introduction of the paper.

(e) Abstract and Keywords

An abstract of about 200 words for research papers, 150 words for review articles, and about 100 words for research notes and short communications should be provided. Appropriate keywords should be given where necessary.

(f) References and Footnotes

References to already published literature should be numbered consecutively in order of their citation in the text and placed at the end of the text. In the text these should be indicated by superscripts (number placed above the line) [(1)]. References to personal communication should not be placed under references, but cited in the text in the parentheses. A reference should be listed only once. Use of *ibid., idem., op.cit.,* should be avoided. An already cited reference when repeated, should be given in parentheses (for example, ref. 5, p. 79; ref. 15, p. 193; etc). Explanatory material may be given as an Appendix.

Defence Science Journal Style uses a notational method of referencing when referring to a source of information within the text of a document. In its simplest form, a citation is given in the text, consisting of a number in superscript. Examples of citations in different types of documents are given below:

(i) Journal Article

Laxminarayana, Karthik & Jalili, Nadar. Functional nanotube-based textiles: Pathway to next generation fabrics with enhanced sensing capabilities. *Text. Res. J.*, 2005, **75**(9), 670-81. doi: 10.1177/0040517505059330

Weifan, C.; Fengsheng, L.; Jianxun, L.; Song, Hongchang & Yu, Jiyi. Nanometer Co_3O_4 powder by solid phase reaction. *Cuitua Xucbao,* 2005, **26**(2), 1073-77 (Chinese).

Standard abbreviations as per the International Serials Catalogue of the International Council of Scientific Unions–Abstracting Board (ICSU–AB) should be used for the titles of journals. However, single and double worded journal titles (for example, *Nature, Science, Scientific American*) should be given in full.

Electronic sources should include the URL and date of access.

Wang, Z.J.; Birch, J.M. & Dickinson, M.H. Unsteady forces and flows in low Reynolds number hovering flight: Two-dimensional computations vs robotic wing experiment. *J. Experi. Biol.,* 2004, **207**(3), 449-60. doi: 10.1242/jeb.00739 http://jeb.biologists.org/cgi/content/full/207/3/449 [Accessed on 17 November 2007].

(*Contd on inner cover*)

Cover: 65-75